Particle Acceleration and Detection

Mikhail Korzhik
Gintautas Tamulaitis
Andrey N. Vasil'ev

Physics of Fast Processes in Scintillators

Springer

Particle Acceleration and Detection

The series *Particle Acceleration and Detection* is devoted to monograph texts dealing with all aspects of particle acceleration and detection research and advanced teaching. The scope also includes topics such as beam physics and instrumentation as well as applications. Presentations should strongly emphasize the underlying physical and engineering sciences. Of particular interest are

- contributions which relate fundamental research to new applications beyond the immediate realm of the original field of research
- contributions which connect fundamental research in the aforementioned fields to fundamental research in related physical or engineering sciences
- concise accounts of newly emerging important topics that are embedded in a broader framework in order to provide quick but readable access of very new material to a larger audience.

The books forming this collection will be of importance to graduate students and active researchers alike

More information about this series at http://www.springer.com/series/5267

Mikhail Korzhik • Gintautas Tamulaitis
Andrey N. Vasil'ev

Physics of Fast Processes in Scintillators

Springer

Mikhail Korzhik
Research Institute for Nuclear Problems
Belarusian State University
Minsk, Belarus

Gintautas Tamulaitis
Semiconductor Physics Department
Vilnius University
Vilnius, Lithuania

Andrey N. Vasil'ev
Skobeltsyn Institute of Nuclear Physics
Lomonosov Moscow State University
Moscow, Russia

ISSN 1611-1052 ISSN 2365-0877 (electronic)
Particle Acceleration and Detection
ISBN 978-3-030-21965-9 ISBN 978-3-030-21966-6 (eBook)
https://doi.org/10.1007/978-3-030-21966-6

Preface

During the last two decades, an impressive progress has been made in fundamental understanding, engineering, and applications of inorganic scintillators. All steps of the transformation of energy in scintillators, production of secondary electronic excitations, thermalization, migration and recombination, and light emission, are considered, and models proposed show good potential for the scintillation property description and prediction as well. As a result, much understanding of complicated features of the phenomenon, like nonproportionality problem, has been demonstrated. One can mention results on interdependence of nonproportionality and deterioration of scintillator energy resolution. Recently, some additional factors which deteriorate energy resolution, like excitation cluster formation, have been augmented.

Nevertheless, new demanding applications of the materials require combining both high energy and time resolutions. It inspired new development for the basic principles of primary processes in energy relaxation, which plays a key role in formation of scintillating centers. The processes are characterized by quite different spatial and time scales. These scales differ for various classes of scintillators, depending on the electron structure of conduction and valence bands, energy position of core levels, phonon spectrum, presence of activators and dopants. Therefore, the microscopic structure of electronically and vibrationally excited regions is material-dependent. In general, this structure is characterized by high nonhomogeneity and controls relaxation and energy transfer rates. The goal is to make them faster, occurring in a ps domain or even faster, to ensure that the timing characteristics of scintillation detectors do not encounter new challenges in view of the demand for substantially shorter response time in the experiments at high-luminosity colliders and medical applications like time-of-flight positron emission tomography. The feasibility of the substantial improvement of timing in radiation detection systems based on scintillators is supported by the recently substantial improvements of time characteristics of the electronic readout, especially, by the advances in development of fast silicon photomultipliers.

Nowadays, further theoretical and simulation efforts towards a picosecond timing target are accompanied by the study of fast optical phenomena to be exploited for timing of material-radiation interaction.

The book considers the fast processes in the scintillation materials, giving much deeper understanding of the fundamental processes in scintillation. The theoretical and ps-spectroscopy research results, performed by the authors during the last decade, showed the way to engineering and to controlling energy transfer processes in the scintillation materials. It opens door for using the scintillators for precise time tagging of events at the level of ten picoseconds or even better. This initiates new era in high-energy physics instrumentation with ultimate timing performance, medical imaging, and industrial applications.

This book reviews modern trends in the description of the scintillation build-up process, particularly in inorganic materials, transient phenomena, and engineering of the scintillation properties. The readers will find in the book, besides reliable scientific background, educational information and new ideas to implement in their own research and engineering as well. Particularly, it will be of interest for students of different levels, university teachers, and researchers, allowing them to catch an overall picture of a progressively developing study, having immediate implementation in technology.

Minsk, Belarus — Mikhail Korzhik
Vilnius, Lithuania — Gintautas Tamulaitis
Moscow, Russia — Andrey N. Vasil'ev

Acknowledgments

The authors, who are members of Crystal Clear Collaboration (CCC, RD18) at CERN, are grateful to all CCC colleagues for the opportunity of gaining versatile expertise and, especially, to the spokesperson of CCC, Dr. E. Auffray, for the fruitful collaboration, and Dr. P. R. M. Lecoq, one of the founders of CCC, whose ideas were leading in many prospective directions for developing scintillators. They also appreciate their collaboration and discussions with colleagues at CERN and other institutions, especially, A. Belsky, A. Borisevich, G. Dosovitskiy, V. Dormenev, T. Tabarelli de Fatis, A. Gektin A. Gola, M. Lucchini, A. Mazzi, M. Nikl, O. Sidletskiy, and V. Slegel, and their collaborators at home institutions, especially, A. Fedorov, I. Kamenskikh, D. Kozlov, V. Mechinsky, S. Nargelas, D. Spassky, E. Talochka, and A. Vaitkevicius. The collaboration in COST Action FAST and Horizon project AIDA2020 substantially contributed to this book.

Contents

About the Authors

Mikhail Korzhik (Korjik) graduated in Physics from the Belarus State University in 1981 and received his PhD degree in 1991 and his Doctoral Diploma in Nuclear Physics and Optics in 2005. Since the beginning of the 1990s, he was deeply involved in the research and development of inorganic scintillation materials. He was instrumental in the development of the technology of a few oxide scintillation materials, pioneering the Pr^{3+}-doped scintillation materials. His study promoted the understanding of scintillation mechanisms in many crystals. He took part in the discovery and development of mass production technology of lead tungstate $PbWO_4$ scintillation crystal for high-energy physics applications including exploitation of this crystal in two ambitious LHC experiments, CMS and ALICE, first of which made an important contribution to the discovery of the Higgs boson. He is a member of the Scientific Advisory Committee of SCINT and a chairman of ISMART biannual international conferences dedicated to the development of scintillation materials.

Gintautas Tamulaitis graduated in Physics in 1979 and received his PhD degree in 1985 and habilitated doctor degree in 2001 from Vilnius University, where he currently works as a professor. He received two Lithuanian National Science Awards (in 2002 and 2008) and did research as a visiting researcher at the University of California, Berkeley, the University of South Carolina, and the Rensselaer Polytechnic Institute. His main research background is in the experimental study of nonequilibrium quasiparticles in semiconductors and their low-dimensional structures by using time-resolved and spatially resolved photoluminescence spectroscopy and techniques based on nonlinear optics. Currently, his research is focused on the study of fast nonlinear optical processes to be exploited in future radiation detectors with timing of the order of 10 ps and search for novel single crystal materials and glass ceramics prospective as fast scintillators.

Andrey N. Vasil'ev graduated from the Faculty of Physics at Lomonosov Moscow State University in 1975 and received his PhD degree in Theoretical and

Mathematical Physics in 1978 and his Doctoral Diploma in Optics in 1995. He is a department head at Skobeltsyn Institute of Nuclear Physics of Lomonosov Moscow State University. His main activities were focused on the investigation of luminescence of inorganic insulators excited by VUV and X-ray synchrotron radiation and by ionizing particles. His in-depth study of all stages of energy relaxation in scintillators contributed to contemporary understanding of nonproportionality, formation of light yield, response kinetics, and energy resolution of scintillators. He is a member of the Scientific Advisory Committee of the International Conference SCINT.

Chapter 1
Release of Ionizing Radiation Energy in Inorganic Scintillator

Abstract This chapter introduces the basic definitions and describes the energy release in the interaction of scintillation material with different kinds of ionizing radiation. The timing property of the energy deposition is under especial focus.

1.1 Introduction

Scintillation materials have been exploited in physical measurements, especially for the measurements of ionizing radiation, for more than a century. Scintillation can be observed in various inorganic and organic crystalline media [1–4], fluids [5–8], gases [9, 10], including liquid noble element gasses [11, 12], polymers [13], and metamaterials [14]. In the current book, we focus on the most extensively used scintillators: crystalline inorganic scintillation materials. To date, a number of monographs describing and classifying the properties of inorganic scintillation compounds have been published to streamline the available knowledge and to introduce new scintillation materials combining an increasing number of their characteristics that are close to the parameters of an ideal scintillator [15–18].

Scintillation is luminescence induced by ionizing radiation in transparent dielectric medium. Like any other luminescence, it might be characterized by a set of measurable characteristics regardless of whether the scintillation material is activated with certain dopants to form the light–emitting centers, emits due to intrinsic defects or excitons (self-activated) or due to cross-luminescence. The main scintillation characteristics related to the physical process of light production in the medium are discussed below.

The scintillation yield (Y) is the number of photons emitted by scintillator at the absorption of the energy E_γ of ionizing radiation. A simple formula accounting the major processes contributing to scintillation is necessary. This idea was first stated explicitly in [19, 20] and the simplified formula was suggested for γ-quanta:

$$Y = \frac{E_\gamma}{\beta \cdot E_g} S \cdot Q \tag{1.1}$$

M. Korzhik et al., *Physics of Fast Processes in Scintillators*, Particle Acceleration and Detection, https://doi.org/10.1007/978-3-030-21966-6_1

Here $\beta \cdot E_g$ is the mean energy necessary for the formation of one thermalized electron-hole pair in a medium with the band gap E_g, E_γ is the absorbed energy, $S < 1$ is defined by the efficiency of the energy transfer from non-equilibrium carriers to the excited states of emitting centers, and $Q < 1$ is the quantum yield of the intracentre luminescence at a given temperature. In practice, to compare the yield of different scintillators measured with different radiation sources the number Y/Eγ abbreviated LY (Light Yield) is used and expressed in ph/MeV. The formula is applied also for other kinds of ionizing radiation with an appropriate proportionality coefficient. The general model of the scintillation yield implicates quite complex expressions [Vasil'ev in 21] accounting for many processes of the scintillation.

The scintillation kinetics is defined as the time evolution of scintillation intensity $S(t)$. The time-integrated intensity $= \int S(t)dt$. The scintillation is detected by photo-sensor. A scintillation pulse observable by photo-sensor consists of two stages: the leading edge and the decay part. The leading edge, as will be shown in this book, is affected by many factors, in particular, those, which are caused by the light propagation in the scintillator and by the time necessary to excite the emitting centers. Therefore, it can be parameterized directly in photons arrived at certain time t to the photo-sensor, or by a corresponding function describing the rise of the scintillation pulse. Hence, we can introduce the rise constant, an effective rise time of the leading edge of the scintillation pulse. It is usually larger than the intrinsic rise time of the emission center which can be measured at intracentre excitation. The intrinsic rise time reflects the population of the excited radiative states of the emission centers. Provided that the interaction of the radiative centers with the defects in the host matrix can be neglected, the intrinsic rise time is caused by intracentre relaxation of the electronic excitations, which can be observed at photoexcitation. The decay part depends on scintillation mechanism and is usually similar or longer than the luminescence decay at photo-excitation. It is common practice to describe such decay kinetics by an exponential function or by a sum of exponentials with different time constants and weight coefficients. Therefore, the process may be characterized by a set of decay time constants τ_i, defined as the time after which the amplitude of the corresponding component decreases by a factor e, and the corresponding fractions of these components in the scintillation response.

Among a wide variety of luminescent inorganic materials, only nearly 200 are known to demonstrate scintillation. Inorganic scintillators are produced by different methods, the benchmark of which is the rate of raw material transformation to crystal mass. Due to this reason, most of the crystals have excess defects of different origin with concentrations by a few orders of magnitude larger than the thermodynamic limit. The defects trap nonequilibrium carriers created under ionizing radiation. As a result, a long phosphorescence tail occurs in addition to relatively scintillation. The afterglow parameter is used as a measure of the contribution of phosphorescence to scintillation. It is defined as the intensity of luminescence excited by ionizing radiation and measured after certain time, e. g., $10 \cdot \tau$, where τ is the decay time of the longest scintillation component.

Next, radio- and photo-luminescence spectra are the wavelength (or frequency/energy) distributions of the luminescence intensity. A luminescence band is characterized by the peak position in scales λ_{sc} (nm), ν_{sc} (cm^{-1}), or E_{sc} (eV) (1 eV = 8065 cm^{-1}) and half-width $\Delta\lambda_{sc}$ ($\Delta\nu_{sc}$, ΔE_{sc}) at a given temperature. The scintillation spectrum is an important parameter for spectral matching of the light emitted by scintillator with the sensitivity spectrum of photosensor. Since the final stages of radiative recombination of nonequilibrium electron-hole pairs do not depend on the type of their excitation, the scintillation spectrum is identical with the spectra of the radio- and, in most cases, photoluminescence, provided that the spatial excitation distribution and the reabsorption of the luminescence are properly accounted for. However, the scintillation light has additional property: the total energy of the light emitted per one scintillation reflects the energy deposit from the ionizing radiation.

At the excitation of scintillation, an important issue is the presence of the interaction mechanism resulting in energy loss by particles and γ-quanta in a medium of the scintillator. The action of any of such mechanisms is limited in space and time due to limitations imposed by the volume of the scintillator and velocity of the ionizing particle in the media. In any event, energy deposit in the media by ionization leaves its trace on the scintillation development in space and time. Therefore, we start our consideration from the analysis of the energy deposit in the media at the interaction with the ionizing radiation of different kinds, focusing on the characterization of its time parameters.

1.2 Energy Deposit and Released Energy Localization in Space and Time

1.2.1 Low Energy Photons, γ-Quanta and Charged Particles

An intracentre absorption of the optical photon by a luminescent center in inorganic luminescent material is a prompt act of electromagnetic interaction of the photon and the luminescent center, which is either an impurity, a matrix-building ionic complex, exciton or structural defect. In the case when the absorbed photon does not conveys to the excited electron the kinetic energy sufficient for autoionization, the excitation occurs in a small volume limited usually by the outer electronic shell of the ion or an anion coordination sphere around the cation or defect, in a more complicated case. Note, this localization is typical for inorganic ionic compounds rather than for semiconductors.

When the photon energy exceeds the threshold for photon multiplication, the kinetic energy of the excited electron is sufficient for the production of additional electronic excitation [Vasil'ev in 22]). The interaction event includes several steps: creation of primary and secondary pairs and their thermalization. The excitation becomes delocalized due to the spreading of nonequilibrium electrons and holes

during their relaxation. Moreover, a luminescent center cannot emit more than one photon simultaneously, so several luminescent centers are involved in the radiative stage of the excitation relaxation.

The excitation delocalization depends on the energy of the incident photon and the composition of the host matrix of the scintillator. At low energies below a few MeV, the electrons of the material are involved in the electromagnetic interaction via the following energy-dependent and competitive processes: (i) photoelectric absorption, (i) Compton scattering, (iii) electron-positron pair production.

The photoelectric absorption is a process of complete absorption of the incident photon with energy E_γ by electrons of inner filled shells having energy E^i_{sh}. An electron is generated with the kinetic energy

$$E_{kin} = E_\gamma - E^i_{sh} \tag{1.2}$$

This absorption is accomplished by femtosecond emission of a set of Auger electrons which total energy is about E^i_{sh}. Therefore, the energy of *X*- or γ-photon is converted totally into the energy of electronic excitations. The probability of the photoelectric absorption is higher for deeper electronic shells. More than 80% of the photons in the incident flux involved in the photoabsorption and having a photon energy larger than that of *K*-shell cause the emission of the *K*-shell electrons. The energy of the *K*-shell varies within an order of magnitude from ~10 keV for the light metals to the tens of keV in high charge *Z* nuclei of stable elements, like *W* or *Pb* (70 and 88 keV, respectively) [23]. The *K*-shell edge for lanthanide ions varies in the range from 57 to 63 keV.

For the photons with the energy lower than the binding energy of the K-shell, the other shells, *L* and *M*, become involved in the photoabsorption. Similarly to the K-shell, the binding energies for *L* and *M* shells and their substructures depend on the atomic number of the absorbing atom Z as $\propto a \cdot Ry \cdot Z^2$, where *Ry* is the Rydberg energy and $a = 1$, 0.25, and 0.11 for *K*-, *L*-, and *M*- shells, respectively.

The electron emitted from the outer shell spends its kinetic energy for the excitation of the atoms and their ionization, creating secondary electrons along with its path in the media. The primary electron energy loss rate d*E*/d*t* depends on the crystal density ρ, charge nucleus *Z* and the atomic number of the material *A* as $dE/dt \propto \rho \cdot Z/A$ [24]. This dependence, in spite of the different energies of the absorbing shells, results in a moderate, ρ dependent difference in the trajectory length of the electrons emitted in different compounds. The average time for the energy deposit <*t*> of a non-relativistic electron knocked out from the inner shells is small but finite. It can be estimated from a simple expression:

$$< t > \sim R_{\text{ext}}/v_{\text{mean}}, \tag{1.3}$$

where R_{ext} is the extrapolated path length of a charged particle and v_{mean} for non-relativistic electrons equals approximately a half of the initial velocity v_0:

$$v_0 = c \cdot \sqrt{\left(1 - \left(mc^2/\left(mc^2 + \mathrm{E}\right)\right)^2\right)}, \tag{1.4}$$

where E and m are the kinetic energy and mass of the ionizing particle. Figure 1.1 shows the dependence of the time of the energy deposit on the kinetic energy E_{kin} of the electron in light and heavy scintillation media: $Y_3Al_5O_{12}$: Ce (density $\rho = 4.55$ g/cm^3) and $PbWO_4$ (8.28 g/cm^3).

The initial energy of the high-energy photon is absorbed locally, however, the excitation is delocalized in space during the subsequent energy deposit in the material. Secondary particles are subjected to a thermalization due to the interaction with phonons. Energy release for the electron, having kinetic energy in the range 10–100 keV varies bellow 100 fs, what is the same order of magnitude with secondary electrons thermalization time (see details in Chap. 3) in crystals with light ions and by an order shorter than in crystals containing only heavy ions [25]. The energy deposition trajectory is a consequence of random collisions in the medium. After their thermalization, the nonequilibrium carriers in the medium occupy a certain volume, which is far beyond the volume of a unit cell of the material. A typical distribution of the electrons and holes created by 200 keV γ-quantum in NaI(Tl) scintillator after their thermalization, is presented in Fig. 1.2.

Being expanded in space, the thermalization of the resulting ensemble of nonequilibrium carriers occurs during a finite but still a very short time. Nevertheless, the distribution of the thermalized carriers in space with a typical path length of a few microns involves a number of other processes accompanying the transfer of excitations to luminescent centers. As shown below, these processes make a significant contribution in the timing parameters of the scintillation pulse.

The energy deposit from the Compton scattering is even more delocalized in space than that from photoabsorption. In the Compton scattering, the incoming photon interacts with an individual electron at rest on the matrix-building atoms.

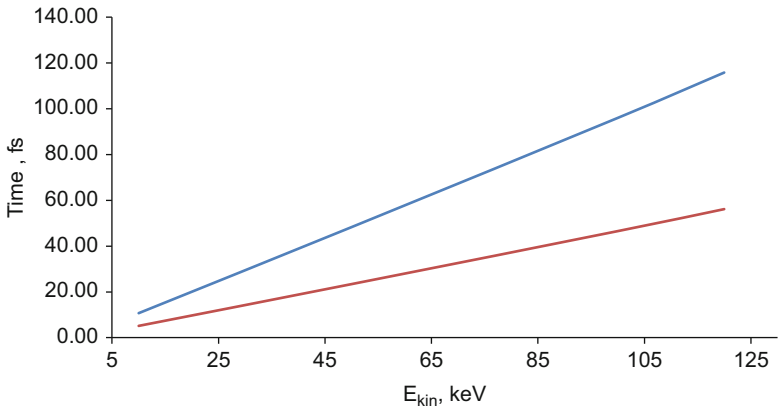

Fig. 1.1 Dependence of the average energy deposit time on kinetic energy of a non-relativistic electron in light and heavy scintillators: $Y_3Al_5O_{12}$: Ce (blue) and $PbWO_4$ (red)

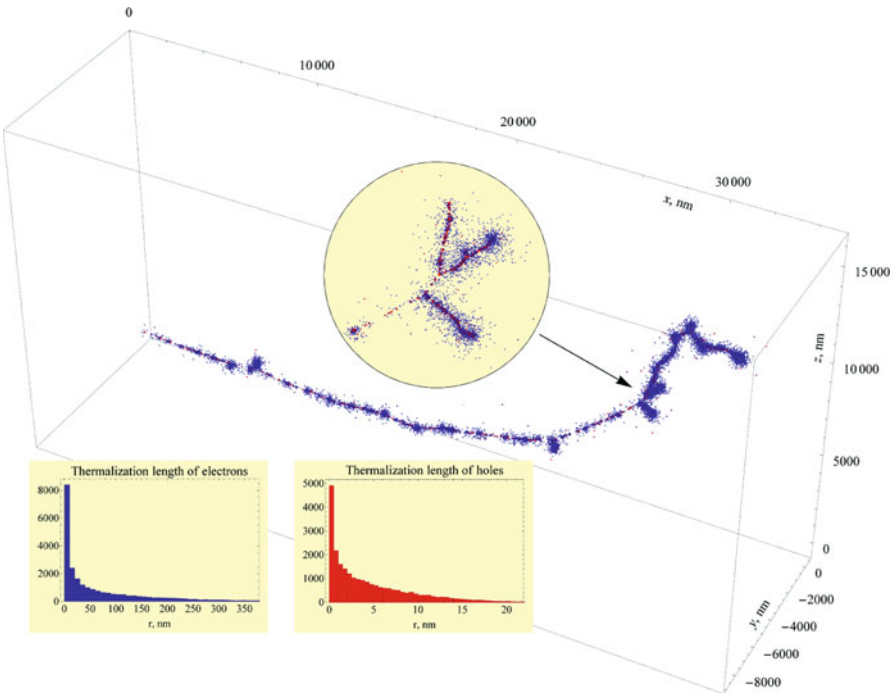

Fig. 1.2 Spatial distribution of electrons and holes after thermalization due to photoabsorption of a 200 keV γ-quantum in NaI(Tl) scintillator

The kinetic energy of the recoil electron and energy of the scattered photon depend on the angles of their propagation in respect to the propagation direction of the incoming photon. Due to the probabilistic nature of the interaction of photons and electrons, the scattering causes a wide volumetric spread of the interactions. A typical mean free path of X-ray photon is much longer than the free path of an electron with the same kinetic energy [26]. Being scattered in one or a few collisions, the gamma-quanta might be finally absorbed far from the primary interaction point or even escape the material. Moreover, the recoil electrons acquire kinetic energy ranging from zero, if γ-quantum is scattered at a small angle, to the edge of the Compton scattering [23]. These electrons also contribute to the energy release. As a result, the energy deposit due to Compton scattering is delocalized in space and delayed in time, in spite of the fast energy deposit of individual recoil electrons or absorbed quanta. In this sense, the distribution of energy deposit due to Compton scattering is similar to that due to interaction with high energy particles, with only one difference, a much smaller magnitude. In practice, the pulse height spectrum, which is the distribution of the amplitudes of many scintillation events, is detected with photosensor and dedicated electronics. A typical pulse height spectrum of 662 keV γ-quanta of ^{137}Co source measured with $Gd_3Al_2Ga_3O_{12}$: Ce (GAGG) scintillator and SiPM photosensor is presented in Fig. 1.3.

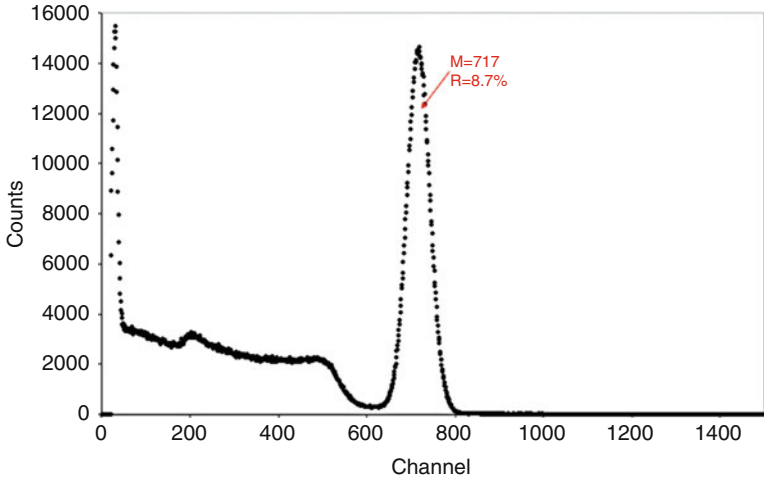

Fig. 1.3 Pulse height spectrum of 662 keV γ-quantua measured at room temperature with dia 18 × 60 mm GAGG scintillation crystal coupled to a 2 × 2 matrix of 6 × 6 mm^2 SensL MicroFC 60,035 SMT silicon SiPM

Peak on the right is a photo-peak, the signals bellow a valley are form Compton scattered γ-quanta and escape peaks as well.

Low-energy charged particles, electrons and positrons, nuclei of different atoms and their fragments may be either incident externally or created in the bulk of the scintillator. The electrons, incident or produced at the decay of isotopes in the scintillator, lose their energy for the excitation of the atoms of the media and their ionization, creating secondary electrons along their propagation path. Positrons, being particles of the anti-matter, annihilate by emitting 511 keV γ-quanta, which lose their energy via the mechanisms described above. Alpha- particles, which are ionized helium He nuclei, lighter deuteron and triton as well can be either incident particles from external sources or occur in the material as a result of spontaneous decay and strong interaction with atomic nuclei of the scintillator.

Figure 1.4 shows the dependence of the energy deposit time on the kinetic energy of an α-particle in light ($Y_3Al_5O_{12}$: Ce) and heavy ($PbWO_4$) scintillation media. Here, formulas (1.3) and (1.4) have been exploited. It is worth noting that the energy release takes a longer time for the heavy alpha particle than for the electron, but still remains of the same order of magnitude as the duration of thermalization of nonequilibrium carriers.

The fragments of nuclei fission, which appear, particularly, in heavy scintillation materials as a result of interaction with heavy energy hadrons, not only deposit energy in the media, but also produce displacements of the atoms resulting in formation of the defects of microscopic dimensions, which are called stars. In practice, scintillators are not exploited for detection of the fragments; however, if the energetic nuclei fragments emerge in the scintillator, they produce local structure

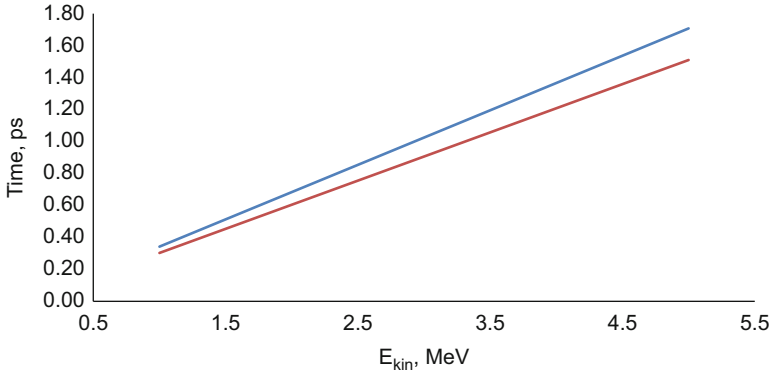

Fig. 1.4 Dependence of the average energy deposit time on the kinetic energy of α -particle in two scintillators: $Y_3Al_5O_{12}$: Ce (blue) and $PbWO_4$ (red)

defects in the matrix and, consequently, might modify scintillation properties of the material. In average, a typical heavy fragment at the fission in $PbWO_4$ under 24 GeV protons has a mass A of ~130 and a number Z of ~50 [27]. Its energy losses and energy deposit time can be estimated as in [28], the averaged path in the material at a kinetic energy of 10 MeV equals 13 microns, whereas the deposit time is estimated to be 10 ps. Note, the energy deposit time is substantially larger than the thermalization time of nonequilibrium carrier.

1.2.2 High Energy γ-Quanta and Charged Particles

With an increase in the energy of the particles interacting with substance through an electromagnetic channel, in addition to photo-absorption and Compton scattering, e^-e^+ pair production becomes the dominant mechanism of the interaction with the scintillator. The electron-positron pair production occurs in the vicinity of nucleus as the energy of the incident photon energy exceeds twice the energy equivalent of the electron mass at rest. The pairs can be produced in the proximity of electrons; however, the threshold energy is by a factor of two higher than that in the proximity of nuclei. The dominant process is the pair production in the proximity of nuclei, especially, in heavy materials, where production cross-section is by $\sim Z$ larger than that in light materials. For low-energy γ-quanta emitted in the interaction, the energy deposit for an individual photon is quite fast, as described above. However, when the energy of incident photons is over a few MeV, a multiple pair production becomes probable. This process is called an electromagnetic shower: the high energy photons lose their energy in the Coulomb field of nuclei or they produce Compton electrons, these electrons and positrons, in turn, produce more photons, which experience Compton scattering et cetera.

Table 1.1 Minimum ionization particle energy deposit per mm in several scintillation media

Material	Plastic scintillator	$Y_3Al_5O_{12}$: Ce,Mg (YAG)	Lu_2SiO_5: Ce (LSO: Ce)	$(Lu_x\text{-}Y_{1\text{-}x})_2SiO_5$: Ce (LYSO:Ce)	$Gd_3Al_2Ga_3O_{12}$ (GAGG) multidoped
ρ, g/cm^3	1	4.55	7.4	7.2	6.63
LY, ph/MeV	10,000	30,000	27,000	29,000	46,000
d*E*/d*x* @ e$^-$, $\pi^\cdot$ MeV/mm	0.158	0.59	0.87	0.85	0.81
Yield, ph per 1 mm per *mip*	1580	17,700	23,500	24,600	37,200

The collision losses formula introduced by Bohr [29] and updated by Bethe [30] and Bloch [31] predicts a fast decrease of specific losses for ionization with aspiration of primary particle velocity to the speed limit. A particle in the energy loss minimum is called a minimum ionizing particle (*mip*). Table 1.1 shows a *mip* energy deposit in different scintillation media. In spite of quite small time of energy release by the individual photo-ionized electron, the *mip* energy deposit occurs in time, which is proportional to the scintillator length and is ~20 ps for a 0.5 cm-long scintillator. As may be concluded from Table 1.1, the higher is the material density, the smaller $<t>$ can be achieved. In a shorter scintillator, the average time for the energy deposit bellow 10 ps can be achieved. This time is by an order of magnitude higher than the thermalization time of noneqlibrium carriers.

A typical pulse height spectrum of mip measured with 3 × 3 × 5 mm LYSO scintillator with SiPM photo-sensor is presented in Fig. 1.5.

When the energy of electron or its antiparticle exceeds a few tens of MeV, the radiative energy losses, called bremsstrahlung, become a substantial contributor into the electromagnetic cascade. This radiation occurs due the deceleration of the particle traversing the scintillator media. For a relativistic particle with a unit charge, the energy losses due to bremsstrahlung d*E*/d*t* is proportional to Z^2/m^2, where *m* is the particle mass. Hence, relativistic light particles, like electrons or μ-mesons have a considerably larger probability for radiative energy losses than protons or charged π-mesons.

Due to the variety of the energy loss process in the electromagnetic shower, it occupies a relatively large volume, which is characterized by two quantities: radiation length X_0 and Moliere radius R_M. Nearly 95% of the energy of the primary particle is deposited within the volume equal to a cylinder with a diameter of $2R_M$ and a length of 25 X_0. Table 1.2 shows the comparison of X_0 and R_M for scintillators extensively used in calorimetry.

Spatial spread of the shower causes relatively long time for energy deposition. Fig. 1.6 shows the spatial distribution of shower and the time profile of energy deposition of a 100 GeV-electron in $PbWO_4$ scintillation element with a cross section of 2 × 2 cm^2 and a length of 1.5 X_0, 5 X_0, and 20 X_0, simulated using GEANT 4 code. The time profile is averaged over 1000 events.

Here and after we will use quite frequently results of the simulation by this code. The object-oriented software package GEANT4 was developed by an international

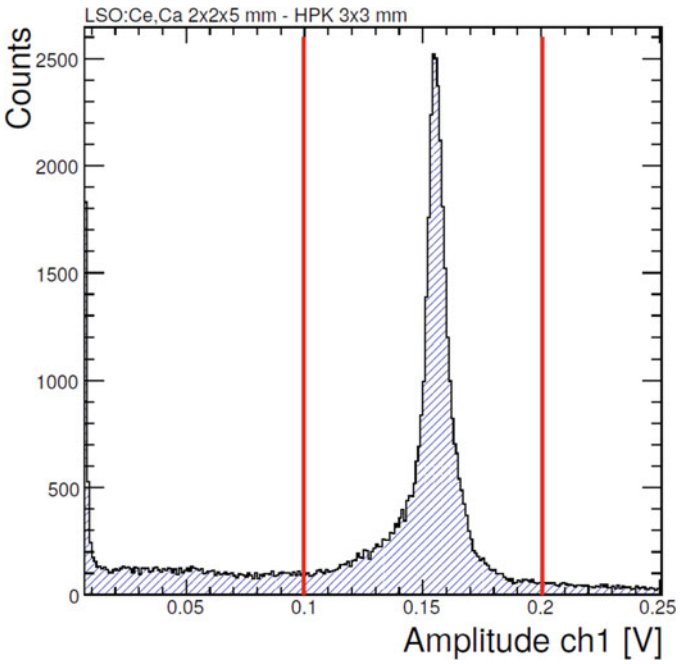

Fig. 1.5 Pulse height spectrum of *mip* measured with 5 mm thick LSO scintillation crystal and HPK SiPM at room temperature at SPS *at* CERN (Courtesy of Dr. M. Lucchini, CMS Collaboration)

Table 1.2 Density, radiation length X_0, and Moliere radius R_M of scintillation materials used in modern homogeneous calorimeters

Material	CsI	BGO	$PbWO_4$	BaF_2
ρ, g/cm^3	4.53	7.13	8.28	4.88
X_0,cm	1.85	1.12	0.89	2
$R_{M,}$ cm	3.8	2.4	2.2	3.4

scientific collaboration at the European Particle Physics Laboratory (CERN) and is designed to make Monte-Carlo simulation of the interaction of radiation with matter. The software package is written in the C++ programming language and is based on an earlier version of the program – GEANT3, which was written in the FORTRAN language. The built-in GEANT4 tools allow to fully describe many things involved in a measurement of the physical quantities and, even more: to simulate the geometry of the detecting system, an influence of the chemical composition on the detector properties, the types of particles participating in the interaction, the physical processes, which control the interaction of the particles and, to visualize the geometry and particle tracks.

The development of the package begins in the 70s of the last century at CERN. The need for such a package was dictated by an increase in the complexity of

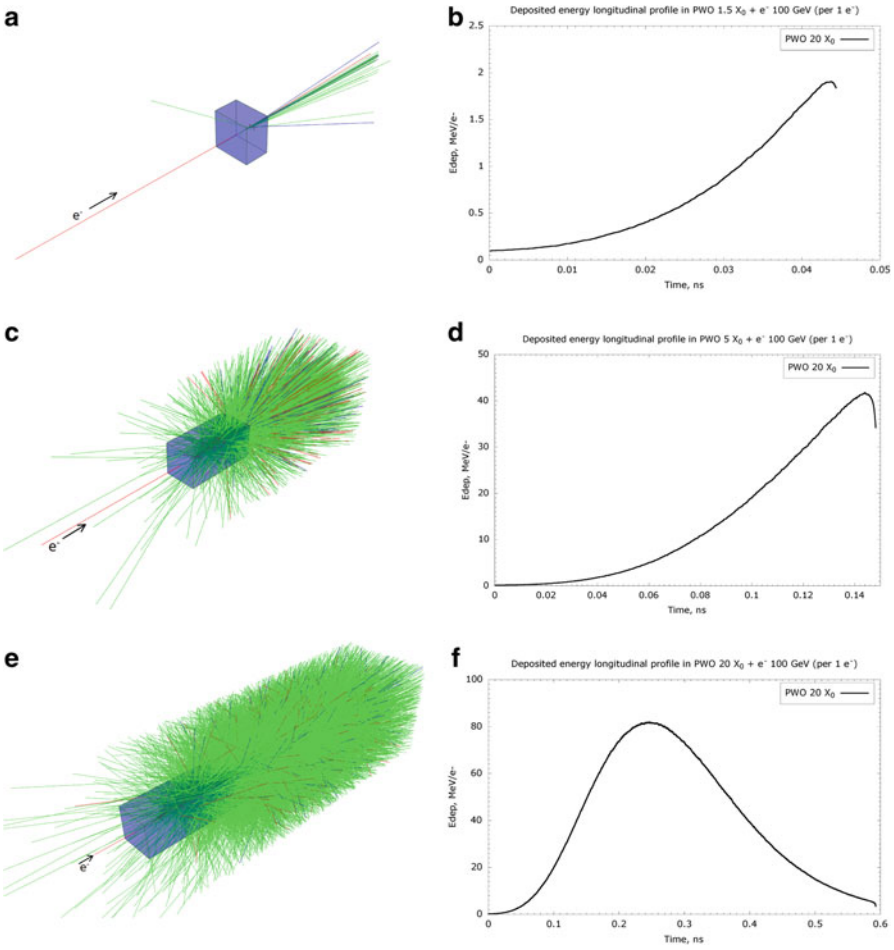

Fig. 1.6 GEANT4 image of interaction products (**a**, **b**, **c**) and time profile (**e**, **d**, **f**) for energy deposit of a 100 GeV-electron in lead tungstate scintillation crystal with a cross section of 2×2 cm^2 and a length of 1.5, 5 and 20 X_0

experimental problems and the structure of installations: the problem of mathematical modeling of both the process of passing particles in a matter and the response of detectors of the experimental setup to various types of radiation became more complex with increasing energy. This approach became a powerful tool to save human and material resources to prepare a physical experiment, to plan the experiment in advance, as well as to interpret its results.

The set of realized interaction processes is quite extensive and includes electromagnetic, hadronic and optical processes, processes of decay, processes of evolution of short-lived particles in the energy range from fractions of eV to several TeV. The package allows setting a very complex system geometry.

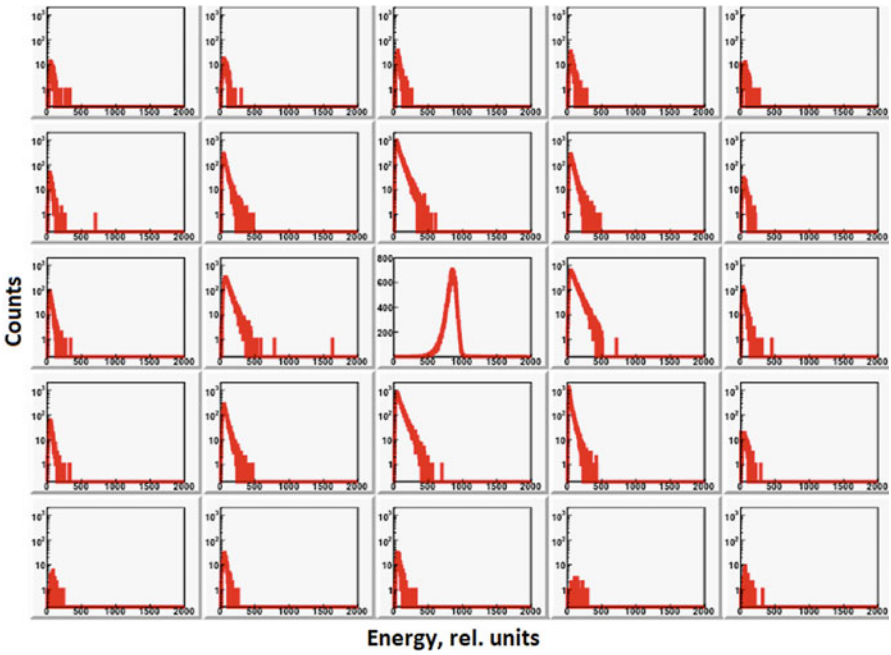

Fig. 1.7 Pulse height spectra of 178 MeV electron beam entering the central cell of a 5 × 5 matrix of 20 cm PWO crystals with PMT readout at room temperature (Courtesy of Dr. V. Dormenev, PANDA Collaboration)

The GEANT4 simulation package is widely used in particle physics, nuclear physics, in the design of accelerators and spacecraft, in medical physics. It is free software.

At a low thickness of the scintillator, just slightly larger than X_0, the energy deposit is accomplished by bremsstrahlung. The duration of the energy deposit is the time, which is necessary for the electron to traverse the medium. The energy deposit ends at the back surface of the scintillation element.

The energy deposit from the shower obviously becomes dominant at the scintillator length of $5X_0$, whereas the peak of the energy release is still close to the end surface. In a long scintillation element, the energy deposit has a peak, which appears due to shower quenching and leak over the scintillation element. Figure 1.7 shows a typical distribution of the energy deposit from the shower in a 5 × 5 matrix of 2 × 2 × 20 cm long PWO scintillator cells.

All the cells in the matrix show signals evidencing a shower spreading away from the central cell of the detector. The central cell with the largest energy deposit shows a well-pronounced peak, whereas the other cells show signals deceasing in amplitude as the distance from the central cell increases.

Both the spreading in space and the increase in time $< t >$ up to a sub nanosecond domain makes the time profile observed with a photo-sensor strongly dependent on the effects related to the light propagation in the medium. This issue will be discussed in Chap. 2.

1.2.3 Uncharged Particles

Among non-charged particles, neutrons are of a particular interest. Most techniques of thermal and epithermal neutron routine measurements are based on the interactions of neutrons with nuclei of several isotopes with a high neutron capture cross section: ^{3}He, ^{6}Li, ^{10}B, Gd, or U. The concentration of such interacting nuclei in a unit volume of a detector determines its volumetric sensitivity. From this point of view, He- and Li-based compounds require enrichment, which makes the materials rather expensive. On the other hand, both B and Gd have enough of isotopes effectively interacting with neutrons even in their natural abundance.

Widespread neutron detectors, ^{3}He proportional gas counters with pressure in a range of 1.5–2 MPa, have acceptable sensitivity in the energy region of thermal and epithermal neutrons [32, 33]. The kinetic energy of the interaction products deposited in the gas is ~0.76 MeV. However, due to a relatively low density of the gas, the energy deposit spreads over a distance of millimeters making the duration of the electric pulse time of gas-filled detectors typically as long as a few microseconds, which limits the counting rate and timing capabilities. Similar response properties demonstrate also various modifications of the counters filled with B gases or gas tubes with boron deposited on their inner walls.

In inorganic scintillation material, where the concentration of interacting nuclei is at a level of $1 \cdot 10^{22}$ atoms/cm^3 the absorption of neutrons by nuclei with high neutron interaction cross-sections results in secondary radiation, γ-quanta or charged particles. A higher concentration of neutron absorbing nuclei is typically achieved in solid state scintillators made from isotopically enriched raw materials, e.g. up to $1.5 \cdot 10^{22}$ atoms/cm^3 for ^{6}Li-based crystals, glasses and glass–ceramics [18]. The energy deposit at a level of ~4.78 MeV in Li-based inorganic material is due to the kinetic energy of α- and triton t- particles created at the interaction of ^{6}Li nuclei. At the interaction of ^{10}B nuclei with a neutron, both γ-quanta (0.48 MeV) and predominantly α-particles with a kinetic energy of 1.47 MeV are emitted. In the compounds of both types, the energy deposit time is reduced and depends on the processes discussed in Sect. 1.2.1.

A natural mixture of gadolinium isotopes has the largest cross section for absorption of thermal neutrons ($E_n = 0.0253$ eV) among the naturally stable isotope mixtures, approximately 46,000 bn [34]. This value by far exceeds that of ^{3}He, ^{6}Li, or ^{10}B nuclei. Moreover, unlike the naturally abundant ^{3}He and ^{6}Li, gadolinium does not require expensive isotopic enrichment to be an effective neutron absorber. A

broad range of resonances additionally increases the neutron absorption efficiency of Gd for neutron energies from ~1 eV up to ~10 keV. For low kinetic energy neutrons, the reaction products of (*n, γ*) reactions on ^{155,157}Gd isotopes are ^{156,158}Gd ions and numerous *γ*-quanta over the wide energy range up to 8.5 MeV. The low-energy *γ*-quanta, which are emitted by nuclei due to relaxation from the first excited state are of particular interest, because they can create short trajectories, as discussed above. The transitions from the first and second excited states of ^{156,158}Gd have transitions at the energies of 89, 79, 192, and 181 keV, respectively. *γ*-quanta of the energies nearly 300 and 278 keV are emitted at the de-excitation of the third excited state [35]. Moreover, some of the emitted γ-quanta can interact with an inner electronic *K*-shell, giving rise to the characteristic *X*-rays and *γ*-quanta of reduced energy.

Starting from the particle energy of ~55 keV of, the neutron inelastic scattering in Gd is accompanied by the γ-quanta emission, forming distinct lines in the spectrum of *γ*-quanta emission [36]. These spectral features provide a potential opportunity of getting information on the energy of incident neutrons directly from the spectra measured with a Gd-based scintillator. In any way, the generation of a set of the low energy *γ*-quanta provide good capabilities to get fast response from the detector.

Moreover, under irradiation by fast neutrons, Gd exhibits a set of distinct lines in the *γ* range in the vicinity of 1 MeV or larger [37]. As shown by GEANT4 calculations and confirmed experimentally [38], the fast neutrons generate a similar set of *γ*- lines. Beside the distinct lines, fast neutrons produce a continuum of γ-quanta expanding over the 1 MeV range. The pair generation can occur inside the material when gamma-quanta with energies above 1022 MeV are produced in interactions with neutrons. The intensity of the annihilation line is expected to correlate with the energy of the neutrons, because the distribution of the *γ*-quanta continuum depends on the energy of incident particles. However, the high-energy gamma-quanta can be generated in surrounding materials: 1885 keV and 10,831 keV nitrogen lines are from the air, the 2224 keV hydrogen line is from the blockhouse walls and air as well. Passing through the scintillation element, these gamma quanta also contribute to the pair production. Thus, the annihilation peak in the crystal has a dual origin. The energy deposit process in the detector material is substantially expanded in time, in comparison with the response time in interaction with low energy *γ*-quanta.

Another approach for the fast timing in detection of fast neutrons is using heavy scintillation materials, like BGO, to detect prompt *γ*-quanta above 1 MeV emitted due to the interaction of fast neutrons with heavy nuclei [39]. However, the neutron capture cross section is relatively low, and the method requires the utilization of rather bulky scintillation elements to get the sufficient signal due to photo-absorption. Moreover, the heaviest scintillators like BGO or PWO possess a low light yield [18], which makes difficult to achieve good timing properties.

Nowadays, the detection of anti-neutrino is a challenging task, particularly, in view of providing practical information on the specific features of nuclear power plants [40]. It is known that the number of antineutrino per fission *of* ^{239}Pu is less than that per fission of ^{235}U. Thus, reliable detection of antineutrino flux gives an opportunity of monitoring the change in the relative amount of the fissile materials in

the reactor. Most of the detectors for antineutrino detection utilize the inverse beta decay $\tilde{\nu}_e + p \rightarrow e^+ + n$, where an antineutrino interacts with a hydrogen nucleus, predominantly in the organic or liquid scintillators, producing a neutron and a positron. The signature of the process is positron annihilation. Various experimental tricks have been exploited to detect either a separate annihilation γ-quanta or the total energy release in the scintillation medium. Bulk organic scintillator is not the optimal medium for of the measurements of this kind. The detector has to be relatively large to detect the low flux of the antineutrino at the level of a few hundred per day at the conditions of a strong background due to events initiated by neutrons. At such circumstances, reliable discrimination of the events generated by neutrons and cosmic rays is one of the key problems in the future development of the experimental techniques. Moreover, the utilization of time-of-flight registration of the annihilation γ-quanta might bring additional benefits for future signal/noise ratio optimization.

The difficulties in neutrino registration cannot be compared with many years of efforts on enabling the detection of a heavy neutral Higgs particle [41]. The experimental results of both ATLAS and CMS collaborations at CERN showed that the mode of boson decay $H \rightarrow \gamma\gamma$ [42] is the most reliable channel for the particle discovery at the condition of the strong background of experiments at LHC. Precise electromagnetic calorimetry in combination with a multilevel trigger enabled identification of reasonable amount of the candidates for this event. The breakthrough in the detection was based on compact localization of the energy deposit of the produced γ-quanta within the Electromagnetic calorimeter [43] made from scintillation material with X_0 bellow 1 cm. In fact, the philosophy behind the short-living neutral particle registration through $\gamma\gamma$-channel is linked to the first results on the registration of π^0 particle decay in the early days of the particle physics at accelerators [44].

1.3 Identification of Energy Deposit Events in Scintillators

1.3.1 Low-Energy γ-Quanta

As discussed above, the energy deposit volume at the photo-absorption of a single low energy γ-quantum in inorganic scintillator is well localized and energy release time is quite short. In the applications based on the detection of each event of the interaction the event might be identified by registration of the first photons of the scintillation. This opportunity is utilized in Positron Emission Tomography (PET) medical imaging technique where the frequency of events in a single detecting unit is quite small and optical noise from the scintillation material within the time gate of the registration is vanishingly small. Obviously, a high light yield and dense scintillation materials allow for improved discrimination of photo-absorbed and Compton scattered γ-quanta. A shorter decay time enables using a smaller registration gate and, as a consequence, having a lower integrated noise of photo-sensor and

electronics. For a long time, the need for reliable separation of the photo-absorption peak from the Compton edge by reducing its half-width was the main line in the search for scintillators for PET scanners that would combine a high light yield and a high photo-absorption efficiency. In a small volume of heavy and high light yield scintillator, a compact space-time localization of a photo-absorption event predetermines the importance of the effects causing population and depopulation of the radiative centers of the scintillator as a limiting factor for better precision in these measurements.

1.3.2 Calorimetry in High Energy Physics

High Energy Physics (HEP) is a driving force in the development of new scintillators because of the high level of performance required for the detectors exploited in particle physics experiments and because of the large volumes of the scintillation material needed for the detectors. A crucial difference between the scintillation detector operation modes in medical imaging and HEP experiments is a strong irradiation background in the latter case. There is a variety of the consequences of the influence of irradiation environment on the conditions of the measurement. Here, we focused just on additional optical noise in the scintillator. The origin of optical noise is the activation of scintillation material. Further physical programs at High Luminosity Large Hadron Collider (HL LHC) or Future Circular Colliders (FCC) will require a substantial increase in the accelerator luminosity. For example, starting from 2026, the luminosity in HL LHC will be increased to 300 fb^{-1} per year, and the integrated luminosity of 3000 fb^{-1} per decade is expected to be accumulated. At such luminosities, the fluence of charged hadrons of up to 10^{15} p/cm^2 is expected in the large pseudorapidity regions of the detectors. The scintillator performance might be affected by the long- and short-living isotopes introduced in the crystal by proton irradiation. This problem never come in medical instrumentation and is a specific problem to operate in a harsh irradiation environment of collider, fix target and spallator experiments.

The induced radioisotopes excite the scintillator and produce a harmful luminescence. This effect is stronger in high-light-yield scintillation materials. The harmful luminescence might be excited by all products of radioactive decay: γ-quanta, alpha, and $\beta^{+,-}$ particles. The harmful luminescence contributes to the optical noise similarly to phosphorescence. The intensity of the harmful luminescence I_{noise} in the entire sample can be estimated by using the following formula:

$$I_{noise}[\text{ph/s}] = G \cdot V \cdot Y, \tag{1.5}$$

where G is the absorbed dose rate from radionuclides [in MeV/(s·cm^3)], V is the sample volume (cm^3), and Y is the light yield of the material (ph/MeV).

The scintillation signal is formed within a limited time interval determined by the scintillation kinetics. Meanwhile, the optical noise is emitted permanently. Consequently, for correct comparison of the scintillation signal and the noise, it is necessary to reduce the value of the harmful luminescence intensity in accordance with the specific time window, the time interval between the collisions of the beams, 25 ns in case of LHC experiments. The contribution of harmful luminescence photons in the noise pedestal can be estimated as in [45]. For the time window Δt, the value of ΔE_{noise} is:

$$\Delta E_{noise} = \frac{2.35\sqrt{G \cdot V \cdot Y \cdot \Delta t}}{Y \cdot \eta}. \tag{1.6}$$

Here, η is the fraction of the scintillation photons emitted during the time window $\Delta t = 25$ ns.

The results of the simulation of the harmful luminescence intensity within the time window of 25 ns, its contribution into the noise pedestal and the noise energy equivalent of two high light yield and dense scintillation crystals, GAGG and LSO, with dimensions of $2 \times 2 \times 0.2$ cm^3 for a half-year high-luminosity LHC operation are described in [46].

As evident in Table 1.3, the effect of activation by hadrons in LSO and *GAGG* is practically similar, however, additional noise intensity makes a reliable detection of the first photons practically impossible. Due to strong spatial delocalization in the shower, the light collection becomes the dominant factor in the formation of the time profile of the scintillation pulse in a bulk scintillation cell. Segmentation in heterogeneous cells is a possible way to avoid this problem. However, this approach works well only if each small element is red separately. This approach does not help in the readout systems containing an additional luminescent material, usually called a wave shifter, which is used to deliver the scintillation light to a photo-sensor. In addition, the fluctuations of the electromagnetic shower head within the distance X_0 leads to additional uncertainty in the identification of the energy deposit event. For the heavy scintillator $PbWO_4$ used in HEP experiments and an ultra-relativistic electron or a high energy γ-quantum it is 0.89 cm/c $\approx$ 30 ps. These fluctuations set a limit for the time precision in measurements with a scintillation pulse from a single shower in a homogeneous $PbWO_4$ cell. Reducing the effective X_0 in heterogeneous detecting cell makes this number smaller. However, the heterogeneous outline requires more scintillating material, which is used in the form of small-cross-section rods or thin plates.

Table 1.3 Contribution of harmful luminescence in optical noise, noise pedestal, and noise energy equivalent within 25 ns gate in GAGG and LSO crystals with dimensions of $2 \times 2 \times 0.2$ cm^3 [46]

Scintillator	GAGG	LSO
Additional noise intensity, ph	1600	1350
Additional pedestal, keV	156	108
Additional noise energy equivalent, keV	9.2	6.9

1.3.3 High-Energy Neutrons

High-energy neutron detection gains more importance due to the dissemination of various destructive examination techniques utilizing accelerator technologies to produce fast neutrons. Fast neutron resonance transmission imaging (FNRT) utilizes a "white" neutron beam created in a beryllium target by deuteron beam with the further selection of the neutrons transmitted through the object by using a Time of Flight (TOF) detector. Due to the compact localization in space and time of the energy deposit by interaction products, scintillators are the materials of choice for such detectors. The exploitation for this purpose of high light yield *Gd*-based scintillation material, like $Gd_3Al_2Ga_3O_{12}$, which we will quite often referred in this book, can shorten the TOF base to a few meters [38]. Another method, the fast neutron resonance radiography (FNRR) exploits the characteristic cross-section structure of different isotopes of the light nuclei to emit γ-quanta in the energy-range of up to 10 MeV. FNRR is promising for detecting explosives by determining the identity and density distribution of light elements, such as *C*, *N*, and *O*, within the inspected object (see a review in [18]). FNRR is a basic technology for geological exploration to locate the deposits of hydrocarbons and diamonds in mineral rock environments.

1.3.4 Demand for Fast Timing Measurements

The demand for fast timing in the measurements with scintillation detectors stirs the minds of the nuclear instrumentation community experts for more than current 10 years. Particularly, the recent years witnessed the emergence of fast timing as a new key requirement mainly driven by the experiments at colliders to cope with the pile up at a higher event rate and the increasing demand for a better spatial resolution in TOF-PET applications progressively moving toward full body PET scanning. This issue is addressed in Chap. 8 and Ref. [18]. In view of the variety of the application of scintillators with different key requirements for their performance, it is important to reveal the key limiting factors of the performance. All parts of the detector, participating in the transformation of the scintillation pulse into an electrical signal, contribute in the time resolution σ_t, which can be formalized by the sum in quadrature of the different terms as it has done in [47]:

$$\sigma_t = \sigma_c \bigoplus \sigma_d \bigoplus \sigma_e \bigoplus \sigma_{ps} \bigoplus \sigma_{sc}, \tag{1.7}$$

where σ indexed by c, d, and e denote clock, digitization, and electronics jitters, σ_{ps} is the noise term of photo-sensor at a given temperature σ_{sc} is a term determined by the shape of the scintillation pulse. The development of the fast detectors is the modern multidetector systems, which are under consideration for application at HL

LHC. The modern state of the art of the electronics and photo-sensors ensures quite small values of $\sigma_{c,\,d,\,e,\,ps}$, at the level of 10–15 ps each, whereas the term reflecting the scintillation properties is worse by at least a factor of three. At the current level of technology of the scintillation materials, which is supported by an increasing level of understanding of scintillation formation, scintillators become the weakest link in radiation detection from the point of view of their timing, although, as discussed above, the energy deposit is well localized in space and time for the majority of interactions. Subsequent chapters are devoted to examining the processes, which are initiated by the energy release of ionizing radiation in the scintillator. However, before addressing these processes, we will briefly discuss some basic issues related to the definition of the time precision measurements, the role of refraction and geometric factors in the formation of the scintillation pulse and will evaluate the differences of the time resolution in various types of inorganic scintillation materials.

References

1. R.J. Moon, Inorganic crystals for the detection of high energy particles and quanta. Phys. Rev. **73**, 1210 (1948)
2. H. Kallmann, Quantitative measurements with scintillation counters. Phys. Rev. **75**, 623–626 (1949)
3. G.B. Collins, R.C. Hoyt, Detection of beta-rays by scintillations. Phys. Rev. **73**, 1259–1260 (1948)
4. P.R. Bell, The use of anthracen as a scintillation counter. Phys. Rev. **73**, 1405–1406 (1948)
5. H. Kallmann, Scintillation counting with solutions. Proc. Phys. Soc. (London) Letters to the Editor **78**, 621–622 (1950)
6. H. Kallmann, M. Furst, Fluorescence of solutions bombarded with high energy radiation (energy transport in liquids). Phys. Rev. **79**, 857–870 (1950)
7. H. Kallmann, M. Furst, Fluorescence of solutions bombarded with high energy radiation (energy transport in liquids). Part II. Phys. Rev. **81**, 853–864 (1951)
8. H. Kallmann, M. Furst, High energy induced fluorescence in organic liquid solutions (energy transport in liquids). Part III. Phys. Rev. **85**, 816–825 (1951)
9. G.T. Reynolds, Scintillation counting. Nucleonics **6**, 488–489 (1950)
10. R.K. Swank, Recent advances in theory of scintillation phosphors. Nucleonics **12**, 4–22 (1954)
11. ATLAS Technical design report, CERN (1999)
12. J.A. Nikkel et al., Liquefied noble gas (LNG) detectors for detection of nuclear matter. J. Instrum. **7**, C03007 (2011)
13. M.G. Schorr, F.L. Torney, Solid non-crystalline scintillation phosphors. Proc. Phys. Soc. (London) Letters to the Editor **80**, 474–475 (1950)
14. T.R. Martinez, S. Gundacker, E. Auffray, P. Lecoq, Towards a metamaterial approach for fast timing in PET: experimental proof-of-concept. Phys. Med. Biol. **12** (2019). https://doi.org/10.1088/1361-6560/ab18b3. (EPb ahead of print)
15. P.A. Rodnyi, *Physical Processes in Inorganic Scintillators* (CRC Press, Boca Raton, 1997)
16. M. Korzhik, *Physics of Scintillation in Oxide Crystals* (BSU Press, Minsk, 2003)
17. P. Lecoq, A. Annenkov, A. Gektin, M. Korzhik, C. Pedrini, *Inorganic Scintillators for Detector Systems* (Springer, Berlin, 2006)
18. P. Lecoq, A. Gektin, M. Korzhik, *Inorganic Scintillators for Detector Systems* (Springer, Cham, 2016)

19. P. Rodnyi, P. Dorenbos, C.W.E. van Eijk, Energy loss in inorganic scintillators. Phys. Status Solidi B **187**, 15–29 (1995)
20. A. Lempicki, The physics of inorganic scintillators. J. Appl. Spectrosc. **62**, 209–231 (1995)
21. M. Korzhik, A. Gektin, *Engineering of Scintillation Materials and Radiation Technologies* (Springer, Cham, 2017)
22. A. Lushchik, M. Kirm, C. Lushchik, Multiplication of anion and cation electronic excitations in luminescent wide-gap ionic crystals. Radiat. Meas. 24, 365–369 (1995); A. Vasil'ev, V. Kolobanov, I. Kuusmann, Ch. Lushchik, Multiplication of electron excitations in MgO crystals. Sov. Phys. Solid State **27**, 1616–1619 (1985)
23. J. H. Hubber, Photon cross sections attenuation coefficients and energy absorption coefficients from 10keV to 100GeV, NSRDS-NBS29, S Department of Commerce, National Bureau of Standards (1969)
24. M. J. Berger, S. M. Seltzer, Tables of energy losses and ranges of electrons and positrons in: studies in penetration of charged particles in matter (Publication of NAS-NRC, 1964)
25. R. Kirkin, V. Mikhailin, A. Vasil'ev, Recombination of correlated electron-hole pairs with account of hot capture with emission of optical phonons. IEEE Trans. Nucl. Sci. **59**, 2057–2064 (2012)
26. C. Leroy, P.G. Rancoita, *Principles of Radiation Interaction in Matter and Detection* (Word Scientific Publishing Co Pte Ltd, Singapore, 2016)
27. A. Barysevich et al., Radiation damage of heavy crystalline detector materials by 24 GeV protons. Nucl. Instrum. Methods Phys. Res. A **701**, 231–234 (2013)
28. E. Lamb Wellis Jr., Passage of uranium fission fragments through matter. Phys. Rev. **58**, 696–702 (1940)
29. N. Bohr, On the theory of the decrease of velocity of moving electrified particles on passing through matter. Philos. Mag. **25**, 10–31 (1913)
30. H.A. Bethe, Zur Theorie des Durchgangs schneller Korpuskularstrahlen durch Materie. Ann. Phys. **5**, 325–400 (1930)
31. F. Bloch, Bremsvermogen von Atomen mit mehreren Electronen. Z. Physic **81**, 363–376 (1933)
32. G.F. Knoll, *Radiation Detection and Measurement* (John Wiley & Sons, New York, 2000)
33. D. Mazed, S. Mameri, R. Ciolini, Design parameters and technology optimization of ^{3}He-filled proportional counters for thermal neutron detection and spectrometry applications. Radiat. Meas. **47**, 577–587 (2012)
34. Evaluated Nuclear Data File (ENDF), https://www-nds.iaea.org/exfor/endf.htm. Accessed Mar 2019
35. P. Reeder, Neutron detection using GSO scintillator. Nucl. Instrum. Methods. Phys. Res. Sect. A **340**, 371–378 (1994)
36. M. Korzhik, K.T. Brinkmann, G. Dosovitskiy, et al., Compact and effective detector of the fast neutrons on a base of Ce doped $Gd_3Al_2Ga_3O_{12}$ scintillation crystal. IEEE Trans. Nucl. Sci. **66**, 536–540 (2019)
37. K. Hagiawara, et al., Prog. Theor. Exp. Phys. arXiv:1809.02664v1 [nucl-ex] (2015)
38. M. Korzhik, K.T. Brinkmann, G. Dosovitskiy, et al., Detection of neutrons in a wide energy range with crystalline $Gd_3Al_2Ga_3O_{12}$, Lu_2SiO_5 and $LaBr_3$ doped with Ce scintillators. Nucl. Instrum. Methods Phys. Res. A **931**, 88–91 (2019)
39. H. Klein, F.D. Brooks, *Scintillation Detectors for fast Neutrons, Proceedings of Science* (FNDA, 2006), p. 097. https://doi.org/10.22323/1.025.0097
40. A. Alireza et al, Observation of reactor antineutrinos with a rapidly-deployable surface-level detector, arXiv18.1202163v1 (2018)
41. C.E.R.N. The, *Large Hadron Collider: Accelerator and Experiments*, vol 1–2 (CERN, Geneva, 2009)
42. CMS Collaboration, Observation of a new bozon at a mass of 125 GeV with the CMS experiment, at the LHC. Phys. Lett. B **716**, 30–61 (2012)
43. A. Annenkov, M. Korzhik, P. Lecoq, Lead tungstate scintillation material. Nucl. Instrum. Meth. Phys. Res. Sect. A **490**, 30–50 (2002)

44. G. von Dardel et al., Mean life of the neutral. Phys. Lett. **4**, 51–54 (1963)
45. Y. Shao, A new timing model for calculating the intrinsic timing resolution of a scintillator detector. Phys. Med. Biol. **52**, 1103–1117 (2007)
46. A. Auffray, G. Dosovitskiy, A. Fedorov, et al., Irradiation effects on Gd3Al2Ga3O12 scintillators prospective for application in harsh irradiation environments. Radiat. Phys. Chem. **164**, 108365 (2019)
47. Technical Proposal for a MIP Timing Detector in the CMS experiment Phase 2 upgrade, Tech. Rep. CERN-LHCC-2017-027. LHCC-P-009, (CERN, Geneva Dec 2017)

Chapter 2
Timing Measurements with Scintillation Pulses

Abstract This chapter addresses the evolution of the scintillation pulse shape under different conditions for the energy deposit, the evaluation of the precision in timing measurements at optical pulses of different forms and the specificity of the time resolution in scintillators of different tapes.

2.1 Scintillation Pulse

2.1.1 Scintillation Pulse in a Thin Inorganic Media

In general, several parameters are important for characterization of a scintillation pulse. Figure 2.1 demonstrates the time evolution of a scintillation pulse. Such pulse, as a rule, is detected by photo-receiver after the scintillator is excited by ionizing radiation.

The response might be characterized by two parameters: the amplitude (*Am*) and the function *S(t),* describing scintillation kinetics at the photo-receiver window. *S* characterizes the leading edge and the decrease of the scintillation intensity. The amplitude is the peak response value. The integral under the scintillation pulse curve is proportional to the light output. The rise and decay of the scintillation response depends on several factors: light collection from bulk scintillation element, optical absorption in the spectral range of the scintillation, physical origin of the scintillation in the media. Besides the intrinsic rise time, the time resolution of the detection might be corrupted due to the limited response rate of the photo-receiver. However, in a thin scintillation element, the influence of at least three listed above factors can be minimized or even neglected. The definition of thin or thick sample depends on the kind of the exciting ionizing radiation. For *a*-particles emitted by radioisotopes, the characteristic distance might be even shorter than 100 microns, whereas for a high energy electron it is at least $\sim X_0$, which characterizes the fluctuation of the electromagnetic shower. For a high-energy hadron, the fluctuation is characterized by so-called nuclear length of the material [1], which is over the 10 cm for dense metals like uranium or tungsten.

M. Korzhik et al., *Physics of Fast Processes in Scintillators*, Particle Acceleration and Detection, https://doi.org/10.1007/978-3-030-21966-6_2

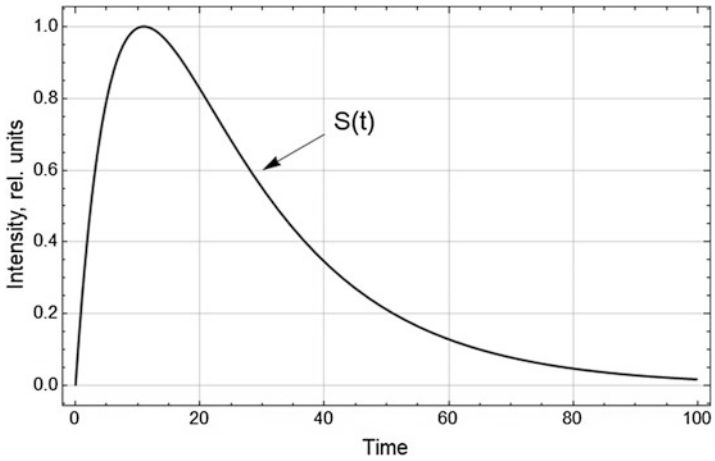

Fig. 2.1 Time evolution of scintillation pulse

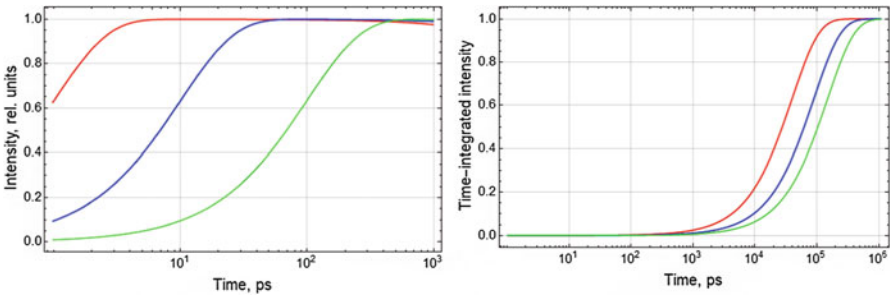

Fig. 2.2 Leading edge of scintillation response (left panel) and time-integrated intensity of the scintillation pulse (right panel) in a thin scintillator with $\tau_r = 1$ ps (red), 10 ps (blue), 100 ps (green) and $\tau_d = 40$ ns

The different parts of the scintillation response pulse are essential for the measurements of timing and deposited energy. For simplicity, let us assume that the rise and decay functions are simple single-exponential functions with the rise and a decay time constant τ_r and τ_d, respectively.

$$S(t, t_0) = \frac{Exp\left(-\frac{t-t_0}{\tau_d}\right) - Exp\left(-\frac{t-t_0}{\tau_r}\right)}{\tau_d - \tau_r} \tag{2.1}$$

This simplification allows for avoiding the sophisticated analysis on the stage of a qualitative consideration and to discuss general trends of the scintillation pulse transformation when its kinetics parameters vary. Figure 2.2 shows the leading edge of the scintillation pulse and its time-integrated intensity at different τ_r and typical τ_d of Ce^{3+} doped scintillator.

For timing measurements, a crucial issue is the number of photons arriving to a photo-receiver to a certain time. The leading edge of the scintillation is strongly affected by the time constant of the rise component. On the other hand, when the deposited energy is measured, only the decay constant is an important parameter, whereas the leading edge does not play a significant role in the time integrated intensity as seen from Fig. 2.2 (right panel). The leading edge of the scintillation usually does not contribute to the integral of the detected signal. However, τ_d contributes to the timing properties due to the relationship of light yield, amplitude, and decay time: $Am \propto Y/\tau_d$. The higher is light yield and the shorter is τ_d, the larger is the amplitude of the scintillation pulse. From these considerations, simple conjunction of Y, τ_d, τ_r and the mean delay of the time stamp $\langle t_{st} \rangle$ for the energy deposit event TR can be written as:

$$TR \sim \sqrt{(\tau_r \cdot \tau_d / Y)} \tag{2.2}$$

This simple formula gives a qualitative characterization of the influence of the parameters of the scintillation pulse on the reachable timing properties in scintillation detection. It is indiscriminately and quite often used in the literature [2–4]; however, as it will be shown in Sect. 2.2.3, it describes mostly a group of self-activated scintillators.

2.1.2 *Propagation of a Short Light Pulse in a Dispersing Medium*

An inorganic scintillator is a dispersing medium. The light dispersion sets the limit for the minimum duration of the scintillation pulse to pass through a thin media without shape deformation. As an example, consider the propagation of a package of short Gaussian-shape optical pulses, described in one-dimension x in a medium with the refraction index $n(\omega)$ as:

$$f(t) = \frac{1}{\sigma\sqrt{2\pi}} Exp\left(-\frac{(t-t_0)^2}{2\sigma^2}\right). \tag{2.3}$$

Under assumption that the pulse consists of a group of waves with the spectral distribution $g(\omega)$, the shape of the pulse is described by the following expression:

$$S(t) = \int_{\omega_{min}}^{\omega_{max}} f\left(t - \frac{x}{c} n(\omega)\right) g(\omega) d\omega, \tag{2.4}$$

For numerical evaluation, we used the dispersion curve presented in Fig. 2.3, which is typical for oxide matrixes with a garnet structure.

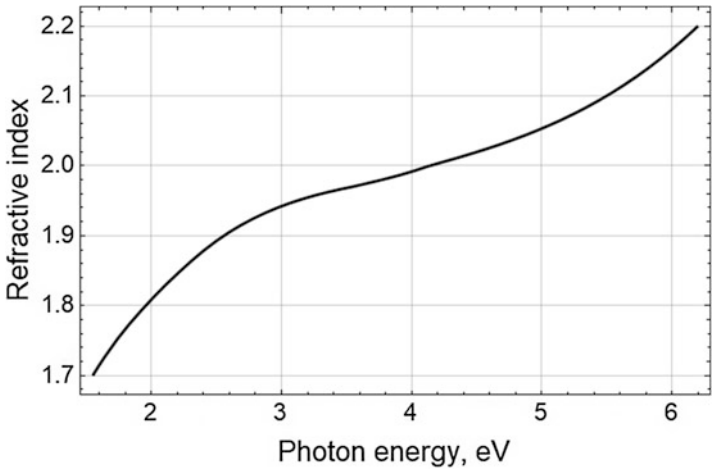

Fig. 2.3 Typical spectrum of refractive index in a crystal with a garnet-type structure

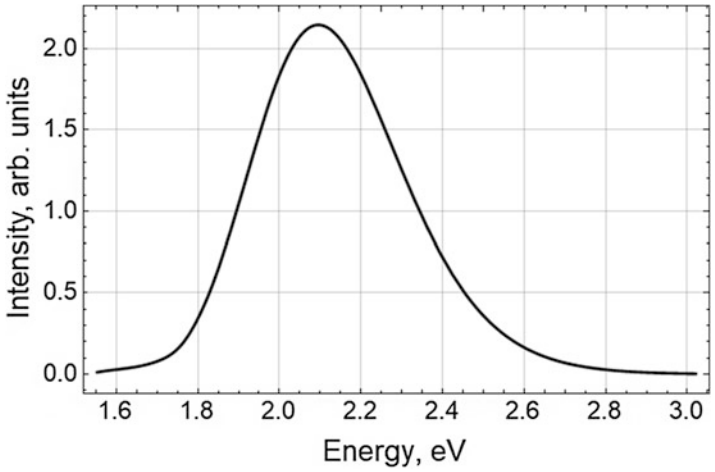

Fig. 2.4 Typical luminescence spectrum of Ce^{3+} ion in GAGG crystal

The low-energy part of the dispersion curve exhibiting the most significant slope overlaps with the spectral range of luminescence of Ce^{3+} ions in the crystals with a garnet-type structure [5]. The intracentre Ce^{3+}luminescence is quite slow for this consideration, but the shape is well fitted with a Gaussian shape, as seen from Fig. 2.4, where, as an example, a typical Ce^{3+}luminescence spectrum in GAGG crystal is shown on energy scale. Just for illustration, let us assume that the luminescence is quite fast, and $\sigma = 0.5$ ps. Fig. 2.5 demonstrates the comparison of the pulse before and after the passage of one cm in the dispersing medium.

As seen in Fig. 2.5, the width of the time profile of the pulse is twice the original width. It is important that the broadening decreases the steepness of the leading edge

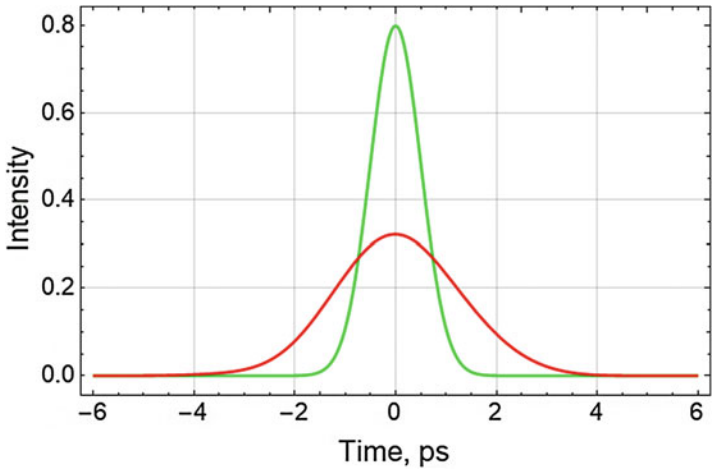

Fig. 2.5 Time evolution of optical pulse with the time-shape described by (2.3) with $\sigma = 0.5$ *ps* and the spectrum shown in Fig. 2.4 before (green) and after passage (red) of 1 cm of the medium with dispersion presented in Fig. 2.3

of the light pulse. So, the broad spectrum of the light pulse might substantially deteriorate the timing properties even for initially short pulses. For that reason, a pulse of "white" and very fast intra-band luminescence, due to optical transitions inside the conduction band [6], will suffer from extension of the leading edge while traversing the scintillator volume. However, it does not preclude utilization of the short laser pulses for probing of the material excited by ionizing radiation, having a relatively small bandwidth, less than a few meV, for probing of dispersing media. For such pulses, the effect of extension is expected to be visible for the pulses with duration ~1 fs. An application of external laser short pulses to probe ionization in inorganic media, not necessary scintillator, is discussed in Chap. 5.

2.1.3 Forming of the Scintillation Pulse by Light Collection in a Scintillator Element

Another property of the refracting medium, which affects the scintillation pulse, is slowing of the light speed by a factor of 1/n, where n is the refractive index of the material. This effect has definitely been discussed long before this book, however, here we would like to draw attention to two features: the corruption of the leading edge of the scintillation pulse with increasing energy deposit volume and the way to maintain the steepness of the leading edge. Let us turn back to the example of the energy deposit from a high-energy particle in PWO scintillation crystals of different length, which is considered in Chap. 1 (see Fig 1.6). The longer is the scintillation crystal, the larger is the volume of the crystal involved in the scintillation generation.

Furthermore, compare the observation of the scintillation pulse with an ideal photo-receiver with the pulse of photons, generated in the refracting media by a fast charged particle due the Cherenkov effect. A remarkable feature of Cherenkov photons is their generation along the trajectory of the moving particle (as long as the particle has energy above certain threshold) with a constant rate [1]. It implies that the Cherenkov photons appear at the photo-receiver faster than the scintillation photons, mainly when the ultra-relativistic particle passes through the media. The Cherenkov photons are discussed in more detail in Chap. 3.

Figure 2.6 shows GEANT4 simulated time dependence of the integral of the scintillation pulse (red) and relative error (blue) of the scintillation pulse measurement at the registration of 100 GeV electron in PWO scintillation element with a length of 1.5, 5, and 20 X_0. The light yield of 200 ph/MeV and decay time constant of 6 ns were used, whereas the leading edge of the scintillation was characterized by a rising time constant of 4 ps, as in [7]. As an example, let us compare, for each case, the time from the energy deposit beginning when a relative error of scintillation pulse measurement becomes 10%. It can be considered to be a figure of distinction for the leading edge. Since bremsstrahlung provides a significant contribution to the energy deposit in a short crystal, a relatively small amount of photons is generated. Due to this reason, 10% relative error is reached in 180 ps. This period decreased to 33 ps in the sample with the length of 5 X_0 and increased to 80 ps in the sample with the length of 20 X_0. The result in a longest crystal is a consequence of the light collection in the scintillation elements. The wider in space and the more extended in time the energy deposit in the scintillation element occurs, the less steep is the slope of the leading edge of the scintillation pulse. In this way, the optimal length of the scintillation element for the high energy electromagnetic particle energy registration, 20–25 X_0, is not necessarily optimal for the timing measurements. However, a too short element also does not show the best timing performance. The optimal length is in the range *5–8* X_0. A higher light yield of the material allows reaching the level of the accepted error in a shorter time; however, the dependence of the time on the length of the scintillation element has the same trends.

A scintillator with a small light yield is convenient to search for tools to modify the leading edge of the scintillation. One of the approaches, which we found to be quite productive, is the creation of an additional very fast decaying component in the scintillation.

Lead tungstate is a good example to illustrate how the approach works. We consider the last modification of the material, the crystals of the quality usually referred to as PWO-II [8], which is doped by a small quantity of lanthanum and yttrium ions at the total concentration not more than 50 ppm. The introduction of trivalent ions in the matrix, substituting divalent lead ions Pb^{2+} promotes the formation of two shallow centers [9]. The luminescence properties of these centers were recently recognized [7].

PWO is a self-activated scintillator with predominant emission of quenched polaronic states, which can be considered as excitations on the host oxy-anionic complexes WO_4^{2-} [10]. The measured photoluminescence rise time was found to be no longer than 4 ps. The decay kinetics has three components at band-to-band

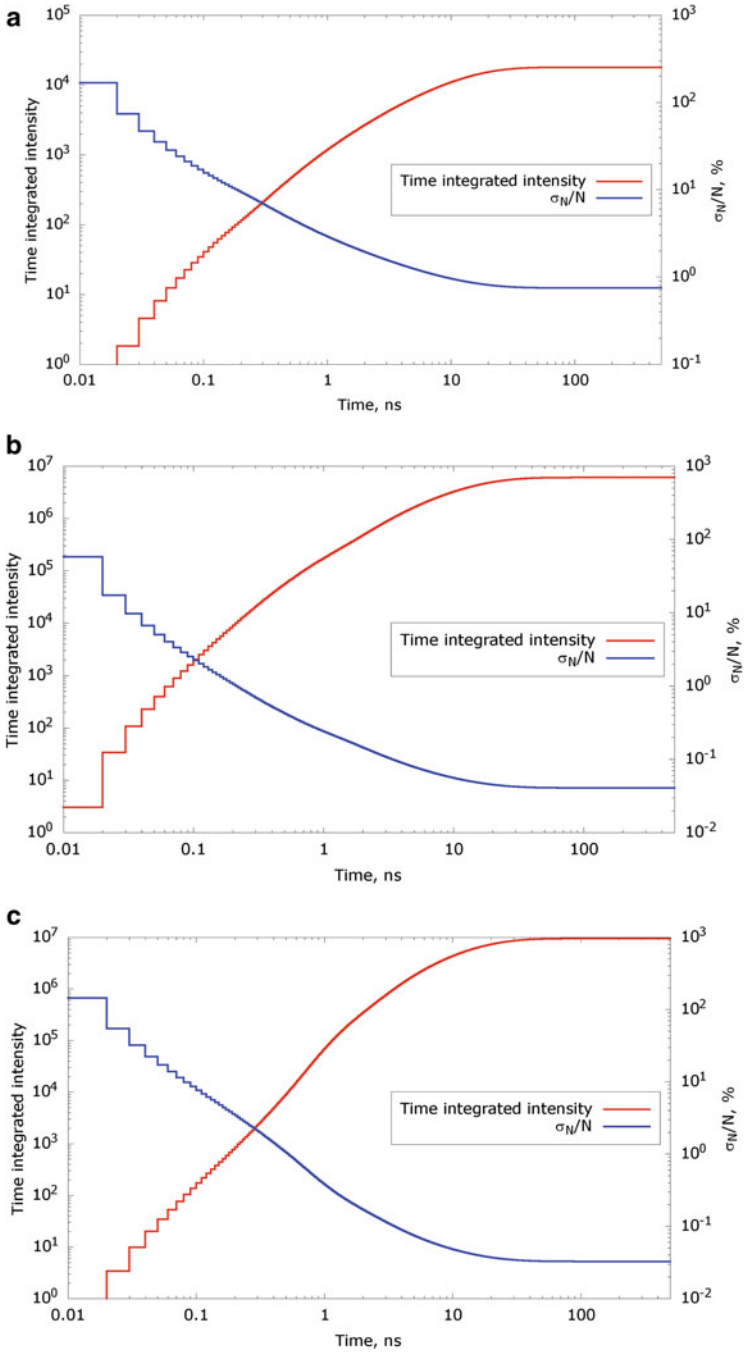

Fig. 2.6 GEANT4 simulated time dependence of the time integrated intensity of the scintillation pulse (red) and relative error (blue) of the scintillation pulse measurement at the registration of 100 GeV electron in PWO scintillation element with a length of 1.5 (**a**), 5 (**b**), and 20 X_0 (**c**)

excitation: $\tau_1 = 5.9$ and $\tau_2 = 824$ ps and a slower component with the time constant of $\tau_3 = 6$–10 ns [7], which is usually observed in routine start-stop measurements of PWO luminescence kinetics. The intermediate component with decay times of approximately 700–800 ps is consistent with that reported in [11]. The fastest decay component was found to be due to green luminescence emitting F^+ center, i.e., the host oxy-anionic complex WO_3 containing oxygen vacancy [7]. The intermediate decay component with the decay time $\tau_2 = 800$ ps is due to the WO_4^{2-} luminescence originating from quenched luminescence of complexes WO_4^{2-} +RE^{3+} (RE = La^{3+} and Y^{3+}). Radiative recombination centers WO_4^{2-}+ La^{3+} and WO_4^{2-}+ $Y^{3+}$are formed with the ground states approximately 0.1 eV below the bottom of the conduction band. Therefore, the intermediate and the slowest components originate from regular WO_4^{2-} complexes, providing simultaneous contribution to scintillation. Both these bands are strongly quenched at room temperature. In addition to the thermal quenching, the centers in the vicinity of lanthanum or yttrium ions have additional, nonradiative losses due to the thermal ionization to the conduction band, so their luminescence kinetics becomes shorter than that of the regular WO_4^{2-} complexes. The fraction of the intermediate component in the scintillation depends on the doping concentration. In PWO-II crystals, the fraction does not exceed 10%. Figure 2.7 shows the results of the GEANT4 simulation of the scintillation kinetics of PWO crystal containing only the 8 ns decay component and two components, the 8 ns and the intermediate decay components. The rise time in both cases was assumed to be 4 ps. The simulation has been performed for three lengths of the scintillation element: 1.5, 5, $20X_0$. As was expected, the 800 ps component significantly modifies the scintillation pulse in all the elements studied, especially, within the first nanosecond. As seen from Fig. 2.8 the relative error at 10% is reached in 120 ps, whereas the time decreases to 25 ps in $5X_0$ long sample and show increase to 60 ps in the $20X_0$ crystal unit. Gain in the time reducing to a previous case to achieve relative error at 10% is nearly 30% for all crystal length. One can conclude that the introduction of a fast decay component in the scintillation can diminish the deterioration of timing properties of the detectors utilizing long scintillation elements.

There are a few ways to add a fast scintillation component into the scintillation pulse. They are discussed below.

The Cherenkov light appears in a refractive medium promptly after the charged particle enters it. However, the appearance of the Cherenkov light on the photo-receiver depends on the light speed. Let us turn our attention again to PWO, having a high refraction index of 2.28 (400 nm) and, consequently, the lowest threshold of the Cherenkov light generation [12]. Cherenkov light intensity at the photo-receiver window for the crystals of different length is in Fig. 2.9. In a short crystal, Cherenkov photons appear at the photo-receiver at the moment when particle leave the crystal, of about 45 ps from the entry moment. A tail part of the signal is formed by the Cherenkov photons created in the initial part of the particle track, since the speed of the photons in the crystal is by a factor of two smaller than the particle speed.

In the 5 X_0- long PWO, a considerable amount of Cherenkov photons is generated by photoelectrons, which appear in the crystal due to the absorption of annihilation

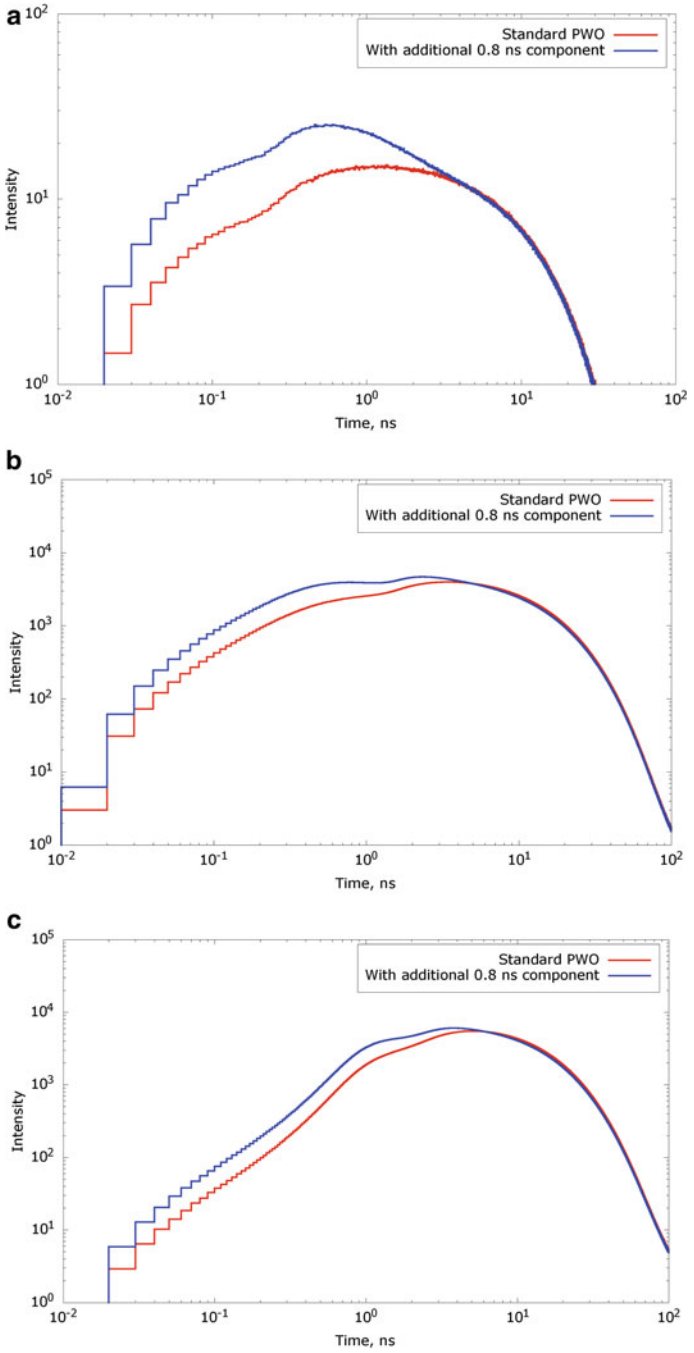

Fig. 2.7 GEANT4 simulated scintillation pulse intensity of PWO, containing only 8 ns scintillation decay component (red) and, additionally, intermediate 800 ps component (blue) at the registration of 100 GeV electron in elements with a length of 1.5 (**a**), 5(**b**), and 20 X_0 (**c**)

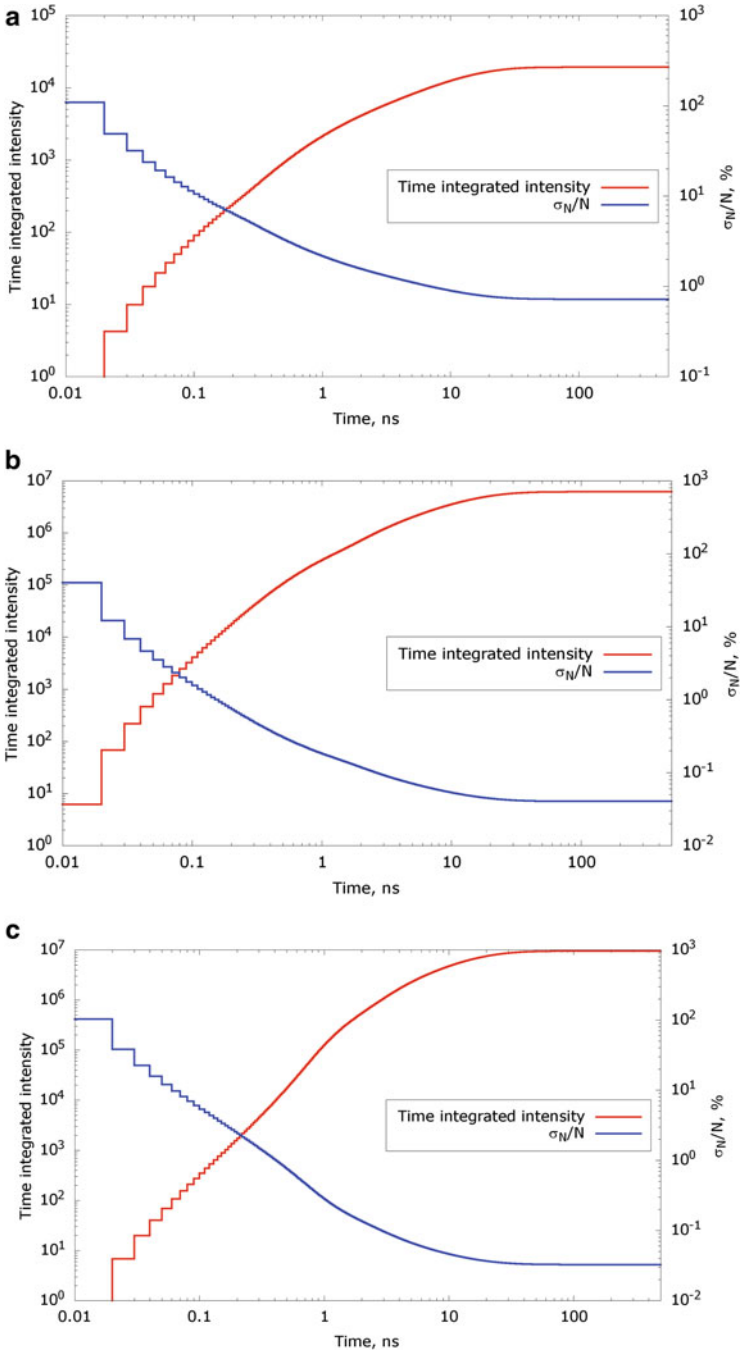

Fig. 2.8 GEANT4 simulated time-integrated intensity of the scintillation pulse (red) and relative error of the scintillation pulse measurement (blue) at the registration of 100 GeV electron in PWO with two emission decay components with time constants of 8 ns and 800 ps at different length of scintillation element: 1.5(**a**), 5(**b**), and 20 X_0 (**c**)

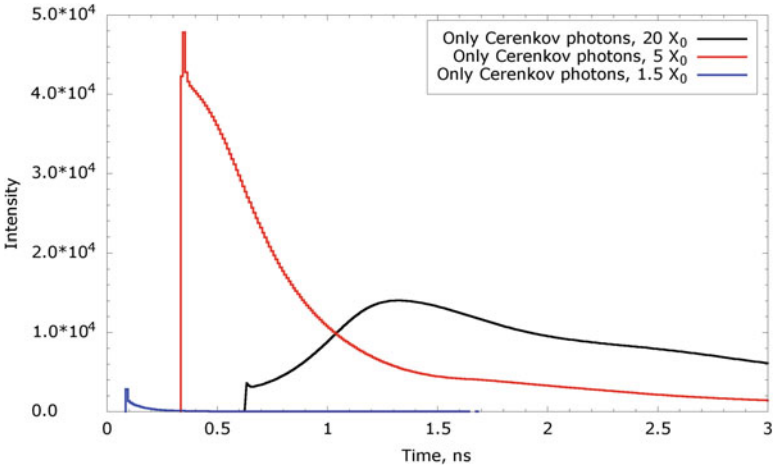

Fig. 2.9 GEANT4 simulated Cherenkov light intensity at the photo-receiver after entering of a 100 GeV electron beam (1000 electrons) in PWO scintillation element with a length of 1.5(blue), 5 (red), and $20X_0$ (black)

gamma-quanta. As a result, the first photons appear at the photo-receiver window later than the time $5X_0/c$. In a long crystal, the light collection causes signal spreading similarly as the scintillation, although a sharp edge, which appears due to the fast delta-electrons created in the shower, is still observable. Exploiting a combination of scintillation and Cherenkov photons in thin and even low light yield scintillators allows constructing high time resolution detectors, as described in [13]. A position-sensitive detector consisting of a scintillating crystal on which is directly deposited a photoelectric layer of refractive index greater than that of the crystal. Such construction combines scintillation and photoelectron generation due to interaction with 511 keV γ-quanta and optimizes the transmission of scintillation and Cherenkov light photons to the photoelectric layer. A gain factor 4 on the probability of optical photon transmission between the crystal and the photoelectric layer is expected in comparison to conventional assemblies using optical contact grease. The crystal will be encapsulated with a micro-channel plate multiplier tube (MCP-MT) in order to amplify the signal and optimize the transit time of the photoelectrons towards the plane of detection anodes (densely pixelated) and thus, better temporal and spatial resolutions of the detection chain. Benefits will be provided by using the mapping of photoelectrons produced at the surface of the crystal to reconstruct the properties of the γ interactions by means of robust statistical estimators and information processing using machine learning algorithms. The scintillation photons provide the necessary statistics for a measurement of the energy deposited in the crystal, modest but compatible with a use on a PET imager, and precise measurement of the coordinates of the interaction position of the γ- quanta. Reading of the signals by this technique from both sides of 2 cm thick PWO crystal is expected to provide 20 ps time resolution, which put the developed detection technology is in the top list for the development of a whole-body PET-TOF scanner.

2.2 Precision of Timing Measurements and Time Resolution with Ideal Photo-Sensor and Electronics

2.2.1 Statistics of Optical Pulse Time Stamp Registration

In this section, we will consider in a more formal way how the shape of the light pulse of scintillation affects the timing properties of the detector. Here, we will not go into details on how the scintillation pulse is formed. This issue will be addressed is Chap. 3. Here we will exploit several known forms of optical pulses that are convenient for analyzing to understand the essential parameters affecting the errors in high-precision timing measurements.

First, we specify that the time resolution is inherent for two or a group of optical signals separated in time.

Time resolution is affected by the accuracy of time measurements, which is defined for a single pulse signal.

To reveal the role of the parameters of the scintillation optical pulses, we consider an ideal detecting chain: 100%-sensitive, zero-noise and prompt photo-receiver and ideal zero-jitter electronics.

Nowadays scintillation pulse, as a rule, is digitized and memorized with an apparatus like Multi-Channel Analyzer (MCA). The process of detecting the scintillation photons on a photodetector is the process of absorbing a portion of energy from the scintillation by a photoreceiver connected to electronics within the time interval $\left[t_i - \frac{\delta}{2}, t_i + \frac{\delta}{2}\right]$, where i is the channel number and δ is its width.

There are three common approaches to create a timestamp. The first approach is based on hunting for the first photons arriving at a photosensor at the assumption of the prior knowing of the *S(t)*.

Next, timestamp might be also obtained by binding to a leading edge point with the acceptable relative statistical error $\sigma_N = 1/\sqrt{N}$ and maximum slope of leading edge max*(dS/dt)*. In this case, the error σ of the time stamp can be estimated as

$$\sigma \sim \frac{\sigma_N}{\frac{dS}{dt}}, \tag{2.5}$$

where N is the number of the photons arrived to the photo-receiver to the time interval $\left[t_i - \frac{\delta}{2}, t_i + \frac{\delta}{2}\right]$. If the energy deposit from the particle or photon has been expected to be low and this is accompanied by low scintillation yield of the material, this method is not suitable for setting a time stamp. It should also be noted that this method requires information on the explicit dependence of the S (t) on time.

Finally, the event can be detected when the signal excesses the noise in a certain time gate, which requires prior information about the noise in the detector. The role of the contribution of the optical noise in the total noise is described in Sect. 1.3 and the last paragraph of this chapter.

In a case when the event is registered under the first approach, the probability density $p_s(t)$ of the energy deposit event registration at time t for the scintillation pulse $S(t)$ with the arbitrary shape of the leading edge is expressed as:

$$p_s(t) = C_s \sum_{l=1}^{Y} \left(1 - \int_0^t S(\tau)\, d\tau\right)^l S(t)\, lp_Y(l). \tag{2.6}$$

The signal $S(t)$ should be normalized to unity: $\int_0^{t0} S(\tau)\, d\tau = 1$, where t_0 is the time of the development of the leading edge to a signal maximum. The probability density $p_s(t)$ is set on the time interval [0, T].

The distribution of the time of event registration for the leading edges under consideration bellow, p_Y (l) has the binomial distribution [14]:

$$p_Y(l) = \binom{Y}{l} P_h{}^l (1 - P_h)^{Y^* - l}, \tag{2.7}$$

where P_h is the probability of registering one photon throughout the leading edge. The expression for $p_s(t)$ in this case is following:

$$p_s(t) = C_s Y S(t) P_h \left(1 - P_h \int_0^t S(\tau)\, d\tau\right)^{Y-1} \left(1 - \int_0^t S(\tau)\, d\tau\right). \tag{2.8}$$

The distribution function $N(t)$ for the probability density $p_S(t)$ is given by the following expression:

$$N(t) = \int_0^t p_s(\tau)\, d\tau \tag{2.9}$$

2.2.2 *Precision of the Measurement of Optical Pulse with a Gaussian Shape*

As the first example, let us assume that the event of interaction with scintillator results in producing of an optical pulse with a Gaussian shape described by the following expression:

$$\mathrm{S}(\mathrm{t}, \sigma, \mathrm{t_A}) = \frac{1}{\sigma\sqrt{2\pi}}\, \mathrm{Exp}\left(-\frac{(\mathrm{t} - \mathrm{t_A})^2}{2\sigma^2}\right), \mathrm{t} \geq 0, \tag{2.10}$$

where σ is the pulse standard deviation, time $\mathrm{t_A}$ is the time when pulse reaches the peak. This situation is hardly expected in inorganic scintillators, but its consideration

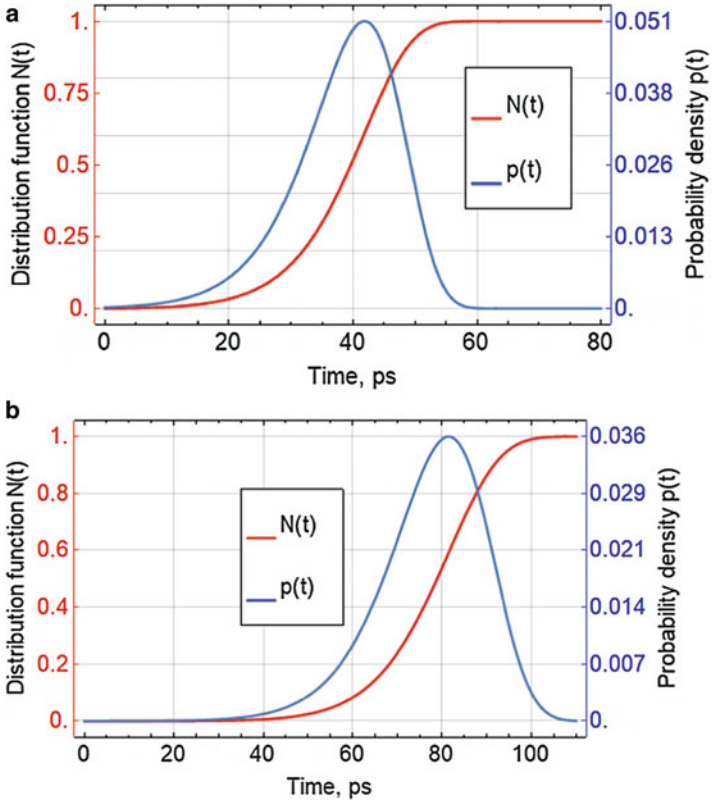

Fig. 2.10 Probability density (blue) and probability registration distribution function (red) of the event registration at time t at the Gaussian distribution of the photons created at the event for Y values of 23,000 (**a**) and 230 (**b**)

is quite useful to evaluate the difference for pulses of various shapes. Consider a hypothetical situation when 511 keV photon produces in a thin scintillator a Gaussian pulse, which reaches the maximum in 160 ps, $Y = 23{,}000$ photons, σ=30 ps and the fraction of the photons corresponding to the leading edge is half of the Y value. Under the first approach, the probability density and the probability distribution of the event registration at time t from the energy deposit are shown in Fig. 2.10.

An interesting property of this pulse shape function is a practically linear dependence of distribution function on σ, when decreased by factor ten, the decrease of the horizontal axis unit by the same factor occurs. However, when Y is significantly lower, for instance, by two orders of magnitude (see Fig. 2.10b), the probability of registering for sure is decreased by a factor two only.

2.2.3 *Precision of the Measurement of the Optical Pulse with an Exponential Shape*

As a second example, consider an optical pulse having a leading edge, which is described by an exponential function:

$$S_1\left(\mathrm{t}, \tau_r, t_0'\right) = \begin{cases} 0 & , t < t_0' \\ Am\left(1 - Exp\left(-\dfrac{t - t_0'}{\tau_r}\right)\right), & t \geq t_0' \end{cases} \tag{2.11}$$

where t_0' is the time moment of the energy deposit, Am is the amplitude.

Consider the same event as in the previous paragraph when 511 keV photon produces in a thin scintillator a pulse, which is characterized by $\tau_r = 100$ ps, $Y =$ 23,000 photons, and a fraction of the photons corresponding to the leading edge $F = 0.024$. This fraction is regulated by the ratio of rise τ_r and decay $\tau_d$constants of the response kinetics. The probability density and the probability distribution of the event registration at time t from the energy deposit are shown in Fig. 2.11. The remarkable point is that a scintillator with not outstanding parameters and having relatively slow rise time could provide registering of the event for sure in a relatively short time. At that, an essential role in the shift of the distribution function to smallest time values plays factor F. Again, F depends on Y, and rise and decay time constants.

It might seem that a further decrease of τ_r results in a better distribution function. However, it also results in a decrease of the F factor if τ_d is not changed. F is a strong factor influencing the distribution function. Figure 2.11b shows a substantial expanding of the distribution function when F is decreased by one order of magnitude. Due to this reason, even a high light yield scintillator having slow τ_d will show a poor distribution function, whereas a scintillator with a short decay time can demonstrate outstandingly short time to reach a plateau of the distribution function even at a low light yield. The development of scintillators with a significant fraction of the fast leading edge in the scintillation pulse promises a remarkable improvement of the accuracy of the timing measurements.

Now consider the second approach in more detail for the exponential leading edge, what is of practical interest. The statistics in a specific channel, $N(t_i)$ can be analytically described, provided that the signal shape $S1(t)$ is known:

$$N(t_i) = \int_{t_i - \frac{\delta}{2}}^{t_i + \frac{\delta}{2}} S1(\tau)\, d\tau. \tag{2.12}$$

Let us assume that the leading edge of the scintillation pulse is described by following the function:

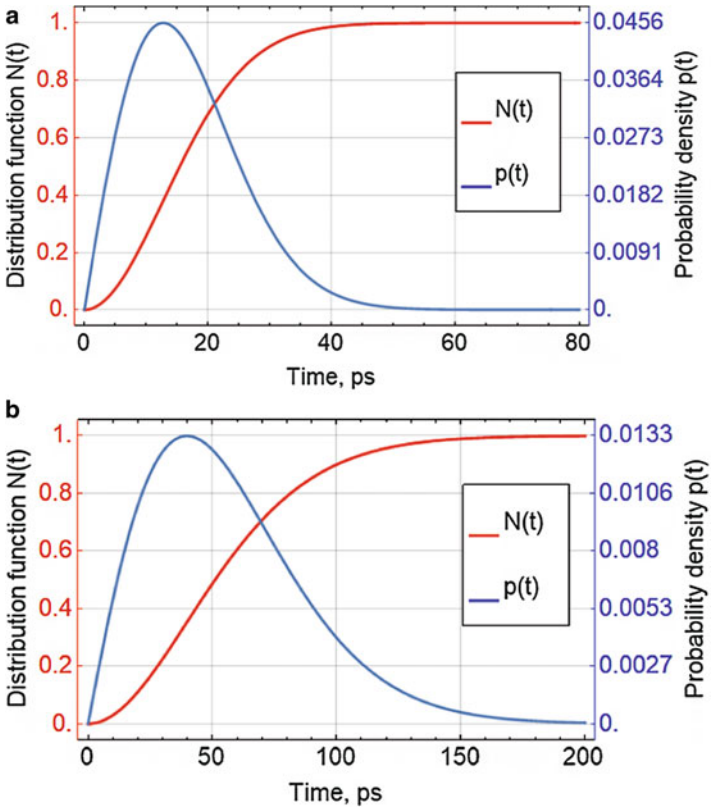

Fig. 2.11 Probability density (blue) and probability registration distribution function (red) of the event registration at time t at the exponential leading edge distribution of the photons created at the event for $F = 0.024$ (**a**) and $F = 0.0024$ (**b**)

$$S1(t, \tau_r) = Am\left(1 - Exp\left(-\frac{t}{\tau_r}\right)\right), t \geq 0. \tag{2.13}$$

According to formula (2.5), $\sigma(t_i)$ can be expressed as

$$\sigma(t_i) = k\frac{\tau_r}{\sqrt{N(t_i)}\,(A - S(t_i))}, \tag{2.14}$$

where k is a proportionality coefficient and

$$N(t_i) = Am\left(\delta + \tau_r\, Exp\left(-\frac{t_i + \frac{\delta}{2}}{\tau_r}\right)\left(1 - Exp\left(\frac{\delta}{\tau_r}\right)\right)\right) \tag{2.15}$$

The minimum value of the error $\sigma(t_i)$ is achieved at

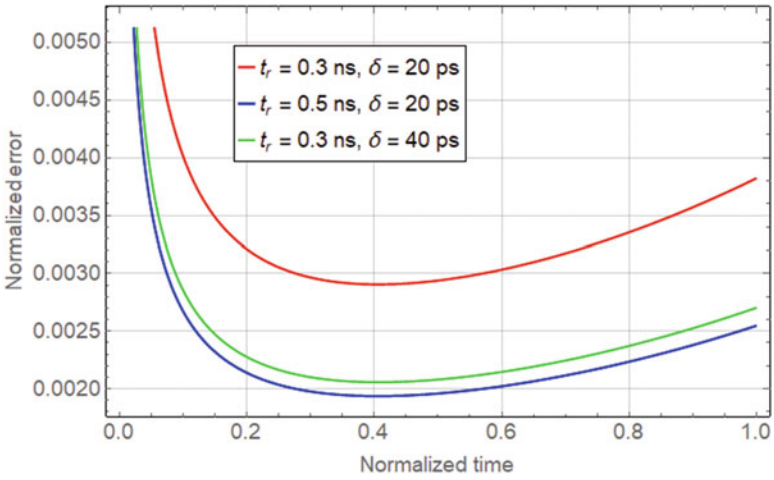

Fig. 2.12 Time evolution of error $\sigma(t_i)$ normalized to $k = 1/\tau_r$ for an exponential leading edge of the scintillation pulse in the time interval from zero to τ_r at different channel width δ and τ_r

$$t_i = \tau_r \ ln\left(\frac{3\left(e^{\frac{\delta}{\tau_r}} - 1\right)\tau_r}{2\delta}\right) - \frac{\delta}{2} \tag{2.16}$$

Figure 2.12 shows the time evolution of $\sigma(t_i)$ for the leading edge of the scintillation pulse in the time interval from zero to τ_r at $k = 1/\tau_r$ and $Am = 1$.

The optimal time range for the event registration is in between 0.2 and 0.6 of τ_r. The position of the minimum directly depends on τ_r: the steeper is the slope of the leading edge, the smaller discretization step δ is applicable.

2.2.4 *Time Resolution and Types of Scintillators*

Three types of inorganic scintillation materials might be pointed in view of the mechanism of luminescence (see [5] for more details). The types are cross-luminescent, selfactivated, and activated materials. The inorganic scintillators might be single crystals, polycrystalline materials, glasses or glass ceramics. Cross-luminescent scintillator emits via radiative transitions during the electron relaxation from the valence band to the core-valence band. It is observed predominantly in fluorides and chlorides [15], in which the band gap is considerably wider than in oxides, bromides, and iodides. The cross-luminescence kinetics is quite fast, with the decay time constant less than a nanosecond, whereas the leading edge is in the picosecond domain. The most recognized cross-luminescent scintillator is BaF_2 [5].

Anionic complexes, i.e., metal ions coordinated by the anions (F^-, Cl^-, Br^-, I^-, O^{2-}, S, Se), and excitons are the luminescence species in self-activated scintillation materials. The luminescence is subjected to a concentration quenching in the self-activated scintillators based of anionic complexes, whereas the scintillation pulse shape due to exciton luminescence depends on the excitation intensity. It is worth noting that the excited states in such materials are created immediately after the excitation thermalization. The shape of the decay is formed by the processes of thermal quenching, which strongly depend on temperature. The leading edge is formed by the thermalization processes and its time is in the range of a few picoseconds. For example, led tungstate ($PbWO_4$) single crystal has a short luminescence rise time in subpicosecond domain and τ_d below 10 ns at room temperature [5, 7].

Activated materials have luminescence centers which are created in inorganic matrices by intentional doping. I addition to doping ions, other point structure imperfections of the host matrix possessing light emission properties can cause scintillation. Usually, relatively low dopant concentrations, not more than a few per cent of a substituted ion in the host matrix, are used. Thus, the transport of the excitations to the luminescence center plays a crucial role in the creation of both the leading edge and the decay part of the scintillation pulse in the doped scintillators. Most of the well-known scintillators are doped or multidoped inorganic materials [5].

The luminescence kinetics corresponding to the three types of scintillators might be characterized in the following way. The cross-luminescence materials exhibit an instantaneous response. The self-activated materials response with certain rise time, which is substantially faster than the decay time. The scintillators activated by doping have a relatively long luminescence response due to the population of the luminescent centers via dipole-dipole interaction with excitons transferring the excitation. The leading edges of such scintillation pulses are presented in Fig. 2.2 (left panel).

Focusing on the analysis of the different scintillator types, let us suppose that the energy deposit due to the interaction of ionizing radiation with a thin layer of scintillator medium occurs instantaneously, what is the case of the low energy gamma-quanta, as discussed in Chap. 1, and the effect of the light collection can be neglected. The mean rate of photon emission after energy deposit is described by emission intensity $S(t)$. The number of photons emitted from the moment of energy deposit until the moment t is equal to $N(t) = \int_0^t S(t')dt'$. For simplicity, we assume that all the photons are emitted independently, and, therefore, the number of photons emitted during the time interval (0, t) is distributed according to the Poisson distribution: $p_n(t) = \frac{N^n(t)}{n!} e^{-N(t)}$.

Consider the scintillation pulse registration with detection threshold N_{th}, what corresponds to a third approach, considered at the beginning of this Chapter, meaning that the registration of at least N_{th} photons is sufficient for the detection of an event. In this case, the probability of the event registration at timestamp t_{ts} is

$$\begin{aligned} p_{n\geq N_{\text{th}}}(t_{\text{st}}) &= \sum_{n=N_{\text{th}}}^{\infty} \frac{N^n(t_{\text{st}})}{n!} e^{-N(t_{\text{st}})} \\ &= 1 - \sum_{n=0}^{N_{\text{th}}-1} \frac{N^n(t_{\text{st}})}{n!} e^{-N(t_{\text{st}})} = 1 - \frac{\Gamma(N_{\text{th}}, N(t_{\text{st}}))}{\Gamma(N_{\text{th}})}, \end{aligned} \tag{2.17}$$

where $\Gamma(x)$ is the Euler gamma function and $\Gamma(x,z)$ is the incomplete Euler gamma function.

The density distribution function of the timestamp t_{st} is

$$G(t_{\text{st}}) = \frac{\mathrm{d}p_{n\geq N_{\text{th}}}(t_{\text{st}})}{\mathrm{d}t_{\text{st}}} = \mathrm{e}^{-N(t_{\text{st}})} \frac{N^{N_{\text{th}}-1}(t_{\text{st}})}{(N_{\text{th}}-1)!} I(t_{\text{st}}). \tag{2.18}$$

The maximum of this function and its width are defined by the mean delay of the timestamp $\langle t_{st} \rangle$ and the standard deviation of the timestamp σ_{tst}:

$$G(t_{st}) \sim e^{\frac{(t_{st}-\langle t_{st}\rangle)^2}{2\sigma_{t_{st}}^2}}. \tag{2.19}$$

The values of $\langle t_{st} \rangle$ and σ_{tst} can be evaluated for the three shapes of the scintillation kinetics described above.

For a negligible rise time, case i), the intensity of photon emission can be written as

$$I^{(1)}(t) = \frac{N_{em}}{\tau_d} e^{-\frac{t}{\tau_d}}, \tag{2.20}$$

where N_{em} is the number of photons emitted per one event and τ_{d} is the decay time. For small t (2.20) can be simplified to

$$I^{(1)}(t) \approx \frac{N_{\text{em}}}{\tau_{\text{d}}}. \tag{2.21}$$

In the case of a short rise time, case ii), the signal exhibits a single-exponential rise. In this case, the intensity of photon emission can be written as:

$$I^{(2)}(t) = \frac{N_{em}}{\tau_d + \tau_r} \left(e^{-\frac{t}{\tau_d}} - e^{-\frac{t}{\tau_r}} \right) \tag{2.22}$$

with the peak value at $t_{\max} = \frac{\tau_d \tau_r}{\tau_d - \tau_r} \, ln \, \frac{\tau_d}{\tau_r}$.

For small t, one can show that

$$I^{(2)}(t) \approx \frac{N_{\text{em}} t}{\tau_{\text{d}} \tau_{\text{r}}} \tag{2.23}$$

The analytical expression for the case of dipole-dipole transfer of excitations to emitting centers, case iii), is more bulky:

$$I^{(3)}(t) = \frac{N_{\mathrm{em}} q}{\sqrt{\tau_{\mathrm{d}}(\tau_{\mathrm{d}} - \tau_{\mathrm{ex}})}} \mathrm{e}^{-\frac{t}{\tau} + \frac{q^2 \tau_{\mathrm{d}}}{\tau_{\mathrm{d}} - \tau_{\mathrm{ex}}}} \times \left(\mathrm{Erfc}\left(q \sqrt{\frac{\tau_{\mathrm{d}}}{\tau_{\mathrm{d}} - \tau_{\mathrm{ex}}}} \right) - \mathrm{Erfc}\left(\sqrt{\frac{t(\tau_{\mathrm{d}} - \tau_{\mathrm{ex}})}{\tau_{\mathrm{d}} \tau_{\mathrm{ex}}}} + q \sqrt{\frac{\tau_{\mathrm{d}}}{\tau_{\mathrm{d}} - \tau_{\mathrm{ex}}}} \right) \right) \tag{2.24}$$

for $\tau_d > \tau_{ex}$ and

$$I^{(3)}(t) = \frac{N_{\mathrm{em}} q}{\sqrt{\tau_{\mathrm{d}}(\tau_{\mathrm{ex}} - \tau_{\mathrm{d}})}} e^{-\frac{t}{\tau_{\mathrm{d}}} - \frac{q^2 \tau_{\mathrm{d}}}{\tau_{\mathrm{ex}} - \tau_{\mathrm{d}}}} \times \left(\mathrm{Erfi}\left(q \sqrt{\frac{\tau_{\mathrm{d}}}{\tau_{\mathrm{d}} - \tau_{\mathrm{ex}}}} \right) + \mathrm{Erfi}\left(\sqrt{\frac{t(\tau_{\mathrm{d}} - \tau_{\mathrm{ex}})}{\tau_{\mathrm{d}} \tau_{\mathrm{ex}}}} - q \sqrt{\frac{\tau_{\mathrm{d}}}{\tau_{\mathrm{d}} - \tau_{\mathrm{ex}}}} \right) \right) \tag{2.25}$$

for $\tau_{\mathrm{em}} > \tau_{\mathrm{ex}}$.

Here, τ_{ex} is the exciton lifetime, $q = \frac{2\pi^2}{3} n_{\mathrm{A}} R_{d-d}^3$, $R_{d\text{-}d}$ is the exciton-to-activator dipole-dipole transfer radius, and n_A is the activator concentration.

For small t, one can show that

$$I^{(3)}(t) \approx \frac{2 N_{\mathrm{em}} q \sqrt{t}}{\tau_{\mathrm{d}} \sqrt{\tau_{\mathrm{ex}}}}. \tag{2.26}$$

The mean number of photons emitted during the period Δt from the energy deposit moment is equal to:

$$N^{(1)}(\Delta t) = N_{\mathrm{em}} \left(1 - e^{-\frac{\Delta t}{\tau_{\mathrm{d}}}} \right) \approx N_{\mathrm{em}} \frac{\Delta t}{\tau_{\mathrm{d}}}, \tag{2.27}$$

$$N^{(2)}(\Delta t) \approx N_{\mathrm{em}} \frac{(\Delta t)^2}{\tau_{\mathrm{d}} \tau_{\mathrm{r}}} \tag{2.28}$$

for cases (i) and (ii), respectively.

The corresponding expression for case (iii) is rather bulky, however, its asymptotic value for small Δt is equal to:

$$N^{(3)}(\Delta t) \approx N_{\mathrm{em}} \left(\frac{4 q (\Delta t)^{3/2}}{3 \tau_{\mathrm{d}} \sqrt{\tau_{\mathrm{ex}}}} - \frac{q^2 (\Delta t)^2}{\tau_{\mathrm{d}} \tau_{\mathrm{ex}}} \right). \tag{2.29}$$

The estimations for the time resolution in the three cases are, correspondingly:

$$\langle t_{\mathrm{st}} \rangle \approx \tau_{\mathrm{d}} \frac{N_{\mathrm{th}}}{N_{\mathrm{em}}}, \tag{2.30}$$

$$\langle t_{\mathrm{st}} \rangle \approx \sqrt{\tau_{\mathrm{d}} \tau_{\mathrm{r}} \frac{N_{\mathrm{th}}}{N_{\mathrm{em}}}} \tag{2.31}$$

$$\langle t_{\mathrm{st}} \rangle \approx \left(\frac{3\tau_{\mathrm{d}} \sqrt{\tau_{\mathrm{ex}}}}{4q} \frac{N_{\mathrm{th}}}{N_{\mathrm{em}}} \right)^{2/3} \tag{2.32}$$

The value of N_{th} has to be chosen, in accordance with signal-to-noise considerations, by taking into account the properties of the photodetector used to read out the signal.

Equation (2.30) shows that in the case of cross-luminescent scintillation, $\langle t_{\mathrm{st}} \rangle$ is proportional to τ_d. Thus, fast luminescence decay is crucial for achieving good time resolution whereas a high light yield of scintillator material increases the ratio $N_{\mathrm{th}}/N_{\mathrm{em}}$, where N_{th} depends on the detecting system and irradiation environment.

In self-activated scintillator, according to (2.31) the time resolution for measurements at high energy deposit is proportional to $N_{\mathrm{em}}{}^{-1/2}$ and can be as fast as 100 ps [16, 17].

The third case described by (2.32) frequently occurs in activated scintillation materials, when photons are emitted after the excitation is transferred to emitting centers, thus, the transfer process deteriorates the time resolution.

Equations (2.30), (2.31) and (2.32) contain an important parameter N_{th}/N_{em}, characterizing the influence of noise for the registration. The value N_{th} has two contributions: the contribution due to scintillation material, as described in Chap. 1, and the contribution due to the registration chain consisting of a photo-receiver and electronics. When the scintillation detector registers quite rare events, and the optical noise due to parasitic luminescence is negligible within the registration gate, the optical noise becomes vanishingly small. Therefore, the regime of counting the first photons, considered above, suits the conditions of reliable registration. A typical example of such an application is medical imaging techniques, like PET imaging, exploiting low-rate events. On the contrary, at the conditions of the HEP experiments or in the cargo control, the optical noise cannot be ignored and its contribution in the noise threshold and the energy noise equivalent can be estimated as described.

2.3 Concluding Remark

The analysis of different aspects of the scintillation evolution showed that the leading edge of the scintillation, its rising rate and the fraction in the scintillation pulse play a crucial role in the improvement of the precise timing measurements and time resolution. In the analysis bellow, we consider the micro-theory of the

scintillation evolution and revealed the mechanisms causing the leading edge of the scintillation response and its fluctuation, which have been not addressed in the publications before.

References

1. C. Leroy, P.G. Rancoita, *Principles of Radiation Interaction in Matter and Detection* (Word Scientific Publishing Co, Singapore, 2016)
2. S. Gundacker, R. Turtos, E. Auffray, P. Lecoq, Precise rise and decay time measurements of inorganic scintillators by means of x-ray and 511 kev excitation. Nucl. Instrum. Methods Phys. Res. A **891**, 42–52 (2018)
3. S. Gundacker, Time of flight positron emission tomography towards 100 ps resolution with L (Y)SO: An experimental and theoretical analysis. J. Instrum. **8**, P07014 (2013)
4. The CMS Collaboration, Technical design report A MIP Timing Detector for the CMS Phase 2 Upgrade CERN-LHCC (2019)
5. P. Lecoq, A. Gektin, M. Korzhik, *Inorganic Scintillators for Detector Systems* (Springer, Cham, 2016)
6. D. Vaisburd, O. Koroleva, S. Kharitonova, Instantaneous spectrum of passively ionized electrons in a dielectric irradiated by a high-power electron beam. Russ. Phys. J. **39**(11), 1114–1121 (1996)
7. E. Auffray, M. Korjik, R. Augulis, et al., Luminescence rise time in self-activated $PbWO_4$ and Ce-doped $Gd_3Al_2Ga_3O_{12}$ scintillation crystals. J. Lumin. **178**, 54–60 (2016)
8. R. Novotny, D. Bremer, V. Dormenev et al., The PANDA Electromagnetic Calorimeter – A High-Resolution Detector Based on PWO-II. 10th International Conference on Inorganic Scintillators and their Applications SCINT-2009, Jeju, Korea. 8–12 June 2009, Conference Record
9. A. Annenkov, M. Korzhik, P. Lecoq, Lead tungstate scintillation material. Nucl. Instrum. Methods Phys. Res. A **490**, 30–50 (2002)
10. M. Nikl, Wide band gap scintillation materials: Progress in the technology and material understanding. Phys. Status Solidi A **178**, 59–600 (2000)
11. M. Nikl, P. Bohasek, et al., Excitonic emission of scheelite tungstates AWO_4 (A=Pb, Ca, Ba, Sr). J. Lumin. **87**, 1136–1139 (2000)
12. N. Akchurin, F. Bedeschi, A. Cardini, R. Carosi, G. Ciapetti, R. Ferrari, S. Franchino, M. Fraternali, M. Korzhik, R. Wigmans, et al., New crystals for dual-readout calorimetry. Nucl. Instrum. Methods Phys. Res. Sect. A **604**, 512–526 (2009)
13. D. Yvon, V. Sharyy, Patent accepted, Réf: FR N° 17/59065, 29 Sep. 2017
14. R. Post, L. Schiff, Statistical limitations on the resolving time of a scintillation counter. Phys. Rev. **80**, 1113 (1950)
15. C.W.E. van Eijk, Cross-luminescence. J. Lumin. **60–61**, 936–941 (1994)
16. M. Kavatsyuk, D. Bremer, V. Dormenev, et al, Performance of the prototype of the electromagnetic calorimeter for PANDA. Nucl. Instrum. Methods Phys. Res. Sect. A **648**, 77–91 (2011)
17. D. del Re, Timing performance of the CMS ECAL and prospects for the future. J. Phys. Conf. Ser. **587**, 12003 (2015)

Chapter 3
Development of Excited Region of the Track. Rise and Decay Kinetics of Scintillation

Abstract In this chapter, we discuss the concept of the electronic excitations created by ionizing particles in solids, their transformation, interaction, and temporal evolution. This evolution is analyzed for different types of scintillators: self-activated, cross-luminescent and crystals with activators. The formation of excited region in the track of an ionizing particle is especially addressed. The rise and decay kinetics of scintillation is analyzed in terms of the spatial distribution of electronic excitations in crystals with different scintillation origin.

3.1 Initial Stage of the Interaction of a High-Energy Particle with Matter

The energy deposit of different kinds by particles in inorganic scintillating media is discussed in Chap. 1. Here, we shortly remind that the interaction of a high-energy particle with the crystal depends on the particle type and energy. In this chapter, the term "high energy" will be used in a wide sense, as the particle energy, which is a much higher than the typical threshold energy of electronic excitations in insulators (5–10 eV). Typically, this interaction starts at the moment when the ionizing particle starts to deposit energy into the crystal. For a neutral high-energy particle, say an X-ray or γ- quantum, the interaction initiates generation of a valence or core hole and an electron at the point, where this quantum is absorbed or where the Compton scattering occurs with creation of the same excitations (in the latter case, the energy of the generated electron-hole pair is smaller than that in the case of direct photo-absorption). The analogous situation occurs in the case of the interaction of neutrons or other neutral particles with matter. For instance, the interaction with neutrons starts at the moment, when an alpha-particle or another charged particle appears as a result of the neutron reaction with a nucleus. Consequently, the electronic excitations appear initially at certain distance from the surface, which exceeds the penetration or scattering length for a neutral particle and the size of the crystal. In the case when the penetration length is approximately equal or longer than the thickness of the crystal, some of the high-energy particles do not interact with the crystal at all.

M. Korzhik et al., *Physics of Fast Processes in Scintillators*, Particle Acceleration and Detection, https://doi.org/10.1007/978-3-030-21966-6_3

On the contrary, a charged particle starts interacting at the moment, when the particle passes through the boundary of the crystal. This kind of interaction occurs due to the electric field of the particle and, in principle, can occur even without penetration of the particle into the media [1]. For instance, a fast electron passing near a nanoparticle can be inelastically scattered with production of electronic excitations within the nanoparticle. In this case, the whole energy of the ionizing particle or a part of it is converted into the energy of electronic excitations.

Charged particles have an additional channel enabling the direct conversion of the energy of this particle into optical photons. The Cherenkov radiation, which occurs when a charged particle propagates through the media with the velocity higher than the phase velocity of the low-energy (optical) photons, is the most common example of such interaction. These "prompt" photons provide the opportunity for the fast detection of the energy deposit of the high energy particle in the scintillator. However, the yield of the Cherenkov radiation is usually rather low. The electron energy threshold for such process equals approximately a hundred of keV (63 keV for crystals with refractive index $n = 2.2$, 144 keV for $n = 1.6$). Another example of the ultrafast conversion into photons is the transient radiation occurring, when the particle crosses a boundary between media with different refraction indexes.

The Bremsstrahlung is another process to be considered. In this case, a part of the energy of a charged particle is converted into an X-ray photon. To be registered, this photon should be further converted into electronic excitations.

Anyway, the registration process in most cases starts with the creation of primary electronic excitations in the crystal. To follow the evolution of the primary excitations, the spectra of the electronic excitations in scintillators have to be analyzed.

3.2 Spectra of Excitations in Insulating Crystals

Inorganic scintillators are mostly insulating crystals. These crystals are characterized by a special spectrum of electronic excitations. Namely, electronic excitations, which can be created by electromagnetic field in such crystals, cannot have energy below the band gap energy E_g. More exactly, this low energy limit is slightly less by approximately the exciton energy E_{ex}. Only phonons (i.e., the quanta of lattice vibrations) have energies less than this limit. The interaction of an ionizing particle with matter is mainly due to its electromagnetic field, and the elementary quanta of this field are photons. Photons in solids differ from the photons in vacuum, since electromagnetic fields polarize the medium. The polarization properties can be described using the complex dielectric function. In bulk uniform crystals, we can use the Fourier transformation of electric fields, and the response of the solid is described by its dielectric permittivity $\varepsilon(\omega, \mathbf{q})$, which is the function of the frequency ω and the wavevector $\mathbf{q}$ of the electric field. The imaginary part of this function $\mathrm{Im}(\varepsilon(\omega, \mathbf{q}))$ is proportional to the rate of transformation of transversal photons into neutral electronic excitations. The electric field of such photons is perpendicular to the wavevector $\mathbf{q}$. $\mathrm{Im}(\varepsilon(\omega, \mathbf{q}))$ is non-zero only for the energies $\hbar\omega$ and the momenta

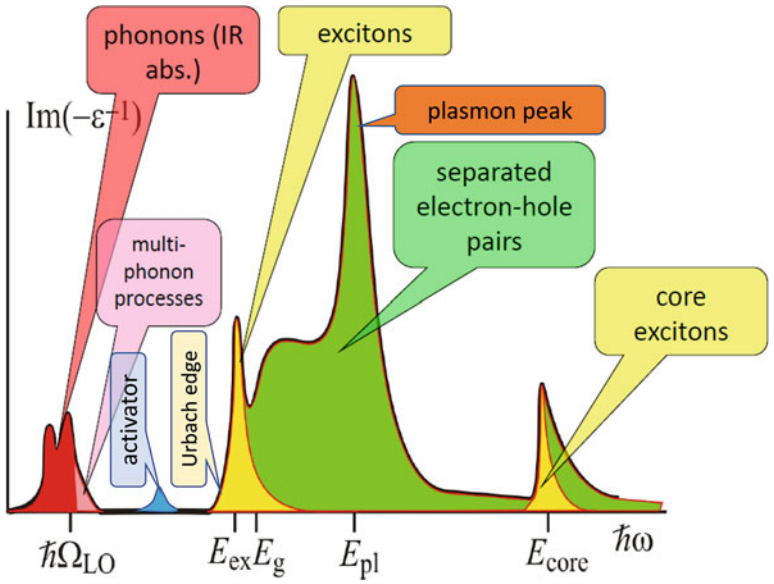

Fig. 3.1 Structure of energy loss function and types of electronic excitations in insulators. Specific energies are indicated on the X axis

$\hbar\mathbf{q}$ corresponding to possible neutral electronic excitations. Coulomb fields can also be described as temporal and spatial Fourier components in the form of longitudinal photons (for which the electric field is parallel to the wavevector $\mathbf{q}$). These photons can also be transformed into elementary excitations with the rate proportional to the electron energy loss function $\mathrm{Im}\left(-\frac{1}{\varepsilon(\omega,\mathbf{q})}\right) = \frac{\mathrm{Im}(\varepsilon(\omega,\mathbf{q}))}{|\varepsilon(\omega,\mathbf{q})|^2}$.

The spectrum of the energy loss function is shown in Fig. 3.1. The spectrum of the imaginary part of dielectric permittivity $\mathrm{Im}(\varepsilon(\omega,\mathbf{q}))$ should be the same, except of the absence of the plasmon resonance (the region, where $|\varepsilon(\omega,\mathbf{q})|$ reaches its minimum).

As pointed out above, the electronic excitations are created by photons with energies higher than the exciton energy E_{ex}. Multiphoton interactions, when two or three photons of a strong electromagnetic field create one electronic excitation are not taken into account in our further considerations. The photons with their energy lower than the band gap energy E_g, i.e., the minimal energy of an electron-hole pair with an infinite distance between them, can create only excitons (a bound state of an electron and hole pair). The photons with energy above E_g create separated electron-hole pairs (still interacting at the first moments due to Coulomb attraction). The kinetic energies of electrons and holes obey the energy conservation rule: $E_e + E_h = \hbar\omega - E_g$. This kinetic energy is distributed between an electron and a hole. The hole kinetic energy can be acquired by holes either in valence band ($0 < E_h < E_v$) or in core bands ($E_h = E_i - E_g$, where E_i is the ionization energy for core level in the crystal). In other words, the electron can be ionized to conduction

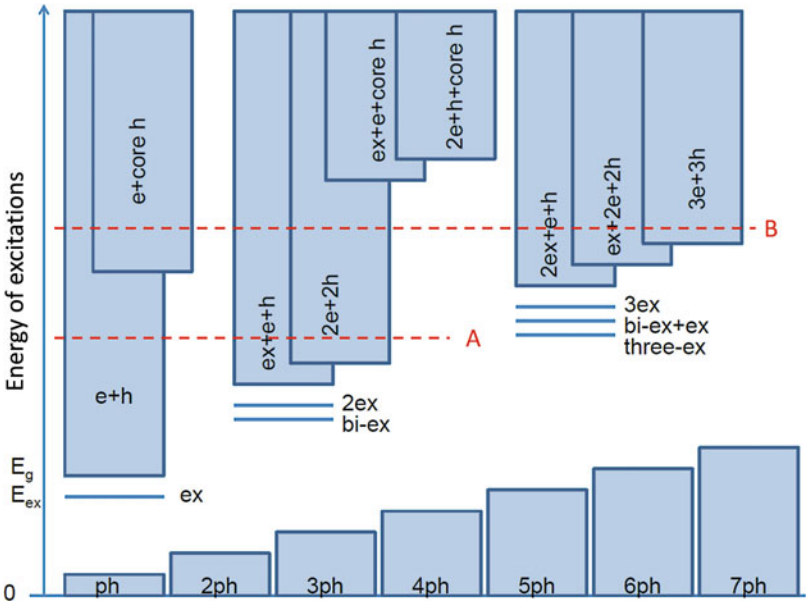

Fig. 3.2 Hierarchy of excited states with different numbers of elementary excitations in insulating crystals

band from different valence or core bands. We take here the width of the core bands equal to zero, except of specific cases like the case of cross-luminescent crystals, when the width of the upper core bands should also be taken into account. The excitons and the different elementary excitations created by photon absorption are schematically plotted on the left column in Fig. 3.2.

There exists another energy region, where transversal photons can be converted into crystal excitations. This is the infrared region, where photons can excite transversal polarization phonons. The phonons reflecting the vibrations of ions or atoms in crystals have energies $\hbar\Omega$, which are substantially smaller than E_g. Excitations in electronic subsystem of the crystal are also involved in the phonon generation, since the electric field of charge carriers induces polarization of the ions or atoms. Such interaction results in the creation and annihilation of longitudinal phonons, in contrary with the phonons produced by transversal photons. Therefore, electronic excitations and phonons in crystals strongly interact. Self-trapping of excitons and holes (in some crystals, of electrons too), the Urbach tail absorption below the excitonic resonance, the Stokes shift between the absorption and emission bands of activators, etc. are the consequences of this interaction. Strictly speaking, the electrons and holes with low kinetic energies are polarons ("naked" carriers surrounded by a phonon cloud). These states might be revealed by in the absorption coefficient and the electron energy loss function. For instance, the direct absorption in diamond at Γ-point starts at ~7.5 eV. Nevertheless, weak absorption starts already at ~5 eV. This absorption occurs over the indirect gap and is a second-

order process assisted by phonon emission or absorption. This input is also present in the energy loss function.

Visible, UV or VUV radiation of low intensity can create individual electronic excitations in crystals – excited defect states, excitons, and separated electron-hole pairs. Such excitations can be regarded as being alone in the crystal volume (individual excitations do not interact with each other due to large distance between them). On the contrary, intense short-pulse laser excitation simultaneously creates a lot of excitations in a small volume. In this case, interaction between these excitations and transformation of them into new types of excitations have to be taken into account. The analogous regions with high density of excitations are created in the tracks of ionizing particles.

To describe how an electronic excitation with a high energy is converted into a set of secondary excitations, we should discuss the crystals with many electronic excitations in general terms. Figure 3.2 shows the hierarchy of excitations with the same energy but with different numbers of excitations. For instance, line A shows that at least three types of electronic excitations ($e + h$, $2e{+}2\,h$, $e + h + ex$) could have the same energy. However, the densities of states are quite different. Rough estimation can be done using an oversimplified picture. Let us suppose that the crystal volume is V, whereas the volume of the unit cell is v. Then the total number of cells $N = V/v$. In these notations, the density of states for excitons is proportional to $g_{ex} \sim N$, for electron-hole pairs, $g_{e+h} \sim N^2$ (since an electron and a hole can occur in each unit cell), for state consisting of an exciton plus e-h pair, $g_{ex+e+h} \sim N^3$, for two electron-hole pairs, $g_{2e+2h} \sim N^4$, etc. If these states with the different numbers of excitations can be transformed in each other, the transformation occurs only in one direction ($e + h \rightarrow 2e{+}2\,h$) if N is high, since the ratio of rates of the direct and reverse transformations is proportional to the ratio of densities of final states (N^2 in the considered case). Only in systems with relatively low N (like nanoparticles) the transformation can occur in both directions ($e + h \leftrightarrow 2e{+}2\,h$). The direct transformation results in multiplication of electronic excitations. This effect was directly studied under VUV radiation with energy $\hbar\omega > 2E_g$, and is called "photon multiplication" in case of luminescent crystals [2–4]).

Line B in Fig. 3.2 shows the ways of transformation for the electron-hole pair when the hole is created at the core level. This state is in resonance with another electron-hole pair with the hole component in the valence band (and with higher electron energy in comparison with initial state). Such transformation can occur only in case when the wavefunctions of electron and core hole overlap. The conversion of the initial electron-hole pair into the final one has either dipole-dipole or exchange nature. The transformation of the initial excitation into a set of two or three electron-hole pairs occurs only with the Auger decay of core hole.

Figure 3.2 also shows a new type of complex excitations like bi-excitons, trions, etc. For instance, bi-exciton can be regarded as a two-exciton "molecule" which is formed due to Coulomb interaction of four charges (or like dipole-dipole interaction, if two excitons are not mixed). Again, the density of states for bi-excitons is proportional to N, and they are important mainly in nanostructured materials or if two excitons are created in the close vicinity.

We also plot schematically multi-phonon states. These states can overlap in energy with electronic excitations (if the number of phonons is larger than $E_g/\hbar\Omega$), and the conversion of an electronic excitation into phonons can be regarded as multi-phonon non-radiative decay of excitations.

3.3 Scattering of Electronic Excitations in Insulators

In reaction like $e + h \rightarrow 2e{+}2h$ ($e + h \rightarrow e + h + ex$) one of the initial charge carriers remains often unchanged. Therefore, we can consider this reaction as inelastic scattering of electron $e \rightarrow 2e + h$ ($e \rightarrow e + ex$), if the hole state remains unchanged, or as Auger process $h \rightarrow e{+}2h$ ($h \rightarrow h + ex$) in case of fixed state of the primary electron. The reactions of such types occur due to Coulomb interaction of initial electron or hole and can be regarded as emission and absorption of longitudinal photon with energy $\hbar\omega$ and momentum $\hbar\mathbf{q}$, for instance, $e \rightarrow e + (\hbar\omega, \hbar\mathbf{q})$, $(\hbar\omega, \hbar\mathbf{q}) \rightarrow e + h$ (or $(\hbar\omega, \hbar\mathbf{q}) \rightarrow ex$). The schemes of these processes are shown in Fig. 3.3.

All of these scattering processes are connected with the interaction of charge carriers (electrons, holes, and their bound states – excitons) with bosons like photons and phonons. The interaction with photons and even phonons has electromagnetic nature. Both types of interaction are connected with the dielectric properties of the media, in the states of thermal equilibrium or non-equilibrium. Therefore, dielectric permittivity and its singularities are important for description of the scattering and relaxation of electronic excitations.

Note, electrons and holes are regarded as quasiparticles with energy and wavefunction determined by taken into account their interaction with other electrons and ions in the crystal. The energy of a quasiparticle depends on the quasi-momentum $\mathbf{p} = \hbar\mathbf{k}$, where $\mathbf{k}$ is the wave-vector which is restricted by the Brillouin zone for ideal crystal. Allowed energies form a set of branches $E_s(\mathbf{p})$. The group velocity of a quasiparticle is $\mathbf{v} = \frac{1}{\hbar}\frac{\partial E_s(\mathbf{p})}{\partial \mathbf{p}}$. For quasiparticles with relatively high energy $E \gg E_g$ (typically for electrons with energies higher than 50 eV) one can neglect their interaction with other electrons and ions, and the dispersion law becomes $E(\mathbf{p}) = \frac{p^2}{2m}$ (in non-relativistic case), where m is free electron mass and $\mathbf{p}$ is now regarded as non-restricted wave-vector. Even for this energy range some solid-state effects remain. They are presented e.g. in EXAFS as elastic scattering of electrons on the nearby ions, with corresponding oscillations of absorption coefficient above the X-ray absorption edges. Roughly speaking, the electrons with energy higher than ~50 eV can be regarded as nearly free electrons, whereas the influence of solid-state effects increases with decreasing electron energy.

A similar situation exists for holes. Holes at deep core levels (with ionization energy deeper than ~50 eV) can be considered as atomic ones, whereas the uppermost core levels form bands with finite width (about 1 eV), like 5p bands of Ba in BaF_2, and such holes can be delocalized and act as free carriers. The width of the valence band (VB) can be as high as ~20 eV (for diamond), the typical VB width is about 6 eV for oxygen-containing crystals and 1 to 2 eV for halide crystals.

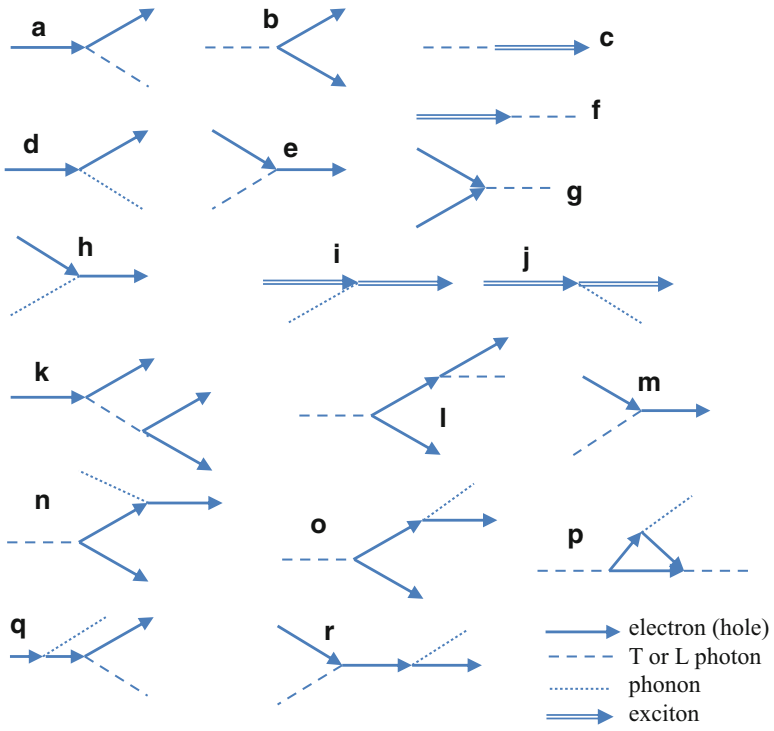

Fig. 3.3 Scheme of different scattering processes in insulators with electrons, holes, excitons, photons and phonons. First order processes: (**a**) emission of longitudinal (L) or transversal (T) photon by an electron (hole); (**b**) conversion of a photon into electron-hole pair; (**c**) conversion of a photon into exciton; (**d**) phonon emission; (**e**) absorption of L or T photon by a carrier; (**f**) photon emission by exciton; (**g**) radiative recombination of electron and hole; (**h**) phonon absorption by an electron (hole); (**i**) phonon absorption by an exciton; (**j**) phonon emission by an exciton; (**m**) photon absorption by "free" carrier (interbranch transition). Second order processes: (**k**) inelastic scattering of electron (hole) with production of additional e-h pair; (**l**) Compton scattering; (**n**, **o**) phonon-assisted photon absorption (indirect interband transition); (**p**) Brillouin scattering; (**q**) phonon-assisted photon emission by "free" carrier; (**r**) phonon-assisted photon absorption by "free" carrier (Drude absorption)

If we disregard in the first order of perturbation the interaction between quasiparticles, the dielectric permittivity can be written in terms of dipole transition matrix element between states m and n $\mathbf{D}_{nm} = \left\langle n \middle| \widehat{\mathbf{D}}(\mathbf{r}) \middle| m \right\rangle$, $\widehat{\mathbf{D}}(\mathbf{r}) = \sum_i e_i \mathbf{r}_i \delta(\mathbf{r} - \mathbf{r}_i)$ (see, e.g., [5, 6]):

$$\varepsilon(\omega, \mathbf{q}) = 1 + \frac{4\pi}{3\hbar} \sum_{nm} \left(|\mathbf{D}_{mn}|^2 \right)_{-\mathbf{q}} (1 - f_m) f_n \left(\frac{1}{\omega - \omega_{nm}} + i\pi\delta(\omega - \omega_{nm}) \right). \quad (3.1)$$

Here f_m and f_n are population of states with energies $E_m(\mathbf{p}_m)$ and $E_n(\mathbf{p}_n)$, $\hbar\omega_{nm} = E_n(\mathbf{p}_n) - E_m(\mathbf{p}_m)$ and $(\cdots)_{-\mathbf{q}}$ denotes spatial Fourier component of the corresponding value.

The kinetic equation for the population functions can be written in Boltzmann form as

$$\frac{df_n}{dt} = \frac{4\pi V}{9\hbar^2}\sum_{mn'm'}\int d\omega \int d^3q \left(|\mathbf{D}_{mn}|^2\right)_{-\mathbf{q}} \left(|\mathbf{D}_{n'm'}|^2\right)_{-\mathbf{q}} \delta(\omega-\omega_{nm})\delta(\omega-\omega_{n'm'})\times \\ \times \left[\frac{1}{|\varepsilon(\omega,\mathbf{q})|^2} + \frac{2}{|\varepsilon(\omega,\mathbf{q}) - c^2\mathbf{q}^2/\omega^2|^2}\right](f_m f_{n'} - f_{m'} f_n). \tag{3.2}$$

The first term in square brackets corresponds to interaction through longitudinal electric fields, whereas the second one, through transversal electric fields. This equation can be regarded as a rate equation, which describes the scattering with explicit account of final states. If we do not interest in the products of the scattering (in the spectrum of secondary excitations), the equation can be rewritten in a form which corresponds to emission of intermediate longitudinal of transversal phonons:

$$\frac{df_n}{dt} = \frac{V}{3\pi\hbar}\int d\omega \int d^3q\, \mathrm{Im}\left[-\frac{1}{\varepsilon(\omega,\mathbf{q})} - \frac{2}{\varepsilon(\omega,\mathbf{q}) - c^2\mathbf{q}^2/\omega^2}\right] \\ \times \sum_m \left(|\mathbf{D}_{mn}|^2\right)_{-\mathbf{q}} \delta(\omega-\omega_{nm}) f_n(1-f_m). \tag{3.3}$$

These formulas describe the scattering (transformation) of excitations of any types, both high- and low-energy. The first term in square brackets includes dipole-dipole energy transfer between excited and non-excited states of activators, Auger processes for holes, etc. The second term corresponds to reabsorption of the emission of these centers. The second term of the equation in form (3.3) describes also radiative processes like emission of activators, excitons, cross-luminescence, intraband luminescence and even Cherenkov radiation. Such radiative processes are included through the pole of the second term in square brackets. Please note that the denominator of this term equals to zero for transversal photons in media, when $cq = \omega\sqrt{\varepsilon(\omega,q)} \equiv \omega n(\omega)$. Here, $n(\omega)$ is the refractive index for transparency region, where the imaginary part of dielectric permittivity is very small.

Moreover, Eq. (3.3) also describes the emission and absorption of phonons, since the singularities of dielectric function in infrared region correspond to optical phonons. In this case, both phonon emission and absorption have to be considered, and the rates of these processes should be corrected by temperature dependent phonon population factors (see, e.g., Eq. (3.14) in [7]).

If the state n described by Eq. (3.3) is occupied by an electron with momentum $\mathbf{p}$ and energy $E = E_e(\mathbf{p})$, the right hand side of the equation shows that it is scattered by the crystal into the state m with momentum $\mathbf{p} - \hbar\mathbf{q}$ and energy $E - \hbar\omega = E_e(\mathbf{p} - \hbar\mathbf{q})$

with emission of a longitudinal photon with energy $\hbar\omega$ and momentum $\hbar\mathbf{q}$ (see, e.g., [8]). This longitudinal photon should be absorbed in the crystal at short distances (on nanometer scale) with production of either an electron-hole pair with the energy of electron component $E_1 = E_e(\mathbf{p}_1)$ and momentum $\mathbf{p}_1$ and the energy of a hole component $\hbar\omega - E_1 = E_h(\hbar\mathbf{q} - \mathbf{p}_1)$ and momentum $\hbar\mathbf{q} - \mathbf{p}_1$ or an exciton with energy $\hbar\omega = E_{ex}(\hbar\mathbf{q})$ and momentum $\hbar\mathbf{q}$. Such states are included in the definition of dielectric permittivity (Eq. 3.1). The ratio of probabilities for these electron-hole and exciton channels is defined by the partial contribution of these excitations in the energy loss function.

In the relaxation of high-energy excitations in scintillators, most secondary excitations are created by fast electrons or other ionizing particles. Such particles are properly described as classical point charges, and a simple kinematic picture for the emission and absorption of photons can be used. In this case, the rate of scattering of a charged particle with charge Ze and mass M is

$$w(E) = \frac{2Z^2}{\pi a_0 m_0 v(E)} \int_0^E d(\hbar\omega) \int_{q_{\min}}^{q_{\max}} \frac{dq}{q} \operatorname{Im}\left[-\frac{1}{\varepsilon(\omega,q)} - \frac{v^2(E)q^2/\omega^2 - 1}{\varepsilon(\omega,q) - c^2q^2/\omega^2}\right] \quad (3.4)$$

Here, in a relativistic case

$q_{\max/\min} = \frac{1}{\hbar c}\left(\sqrt{E(E+2Mc^2)} \pm \sqrt{(E-\hbar\omega)(E-\hbar\omega+2Mc^2)}\right)$, $v(E) = c\sqrt{E\left(E+2Mc^2\right)}/\left(E+Mc^2\right)$, and $a_0 = \frac{4\pi\varepsilon_0\hbar^2}{m_0e^2}$ is the Bohr radius for hydrogen.

In a non-relativistic case, these formulas are simplified to $v(E) = \sqrt{2E/M}$, $q_{\max/\min} = \frac{\sqrt{2M}}{\hbar}\left(\sqrt{E} \pm \sqrt{(E-\hbar\omega)}\right)$. A detailed description of the derivation of formula (3.4) is presented, e.g., in [7].

In non-relativistic case, the stopping power (the mean energy which is lost by the particle per unit length of its trajectory) equals to

$$-\frac{dE}{dx} = \frac{2Z^2}{\pi a_0 m_0 v^2(E)} \int_0^E \hbar\omega\, d(\hbar\omega) \int_{q_{\min}}^{q_{\max}} \frac{dq}{q} \operatorname{Im}\left[-\frac{1}{\varepsilon(\omega,q)} - \frac{v^2(E)q^2/\omega^2 - 1}{\varepsilon(\omega,q) - c^2q^2/\omega^2}\right]. \quad (3.5)$$

This equation leads to different traditional forms of Bethe formula for stopping power.

Typical optical functions for wide-band-gap insulators are shown in Fig. 3.4a. We use BaF_2 as an example. We should note that excitonic peaks are well pronounced both in the dielectric function ε_2 and in the energy loss function. Meanwhile the

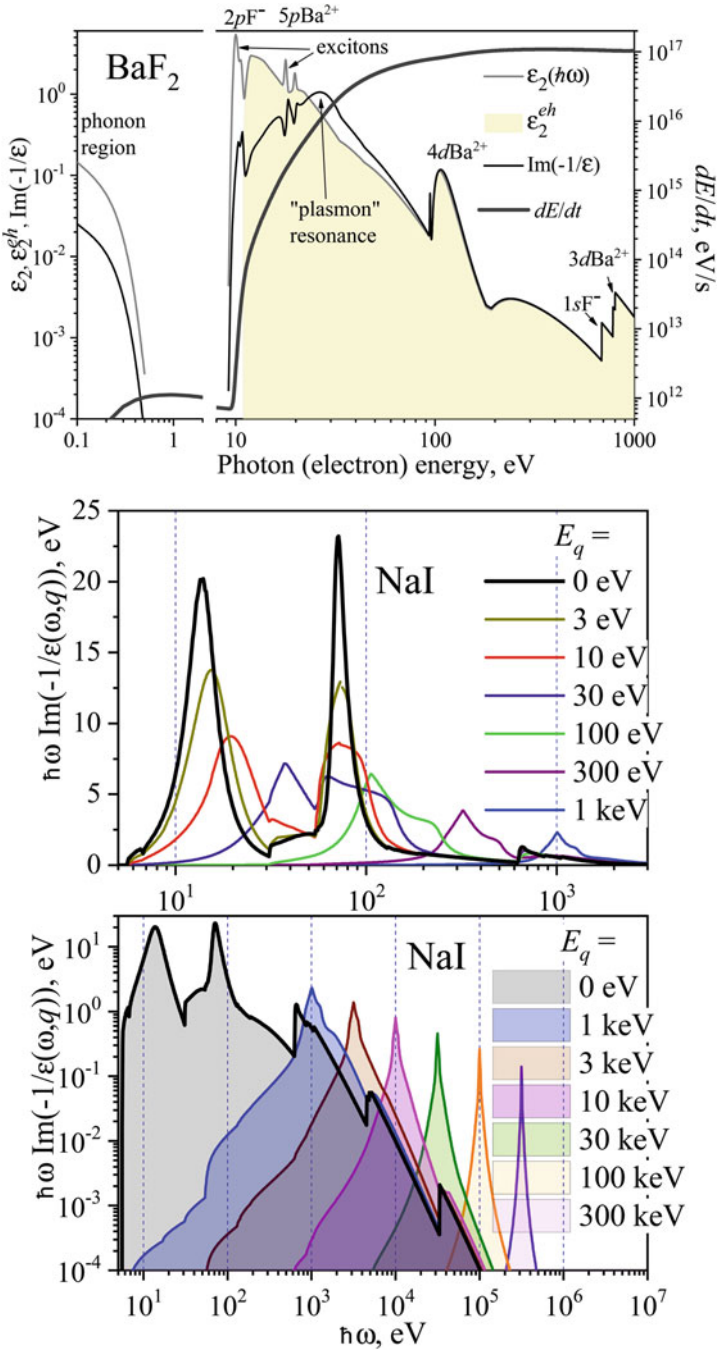

Fig. 3.4 Top panel: simulated photon energy dependences of dielectric function ε_2 (with electron-hole contribution ε_2^{eh} shown in grey), energy loss function $\mathrm{Im}(-\varepsilon^{-1}(\omega, q))$, and electron kinetic

plasmonic peak in energy loss function at 28 eV is very broad (according to the peak width, the plasmon lifetime, estimated from the uncertainty relation $\Delta E\,\Delta t \geq \hbar$, is ~0.1 fs), and plasmons in such wide-band-gap insulators should be treated as resonances rather than real quasi-particles.

The result for NaI is also presented in Fig. 3.4. Let us discuss the peculiarities of the electron loss function. First of all, we introduce the variable $E_q = \hbar^2 q^2/2m_0$ instead of q. In this case, the limits of integration over this variable become $\left(\sqrt{E} \pm \sqrt{E-\hbar\omega}\right)^2$. The maximal value of the upper integration limit (for $\hbar\omega = 0$) equals $4E$. Simple kinematic considerations show that this case corresponds to the back scattering of the primary electron by a massive scattering center at $\hbar\mathbf{q} = -2\mathbf{p}$, and the scattering angle is π. When $E_q \approx E$, the mean scattering angle for primary electron is approximately $\pi/2$. The scattering angle is small, if $E_q << E$.

For high electron energies ($E > 1$ keV), most of the scattering events occur for small E_q due to two reasons: (i) the factor $1/q$ in the integrand makes q small and, therefore, a small E_q is more preferable for scattering, and (ii) the energy loss function rapidly decreases with increasing E_q, as shown in Fig. 3.4 (lower panel). Therefore, the primary electron trajectory is slightly changed at each scattering event. The scattering events with higher angular deviations of the trajectory are relatively rare. The Bethe ridge (see, e.g., [9]) of the energy loss function plays an important role in these rare scattering events. The Bethe ridge is the peak in the energy loss function near the energy $\hbar\omega = E_g$. The ridge is evident in the bottom panel of Fig. 3.4. It corresponds to the Mott scattering of the primary electron by quasi-free electrons, if the exchange is taken into account. This scattering is the main origin of so-called δ-rays, i. e., the electrons emitted with relatively high energy. The creation of high-energy Auger electrons after the ionization of K- and L-shells of heavy ions is an additional origin of the δ-rays. Again, these processes are rather rare, as can be concluded from the energy loss function presented in Fig. 3.4. These K- and L-shells can also be filled with the emission of X-ray photons instead of the escape of an Auger electron. The absorption of these photons results in formation of high-energy electron-hole pairs far from the main track. The events producing deep core holes and δ-rays are relatively rare. Therefore, the main part of energy is deposited in the crystal as a result of sequential low angle scattering of the primary electron.

The energy loss function for NaI has many peculiarities, since there are 22 core levels. Some of them have rather low ionization energy. Valence band (six 5*p*I electrons per unit cell) form "plasmon" peak in the region from 12 to 15 eV. The energy loss function for NaI exhibits also the prominent peak due to the ionization of 4*d*I core level in the region from 60 to 80 eV. The electrons from these levels (ten electrons per unit cell) form the second plasmon in this energy range. Usually, the energy loss function rapidly decreases with the increase of transferred energy $\hbar\omega$.

Fig. 3.4 (continued) energy dependence of the rate dE/dt of energy losses for electron inelastic scattering in BaF_2 (see details in [19]). Middle and bottom panels: energy loss function $\mathrm{Im}(-\varepsilon^{-1}(\omega, q))$ multiplied by the energy loss $\hbar\omega$ versus energy loss $\hbar\omega$ for different values of q. Here, $E_q = \hbar^2 q^2/2m_0$, the dependences are simulated for$E_q \leq 1$ keV in upper panel and for $E_q \geq 1$ keV in lower panel

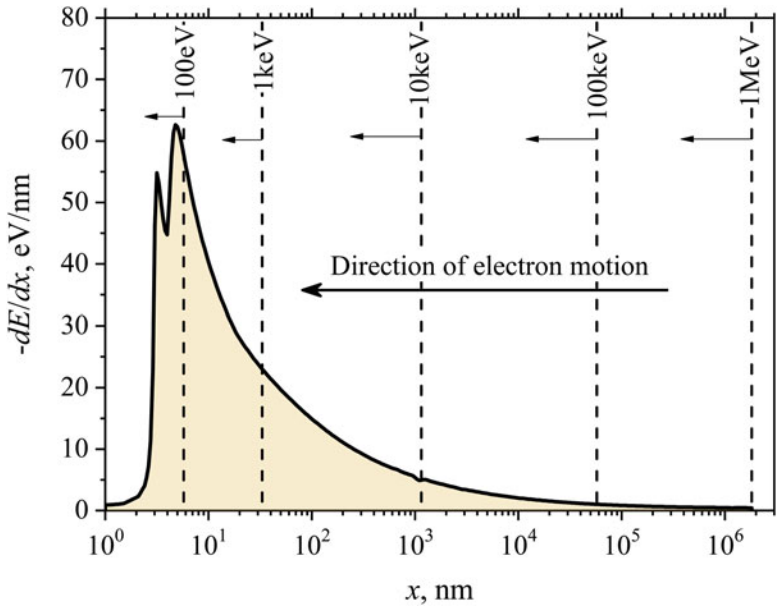

Fig. 3.5 Energy losses for electron in NaI as a function of track coordinate in continuous-slowing-down approximation (CSDA). The zero point of the coordinate is at the end of the track. Track lengths for different energies of primary electron are indicated by vertical lines

If the energy loss function is known, $-dE/dx$ can be calculated as a function of energy E using Eq. (3.5). The coordinate x along the track can be calculated by integration of reverse stopping power: $x(E) = \int_{E_g}^{E} (-dE/dx)^{-1} dE$. The zero point for the coordinate is taken at the track end. The reverse function $E(x)$ shows how the energy of initial particle changes with coordinate along the track. This approximation is known as continuous-slowing-down approximation (CSDA), whereas the data are tabulated for many substances in ESTAR tables [10]. The energy losses for electron as a function of track coordinate for NaI are shown in Fig. 3.5.

Figure 3.6 schematically shows different relaxation processes and their rates. Inelastic electron scattering processes $e \rightarrow 2e + h$ are shown by arrows 1a and 1b. The rate of these processes for an electron with energy well above the threshold (1b) reach inverse femtoseconds or higher. These values are in good correspondence with the better-known fact that the mean free path between scattering events for electrons with energy of 20–50 eV is less than one nanometer. The scattering of electrons with such energies produce secondary excitations with kinetic energy of several eV. The scattering of electrons with lower energy (closer to threshold, case 1a) has lower rate and results in the production of electrons and holes with low kinetic energy. It is worth to note that the threshold for inelastic electron-electron scattering with production of additional electronic excitations for wide-band-gap insulators is very close to exciton energy E_{ex}. Detailed analytical analysis of this threshold for multiple-parabolic-branch-band (MPBB) approximation is presented in

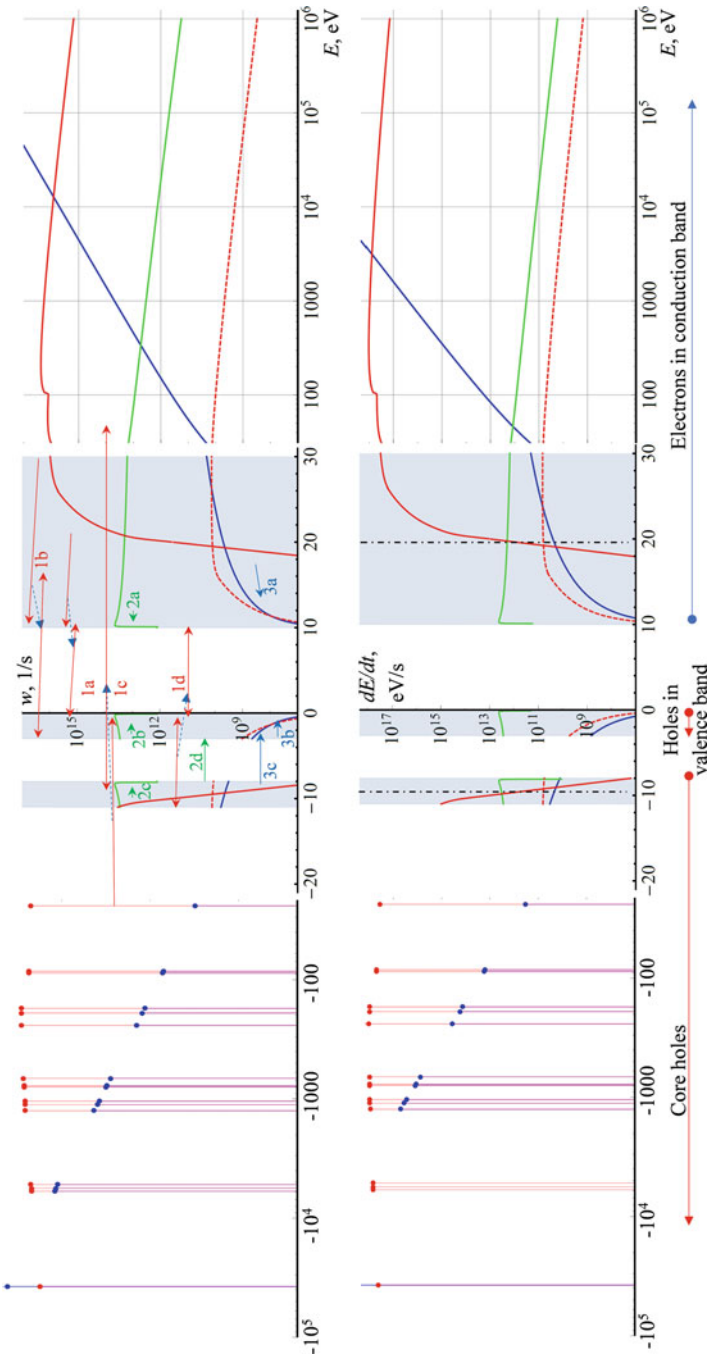

Fig. 3.6 Schematic representation of the rates of different relaxation processes (top panel) and the rate of energy losses (bottom panel) for hot electrons (right column) and hot holes (left column) for BaF_2 crystal ($E_g \approx 10$ eV)

[11]. The threshold kinetic energy for inelastic scattering with production of an exciton is very close to E_{ex}, and the threshold for the processes with production of separated *e-h* pair is close to E_g. The traditional single-parabolic-branch band (SPBB) model (used for several direct-band-gap semiconductors and proposed by Lushchik for ionic crystals [2, 8]) results in much higher threshold energies (e.g., $(1 + m_e/(m_e + m_h))E_g$ for production of *e-h* pairs, where m_e and m_h are electron and hole effective masses, respectively). The reason of this discrepancy is the momentum conservation law. The number of possible combinations of the momenta of secondary particles satisfying the moment conservation law is much higher for MPBB model than that for SPBB.

The inelastic scattering of electrons with production of additional electronic excitations has no abrupt threshold, since even electrons with kinetic energy slightly below the exciton energy ($E_{ex} < E_g$) could produce electronic excitation via the process $e \rightarrow e + ex$ at the Urbach exciton absorption region, where $\mathrm{Im}(\tilde{\varepsilon}(\omega, q)) \propto \exp((\hbar\omega - E_{ex})/\sigma k_B T)$. See the exponential decrease of inelastic electron scattering rate for electron energies below $2E_g$; red curve in the right column of Fig. 3.6. Here, σ is the Urbach constant, and this formula is written for high temperatures.

The cascade of inelastic scattering events has the duration of several femtoseconds and is finished when its rate becomes smaller than the rate of phonon emission, another relaxation process. The cascade results in the formation of electronic excitations with kinetic energy below the threshold of inelastic electron-electron scattering, i.e. approximately below the band gap energy E_g.

The rate of phonon emission is shown in Fig. 3.6 by green curves. The energy dependence of the phonon emission rate will be discussed below, when describing the carrier thermalization.

Two specific regions of the relaxation rate might be pointed out in Fig. 3.6. The region, where the electron kinetic energy is above $E_{ex} = 10$ eV, is named as "active" energy region [12], whereas the region corresponding to kinetic energy below E_g is known as "passive" region. Strong inelastic scattering with production of new electronic excitations can occur only in the "active" region. The bottom panel of Fig. 3.6 shows the energy relaxation rates for different processes. In this case, the difference in $-dE/dt$ between scattering processes $e \rightarrow e + ex$ and $e \rightarrow e + phonon$ is even more pronounced, since the phonon energy released in the latter process (0.01 to 0.1 eV) is by a few orders of magnitude smaller than the energy of the secondary excitation ($>E_{ex}$).

The analogous cascade $h \rightarrow e{+}2\ h$ is caused by Auger decay after creation of a deep core hole. The corresponding process is indicated in Fig. 3.6 by arrows 1c and 1d. The boundaries between "active" and "passive" regions are indicated by dash-dotted lines. For BaF_2, the boundary is within the uppermost 5pBa core band.

At this stage, certain amount of energy is converted into photons. These processes are described by the second term in square brackets in Eq. (3.4). Their rates are shown by blue curves and increase significantly with the increase of the energy of emitted photon. The photon might be a X-ray photon produced in the process of fluorescence due to filling of deep core holes by electrons from higher-lying core and

valence bands. Alternatively, there can be X-ray photons generated due to Bremsstrahlung. The Cherenkov radiation generating photons with energy below E_g (i.e., in light transparency region) can also be produced by primary electrons or δ-electrons with energies above the Cherenkov threshold. Here, we do not consider the case of electrons and positrons with energies high enough for electromagnetic shower to develop (> 1 MeV).

The rate of phonon emission is presented in Fig. 3.6 by green curves (process 2a for electrons, 2b for valence holes, and 2c for holes in upper core levels or in separated valence subbands). This rate depends mainly on the energy of longitudinal optical phonon $\hbar\Omega_{LO}$ and equals 10^{13}–10^{14} s^{-1} for carriers with kinetic energy above this phonon energy. For ionic crystals consisting of light elements (like fluorine, oxygen), $\hbar\Omega_{LO}$ is higher than 100 meV, and this rate is more than 10^{14} s^{-1}, whereas for crystals without light elements in their composition $\hbar\Omega_{LO}$ is in the range from 10 to 20 meV, and the rate is much lower, ~10^{13} s^{-1} (see, e.g. [13–15]). For covalent crystals (like diamond), the interaction with phonons occurs via deformation potential. Therefore, the rate of phonon emission is even lower. The stage with emission of longitudinal optical phonons is followed by a stage of slower relaxation, i. e., the stage of thermalization via scattering by phonons with lower energies (including acoustic phonons). The result of this stage is accumulation of thermalized electrons at the bottom of the conduction band and thermalized holes at the top of the valence band with their average kinetic energies k_BT (Boltzmann distribution is established). If the density of states (DOS) for valence bands have gaps, like those in Fig. 3.6, the transition of a hole between different subbands can occur through a multiphonon process (2d) at substantially lower rate. This rate exponentially decreases with the increase of the gap as $\exp(-p\Delta E/\hbar\Omega_{LO})$, where p is a dimensionless parameter with a value close to 1.

The thermalizing electrons and holes can emit not only phonons, but also photons with energies in the light transparency region (below E_g). The rate of this process is shown schematically in Fig. 3.6 by blue curves and is much lower than the thermalization rate. The resulting emission is called Intra Band Luminescence (IBL) of *e*-type (process 3a) or *h*-type (process 3b) (see, e.g., [16–18] and references therein). The rate of this emission can be significant only when a hole is located at energy on the top of the uppermost core band (process 3c) or on the top of a well-separated subband, when this hole cannot emit any more optical phonon and when the rate of multiphonon process (2d) is approximately equal or lower than the radiation rate. In this case, the photon emission is called cross-luminescence (CL). Some authors use the terms core-valence transitions and Auger-free luminescence instead of CL. This type of emission will be discussed in detail in Sect. 3.6.

In highly excited systems, there is an additional type of scattering of electronic excitations: various Auger processes like $2e + h \rightarrow e$ or $e + ex \rightarrow e$. Such processes result in the decrease of the number of excitations (excitation quenching) and occur in the regions with a high concentration of excitations. Their rates strongly increase with the increase of excitation density (as square or cube of the density) and are schematically shown in Fig. 3.6 by red dashed curves. If the rates of these processes are higher than the radiative recombination rate, the Auger quenching makes the scintillation emission faster.

3.4 Stages of Energy Transformation in Scintillators

3.4.1 Stages of Energy Transformation in Self-Activated Crystals

In the previous section, we discussed the hierarchy of various relaxation rates for electronic excitations in scintillators. Let us consider the scheme of the relaxation of excitations in ionic crystals paying attention on energy distribution and space correlation of the excitations. We start discussing the relaxation in ionic crystal with a simple energy structure.

Propagation of an ionizing particle through a crystal results in the production of a large number of secondary electronic excitations. The relaxation of the excitations in the crystal can be roughly subdivided into the following main stages (see Fig. 3.7):

(a) Emission and absorption of longitudinal photons by hot electrons and holes (inelastic scattering of electrons and Auger decay of deep core holes). The rates of these processes are 10^{15}–10^{16} s^{-1}. The number of electronic excitations increases only at this relaxation stage. The energy of the electronic subsystem is defined by the total ionization losses of the primary particle and does not decrease during this stage (see middle panel of Fig. 3.7). The energy and spatial distribution of hot excitations can be described by the function $g_i^a(E, \mathbf{r})$, which is a convolution of the functions describing the elementary scattering events. This function describes the distribution of excitations along the track of primary particle and δ-electrons and has mainly a 1D character. This function controls further relaxation stages. The index i refers to specific electronic excitation types. From the relaxation point of view, as specific excitations have to be considered those excitations, which do not undergo mutual transformations during the first stage of relaxation. Crystals with relatively simple electronic structure, such as alkali halides, have three types of such excitations: holes in the valence band, electrons in the conduction band (with the energies below the threshold for production of secondary excitations), and excitons.

(b) The second stage is the thermalization of electronic excitations with the emission of phonons. The duration of this stage is $\sim 10^{-12}$ s. The number of electronic excitations does not change. This is the main stage for transferring the kinetic energy of the excitations into heat via phonon emission. To describe this stage, the distribution of hot excitations $g_i^a(E, \mathbf{r})$ has to be convolved with the distribution function $\lambda_i^b(E, \mathbf{r})$, which describes the thermalization of excitation of type i with energy E, to obtain the spatial distribution of thermalized excitations $g_i^b(\mathbf{r}) = \int \left(g_i^a(E, \mathbf{r}) \otimes \lambda_i^b(E, \mathbf{r})\right) dE$, where symbol $\otimes$ denotes a convolution over space coordinates. The fraction of the energy in electron subsystem decreases by a factor of β, and the fraction $1 - 1/\beta$ of the total energy of the primary ionizing particle is passed to the phonon system.

(c) During the next stage, the thermalized excitations might be trapped, self-trapped, captured by the centers of radiative or nonradiative emission. The duration of

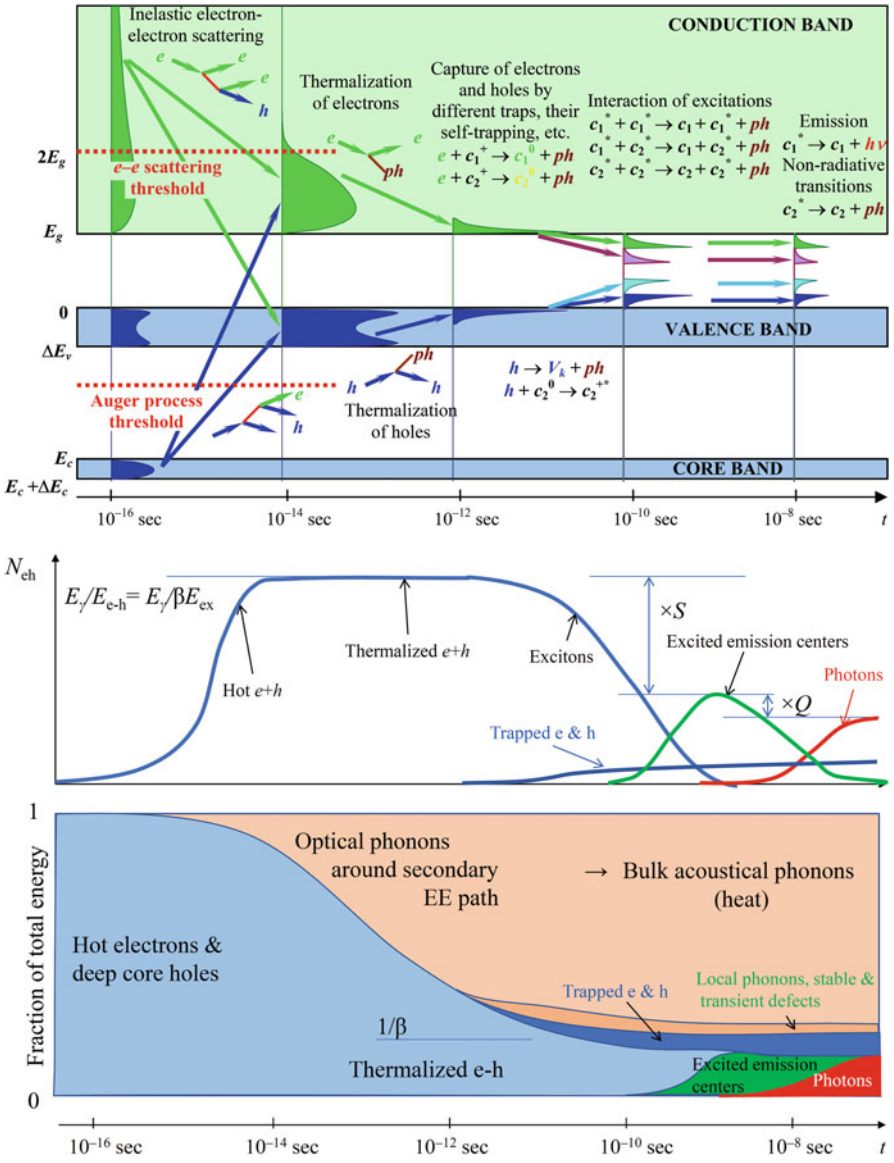

Fig. 3.7 Top panel: scheme of relaxation of electron excitations in insulator with two relaxation channels. Middle panel: time evolution of the mean number of electronic excitations. Bottom panel: fraction of energy in different relaxation channels. According to [19, 20]

this stage depends on the rates of different monomolecular (for self-trapping) and bimolecular (for capture by centers and traps) and can vary substantially. The spatial distribution of excitations $g_i^c(\mathbf{r})$ depends on the parameters of these

reactions and the distribution at previous stage $g_i^b(\mathbf{r})$: $g_i^c(\mathbf{r}) = g_i^b(\mathbf{r}) \bigotimes \lambda_i^c(\mathbf{r})$. The excitation number is conserved, and the total energy in electron subsystem slightly decreases due to the phonon emission. This stage can be considered as interaction of nonequilibrium excitations with traps, defects and impurities in the crystal.

(d) The next stage is the migration of these relaxed excitations. Its time domain overlaps with that of stage (c), however, here we take into account also the interaction with other excitations (in (c) we consider only the interactions with crystal defects). This stage results in a decrease of the excitation number or in redistribution over the excitations of different types. Since the interaction between excitations depends on the inter-excitation distances, this stage is controlled by the spatial distribution function $g_i^c(\mathbf{r})$. Therefore, the interaction intensity depends on the parameters of elementary scattering events, which play the main role in stages (a) – (c). This stage is responsible for the density effects, the non-proportionality of energy response of scintillator, and the non-exponential decay kinetics. At this stage, the energy of excitons can be transferred to emission centers (see green curves in the middle and bottom panels of Fig. 3.7).

(e) The last stage is radiative and non-radiative decay of the excitations. This is the final stage; the main processes are local, and the decay occurs at the emission centers. Therefore, this stage is hardly affected by the processes involved in the stages (a) – (d). The scintillation photons are emitted at this stage (see red curves in Fig. 3.7).

3.4.2 Relaxation in the Matrixes Created by Ce Ions

In crystals with more complicated electronic structure, the excitations of additional types exist. In subsections 3.4.2 and 3.4.3, we discuss two examples. In cross-luminescent crystals, the highest-lying core holes cannot decay via Auger processes due to energy conservation law and should be considered separately (see next subsection). In cerium-containing compounds (like CeF_3 or $CeBr_3$), the energy of cerium 4*f* levels are in the matrix band gap. Cerium Frenkel excitons (4*f*-5*d*) should be regarded as an additional excitation type. Both in cross-luminescent crystals and in cerium compounds, the excitations of this type play the major role in the scintillation processes. In crystals with several types of relaxed excitations, not all of them participate in scintillation process. In many cases, the scintillation is dominated by excitations of only one type (e.g., by the uppermost core hole in cross-luminescent crystal or a Frenkel exciton in a rare-earth-created matrix). These excitations can be considered "useful". The presented scheme allows tracing the evolution of such "useful" excitations during each stage of relaxation.

The "useful" excitations in the crystals with a rare-earth subband in the matrix band gap can be produced through impact excitation only by electrons with kinetic energies in a quite narrow range, since the kinetic energy should be higher than the rare-earth-ion excitation energy but lower than the threshold for production of electron-hole pair with hole in the valence band, since the density of states in the valence band is much higher than that in the rare-earth subband (see [21, 22]). This threshold reduces the number of the "useful" excitations by a factor of ~5.

In certain rare-earth halide crystals, where two types of excitons can coexist (e.g., CeF_3), the anion excitons are not efficient in the energy transfer to rare-earth excitons, so only cation excitons are "useful" for rare-earth emission. The final relaxation of these two types of excitons can be regarded as independent, since the energy of each relaxed exciton is insufficient for the excitation of another type [21, 22]. Figure 3.8 presents a simplified relaxation scheme, which shows that the energy transfer from fluorine subsystem to cerium subsystem can occur only at the hot relaxation stage and, therefore, has a low probability.

The inelastic scattering can be considered as emission of longitudinal photons followed by their absorption with creation of the new excitations. Therefore, the distribution of secondary excitations over types is proportional to the fraction of these types in the energy loss function $\mathrm{Im}(-1/\varepsilon(\omega, \mathbf{k}))$ [8]. Since the energy loss function is a sum over additives describing the creation of different types of

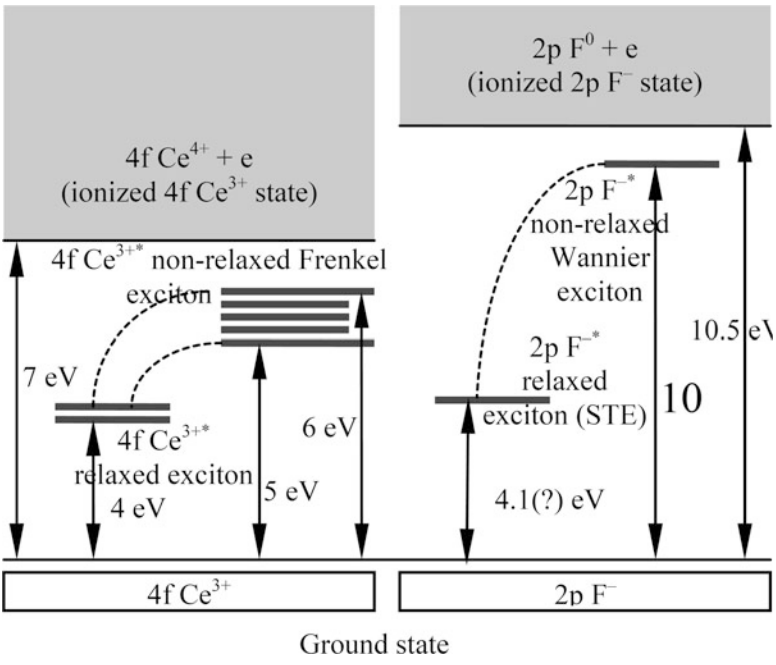

Fig. 3.8 Simplified scheme of coexistence of two types of excitons in cerium fluoride. After [19]

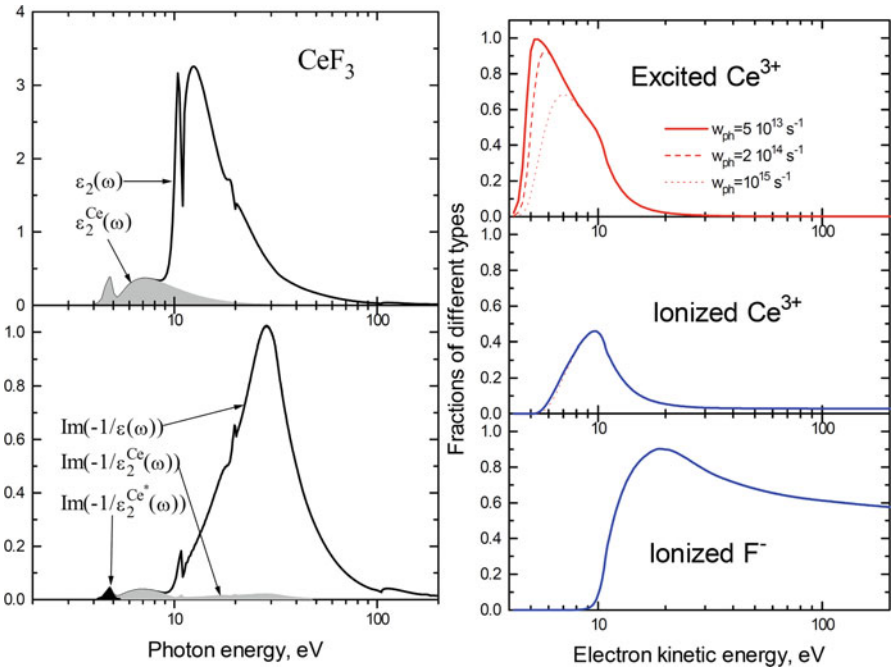

Fig. 3.9 Simulated imaginary part of dielectric permittivity (upper left panel) and energy loss function (lower left panel) for CeF_3 (filled areas represent addition "useful" excitations: excited and ionized cerium states for CeF_3) and the electron kinetic energy dependence of the fraction of ionized and excited ions and ionized ions produced by a single electron, in CeF_3 (right panel). (After Ref. [23])

excitations, one can estimate the number of the "useful" excitations produced in each scattering event.

Figure 3.9 presents the contribution of Ce-transitions to the imaginary part of dielectric function, which is responsible for absorption, and to the energy loss function. Cerium excitons are produced at final stages mainly by secondary excitations in rather narrow energy range between the thresholds of inelastic scattering with production of different excitations. The secondary excitation should have energy above the threshold for the production of rare-earth ion excitation. However, when this energy is higher than the threshold of the production of anion excitation, mainly the rear-earth-related excitons are produced, since the oscillator strength for the production of excitations in anion sub-system is much higher than for the production of the rare-earth-related excitons. Therefore, Ce ions can be excited only by the electrons with a kinetic energy from 5 to 15 eV (see Fig. 3.9). This fact partially explains the relatively low yield of CeF_3. This case is shown also in the general scheme of relaxation (see Fig. 3.10). The main difference between the cases depicted in Figs. 3.7 and 3.10 is that the excited activator ions appear in the first case much earlier, because of the impact of cerium ionization. Note that not all but only a

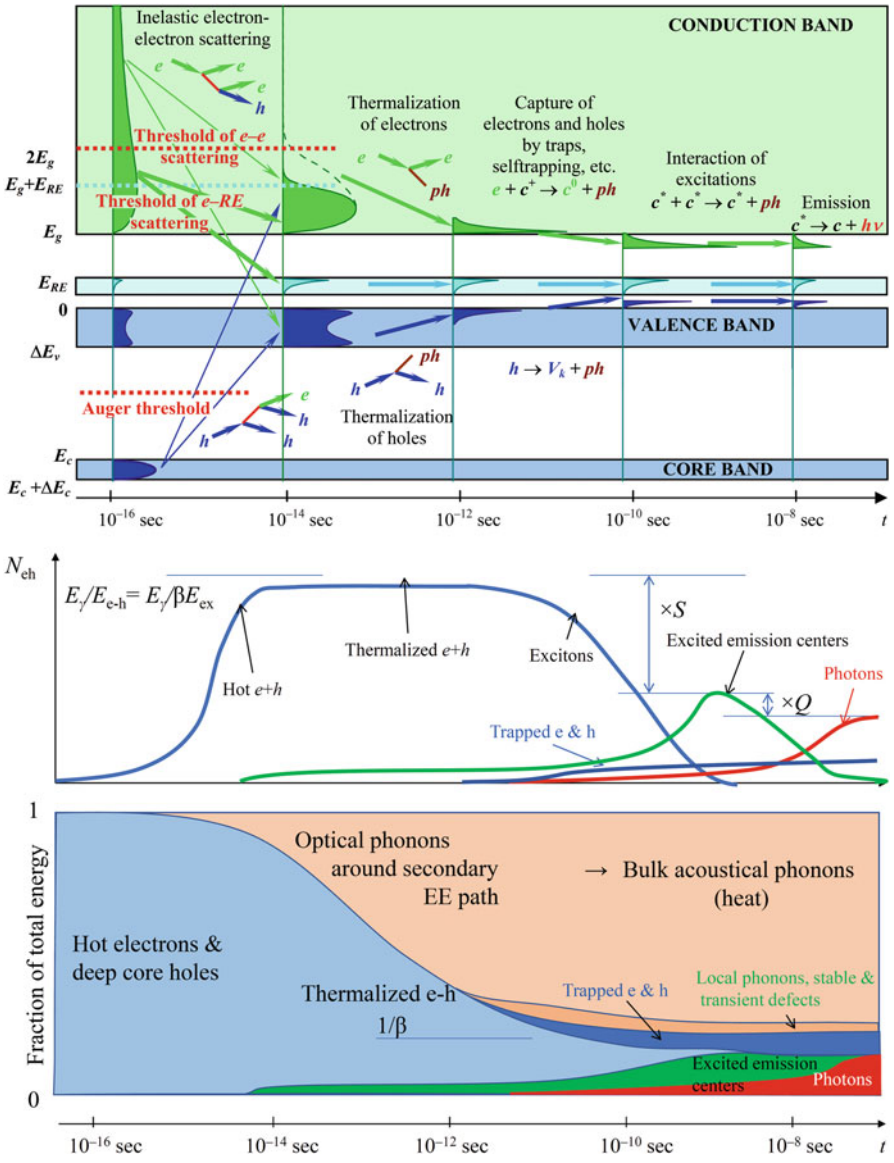

Fig. 3.10 Scheme for relaxation of electronic excitations in crystals with cerium as a matrix component. The description of the panels is the same as presented in the caption of Fig. 3.7

fraction the ions excited by impact excitation appear at this earlier stage. Ionized Ce^{3+} ions also do not participate in the formation of such fast response, since the electron in the resulting Ce^{4+}+*e* pair should return to Ce^{4+} ion. This process proceeds with an additional delay (see below).

3.4.3 *Energy Relaxation in Cross-Luminescent Systems*

Two points are important to emphasize considering the relaxation process in cross-luminescent crystals. Firstly, the mean energy required for the creation of a hole in a high-lying core level, serving as which is a "useful" excitation in this case, is much higher than the value exceeding the band gap by a factor of 2–3 forbidden, which is commonly used in such case. The threshold for the impact of the production of such excitations is about two times higher than that of the production of a conduction-band-electron and valence-band-hole pair. Therefore, a large fraction of the secondary excitations has no energy sufficient to produce core holes (see Fig. 3.11). Secondly, the rate of the radiative relaxation of the core hole is by 5 orders of magnitude lower than the rate for allowed Auger processes. Therefore, in the medium favorable for cross-luminescence, the Auger process should be preferably forbidden. Even small a contribution of the Auger process (involving impurities or adjacent excitations) quenches luminescence. Thus, the cross-luminescence is very sensitive to the track effects [24–27].

In crystals with two types of holes, i.e., valence band hole and outermost core band hole, e.g., 5*p*Ba for BaF_2, only the holes of the latter type are responsible for cross-luminescence. Such holes can be produced only by high-energy excitations, since the threshold for the production of the core holes is higher than that for the valence band holes and anion excitons. Figure 3.12 shows the corresponding permittivity imaginary part and the energy loss function and displays the fractional composition of the secondary excitations.

In these scintillators two or more types of excitations can coexist during a relatively long period (longer than 1 ns). For BaF_2 these excitations are 5pBa holes, valence holes, and anion excitons. Therefore, one has to estimate only the number of "useful" excitations, which is less than the total number of any second excitations. The corresponding mean energy for the production of a "useful" excitation is substantially higher than the typically used value by a factor of 3–4 larger than the the band gap. These values can be calculated only by taking into account the energy distribution of the secondary excitations in inelastic electron-electron scattering (secondary 5*p*Ba holes generated by high-energy electrons with energies above 18 eV). Therefore, the number of new excitations depends not only on the most probable energy losses, which approximately coincides with the energy of the main peak in the energy loss function), but also on the rates of scattering.

Figure 3.11 shows that the outermost core holes appear only at the very initial relaxation stages. Therefore, only the photons emitted in the radiative filling of these holes by electrons from the valence band ensure a fast emission rise time. The fast timing properties of such crystal are discussed below, in Chap. 6.

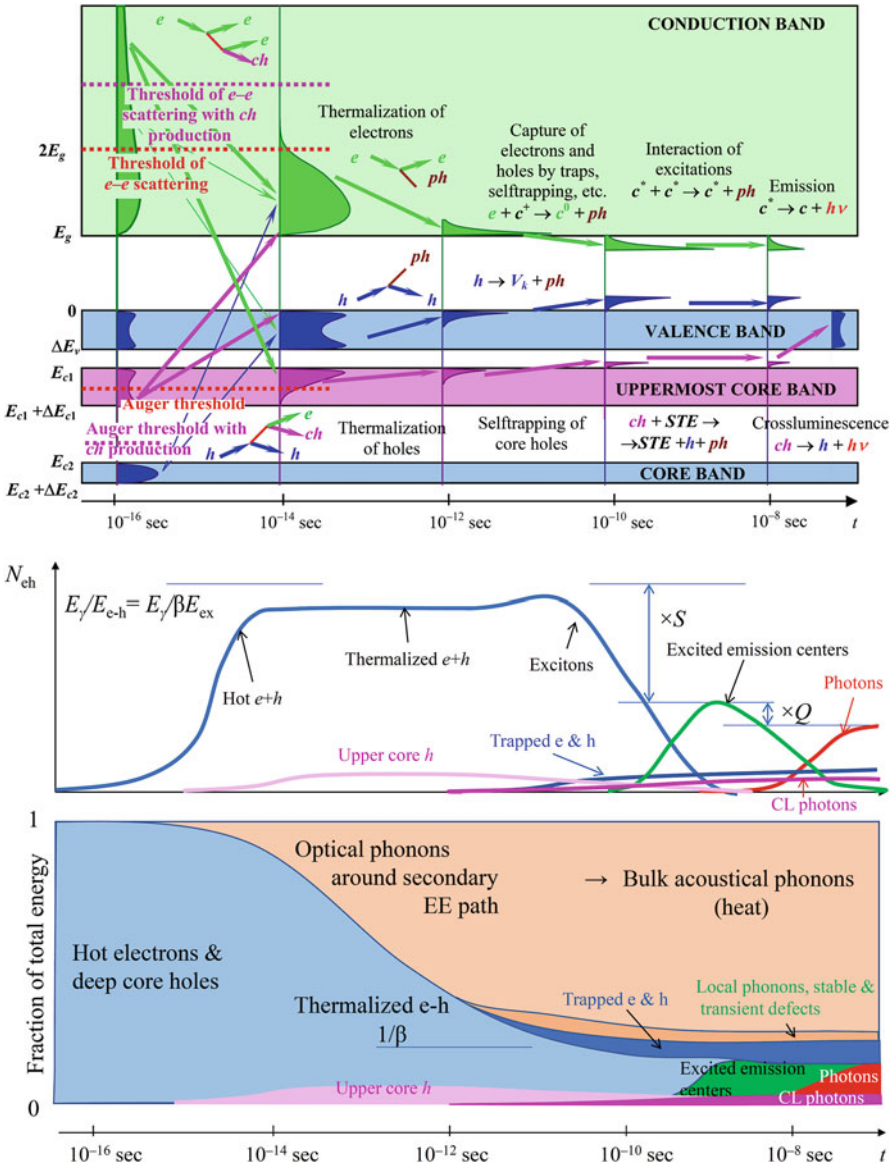

Fig. 3.11 Scheme for relaxation of electronic excitations in cross-luminescent crystals. The description of the panels is the same as presented in the caption of Fig. 3.7

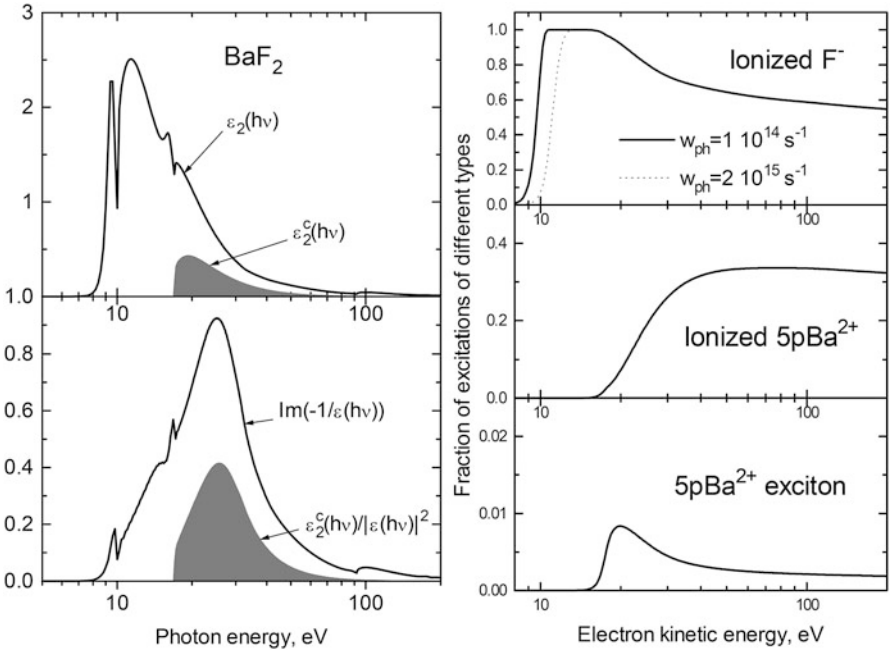

Fig. 3.12 Simulated imaginary part of dielectric permittivity (upper left panel) and energy loss function (lower left panel) for BaF_2 (filled areas represent the addition due to 'useful' excitations (outermost core holes for BaF_2) and the electron kinetic energy dependence of the fraction of ionized and excited ions and the ionized ions produced by the electron, for BaF_2 (right panel). (After Ref. [23])

3.5 An Example of a Cascade of Electronic Excitations

Figure 3.13 illustrates the dynamics of electronic excitation distribution in BaF_2 simulated by Monte-Carlo technique [28]. The initial distribution corresponds to ionization of a crystal by a 1-keV electron (left column) or a 1-keV photon (right column). Let us first discuss the interaction of the initial electron with crystal. The top row corresponds to the processes proceeding within several tens of attoseconds after the interaction with an electron or absorption of a photon. Primary electrons are scattered into states with energies $E - \hbar\omega$ and appear in the energy distribution as a satellite below 1 keV. The profile of this satellite reflects the energy loss function: the main peak at the energy of 975 eV and the peak at 890 eV correspond to the 25 eV and 110 eV peaks in the energy loss function (see Fig. 3.4). The secondary electrons with energies E_1, i.e. those expelled from various valence and core states with energies $\hbar\omega - E_1$ down to -100 eV) are located in a low-energy region (below 50 eV) of the energy loss function.

The second row in Fig. 3.13 corresponds to the energy distribution of elementary excitations few femtoseconds after interaction with a high energy quantum. The

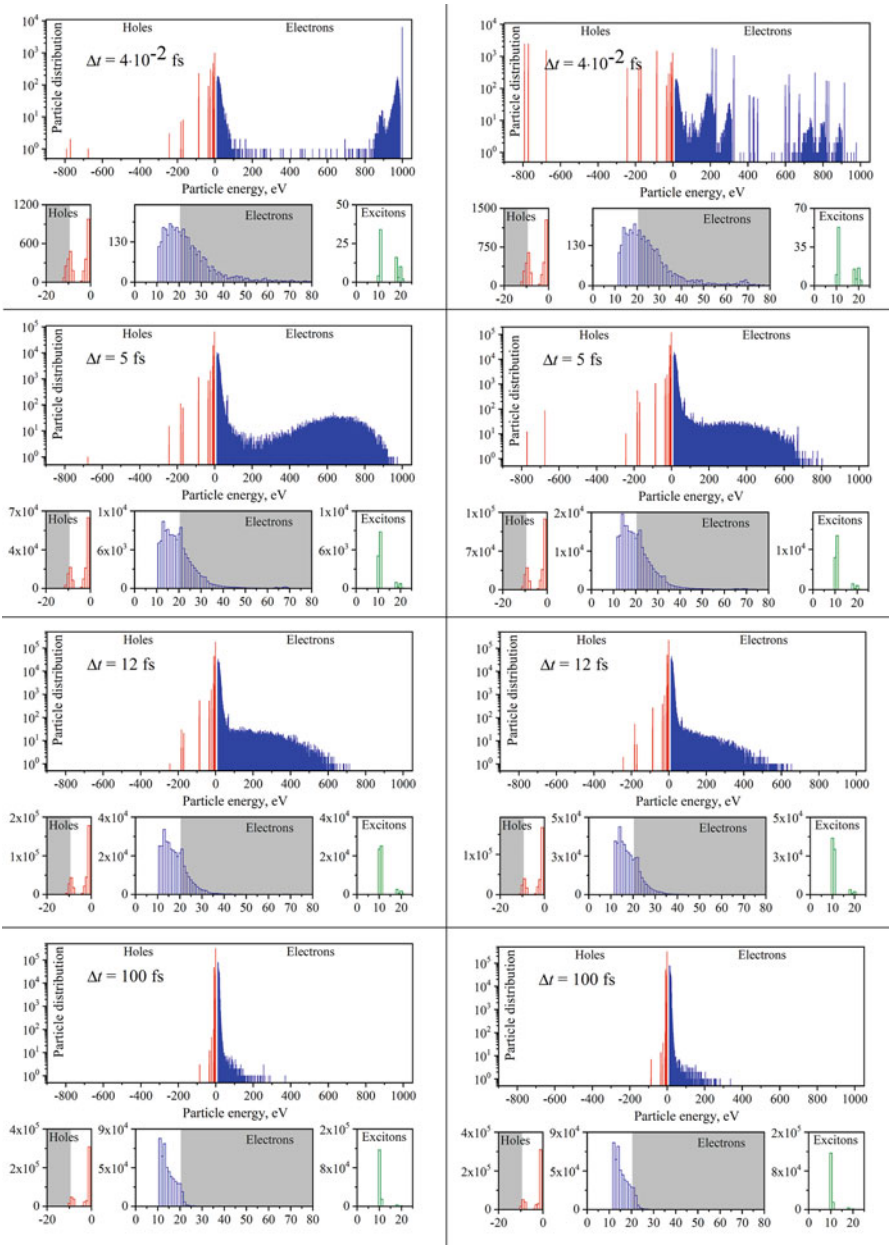

Fig. 3.13 Temporal evolution of energy distribution of electronic excitations in BaF_2 for excitation by 1 keV electron (left column) and 1 keV photon (right column). Gray background corresponds to the "active" region for the electrons and holes, where the electron kinetic energy is above the threshold of inelastic scattering or the hole energy is above the threshold of Auger processes

low-energy part of this distribution determined predominantly by the distribution of secondary electrons has the same shape as that presented in the top row, whereas the high-energy wing determined predominantly by scattered primary electrons becomes rather wide and smooth. This part of the electron energy distribution shifts to the lower energy region with time (third row in Fig. 3.13). At the same time, the energy distribution of secondary electrons in the low-energy region starts to change. The electrons in the "active" region (shown on the gray background) are scattered with the production of additional electronic excitations (compare third and bottom row in Fig. 3.13).

Deep core levels are more important at the initial relaxation stages, when the crystal is excited by a photon (right column of Fig. 3.13). They are populated at the initial state (top row) due to photon absorption (the partial absorption cross-section for deep levels increases with increasing incident photon energy). Sharp electron peaks with satellites at the low-energy side correspond to the primary electrons produced by 1 keV photons together with the primary holes at various deep core levels. Auger electrons with various energies appear at the very beginning of the relaxation process (sharp peaks without satellites at low-energy side) due to Auger decay of core holes. Further stages of the energy distribution relaxation for electrons, holes and excitons do not differ significantly from those in the case of ionization by an electron (compare dependences presented in right and left columns in two bottom rows of Fig. 3.13).

At the end of the cascade stage, all the electrons and holes have their kinetic energies smaller than $E_{th}^{e(h)}$ and, therefore, no new electronic excitations can be produced any more. The electron and hole kinetic energies after the cascade stage can be described by the distribution functions $g_{e(h)}(E_{kin})$ with the argument ranging from zero to the energies slightly higher than $E_{th}^{e(h)}$. The distributions of electrons and holes after cascading down in BaF_2 demonstrate that the fraction of carriers with low kinetic energy is higher than that with kinetic energy close to the threshold. To obtain an analytical form of this distribution one can use the analytical estimation obtained for the case of a narrow valence band and a uniform density of states in the conduction band [29, 30]:

$$g_e(E_{kin}) = \frac{1}{E_g} e^{-2\mathbb{C}} \left[1 + \left(1 - E_{kin}/E_g\right) \int_0^\infty e^{\left(1-E_{kin}/E_g\right)z} \left(1 - e^{2\mathrm{Ei}(-z)}\right) dz \right]. \quad (3.6)$$

Here, $\mathbb{C}$=0.5772 is the Euler constant and Ei($-z$) is the integral exponential function. This distribution is plotted in Fig. 3.14. The main feature of this distribution is that the population of the states with low kinetic energy is approximately by a factor of 5 higher than the population of the electrons with energies just below the threshold of inelastic scattering E_g. This qualitative result does not depend on the details of the scattering process, since the electrons with energy E slightly above the threshold E_g can produce only low-energy secondaries in the range from 0 to $E - E_g$, whereas electrons with the kinetic energy well above E_g produce the secondaries in a much

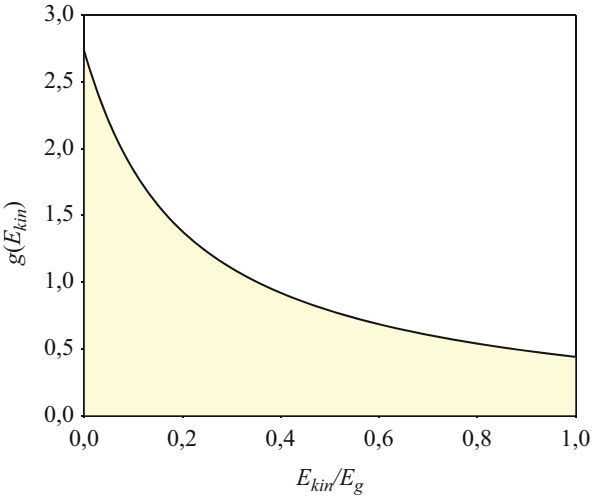

Fig. 3.14 Energy distribution of secondary electrons after their cascading down after high-energy excitation in the case of a narrow valence band and an uniform distribution of the kinetic energy of secondary electrons E_{kin} ranging between 0 and $E - E_g$ after scattering of an electron with energy E

wider energy range. This general feature results in the predominant population of the low-energy part of conduction band. Similar results were obtained using the Monte-Carlo simulation [31–33].

The electron and hole distribution functions have to be normalized: $\int g_e\left(E^e_{kin}\right) dE^e_{kin} = 1$ and $\int g_h\left(E^h_{kin}\right) dE^h_{kin} = 1$. The mean energy required for the creation of one electronic excitation, $E_{eh} = \beta E_g$, is directly connected with this distribution [20]:

$$E_{eh} = E_g + \int E^e_{kin}\, g_e\left(E^e_{kin}\right) dE^e_{kin} + \int E^h_{kin}\, g_h\left(E^h_{kin}\right) dE^h_{kin} \equiv \beta E_g. \tag{3.7}$$

As mentioned above, a typical value of β is in the range from 1.5 to 3. For semiconductors, β is higher (up to 4) since the valence band width is much larger than E_g and the second integral becomes dominant. In a simplified model assuming narrow valence and conduction bands, β=1.397 [30]. The analysis on how the electron structure influences the value of β is presented in [21, 31].

3.6 Free Carrier Thermalization and Track Formation

At the thermalization stage (within the time up to 10 ps), the interaction of the charges mobile in a medium is still might be described by the same formulas as in the previous stage, including the energy loss function as it is defined in Eq. 3.4. However, the phonon emission channel (as described by Eq. 14 in [7]) is the only energy loss channel at this stage. During this stage, all the residual kinetic energy of electrons and holes will be transferred to phonons. At this relaxation stage, a fraction

$1 - 1/\beta$ of the total energy deposit is emitted as phonons. This fraction can be quite large (see bottom panels in Figs. 3.7, 3.10 and 3.11). The typical values of β are 1.5–3 corresponding to 30–70% of the energy released as phonons. Long-wavelength longitudinal optical (LO) phonons is the main type of phonons emitted by hot electrons in ionic crystals. The real part of the dielectric permittivity in the case of one LO phonon branch can be written as

$$\varepsilon^{-1}(\omega) = \varepsilon_\infty^{-1} + \frac{\left(\varepsilon_\infty^{-1} - \varepsilon_0^{-1}\right)\Omega_{LO}^2}{\omega^2 - \Omega_{LO}^2}, \tag{3.8}$$

where ε_0 is the static dielectric permittivity, ε_∞ equals the square of the refraction index in the transparency region (i. e., for photon energies between $\hbar\Omega_{LO}$ and E_{ex}). It is convenient to introduce an effective dielectric permittivity defined as

$$\varepsilon^* = \left(\varepsilon_\infty^{-1} - \varepsilon_0^{-1}\right)^{-1}. \tag{3.9}$$

The energy loss function for LO phonon region becomes

$$\mathrm{Im}\left(-\frac{1}{\tilde{\varepsilon}(\omega, \mathbf{q})}\right) = \frac{\pi\,\Omega_{LO}}{2\varepsilon^*}\delta(\omega - \Omega_{LO}). \tag{3.10}$$

For calculating of the energy loss rate, we also introduce the acoustic phonon scattering by amending the energy loss function with the term

$$\mathrm{Im}\left(-\frac{1}{\tilde{\varepsilon}(\omega, \mathbf{q})}\right) = \frac{\pi\,\varepsilon_0\sigma_d^2 q^3}{2c_{LA}e^2\rho}\delta(\omega - c_{LA}q) \tag{3.11}$$

where σ_d is the deformation potential constant, c_{LA} is the longitudinal sound velocity, and ρ is the crystal density.

It is possible to estimate the distance of thermalization of a carrier with effective mass m_e from the initial kinetic energy E_{kin} down to the optical phonon energy $\hbar\Omega_{LO}$ [13]:

$$\left\langle r^2\right\rangle_{E_{kin}\to\hbar\Omega_{LO}} \approx \frac{8}{9}a_B^2\left(\frac{\varepsilon^* m_0}{m_e}\right)^2 \tanh\left(\frac{\hbar\Omega_{LO}}{2k_BT}\right)\left(\frac{E_{kin}}{k_BT}\right)^3 / \ln\left(\frac{4E_{kin}}{k_BT}\right). \tag{3.12}$$

The evolution of $\langle r^2\rangle$ with decreasing electron kinetic energy for two initial values of the initial kinetic energy (1 and 5 eV) is shown in Fig. 3.15 for four cases: (i) one LO phonon branch with rather high $\hbar\Omega_{LO} = 0.1$ eV (the case of most crystals with light elements, e.g. oxygen of fluorine); (ii) one LO phonon branch with small $\hbar\Omega_{LO}$ =0.01 eV (the case of CsI – a crystal with only heavy ions); (iii) the cases with two LO phonon modes, for which thermalization becomes faster. The

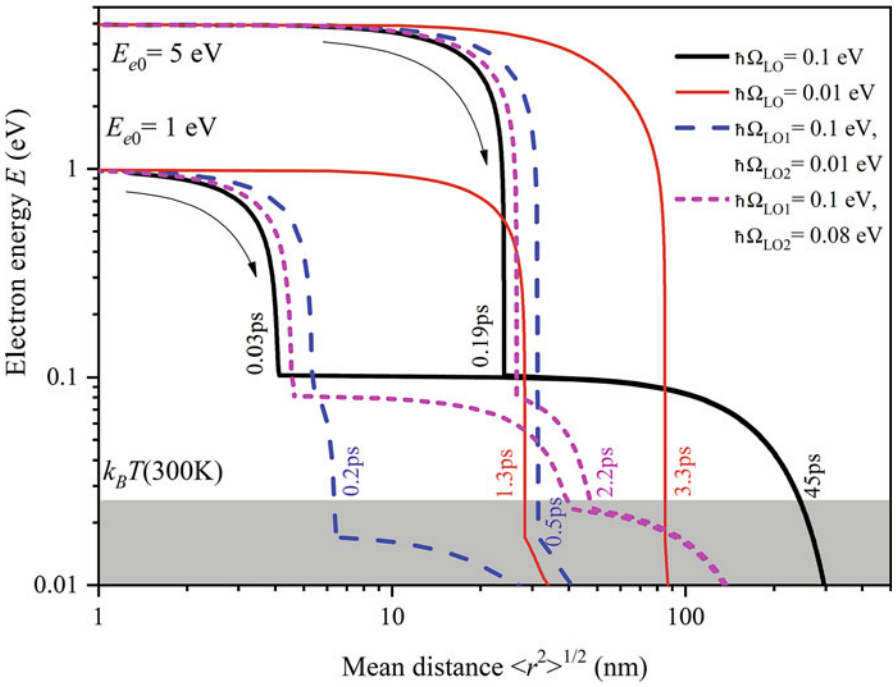

Fig. 3.15 Relationship between the mean distance from the birthplace (horizontal axis) with the electron energy (vertical axis) during thermalization for the cases of single and double LO phonon branches. Arrows show the direction of time. The simulation parameters (effective masses, electron phonon strengths, etc.) are described in [13]. The thermalization times are indicated by the corresponding curves. Gray region corresponds to thermalized carriers at 300 K. (After Ref. [13])

thermalization from $\hbar\Omega_{LO}$ to energies k_BT is due to interaction with acoustical phonons and the rate of energy relaxation also can be estimated according to Eq. 3.15 from [13].

Figure 3.15 demonstrates the connection of the thermalization in energy and space. If the initial energy E_{e0} of a secondary electron is 1 eV, and optical phonon has a high energy (e.g., ~0.1 eV in LiF), the energy of electron very rapidly (in 30 fs) falls down to energy close to the phonon energy, but the further thermalization occurs with emission of acoustical phonons and takes a long time, approximately 45 ps. During this stage, electron moves far away from its birthplace. On the contrary, if the phonon energy is low (for instance, 10 meV in CsI), the emission of phonons is much slower, and much higher number of phonons should be emitted. In this case, the thermalization lasts 1 to 3 ps, depending on initial energy, and the mean thermalization distance is 20 to 100 nm. In this case, the Boltzmann distribution of electrons is achieved at 300 K without the stage of emission and absorption of acoustical phonon. The systems with several branches of optical phonons also show rather fast thermalization [13].

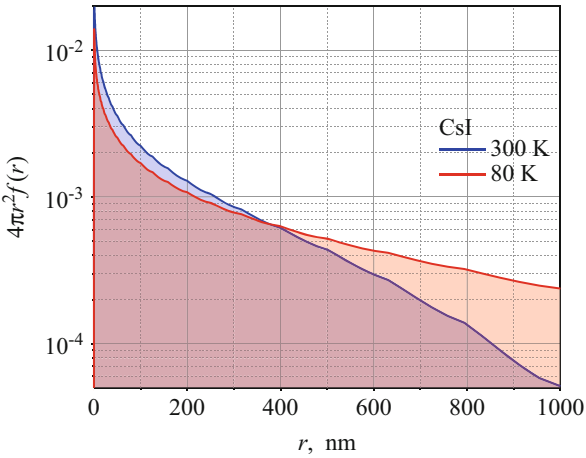

Fig. 3.16 Spatial distribution of thermalized secondary electrons over thermalization length for CsI at 300 K and 80 K in case of the distribution of initial kinetic energy described by Eq. (3.6)

Therefore, the electrons with kinetic energy E_{kin} are distributed after thermalization in space around holes according to the following expression:

$$G\left(r, E^e_{kin}, E^h_{kin}\right) = \frac{3\sqrt{6}\,r^2}{\sqrt{\pi}\left(\left\langle r_e^2\right\rangle_{E^e_{kin}} + \left\langle r_h^2\right\rangle_{E^h_{kin}}\right)^{3/2}} \exp\left(-\frac{3r^2}{2\left(\left\langle r_e^2\right\rangle_{E^e_{kin}} + \left\langle r_h^2\right\rangle_{E^h_{kin}}\right)}\right). \tag{3.13}$$

Taking into account that the kinetic energies of secondary electrons after the cascade stage are distributed from 0 to E_{ex} according to Eq. (3.6) (see Fig. 3.14), $G\left(r, E^e_{kin}, E^h_{kin}\right)$ from Eq. (3.13) has to be averaged taking into account the distribution of electrons and holes over their kinetic energies $g_{e(h)}(E_{kin})$. Assuming that holes are generally less mobile than electrons, and the width of the valence band is typically smaller than E_{ex}, we can conclude that the separation of electrons and holes in geminate pairs is predominantly determined by electrons. A similar distribution was obtained using Monte-Carlo technique [32]. Figure 3.16 shows the typical distribution of thermalized electrons in CsI for two temperatures.

3.7 Reactions Between Thermalized Electronic Excitations

In the previous sections, we mentioned two types of events which result in the production of fast photons in processes with a constant number of electrons and holes (Cherenkov radiation and IBL + CL). All other types of emission involve recombination of electrons and holes. The recombination occurs mainly after carrier thermalization (here, we do not consider recombination of hot carriers). The next

step of energy relaxation after thermalization is the migration of electrons and holes and interaction of them with production of excitons, capture by traps, centers of recombination, etc. (see, e.g [7, 34–37].). One of the most important types of excitations are excitons, which are created mainly in the reaction $e + h \rightarrow ex$. Note that some excitons are created directly in the cascade process: $e \rightarrow e + ex$. The fraction of directly created excitons is typically no more than 5%. The reaction $e + h \rightarrow ex$, i.e., the capture of an electron by a hole, is a bi-molecular reaction, meaning that the corresponding term in rate equations is proportional to the concentrations of two components:

$$\begin{aligned}\frac{dn_e(t)}{dt} &= \cdots - \beta_{eh}(t)n_e(t)n_h(t) - \cdots,\\ \frac{dn_h(t)}{dt} &= \cdots - \beta_{eh}(t)n_e(t)n_h(t) - \cdots,\\ \frac{dn_{ex}(t)}{dt} &= \cdots + \beta_{eh}(t)n_e(t)n_h(t) - \cdots,\end{aligned} \tag{3.14}$$

where $\beta_{eh}(t) \approx 4\pi(D_e + D_h)R_{Ons}$ for the simplest case, D_e and D_h are the diffusion coefficients for electrons and holes, respectively, and $R_{Ons} = \frac{e^2}{4\pi\varepsilon_0\varepsilon k_B T}$ is Onsager radius (the distance at which the potential energy of e and h attraction equals $-k_B T$). The Onsager radius serves as the radius of capture sphere for recombination of oppositely charged particles. In self-activated crystals, excitons can be self-trapped $ex \rightarrow$ STE and act as emission centers. $CdWO_4$ and $Bi_4Ge_3O_{12}$ (BGO) are such self-activated crystals, where STE is located on oxyanion complex.

In most activated crystals like Ce^{3+}- and Tl^{+}-activated ones, the energy transfer to the activator is more complicated and depends on the energy location of activator levels within the band gap. For instance, if $4f$ Ce^{3+} level is located far from the valence band, a hole cannot be captured by the activator due to the large energy difference between the activator level and the top of the valence band, which cannot be covered by multi-phonon process. The capture of an electron by free $5d$ Ce^{3+} level can also not be realized, since Ce^{2+} ion is unstable in most compounds. Therefore, the most probable way to excite Ce^{3+} ion is the energy transfer from exciton in the reaction $ex + Ce^{3+}$ or STE + Ce^{3+}. The products of these reactions are discussed below.

On the contrary, thallium ion in alkali halide crystals can participate in all three reactions: $e + Tl^{+} \rightarrow Tl^{0}$, $h + Tl^{+} \rightarrow Tl^{2+}$, and $ex + Tl^{+} \rightarrow Tl^{+*}$. The excited state of thallium is formed directly in third reaction, whereas other two reactions require an additional capture act like $h + Tl^{0} \rightarrow Tl^{+*}$ or $e + Tl^{2+} \rightarrow Tl^{+*}$.

The rates of all these reactions depend on carrier concentration, and, therefore, we have to discuss, how the track region can be described in terms of the concentration of thermalized electronic excitations.

The role of the concentration in bi-molecular reactions can be illustrated schematically, provided that the number of excitations in the volume of a sphere with Onsager radius is estimated. The Onsager radius for most crystals at 300 K is 5 to

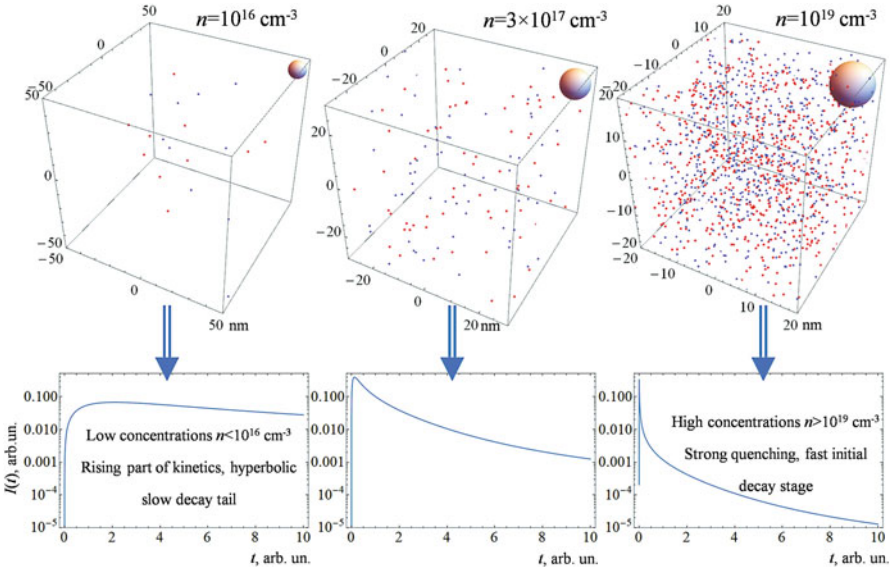

Fig. 3.17 Distribution of electrons concentration in a track in CsI at 300 K with thermalization taken into account (top row) and typical decay curves for bi-molecular reactions (bottom row)

10 nm. The electron concentration is about $n_c = \left(\frac{4}{3}\pi R_{Ons}^3\right)^{-1}$, i.e., 10^{17}–10^{18} cm^{-3} (we introduce the notation of critical density n_c). An electron is with high probability within Onsager sphere surrounding a hole and together with the latter can be regarded as excited state of exciton (thermal phonons cannot destroy this exciton). The relaxation of the exciton to the lowest state and possible self-trapping last less than few picoseconds (even for CsI with low-energy optical phonons) [38]. Therefore, for such concentrations, excitons are created in sub-picosecond domain. Afterwards, the excitons can emit photons (in case of self-activated crystals) with characteristic exciton decay time. This case is shown schematically in the middle column of Fig. 3.17.

If the concentration n of the electrons surrounding a hole is much smaller than the critical density n_c, electrons have to spend some time to reach the capture sphere. This time can be estimated as the time required for carrier diffusion by a distance $n^{-1/3}$, i.e., $6n^{-2/3}/(D_e + D_h)$ (we use the estimation of the shift of a particle in diffusion process $(\Delta r)^2 = \frac{1}{6} D\,\Delta t$). This is a rough estimation of the rise time for creation of excitons at low concentrations. More detailed calculation of the rise profile is presented below. This rise time increases with decreasing electron concentration as $n^{-2/3}$. This profile is schematically shown in the left column in Fig. 3.17.

If the electron concentration n is higher than the critical density n_c, two effects should be taken into account. First of all, we cannot consider the recombination as recombination of individual electron and hole, since a few other electrons (and, probably, holes) are within the Onsager radius. This case looks like non-ideal plasma, when the potential energy of interaction with surrounding carriers is higher than $k_B T$. In this case, we have to use the screened Onsager radius [30] for the

screened Coulomb potential (like Debay screening in plasma). The second effect is that the excitons, which are formed in this region of high electron concentration, should interact strongly with surrounding charge carriers. These interactions are Auger-type processes involving free carriers: $ex + ex \rightarrow e + h \rightarrow ex$, $ex + e \rightarrow e$, $ex + h \rightarrow h$, $2e + h \rightarrow e$, and $e+2h \rightarrow h$. Exciton recombines and passes its energy to the third particle due to dipole-dipole or exchange energy transfer. These processes result in quenching of excitations and emerging of fast decay components like that shown in the right column of Fig. 3.17. A detailed description of the profile for this type of interaction is presented below.

Therefore, the concentration of excitations in the track region is one of the main factors determining the time profile of the scintillation in many crystals. In the following section, we will estimate the distribution of the concentrations.

3.8 Distribution of Concentrations of Electrons and Holes

The simplest way to study various reactions between electronic excitations is solving the rate equations for concentration of excitations (electrons, holes, excitons, various states of traps and activators, etc.). A part of a set of rate equations is presented as Eq. 3.14. Such rate equations are often used for the description of scintillation decay kinetics. These equations are nonlinear, and, therefore, the character of their solution strongly depends on initial conditions for concentrations. As mentioned above, the cascade and thermalization stages are described by monomolecular reactions, whereas the stage of recombination and interaction requires taking account of at least bi-molecular reactions, and the approach of using rate equations is natural for this stage. The distribution of excitations just after the end of thermalization (see, e.g [7]) can be used as the initial conditions.

The distribution of thermalization lengths can be combined with the linear distribution of birthplaces of secondary excitations along the track shown in Fig. 3.5. The linear density of secondary excitations along a straitened track can be estimated as $(-dE/dx)/(\beta E_g)$. If we convolve this 1D distribution with 3D distribution of electrons and holes after the thermalization of geminate pairs (Fig. 3.16 and Eq. 3.13), we can calculate the 3D distribution of concentration of excitations in the track region. This distribution of concentrations is shown in Fig. 3.18 for CsI at 300 K for different energies of ionizing particles. The plot shows the significant shift of the mean concentration of excitations when the energy of ionizing particle increases from 10 keV to 1 MeV. Such distribution can be used for the analysis of the last stage of scintillation processes (see Sect. 3.9).

The stopping power expression (Eq. (3.5)) does not take the fluctuations of the emission of secondary excitations (Landau fluctuations) into account and is calculated in CSDA approximation. Thermalization is also described in terms of a probability distribution function. The real number of electronic excitations in the track is low enough for correct application of statistical approach. So, the distributions shown in Fig. 3.18 are a result of averaging over many tracks.

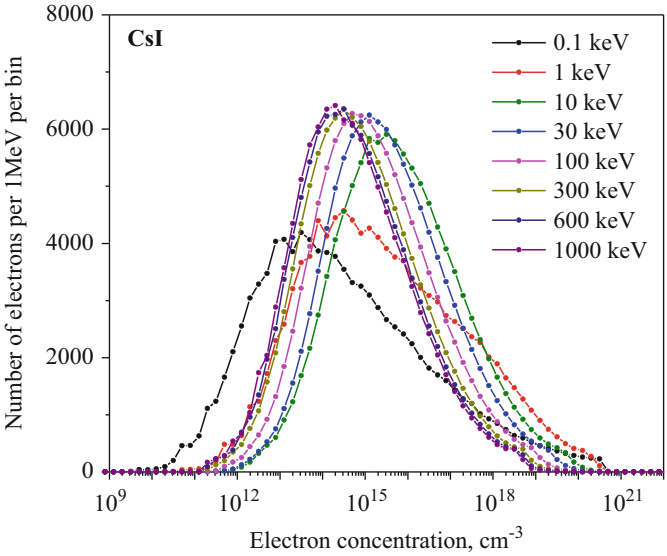

Fig. 3.18 Distribution of electron concentration in a track in CsI at 300 K with thermalization taken into account. The histogram is plotted with bins equally separated in log$n$

Electronic excitations in track region are distributed in a very inhomogeneous way. Figure 1.2 presents the typical distribution of electrons and holes in NaI crystal after absorption of a 200 keV X-ray photon. Simulation demonstrates the formation of clusters of excitations due to the relaxation of deep core holes and high-energy electrons. NaI has significant thermalization lengths for electrons (up to 100 nm for 5 eV electron kinetic energy before the thermalization), whereas holes are shifted during thermalization on much smaller distances (compare insets b and c in Fig. 3.19).

Straightforward use of the term "concentration" for such tracks is not completely correct. Nevertheless, the recombination properties described in the previous section depends on the distances to the nearest electrons and holes. Let us define the "concentration" of excitations through the distance between the closest pairs. If the concentration of, say, electrons is n_e, then the mean distance between an electron and its neighboring electrons is $\langle r_{ee} \rangle = n_e^{-1/3}$. Figure 3.20 shows the histogram of the "concentrations" calculated as the inverse cube of the mean distance to three closest neighbors. These distributions (especially for *e-h* and *h-h* pairs) are shifted to higher concentrations in comparison with Fig. 3.18. The difference is that Monte-Carlo calculations reproduce clusterization of excitations due to their correlation, whereas for the results presented in Fig. 3.18 calculated using CSDA approximation supposing that the energy losses are distributed along the track in a continuous way. So, taking the Landau fluctuations in tracks into account shifted the distributions to higher values.

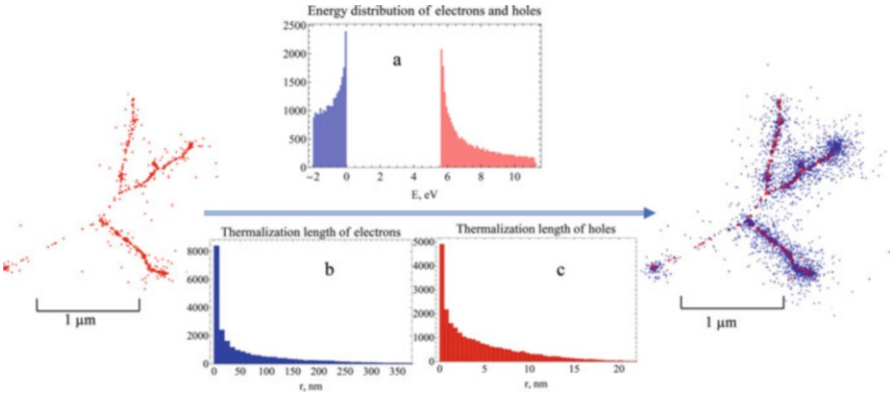

Fig. 3.19 Evolution of a part of a track created due to absorption of 200 keV γ-quantum in NaI(Tl) scintillator. The entire track is presented in Fig. 1.2. Part of the track before thermalization (just after the cascade) is shown in the left part of the figure, whereas the right part shows the distribution of electrons (blue) and holes (red) after thermalization. The insets show the energy distribution of electrons and holes before thermalization (top panel, **a**) and distribution of thermalization lengths for electrons (**b**) and holes (**c**) in NaI crystal

This example demonstrates that an electron "feels" surrounding electrons as if the initial concentrations were distributed between 10^{14} and 10^{20} cm^{-3}. On the other hand, electrons "feel" traps or activators with uniform concentrations of these centers. This range of concentrations covers all three regions of low, intermediate and high concentrations considered in Fig. 3.17. Therefore, branching between different reactions involving electrons and the profiles of emission from different parts of a track depend on local concentrations, and the results should be weighted over the distribution of concentrations of excitations similar to that presented in Fig. 3.20.

3.9 Reactions at the Kinetic Stage of Scintillation Pulse Development

3.9.1 General Considerations on the Kinetic Stage of Scintillation Signal Development

Let us discuss the general properties of the stage which defines the kinetics of a scintillation pulse. This is the stage starting from the end of thermalization and lasting until scintillation photons are emitted. During this time, a lot of different reactions with electronic excitations (EEs) occur: migration of EEs, transformation

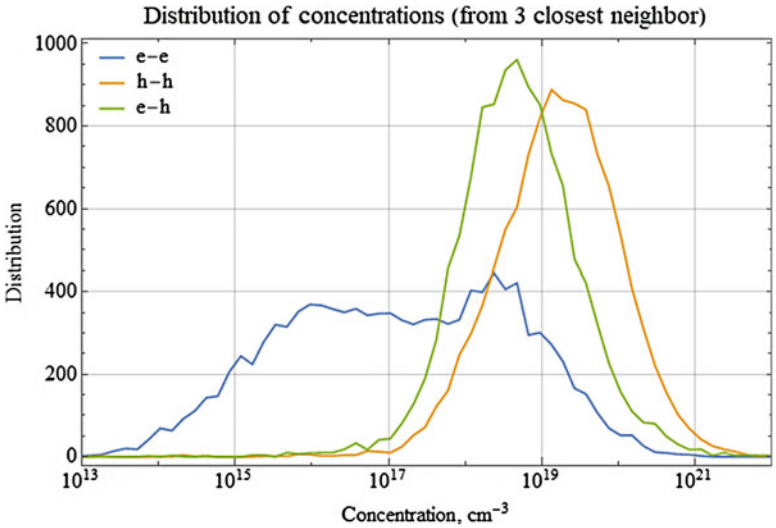

Fig. 3.20 Histogram of electron concentration (blue), hole concentration (yellow) and concentration of electrons around holes (green) obtained by Monte-Carlo simulation for 200 keV electron track in NaI after thermalization presented in Figs. 1.2 and 3.19. The histogram is calculated using equidistant binning on log(n) scale

of EE types, interaction of EEs with quenching of them or creation of new EEs, radiative and non-radiative decay, reabsorption of emitted photons, etc.

The following reactions describe the transformation of different types of EEs (here, e indicates electrons, h – holes, ex – excitons, c – defects of various types in various states, STE and STH – self-trapped excitons and holes, V – vacancies, F – F-centers, etc.):

$$\begin{aligned} &ex \leftrightarrow e + h, \quad ex \leftrightarrow \mathrm{STE}, ex + c \rightarrow c^*, \mathrm{STE} + c \rightarrow c^*, \\ &c^* \rightarrow c + h\nu, \mathrm{STE} \leftrightarrow \mathrm{STH} + e, e + \mathrm{V} \leftrightarrow \mathrm{F}, e + c \leftrightarrow c^-, \\ &e + c^+ \rightarrow c^*, h + c \leftrightarrow c^+, h + c^- \rightarrow c^*, \text{etc.} \end{aligned} \tag{3.15}$$

All the reactions are bidirectional (e.g., $ex \leftrightarrow e + h$). The direct and reverse reactions can have quite different rate coefficients with different temperature dependences. For instance, the rate of binding of $e + h$ into an exciton has a power law dependence on temperature, whereas the reverse reaction demands activation energy and, therefore, has an exponential dependence on the inverse temperature (Arrhenius law). When the rate of the reverse reaction is extremely small, this reaction can be regarded as one-directional (these reactions are indicated by a one-directional arrow). The major reaction for many types of crystals with activator emission (i.e., the final de-excitation of excited activator, $c^* \rightarrow c + h\nu$ with production of a photon) is regarded to be one-directional. Even for these one-directional reactions, we have probably to take the reverse reactions into account as well. This is important when

the radiation reabsorption for bulk scintillations or concentration quenching for high activator concentrations have to be taken into account.

As mentioned above, the excitations are distributed in the track region strongly inhomogeneously. Nevertheless, we start with the case of a homogeneous distribution of initial excitations, and then average the results over the distribution of concentrations which is described in the previous section. This approximation of uniform distribution works better for photoexcitation, but the averaging is required even in this case. The rate equations at the kinetic stage can be described by the following set of equations for concentrations (see, e.g., [34, 39–42]):

$$\frac{dn_i(t)}{dt} = \sum_{j\neq i} \alpha_{j\to i}\, n_j(t) - \sum_{j\neq i} \alpha_{i\to j}\, n_i(t) + \sum_{j\neq i,\, k\neq i} \int K_{jk\to i}(r)\, f_{jk}(r,t)\, d^3r - \sum_{j\neq i,\, k\neq i} \int K_{ik\to j}(r)\, f_{ik}(r,t)\, d^3r. \tag{3.16}$$

Here $n_i(t)$ are time-dependent concentrations of i-th type of EEs, $f_{ij}(r,t)$ are binary two-particle distribution functions, which depend not only on time but also on the distance r between two EEs of i-th and j-th types and can be written in terms of correlation functions $g_{ij}(r,t)$ defined as $f_{ij}(r,t) = n_i(t)\, n_j(t)\, g_{ij}(r,t)$ (with natural condition $g_{ij}(\infty,t) = 1$, which describes ceasing of correlations at large distances); $\alpha_{i\to j}$ are the rates of the reactions with only one initial component (e.g., $ex \to e + h$, $ex \to$ STE, and STE $\to ex$), $K_{jk\to i}(r)$ are rates of the reactions with two initial components separated by the distance r. Rates $\alpha_{i\to j}$ can also be expressed in terms of partial lifetimes: $\alpha_{i\to j} \equiv 1/\tau_{i\to j}$. This notation is often used for reactions with production of luminescence photons, and in this case, the lifetimes are radiative. The intra-center thermal quenching can also be included in these rates.

The reactions between two or more species can be described in two different ways depending on the ratio between the mean free path of moving reagents and the interaction radius. If the mean free path of excitations is much longer than the interaction radius, the reactions can be considered like in gas kinetics, i.e., by using reaction cross-section. The reagents are not correlated in space ($g_{ij}(r,t) = 1$). In this case, the bi-molecular rate of reaction between species i and j depends only on the concentration of the species:

$$\int d^3\mathbf{r}\, K_{ij\to k}(r) f_{ij}(r,t) = \beta_{ij\to k} n_i(t) n_j(t), \qquad \beta_{ij\to k} = \int d^3\mathbf{r}\, K_{ij\to k}(r). \tag{3.17}$$

In this case, the reaction cross-section σ_{ij} can be introduced using the thermal velocity of mobile species: $\beta_{ij} = \sigma_{ij} v_T$, $v_T = \sqrt{3k_BT\left(m_i^{-1} + m_j^{-1}\right)}$ (both are

supposed to be movable and have effective masses m_i and m_j). This case is often considered in semiconductors.

In ionic systems, the mean free path of carriers are often small due to strong interaction with optical phonons and can be less than nanometer. In this case, a strong correlation between reagents can occur. For instance, due to the correlation, the two-particle distribution function $f_{ij}(r,t)$ for distances smaller than the interaction radius is smaller than $n_i(t)\,n_j(t)$ (this means that $g_{ij}(r,t) < 1$). On the other hand, electrons and holes in such systems can have initial correlation with typical radius equal to thermalization length, and initial correlation function can be larger than one: $g_{ij}(r,0) > 1$. The typical evolution of correlation function in time and space is demonstrated in Fig. 3.21. In the initial part of reaction, only particles at small distances enter into reaction. This dependence of correlation function on time is the main reason of non-trivial decay and rise profile of scintillation signal.

If three-particle correlations are neglected, the equations for correlation functions can be written as

$$\frac{\partial g_{ij}(r,t)}{\partial t} - \frac{1}{r^2}\frac{\partial}{\partial r}\left[\left(D_i + D_j\right)r^2\frac{\partial g_{ij}(r,t)}{\partial r} - \left(\mu_i + \mu_j\right)\frac{dU_{ij}(r)}{dr}g_{ij}(r,t)\right] = -K_{ij\to k}(r)g_{ij}(r,t). \tag{3.18}$$

Here, D_i and μ_i are the diffusion coefficient and the mobility of i-th type of EE (the Einstein-Smoluchowski relation $\mu_i = D_i/k_BT$ cab be taken into account, T is the temperature, k_B is the Boltzmann constant), $U_{ij}(r)$ is the potential energy of the interaction of two EEs of i-th and j-th types (e.g., Coulomb attraction between an electron and a hole, etc.). Typical values of the diffusion coefficients and mobilities are quite different in different crystals.

Equation (3.18) can be solved for each pair of interacting EEs, and the evolution of correlation functions $g_{ij}(r,t)$ can be obtained explicitly for any type of interaction. These solutions can be inserted into Eq. (3.16), which can be rewritten as

$$\frac{dn_i(t)}{dt} = \sum_{j\neq i}\alpha_{j\to i}\,n_j(t) - \sum_{j\neq i}\alpha_{i\to j}\,n_i(t) + \sum_{j\neq i,\,k\neq i}\beta_{jk\to i}(t)n_j(t)n_k(t) - \sum_{j\neq i,\,k\neq i}\beta_{ik\to j}(t)n_i(t)n_k(t). \tag{3.19}$$

The initial conditions for this set of ordinary differential equations are the concentrations of all types of EEs $n_i(0)$.

These equations are written for the uniform distribution of EEs. One of the consequences of non-uniformity is the violation of local neutrality. The electron thermalization length is often higher than that of holes, thus, electrons form a kind of halo surrounding the positive part of the track. In this case, macroscopic electric fields have to be taken into account. The equation for electric field $\mathbf{E}(\mathbf{r},t)$ can be written as

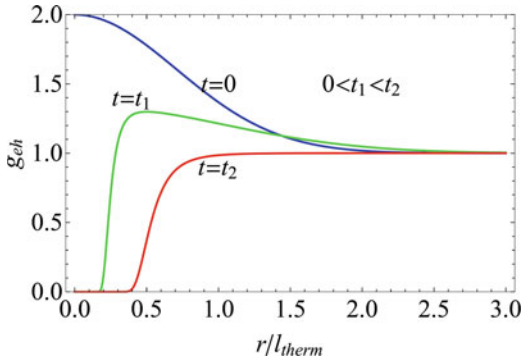

Fig. 3.21 Schematic representation of correlation function evolution of initially correlated electrons and holes

$$\varepsilon \frac{\partial \mathbf{E}(\mathbf{r},t)}{\partial \mathbf{r}} = e\sum_i z_i n_i(\mathbf{r},t), \tag{3.20}$$

where z_i are the charges of excitations of i-th type. Electric fields exist in excited region even in the case of uniform distribution (see the term $dU/\partial r$ in Eq. (3.18)), but the macroscopic electric fields vanish after averaging over certain small volume containing many excitations.

The equations for concentrations (in this case, the concentrations depend on the coordinate $\mathbf{r}$) with diffusion taken into account have the form:

$$\begin{aligned}&\frac{\partial n_i(\mathbf{r},t)}{\partial t} - \frac{\partial}{\partial \mathbf{r}}\left[D_i \frac{\partial n_i(\mathbf{r},t)}{\partial \mathbf{r}} - z_i \mu_i e \mathbf{E}(\mathbf{r},t) n_i(\mathbf{r},t)\right] = \\ &\sum_{j\neq i} \alpha_{j\to i}\, n_j(t) - \sum_{j\neq i} \alpha_{i\to j}\, n_i(t) + \\ &\sum_{j\neq i,\, k\neq i} \beta_{jk\to i}(t) n_j(t) n_k(t) - \sum_{j\neq i,\, k\neq i} \beta_{ik\to j}(t) n_i(t) n_k(t).\end{aligned} \tag{3.21}$$

Contrary to quasi-homogeneous case, the solution of this system is very sensitive to the initial distributions, correlations, etc. (see, e.g., [27]). Here, we have to note that Eq. (3.21) have additional non-linear terms proportional to the electric field, whereas $\mathbf{E}(\mathbf{r},t)$, in turn, is proportional to EE concentration. In the following considerations, such macroscopic electric fields will be neglected. The track evolution taking account of the arising mesoscopic separation of charges is discussed in the model of cylindrical track in [43–45].

The rates of bimolecular reactions in Eqs. (3.19), (3.21) depend on time according to the solution of Eq. (3.18):

$$\beta_{ij\to k}(t) = 4\pi \int r^2\, dr\, K_{ij\to k}(r) g_{ij}(r,t). \tag{3.22}$$

This equation underlines the role of binary correlation function in the estimation of rate coefficients. Let us discuss several important cases demonstrating how interaction and correlation functions of various types influence the process kinetics.

3.9.2 Recombination and Capture of Nonequilibrium Carriers

The capture process in the reactions $e + h \rightarrow ex$, $e + c^+ \rightarrow c^*$ and similar reactions between positive and negative species is not a simple process and often can be considered as cascade process of the diffusion in the attractive Coulomb potential $U(r) = -\frac{e^2}{4\pi\,\varepsilon_0\,\varepsilon\,r}$. We will consider electrons and holes as the interacting species, but the results can be easily generalized to other interacting pairs. In the presence of other charged particles near the pair under consideration, this potential is screened as $U(r) = -\frac{e^2}{4\pi\,\varepsilon_0\,\varepsilon\,r}\exp\left(-\frac{r}{\lambda_D}\right)$ where the Debye screening constant λ_D is defined as

$$\frac{1}{\lambda_D} \equiv \sqrt{\frac{e^2(n_e + n_h)}{\varepsilon_0\,\varepsilon\,k_B T}} = \sqrt{4\pi R_{Ons}(n_e + n_h)}. \tag{3.23}$$

This potential has singularity at $r = 0$ and cannot be applicable at the distances of the order of interatomic distances. In this case, pseudopotential can be used instead of the Coulomb potential. An example of such potential is shown in Fig. 3.22. Slight oscillations correspond to atomistic structure of the crystal. Such potential could have many bound states (infinite number in the case without screening), and the capture of an electron by a hole with production of exciton in the lowest bound state

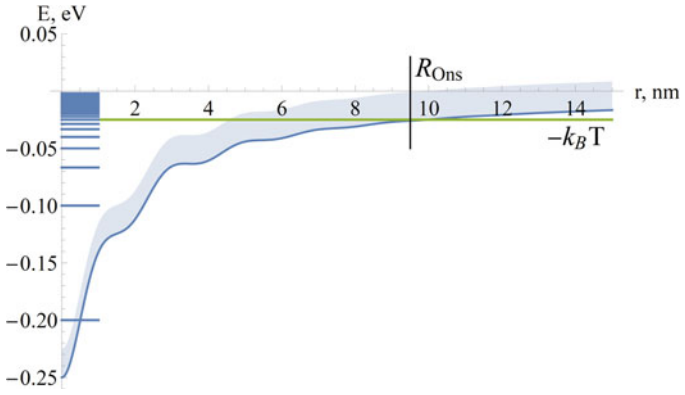

Fig. 3.22 Schematic plot of Coulomb attraction pseudopotential for interaction between electrons and holes. Shadow region shows the states with kinetic energies below k_BT. Horizontal lines at the left of the plot indicate the energy levels in this potential

can be considered as a cascade over these bound levels. Electron can be considered as captured if phonons could not provide sufficient energy for its transfer to a state with positive energy. Roughly speaking, if the bound state has energy below $-k_BT$, the electron-hole pair can be considered as a bound pair (excited state of the exciton). In this picture, the capture can be considered as two-stage process: the capture of electron to one of the excited states below $-k_BT$, and the relaxation of the electron to the lowest level. The duration of the relaxation depends on the probability of transfer from one level to another. If the energy distance between the levels is smaller than the maximal phonon energy $\hbar\Omega_{LO}$, the transfer is rather fast (with typical times of tens of femtoseconds). On the contrary, if the separation is larger than $\hbar\Omega_{LO}$, multi-phonon processes are required for relaxation to the lowest level, and the delay can be as long as few picoseconds. This is also a typical time for self-trapping of exciton when the lattice displacement of surrounding ions could additionally reduce the energy of the bound state. The self-trapping time was directly measured in [38].

The capture can also be considered in a quasi-classical way, when electron wavefunction is presented as a wave packet localized in space. In this case, we can use pseudopotential for describing the interaction between electron and hole and consider the capture as the diffusion of the electron in attractive potential. This is the case when Eq. (3.18) can be applied for description of the initial stage of the capture (electron diffusion into the region where the potential energy of interaction is below $-k_BT$). The second stage is related with relaxation at short distances, for which $K_{eh}(r) \neq 0$. Under assumption that the recombination occurs at very short distances, $K_{eh}(r) = 0$ in the major part of the volume where the carriers move. The equation for the first (diffusion) stage can be considered as Eq. (3.18) with $K_{eh}(r) = 0$ and boundary conditions $g_{eh}(r \to 0) = 0$, $g_{eh}(r \to \infty) = 0$ (no correlation at large distances and fast recombination at short distances). This equation has analytical solution in stationary case. It is known that a particle which is initially at a distance r from the center, can either drift to the center and recombine with probability $p(r) = 1 - \exp\left(\frac{U(r)}{k_BT}\right)$ or go to the infinity with probability $1 - p(r)$. If electron and hole are created in one event (either photon absorption or inelastic scattering), they are correlated in space after thermalization, and their recombination is called geminate. For pure Coulomb attraction, the probability of geminate recombination is $p(r) = 1 - \exp\left(-\frac{R_{Ons}}{r}\right)$. The rest of electrons go away from the hole and can recombine with other holes created in the track of ionizing particle.

The typical time for the diffusion from initial point to the origin is approximately $r^2/(D_e + D_h)$. Taking into account the mean thermalization length and typical diffusion coefficients for electrons, estimations show that this time is in the range from picoseconds to a few nanoseconds, depending on the diffusion coefficients and thermalization distances. The recombination kinetics in this time domain is defined mainly by diffusion at the distances approximately equal to the Onsager radius or longer. Unfortunately, time-dependent Eq. (3.18) has no simple analytical solution even for pure Coulomb case. Therefore, the model of black sphere of recombination

is often used instead of the Coulomb attraction model. Namely, the interaction potential is neglected at distances above capture radius $r > R_c$ and the recombination is supposed to be instantaneous for $r < R_c$. This instantaneous recombination means that $g_{eh}(r < R_c) = 0$, whereas for region $r > R_c$ the correlation function is controlled by the equation

$$\frac{\partial g_{eh}(r,t)}{\partial t} = (D_e + D_h)\frac{1}{r^2}\frac{\partial}{\partial r}r^2\frac{\partial g_{eh}(r,t)}{\partial r} \tag{3.24}$$

with the boundary conditions $g_{eh}(R_c, t) = 0$, $g_{eh}(\infty, t) = 0$ and the initial condition $g_{eh}(r, 0) = \frac{1}{4\pi r_0^2}\delta(r - r_0)$ (the particle initially at $t = 0$ is on the sphere with radius r_0). Below, we use a shorter notation $D \equiv D_e + D_h$.

This equation has the well-known solution in the form of Green function

$$g_{eh}(r,t;r_0) = \frac{1}{4\pi r r_0\sqrt{4\pi D t}}\left(\exp\left(-\frac{(r-r_0)^2}{4Dt}\right) - \exp\left(-\frac{(r+r_0-2R_c)^2}{4Dt}\right)\right). \tag{3.25}$$

Consequently, the flux through the "black" sphere surface equals

$$S(t;r_0) = 4\pi D R_c^2\left.\frac{\partial g_{eh}(r,t;r_0)}{\partial r}\right|_{r=R_c} = \frac{R_c D(r_0 - R_c)}{2\sqrt{\pi}\, r_0 (Dt)^{3/2}}\exp\left(-\frac{(r_0-R_c)^2}{4Dt}\right). \tag{3.26}$$

After integration of this flux over time, we get that the total recombination probability for $r > R_c$ is equal to $p(r) = 1 - \frac{R_c}{r}$. It is evident that in this model $p(r < R_c) = 1$ (particles recombine instantly). Comparison of this result with the result obtained for the Coulomb case leads to conclusion that $R_c = R_{Ons}$ is a good choice for this model (taking into account that $1 - \exp\left(-\frac{R_{Ons}}{r}\right) \approx 1 - \frac{R_{Ons}}{r}$ for $r > R_{Ons}$).

Let us suppose that the electron kinetic energy before thermalization is E_e, whereas the energy of hole is E_h. After thermalization the electrons and holes are spatially distributed as described by Eq. (3.13). The recombination kinetics should be, therefore, integrated using this 3D Gaussian distribution function: $G_0(r) \equiv G\left(r, E_{kin}^e, E_{kin}^h\right) = \frac{3\sqrt{6}\, r^2}{\sqrt{\pi}\, l^3}\exp\left(-\frac{3r^2}{2l^2}\right)$ normalized as $\int_0^\infty G_0(r)dr = 1$. Here, we use mutual thermalization length $l \equiv \sqrt{\left\langle r_e^2\right\rangle_{E_{kin}^e} + \left\langle r_h^2\right\rangle_{E_{kin}^h}}$. To simplify the expressions, we neglect the dependence of l on the kinetic energies of electron and hole before thermalization. The results should depend only on the dimensionless parameter l/R_c.

After the integration of this Green function with the primarily distribution of electrons $g_{eh}(r, 0) = G_0(r)$, we get the equation for the rate of exciton production in recombination of geminate pairs:

$$\left(\frac{dn_{ex}(t)}{dt}\right)_{gem} = \delta(t)\int_0^{R_c} G_0(r)dr + \int_{R_c}^{\infty} G_0(r)S(t;r)dr =$$
$$\left[\mathrm{Erf}\left(\sqrt{\frac{3}{2}}\frac{R_c}{l}\right) - \sqrt{\frac{6}{\pi}}\frac{R_c}{l}\exp\left(-\frac{3R_c^2}{2l^2}\right)\right]\delta(t) +$$
$$3\sqrt{6}\frac{R_c^2 l\sqrt{D}}{\pi\sqrt{t}\left(l^2+6Dt\right)^2}\exp\left(-\frac{3R_c^2}{2l^2}\right) +$$
$$3\sqrt{6}\frac{R_c D\left(l^2+6Dt-3R_c^2\right)}{\sqrt{\pi}\left(l^2+6Dt\right)^{5/2}}\exp\left(-\frac{3R_c^2}{2\left(l^2+6Dt\right)}\right)\left[1-\mathrm{Erf}\left(\frac{3R_c}{l}\sqrt{\frac{Dt}{l^2+6Dt}}\right)\right]. \tag{3.27}$$

Let us estimate the fraction of electron-hole pairs recombining in geminate way. Figure 3.23 shows the fraction of instantly captured electrons $\int_0^{R_c} G_0(r)dr = \mathrm{Erf}\left(\sqrt{\frac{3}{2}}\frac{R_c}{l}\right) - \sqrt{\frac{6}{\pi}}\frac{R_c}{l}\exp\left(-\frac{3R_c^2}{2l^2}\right)$ (blue curve), the fraction of electrons captured after diffusion $\int_{R_c}^{\infty} G_0(r)\frac{R_c}{r}dr = \sqrt{\frac{6}{\pi}}\frac{R_c}{l}\exp\left(-\frac{3R_c^2}{2l^2}\right)$ (violet curve), and the fraction of escaped electrons (all other electrons) $1-\mathrm{Erf}\left(\sqrt{\frac{3}{2}}\frac{R_c}{l}\right)$ (dark yellow curve). Here, $\mathrm{Erf}(x) = \frac{2}{\sqrt{\pi}}\int_0^x e^{-z^2}dz$ is the error function. To compare Onsager and "black sphere" models, the fraction of escaped electrons in Onsager model $\int_0^{\infty} G_0(r)\exp\left(-R_{Ons}/r\right)dr$ is plotted in Fig. 3.23 as well (green curve). All escaped electrons will recombine with holes generated in other events.

The fraction of excitons created in this process from initial moment to the moment t can be calculated as

$$\left(n_{ex}(t)\right)_{gem} = \int_0^{R_c} G_0(r)dr + \int_{R_c}^{\infty} G_0(r)\int_0^t S(t_1;r)dt_1 dr \tag{3.28}$$

or, using the expression for the integral $\int_0^t S(t_1;r)dt_1 = \frac{R_c}{r}\left(1-\mathrm{Erf}\left(\frac{r-R_c}{2\sqrt{Dt}}\right)\right)$, we can get the final form

$$(n_{ex}(t))_{gem} = \mathrm{Erf}\left(\sqrt{\frac{3}{2}}\frac{R_c}{l}\right) - \sqrt{6}\frac{R_c}{\sqrt{\pi\left(l^2+6Dt\right)}}\exp\left(-\frac{3R_c^2}{2\left(l^2+6Dt\right)}\right)\left[1-\mathrm{Erf}\left(\frac{3R_c}{l}\sqrt{\frac{Dt}{l^2+6Dt}}\right)\right]. \tag{3.29}$$

Figure 3.24 shows $n_{ex}(t)$ as a function of dimensionless time Dt/R_c^2. The rise part is a combination of an instant step with the amplitude shown by blue curve in Fig. 3.23 and the rise with square root singularity at small times. We can see that typical time for capture process is R_c^2/D and strongly depends on diffusion coefficient. For CsI, the electron diffusion coefficient was estimated to be 0.2 cm^2/s [46]. For Onsager capture radius equal to 10 nm, the characteristic time is 5 ps. The diffusion coefficient is quite different in various crystals, so this estimation is not universal, and the characteristic diffusion time in different crystals varies from subpicoseconds to nanoseconds.

If excitations are not correlated at initial moment ($g_{eh}(r,0) = 1$), the recombination is bi-molecular. In this case, the black-capture-sphere model gives the bimolecular reaction rate [39, 40]:

$$(\beta_{eh\to ex}(t))_{stoch} = 4\pi D R_c\left(1+\frac{R_c}{\sqrt{\pi Dt}}\right) + \frac{4}{3}\pi R_c^3\delta(t). \tag{3.30}$$

This formula has two types of singularities: instantaneous recombination for particles within the 'black' sphere (described by the term with delta-function in Eq. (3.30)) and square root singularity due to diffusion of excitations towards the recombination sphere.

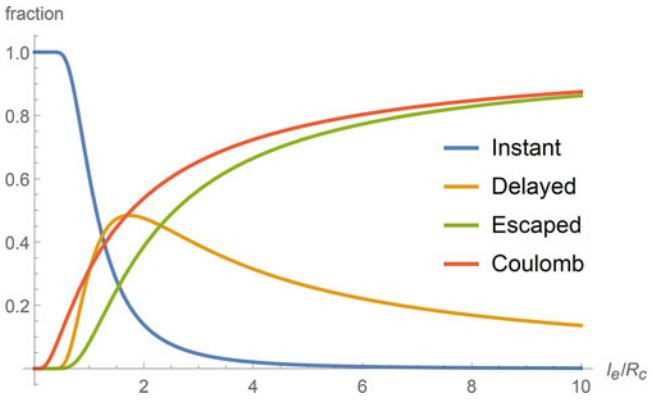

Fig. 3.23 Fractions of recombination of geminate electron-hole pair as a function of the ratio of thermalization and capture radii l/R_c

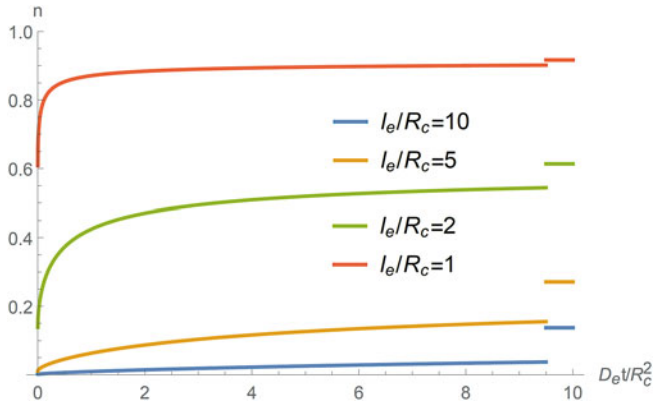

Fig. 3.24 Time dependence of the fraction of excitons created in geminate recombination for different ratios of thermalization and capture radii l/R_c (indicated). Lines at the right part of the plot show the fractions at infinite time

In the general case of N electron-hole pairs simultaneously created in volume V, the initial electron-hole correlation function is a superposition of the correlation function for one pair and the input from non-correlated electrons and holes [34]:

$$G(r) = \frac{V}{N} G_0(r) + 1 - \frac{1}{N}. \tag{3.31}$$

Equation (3.31) shows that the Gaussian term of the geminate part of correlation function depends inversely on the excitation density (the higher the excitation density $n_e = n_h = N/V$, the smaller this term in the correlation function). The same effect of excitation density is observed in the bimolecular rate $\beta_{eh}(t)$: the rate contains a term, which inversely depends on the excitation density. Therefore, the equation for excitons created via recombination of both types is

$$\frac{dn_{ex}(t)}{dt} = \left(\frac{dn_{ex}}{dt}\right)_{gem} n_e(0) + (\beta_{eh}(t))_{stoch} n_e(t) n_h(t) \tag{3.32}$$

and has both linear and quadratic terms. For the case of strong initial correlation, certain fraction of the two-excitations reaction turns out to be monomolecular. Geminate electron-hole pairs recombine in monomolecular way, and the escaped electrons recombine with non-geminate holes in stochastic bi-molecular way.

This type of capture can be applied not only for electrons and holes, but also for returning of electrons to impurity after its ionization. An example of this process is ionization of activator Ce^{3+} with its transformation into Ce^{4+} and electron in the conduction band. This process is discussed in detail in Chap. 5. The ionization of cerium ions by VUV photons in wide-band-gap crystal $LiYF_4$:Ce^{3+} can also be pointed out [47]. In this crystal, the diffusion coefficient for electrons in *3d* Y^{3+} subband in the conduction band was estimated to be 0.5×10^{-3} cm^2/s, and the rising

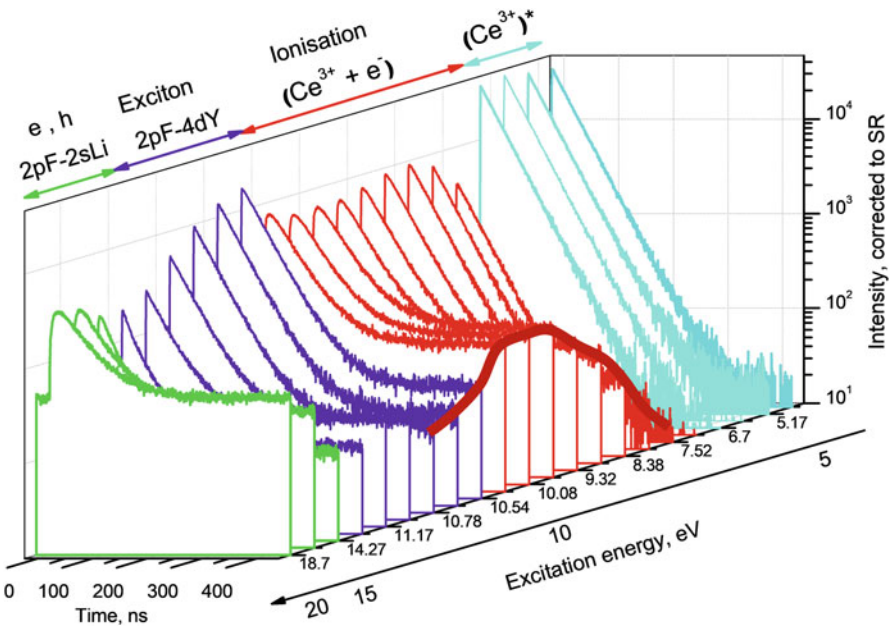

Fig. 3.25 Fluorescence decay curves of $LiYF_4:Ce^{3+}$ for different excitation energies from 5.17 to 11.17 eV. Red line is a guide to the eye to point out the emergence of a slow component at excitation energies above 8 eV. The curves with substantial rising sections are also indicated in red. Three regions of interest (direct excitation−ionization to the Y4d and to Li2s as well as exciton formation) are mentioned. After [47]

part is in nanosecond domain. The increase of photon energy in the range between the ionization threshold for Ce^{3+} and the band gap results in an increase of thermalization length of ionized electron and emerging of a slow component as a result of stochastic recombination of escaped electrons with other ionized Ce^{3+} centers (Fig. 3.25).

3.9.3 *Dipole-Dipole Energy Transfer Between Excitations*

The energy transfer from one neutral excitation to another is usually considered by assuming that any correlations are absent at the initial state: $g_{da}(r, 0) = 0$. Here, we introduce, as commonly used in the theory of dipole-dipole energy transfer, the term "donor" (d) for the initial excitation and "acceptor" (a) for the center, which is initially not excited but might accept energy from donor. The reaction in this case will be $d^* + a \rightarrow d + a^*$. This type of notations is natural if the energy is transferred between ions of different kinds, like a pair of Gd^{3+} and Ce^{3+}. In this case, both donor and acceptor are immobile, thus, no diffusion should be taken into account. In the case when exciton serves as donor, the reaction should be $ex + a \rightarrow a^*$. The exciton

can move through the crystal, so its diffusion should be taken into account in this case (except of self-trapped excitons at low temperatures). An interesting case can also be pointed out: both donor and acceptor are mobile, e.g., excitons. This is the reaction between two excitons, when the energy of one exciton is passed to another one. As a result, the latter exciton is transferred to the state of uncorrelated electron-hole pair with the total kinetic energy equal to $2E_{ex} - E_g$. This case will be studied later separately.

We start with the simplest and well-known case of the dipole-dipole energy transfer without particle diffusion when $D_d + D_a = 0$ (see, e.g. [34]). The energy transfer rate strongly depends on the distance between donor and acceptor: $K_{da}(r) = \tau_d^{-1}(R_{da}/r)^6$, τ_d is the donor radiation time, and R_{da} is a characteristic distance for energy transfer (the distance between donor and acceptor for which the rates of donor emission and energy transfer are equal). R_{da}^6 is proportional to the overlap integral of donor emission spectrum and acceptor absorption spectrum:

$$R_{da}^6 = \frac{3c^4\hbar^4}{4\pi} \int \frac{d(\hbar\omega)}{(\hbar\omega)^4 n^4(\hbar\omega)} I_d(\hbar\omega)\sigma_a(\hbar\omega), \tag{3.33}$$

where $I_d(\hbar\omega)$ is normalized donor emission spectrum ($\int I_d(\hbar\omega)\, d(\hbar\omega) = 1$), $\sigma_a(\hbar\omega)$ is photon absorption cross-section for acceptor (absorption coefficient divided by acceptor concentration), $n(\hbar\omega)$ in this formula is the refraction index. Typical values of R_{da} are below 2–4 nm.

The rate of bimolecular reaction has a square root singularity

$$\beta_{da}(t) = 4\pi \int_0^\infty K_{da}(r)\exp(-K_{da}(r)\ t)\ r^2 dr = \frac{2\pi^{3/2}}{3} \frac{R_{da}^3}{\sqrt{t\tau_d}}. \tag{3.34}$$

The rate equations for donors $n_d(t)$ and excited acceptors $n_{a*}(t)$ are

$$\begin{aligned} \frac{dn_d(t)}{dt} &= -\tau_d^{-1} n_d(t) - \frac{2\pi^{3/2}}{3\sqrt{\tau_d t}} R_{da}^3 n_d(t)(n_a(0) - n_{a*}(t)), \\ \frac{dn_{a*}(t)}{dt} &= -\tau_a^{-1} n_{a*}(t) + \frac{2\pi^{3/2}}{3\sqrt{\tau_d t}} R_{da}^3 n_d(t)(n_a(0) - n_{a*}(t)). \end{aligned} \tag{3.35}$$

If the concentration of non-excited acceptors (e.g., activator ions) at zero time $n_a(0)$ is higher than the concentration of donors (e.g., excitons), this singularity results in Förster energy transfer formula (see, e.g [48]):

$$n_d(t) = n_d(0) \exp\left(-\frac{t}{\tau_d} - \frac{4\pi^{3/2}}{3} n_a(0) R_{da}^3 \sqrt{\frac{t}{\tau_d}}\right). \tag{3.36}$$

The analytical expression for concentration of excited acceptors is quite bulky:

$$n_{a*}(t) = \frac{1}{2} n_d(0) q \sqrt{\frac{\pi \tau_a}{\tau_a - \tau_d}} \exp\left(-\frac{t}{\tau_a} + \frac{q^2 \tau_a}{4(\tau_a - \tau_d)}\right) \times \left(\mathrm{Erfc}\left(\frac{q}{2}\sqrt{\frac{\tau_a}{\tau_a - \tau_d}}\right) - \mathrm{Erfc}\left(\sqrt{\frac{t(\tau_a - \tau_d)}{\tau_a \tau_d}} + \frac{q}{2}\sqrt{\frac{\tau_a}{\tau_a - \tau_d}}\right)\right) \tag{3.37}$$

for $\tau_a > \tau_d$ and

$$n_{a*}(t) = \frac{1}{2} n_d(0) q \sqrt{\frac{\pi \tau_a}{\tau_d - \tau_a}} \exp\left(-\frac{t}{\tau_a} - \frac{q^2 \tau_a}{4(\tau_d - \tau_a)}\right) \times \left(\mathrm{Erfi}\left(\frac{q}{2}\sqrt{\frac{\tau_a}{\tau_d - \tau_a}}\right) + \mathrm{Erfi}\left(\sqrt{\frac{t(\tau_d - \tau_a)}{\tau_a \tau_d}} - \frac{q}{2}\sqrt{\frac{\tau_a}{\tau_d - \tau_a}}\right)\right) \tag{3.38}$$

for $\tau_d > \tau_a$. Here, τ_a is the radiation time of the excited acceptor, Erfc(x) and Erfi(x) are complementary error function and imaginary error function, respectively. Parameter $q = \frac{4\pi^{3/2}}{3} n_a(0) R_{da}^3 = 7.42 n_a(0) R_{da}^3$ is proportional to the number of acceptors in a sphere with radius R_{da} surrounding each donor (the volume of this sphere is $\frac{4\pi}{3} R_{da}^3$).

For a small t,

$$n_{a*}(t) \approx n_d(0) q \sqrt{\frac{t}{\tau_d}}. \tag{3.39}$$

Figure 3.26 shows the typical decay kinetics for donor concentration and rise kinetics of leading edge for acceptor concentration (which is proportional to their emission kinetics).

In case of the interaction between excitations of the same type mentioned above (e.g., STE + STE $\rightarrow e + h \rightarrow$ STE), the concentration decay is described as

$$n_{ex}(t) = \frac{n_{ex}(0) e^{-t/\tau_{ex}}}{1 + \frac{2\pi^2}{3} n_{ex}(0) R_{ex-ex}^3 \mathrm{Erf}\left(\sqrt{t/\tau_{ex}}\right)}. \tag{3.40}$$

This dependence is typical of the luminescence yield for scintillators with predominantly excitonic luminescence (see, e.g., [49]). In both cases, the kinetics described by Eqs. (3.36), (3.37), (3.38), (3.39) and (3.40) are non-exponential, and the bi-molecular kinetics for reaction between identical excitations (Eq. (3.40)) nonlinearly depends on the initial concentration of excitations.

This formula can explain the kinetics in $CdWO_4$ under intense laser excitation by photons with energy in the fundamental absorption range (Fig. 3.27) [50]. For this

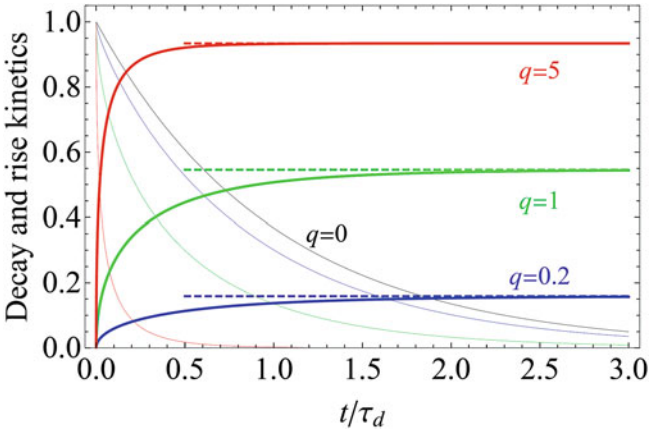

Fig. 3.26 Decay kinetics of donor concentration (thin lines) and rise kinetics of the leading edge for acceptor concentration (thick lines) for dipole-dipole energy transfer from donors to acceptors. Characteristic decay time of acceptors is much higher than that for donors. Dashed lines show the limit concentration of acceptors

crystal, the STE emission strongly overlaps with the STE absorption (curve 3 in the inset of Fig. 3.27). Therefore, the dipole-dipole energy transfer in the reaction STE + STE $\rightarrow e + h \rightarrow$ STE is efficient (the radius of dipole-dipole transfer R_{ex-ex} estimated from decay kinetics equals 2.1 nm [50]). Formula (3.40) cannot be directly applied to this type of excitation, since a uniform initial exciton distribution had been supposed in its derivation. The kinetics has to be integrated over the excitation distribution. In case of excitation by laser beam with a high-quality Gaussian profile, the initial excitations are distributed in a Gaussian way on the surface plane and have exponential distribution into the crystal interior. The details of this integration are presented in [34, 50]. The luminescence decays with time as

$$I_{lum}(t)\frac{-\mathrm{Li}_2\left(-2\pi^2 n_0^{\max}\tilde{R}_{ex-ex}^3\mathrm{Erf}\left(\sqrt{t/\tau_{ex}}\right)/3\right)}{2\pi^2 n_0^{\max}R_{ex-ex}^3\mathrm{Erf}\left(\sqrt{t/\tau_{ex}}\right)/3}e^{-t/\tau_{ex}} \tag{3.41}$$

where $\mathrm{Li}_2(x) = \sum_{k=1}^{\infty} x^k/k^2$ is the dilogarithmic function, and $n_0^{\max}$ is the initial exciton concentration near the surface at the center of the excitation spot (peak concentration). Fitting of the decay kinetics with this function demonstrates a good approximation and allows estimating the dipole-dipole radius.

In the case of pure dipole-dipole energy transfer, the reaction rate (3.34) decreases to zero with time, since the interaction strongly decreases with distance, and donors are exhausted in the vicinity of acceptors. If one or both of the reagents are mobile, the situation is more complicated, since new excitations can drift into the interaction region, therefore, the energy transfer is stimulated by this diffusion.

The diffusion-controlled dipole-dipole transfer is studied in [52] and used for describing the luminescence decay in, e.g., [53–55]. The decrease of concentration

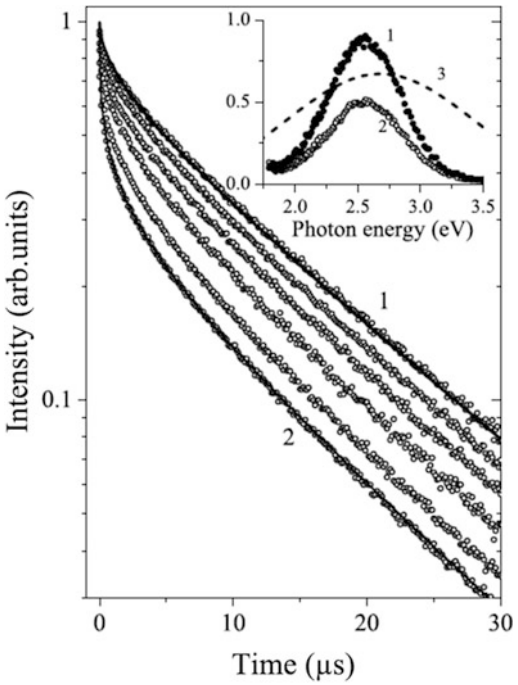

Fig. 3.27 Normalized decay curves of $CdWO_4$ emission, recorded at the same intensity but different densities of VUV femtosecond excitation (circles). Curve 2 corresponds to the focal position with the highest excitation density (spot diameter 10 μm), curve 1 corresponds to 64 times lower density (spot diameter 80 μm). Solid lines show the best fit. The inset represents the luminescence spectra recorded at the lowest (curve 1) and the highest excitation density (curve 2), and the transient absorption spectrum (curve 3) [51]. Reprinted from [50] with permission

of the mobile donors, which can move with diffusion coefficient D_d and interact with quenchers within the characteristic radius of dipole-dipole transfer R_{da}, is described by the formula

$$n_d(t) = n_d(0)\exp\left(-\frac{t}{\tau_d} - n_a(0)\frac{4\pi^{3/2}}{3}\left(\frac{R_{da}^6}{D_d\tau_d}\right)^{3/4}\left(x\frac{1+10.87x+15.5x^2}{1+8.743x}\right)^{3/4}\right) \equiv$$
$$n_d(0)\exp\left(-\frac{t}{\tau_d} - n_a(0)\frac{4\pi^{3/2}}{3}R_{da}^3 f(t/\tau_d,\delta)\right) = n_d(0)\exp\left(-\frac{t}{\tau_d} - qf(t/\tau_d,\delta)\right), \tag{3.42}$$

where $x = \delta\left(\frac{t}{\tau_d}\right)^{2/3}$, $\delta = \frac{D_d\tau_d}{R_{da}^2}$ and function

$$f(z,\delta) = \sqrt{z}\left(\frac{1+10.87\delta z^{2/3}+15.5\left(\delta z^{2/3}\right)^2}{1+8.743\delta z^{2/3}}\right)^{3/4} \tag{3.43}$$

is introduced for simplicity in the following considerations. The rational expression used in this formula is a result of approximation of analytical solution [52]. Parameter δ is the square of the ratio between the diffusion length during donor radiation time $\sqrt{D_d\tau_d}$ and the dipole-dipole energy transfer radius. For small

$x \ll 1$ (low diffusion coefficient or initial stages of the decay) this formula is transferred into the well-known formula for dipole-dipole energy transfer for immobile excitations (Eq. (3.36)), whereas in an opposite case, when $x \gg 1$, the formula is converted to the decay law for bi-molecular interaction with capture sphere of radius $R_c = 0.9077 R_{da} \left(R_{da}^2 / D_d \tau_d\right)^{1/4}$:

$$n_d(t) = n_d(0) \exp(-t/\tau_d - 4\pi n_a(0) D_d R_c t). \tag{3.44}$$

Compare the additional binominal recombination rate $\beta = 4\pi D_d R_c$ with the first term in the black sphere model, Eq. (3.30). This transformation of decay kinetics from dipole-dipole square root singularity $\frac{4\pi^{3/2}}{3} n_a(0) R_{da}^3 \sqrt{\frac{t}{\tau_d}}$ in the exponent in Eq. (3.36) to bi-molecular linear term $4\pi n_a(0) D_d R_c t$ in the exponent in Eq. (3.44) is shown in the top left panel of Fig. 3.28.

The equation for concentration of donors and excited acceptors in the case of energy transfer to acceptors, the concentration of which is higher than that for donors, can be obtained from Eq. (3.42):

$$\begin{aligned} \frac{dn_d(t)}{dt} &= -\tau_d^{-1} n_d(t) - q\, n_d(t) \frac{df(t/\tau_d, \delta)}{dt}, \\ \frac{dn_{a*}(t)}{dt} &= -\tau_a^{-1} n_{a*}(t) + q\, n_d(t) \frac{df(t/\tau_d, \delta)}{dt}. \end{aligned} \tag{3.45}$$

Parameter $q = \frac{4\pi^{3/2}}{3} n_a(0) R_{da}^3$ is defined for Eq. (3.38). If $\tau_a \gg \min\left(\tau_d, (4\pi n_a(0) D_d R_c)^{-1}\right)$, the transfer to acceptor is finished before the excited acceptors emit photons. The rising part of the kinetics for excited acceptors can be calculated from the second equation in the set (3.45):

$$\begin{aligned} n_{a*}(t) =& q\, n_d(0) \int_0^t \exp\left(-t'/\tau_d - q f(t'/\tau_d, \delta)\right) \frac{df(t'/\tau_d, \delta)}{dt'} dt' = \\ & q\, n_d(0) F(t/\tau_d, \delta), \end{aligned} \tag{3.46}$$

where

$$\begin{aligned} F(z, \delta) =& \int_0^z e^{-z'} \frac{d \exp\left(-q f(z', \delta)\right)}{dz'} dz' = \\ & 1 - e^{-z - q f(z, \delta)} + \int_0^z \exp\left(-z' - q f(z', \delta)\right) dz'. \end{aligned} \tag{3.47}$$

The rise kinetics for different q=0.2, 1, 5 and δ=0, 1, 4 are plotted in the top right panel of Fig. 3.28. For $\delta = 0$ the kinetics of excited acceptors coincides with that calculated using Eq. (3.38) for $\tau_a \gg \tau_d$ and with the curves plotted in Fig. 3.26:

$$n_{a*}(t) = \frac{1}{2} n_d(0) q \sqrt{\pi} \exp\left(\frac{q^2}{4}\right)\left(\mathrm{Erf}\left(\sqrt{\frac{t}{\tau_d}} + \frac{q}{2}\right) - \mathrm{Erf}\left(\frac{q}{2}\right)\right), \tag{3.48}$$

with square root dependence on time (Eq. (3.39)) for $t < \tau_d \min(1, 1/q)$. On the contrary, for $\delta \gg 1$ a simple rising law is observed

$$n_{a*}(t) = 4\pi D_d R_c n_a(0) n_d(0)(1 - \exp(-t/\tau_d - 4\pi n_a(0) D_d R_c t))\tilde{1} - \exp(-t/\tau_{rise}) \tag{3.49}$$

with the rising time $\tau_{rise} = (1/\tau_d + 4\pi n_a(0) D_d R_c)^{-1}$. For small times $t \ll \tau_{rise}$, the rise of excited acceptor concentration is linear (except of the very beginning of the rise, where square root behavior is observed). The bottom panel in Fig. 3.28 shows the rise of excited activator concentrations (the same as for top right panel) in log-log scale together with $\sqrt{t}$ and t trends.

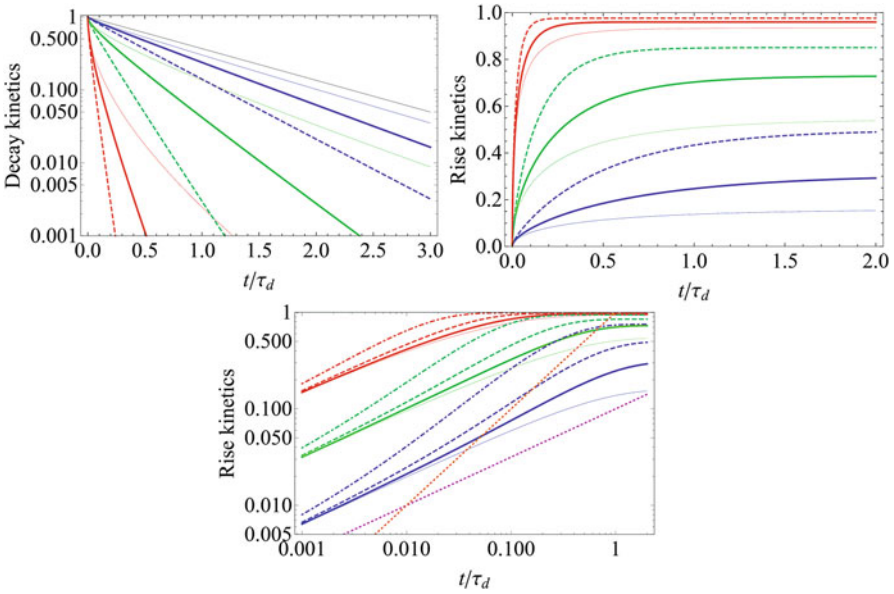

Fig. 3.28 Decay kinetics of donor concentration (top left panel) and rise kinetics of the leading edge for acceptor concentration (top right panel) for diffusion-controlled dipole-dipole energy transfer from donors to acceptors. Characteristic decay time of acceptors is much higher than that for donors. q=0 (black curve), 0.2 (blue), 1 (green), and 5 (red), δ=0 (thin curves), 1 (thick), 4 (dashed), and 20 (dot-dashed curves, only in the bottom panel). The kinetics in log-log scale in the bottom panel demonstrate the trends of $\sqrt{t}$ rise (magenta dotted line) and depicts t dependence (orange dotted line)

The equation for exciton concentration in the case of exciton-exciton annihilation can be written in analogy with Eq. (3.45):

$$\frac{dn_{ex}(t)}{dt} = -\ \tau_{ex}^{-1} n_{ex}(t) - \frac{4\pi^{3/2}}{3} R_{ex-ex}^{3} n_{ex}^{2}(t) \frac{df(t/\tau_{ex}, \delta)}{dt}. \tag{3.50}$$

The function $f(z, \delta)$ is the same as in Eq. (3.43), the only difference is that the diffusion coefficient in this formula is twice as large as the exciton diffusion coefficient, since both excitons are mobile: $\delta = \frac{2D_{ex}\,\tau_{ex}}{R_{ex-ex}^{2}}$.

The solution of Eq. (3.50) is [55].

$$n_{ex}(t) = \frac{n_{ex}(0) \exp\left(-t/\tau_{ex}\right)}{\tau_{ex}\left(1 + n_{ex}(0)\,\frac{4\pi^{3/2}}{3} R_{ex-ex}^{3} F_1(t/\tau_{ex}, \delta)\right)}, \tag{3.51}$$

where

$$F_1(z, \delta) = \int_0^z e^{-z'} \frac{df(z', \delta)}{dz'} dz' = e^{-z} f(z, \delta) + \int_0^z e^{-z'} f(z', \delta) dz'. \tag{3.52}$$

This formula was used for simulation of the decay kinetics in molibdate crystals after intense femtosecond laser excitation [55].

The dipole-dipole interaction is not the only type of short-range energy transfer. Another type of transfer is the Dexter exchange transfer. The efficiency of this transfer falls exponentially with the increase of the distance between donor and acceptor, since this mechanism requires overlapping of wavefunctions of interacting donor and acceptor, and the tails of the localized wavefunctions fall exponentially with distance. So, the decay kinetics is not exponential, but becomes hyperbolic $n_d(t) \sim t^{-\alpha}$, where α is close to 1. This type of energy transfer can be important only for a high concentration of acceptors.

Tunnel recombination (for instance, transfer of an electron from one trap to another) can also result is such slow hyperbolic decays. The observation of such transfer in scintillators is reviewed in [56].

3.10 Rise and Decay Kinetics in Scintillators

3.10.1 Decay Kinetics in Self-Activated Materials

Self-activated materials are characterized by exciton emission. Excitons in most ionic crystals show charge transfer in a form of electron transition from anion to cation. Electronic states of anions (mostly halide or oxide ions) form the valence

band, whereas cations form the conduction band. In crystals with complex oxyanion, the bottom of the conduction band is often formed by the oxyanion (like in many tungstate crystals: $CaWO_4$, $CdWO_4$), and exciton is just the excitation of oxyanion complex. In case of self-activated crystals, the emission centers are formed directly after the capture of electron by a hole followed by lattice relaxation around exciton. Each unit cell can serve as such center. Therefore, the creation of the excitons is controlled by recombination of electrons and holes, as it is described by Eq. (3.16). The recombination of electrons and holes is controlled not only by their concentrations, but also by the electron-hole correlation function. The details are described above in Sect. 3.9.2 (see also [34]). In case of stationary excitation producing non-correlated electrons and holes, the rate coefficient of this reaction is $\beta_{eh}(t) \approx 4\pi(D_e + D_h)R_{Ons}$ and does not depend on time. The situation changes when electrons and holes are created by ultrafast processes like in a cascade process after the passage of an ionizing particle or after femtosecond laser excitation. In this case, the electron-hole correlation function varies in time, and the rate also depends on time. These effects influence the leading edge of the scintillation signal. Now, we are going to concentrate on the effects resulting from the non-uniform distribution of thermalized excitations in the track region discussed in Sect. 3.8. We will neglect the dependence of rate coefficients on time for simplicity.

The created excitons can emit photons with rate τ_{ex}^{-1}. In case of thermal luminescence quenching, the total exciton lifetime τ_{ex} is less than the exciton radiative lifetime τ_{rad}, and the quantum yield $Q=\tau_{ex}/\tau_{rad}$ of the emitting center is less than one. The lifetime of self-trapped exciton typically equals hundreds of nanoseconds or even microseconds, and the excitons can interact with each other during their lifetime. Here we suppose that excitons are mobile species, and can interact through Auger-type reaction, when the energy of one exciton is passed to another one with creation of electron-hole pair, which with some probability can, in turn, form a secondary exciton. Here, we also use the simplest reaction rate, the rate of bi-molecular recombination, for mobile excitons, as described above for the case $\delta = \frac{2D_{ex}\tau_{ex}}{R_{ex-ex}^2} \gg 1$.

Certain qualitative results can be found for rather simple analytically solvable set of equations studied in [57]. This model preserves the most important features of more complicated case, such as emergence of a rising part in the response, fast initial decay stage and long emission components. A uniform distribution of excitations (excitons with concentration n_{ex} and holes and electrons with equal concentrations $n_h = n_e$) is considered. No Auger recombination for free electrons and holes is included (these terms should be of the third order on concentration, proportional to $n_h n_e^2$ or $n_h^2 n_e$; this case is studied in [37, 43–46, 58]). The set of equations includes only second order terms and can be written as:

$$\begin{aligned} \frac{dn_{ex}(t)}{dt} &= -\frac{n_{ex}(t)}{\tau_{ex}} - \beta_{ex-ex}n_{ex}^2 + \beta_{eh}n_e(t)n_h(t), \\ \frac{dn_e(t)}{dt} &= -\beta_{eh}n_e(t)n_h(t), \\ n_e(t) &= n_h(t). \end{aligned} \tag{3.53}$$

The equation for excitons describes their radiative recombination (linear term), exciton-exciton annihilation with the rate coefficient β_{ex-ex} (quadratic term), and binding of electrons and holes into excitons with the rate coefficient β_{eh} (bi-linear term). The equation for electrons includes only bi-linear term describing exciton production. Therefore, this model includes one radiative channel (for excitons) and one quenching process due to exciton-exciton non-radiative quenching. The equations should be amended by the initial conditions for the total concentration of excitations created after thermalization. We suppose that all excitations are created as electron-hole pairs with probability $(1 - f_{ex})$ and excitons are directly created in the cascade process with probability f_{ex}: $n_e(0) = n_h(0) = (1 - f_{ex})n^0$, $n_{ex}(0) = f_{ex}n^0$. The formulas for kinetics of exciton emission studied in Sect. 3.9.3 are not directly applicable for this case, since excitons are not created simultaneously. The standard convolution of decay curves, which is often used for the description of sequential processes, are also not applicable, since the problem is non-linear.

Fortunately, this set of equations can be analytically solved in terms of modified Bessel functions, similarly to the solution presented in [57]. The equation for electron (hole) concentration does not contain excitonic term and can be easily solved:

$$n_e(t) = n_h(t) = \frac{n^0(1 - f_{ex})}{1 + \beta_{eh}n^0(1 - f_{ex})t}. \tag{3.54}$$

The first equation from the set (3.53) is Riccati equation:

$$\frac{dn_{ex}(t)}{dt} = -\frac{n_{ex}(t)}{\tau_{ex}} - \beta_{ex-ex}n_{ex}^2(t) + \beta_{eh}\left(\frac{n^0(1 - f_{ex})}{1 + \beta_{eh}n^0(1 - f_{ex})t}\right)^2 \tag{3.55}$$

with a rather cumbersome solution:

$$\begin{aligned} n_{ex}(t) =& \frac{1}{2\tau_{ex}(\tau + \tau_0)\beta_{ex-ex}}[(1 + 2\nu - \tau - \tau_0) + (\tau + \tau_0) \\ &\times \left(\varsigma_K I_{\nu+1}\left(\frac{\tau + \tau_0}{2}\right) + \varsigma_I K_{\nu+1}\left(\frac{\tau + \tau_0}{2}\right)\right)/\left(\varsigma_K I_\nu\left(\frac{\tau + \tau_0}{2}\right) - \varsigma_I K_\nu\left(\frac{\tau + \tau_0}{2}\right)\right)], \end{aligned} \tag{3.56}$$

where

$$\begin{aligned} \varsigma_K =& \varsigma_1 K_\nu(\tau_0/2) + K_{\nu+1}(\tau_0/2), \quad \varsigma_I = \varsigma_1 I_\nu(\tau_0/2) - I_{\nu+1}(\tau_0/2), \\ \nu =& \frac{1}{2}\sqrt{1 + 4\beta_{ex-ex}/\beta_{eh}}, \\ \varsigma_1 =& 1 - n^0\tau_{ex}(\beta_{eh}(1 - f_{ex})(1 + 2\nu) - 2\beta_{ex-ex}f_{ex}), \\ \tau =& t/\tau_{ex}, \quad \tau_0^{-1} = 4\tau_{ex}\beta_{eh}n^0(1 - f_{ex}), \end{aligned} \tag{3.57}$$

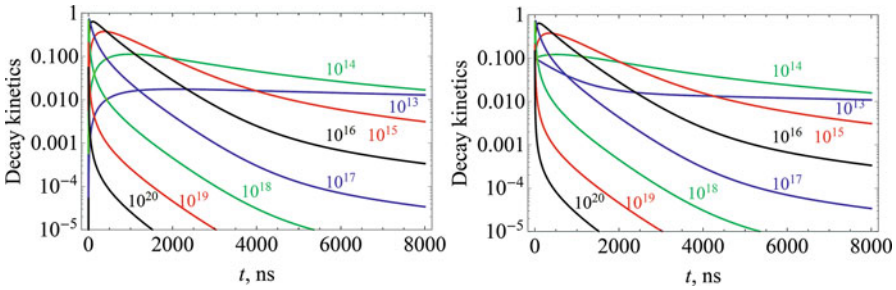

Fig. 3.29 Decay curves for emission from regions with different initial concentrations n^0 (indicated near corresponding curves, in cm^{-3}) for the model expressed by Eq. (3.53) for $\beta_{ex-ex}n_{inter} = \tau_{ex}^{-1}$, τ_{ex}=600 ns, n_{inter}=10^{16} cm^{-3}, $\beta_{eh} = 20\beta_{ex-ex}$, when excitons are not created (f_{ex}=0), left panel, and when 10% of electron-hole pairs are created as excitons (f_{ex}=0.1), right panel

$I_\nu(x)$ and $K_\nu(x)$ are modified Bessel functions. Nevertheless, this solution is convenient for studying the dependence of the decay on parameters.

We can introduce the critical concentration n_{inter} as the concentration of excitons, at which the rate of the exciton-exciton annihilation equals the inverse lifetime: $\beta_{ex-ex}n_{inter} = \tau_{ex}^{-1}$. For demonstration of how the kinetics changes with initial concentration n^0, we choose τ_{ex}=600 ns, n_{inter}=10^{16} cm^{-3}. The electron-hole recombination constant is chosen as $\beta_{eh} = 20\beta_{ex-ex}$. The results for the simulation of the model with these parameters are presented in Fig. 3.29 for two cases: without creation of excitons under initial excitation (left panel) and when 10% of all excitations are excitons rather than electron-hole pairs (right panel). The difference in the decay curves is observed only for low concentration of initial excitations (below 10^{15} cm^{-3}).

The results of decay simulation shown in Fig. 3.29 are presented for spatially homogeneous distribution of initial excitations with concentration n^0. The concentration of excitations in track region is distributed, according to Sect. 3.8, as shown in Fig. 3.18 for CsI. The thermalization length for major part of self-activated crystals is much shorter than that for CsI. Therefore, the peak of this distribution is shifted to higher concentrations. Figure 3.30 shows schematically three distributions of concentrations peaked at 10^{16}, 10^{17}, and 10^{18} cm^{-3}. These histograms are constructed using logarithmical scale for bins. The first concentration corresponds to that expected after interaction with ionizing particle with energy of hundreds keV, whereas 10^{18} cm^{-3} is typical for low-energy ionizing particles (with energy of several keV). The decay curves are the convolution of these distributions with exciton decay curves for various uniform concentrations n^0. We use decay curves presented for left panel in Fig. 3.29 (without primary exciton production). The results are shown in the middle panel of Fig. 3.30. The decay profiles vary with the increase of the mean concentration in the track, the emission becomes faster, especially in the initial stages. Moreover, the rising part of the response (right panel) changes dramatically. The decay has fast (subnanosecond) rise up to certain amplitude. The rise time afterwards significantly depends on the mean concentration. Decay kinetics for BGO crystal measured using X-ray synchrotron radiation show the similarity with obtained curves (Fig. 3.31).

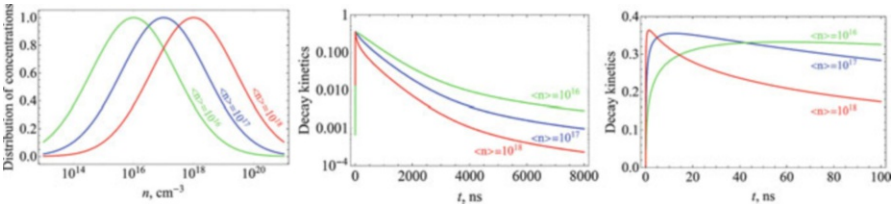

Fig. 3.30 Distribution of initial concentrations of excitations with three mean concentrations $\langle n^0 \rangle = 10^{16}$, 10^{17},and 10^{18} cm^{-3} (left panel) and corresponding response kinetics on different time scales (middle and right panels) for parameters used in the model exploited to calculate results presented in Fig. 3.29 without creation of excitons

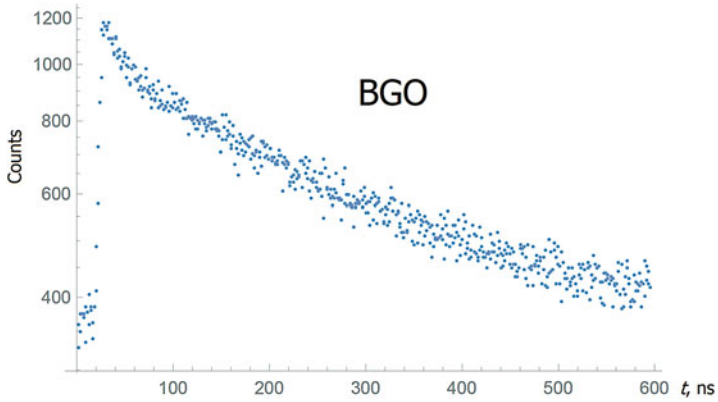

Fig. 3.31 Decay kinetics for BGO crystal excited by X-ray synchrotron radiation [59]

According to this model, the scintillation yield (which is the integral under decay curve) decreases with increasing mean concentration in the track. This decrease corresponds to non-proportionality curves measured for most oxyanion scintillators, which fall down for low energies of ionizing electrons [58].

3.10.2 Rise and Decay Kinetics in Activated Materials

The case of energy transfer from the host material to activators is not so prompt (see, e.g. [47, 60–63]). The energy can be transferred to activators mostly by two ways: sequential capture of charged carriers by activators and through dipole-dipole energy

transfer from excitons, either free or self-trapped. In both cases, there should be two subsequent reactions to form the excited state of activators. In the case of sequential capture, a carrier of one type (for instance, an electron) should be captured by an activator ion (e.g. $e + Tl^{+} \rightarrow Tl^{0}$) and then a carrier of the second type should be captured by the charged state of the activator ($h + Tl^{0} \rightarrow Tl^{+*}$ in this example). For the case of exciton transfer, two reactions should also occur: $e + h \rightarrow ex$; $ex + Tl^{+} \rightarrow Tl^{+*}$. Modification to a three-step reaction is possible: $e + h \rightarrow ex$; $ex \rightarrow$STE; STE + $Tl^{+} \rightarrow Tl^{+*}$. In comparison with self-activated crystals with the excitonic luminescence described in the previous sub-section, the energy transfer demands one additional step. In general, the rise time of activated scintillators should be longer than that for self-activated crystals.

In the previous example we took thallium ions as activators. Such ions can be metastable in three charge states: Tl^{0}, Tl^{+} and Tl^{2+}. For this case, both electrons and holes could be the first reagent. Note that such heavy relativistic ions with strong spin-orbit interaction form complex states in the crystals. For instance, in iodine crystals 6s electrons of thallium ions are strongly hybridized with iodine electrons forming the valence band [63]. Therefore, Tl^{2+} state should be considered rather as a state with hole on hybridized thallium-iodine state. Sometimes such state is considered as a hole localized near activator.

Other reaction types should be considered in crystals with cerium as activator. In many crystals, $4f\,Ce^{3+}$ level is well above the top of the valence band (by up to 3 eV) [64, 65], and holes can hardly be captured by cerium. If excitation center cannot capture electrons and holes sequentially, the energy transfer from excitons is the only way to excite these centers [66–68]. The process can be described by the following sequence of reactions:

$$\begin{aligned} e + h \rightarrow ex;\ \ ex \rightarrow \text{STE};\, \text{STE} + Ce^{3+} \rightarrow Ce^{4+} + e;\, Ce^{4+} + e \\ \rightarrow Ce^{3+*};\, Ce^{3+*} \rightarrow Ce^{3+} + h\nu. \end{aligned} \tag{3.58}$$

If the energy of STE is insufficient to ionize Ce^{3+} ion, two intermediate reactions are merged to one: STE + $Ce^{3+} \rightarrow Ce^{3+*}$. In most cases the two reactions, the direct excitation of cerium and the excitation due to ionization, coexist. The rate of the $e + h \rightarrow ex$ reaction bi-linearly depends on the concentrations of electrons and holes. Therefore, these reactions depend on the distribution of densities of excitations in the track region.

To demonstrate the peculiarities of decay kinetics and rising part of the leading edge of the kinetics, we solve typical rate equations for concentrations of electrons $n_e(t)$, holes $n_h(t)$, free excitons $n_{ex}(t)$, self-trapped excitons $n_{STE}(t)$, excited cerium ions $n_{Ce^{3+*}}(t)$, and ionized cerium ions Ce^{4+} $n_{Ce^{4+}}(t)$. The meaning of the rate coefficients is evident from the analysis of the rate Eq. (3.59):

$$
\begin{aligned}
\frac{dn_e(t)}{dt} &= -w_{e+h}n_e(t)n_h(t) - w_{e+Ce^{4+}}n_e(t)n_{Ce^{4+}}(t) \\
&\quad + f_{ion}w_{STE\to Ce^{3+}}\left(n^0_{Ce} - n_{Ce^{3+*}}(t) - n_{Ce^{4+}}(t)\right)n_{STE}(t), \\
\frac{dn_h(t)}{dt} &= -w_{e+h}n_e(t)n_h(t), \\
\frac{dn_{ex}(t)}{dt} &= w_{e+h}n_e(t)n_h(t) - w_{ex\to STE}n_{ex}(t), \\
\frac{dn_{STE}(t)}{dt} &= w_{ex\to STE}n_{ex}(t) - \frac{1}{\tau_{STE}}n_{STE}(t) - w_{STE\to Ce^{3+}}\left(n^0_{Ce} - n_{Ce^{3+*}}(t) - n_{Ce^{4+}}(t)\right)n_{STE}(t), \\
\frac{dn_{Ce^{3+*}}(t)}{dt} &= -\frac{1}{\tau_{Ce^{3+*}}}n_{Ce^{3+*}}(t) + w_{e+Ce^{4+}}n_e(t)n_{Ce^{4+}}(t) \\
&\quad + (1-f_{ion})w_{STE\to Ce^{3+}}\left(n^0_{Ce} - n_{Ce^{3+*}}(t) - n_{Ce^{4+}}(t)\right)n_{STE}(t), \\
\frac{dn_{Ce^{4+}}(t)}{dt} &= -w_{e+Ce^{4+}}n_e(t)n_{Ce^{4+}}(t) + f_{ion}w_{STE\to Ce^{3+}}\left(n^0_{Ce} - n_{Ce^{3+*}}(t) - n_{Ce^{4+}}(t)\right)n_{STE}(t).
\end{aligned}
\tag{3.59}
$$

In these equations, we suppose that f_{ion} fraction of reactions STE + Ce^{3+} result in ionization of Ce^{3+} ion toCe^{4+}+e, and the rest of the reactions, i.e., fraction $(1-f_{ion})$, results in creation of excited ions Ce^{3+*}. We use here a simplified version for rate coefficients, which do not depend on time at initial recombination stages. Time-dependent rate coefficients are studied in Sect. 3.9.

The typical kinetics of excited cerium ion are presented in Fig. 3.32 by solid curves. Curves of different color represent different initial concentration of electrons and holes $n_e(0) = n_h(0)$ measured in units of critical concentration n_c, for which the rate of electron-hole recombination equals $10^{10}\ s^{-1}$. Cerium concentration is equal to n_c, the rates of $ex\to$STE and STE + Ce^{3+} reactions are equal to $10^{12}\ s^{-1}$. Here, we take $f_{ion} = 1$, i.e., excitons ionize cerium instead of exciting it, and the excitation is caused only by the capture of electron by Ce^{4+}.The parameters are chosen just to illustrate the effect. As evident in Fig. 3.32, the rise time of such cascade energy transfer for high electron initial concentration $n_e(0) = n_c$ (black solid curve) is ~100 ps, whereas for lower initial concentrations it can be as long as tens of nanosecond (magenta curve for $n_e(0) = 0.001\,n_c$). The decay at high initial concentration is exponential with Ce^{3+*} emission time (we take 30 ps as typical time for these estimations) except of a weak deviation at hundreds of nanoseconds. On the contrary, the long-time decay for low electron concentrations is hyperbolic (linear on double logarithmic scale), and its contribution strongly increases with the decrease of initial electron and hole concentration. For the selected parameters, both the rising time and the long decay are controlled by bi-molecular coupling of electrons and holes into excitons.

During the last few years, the extensive study of co-dopants in garnet crystals showed that introduction of even a small number of bivalent ions (Mg^{2+}, Ca^{2+}) can significantly reduce the rise time and the afterglow [67–69]. This effect might have various origins. One of them is the formation of Ce^{4+} ions in the crystal as a consequence of the shift of the Fermi level. Figure 3.32 shows the role of small

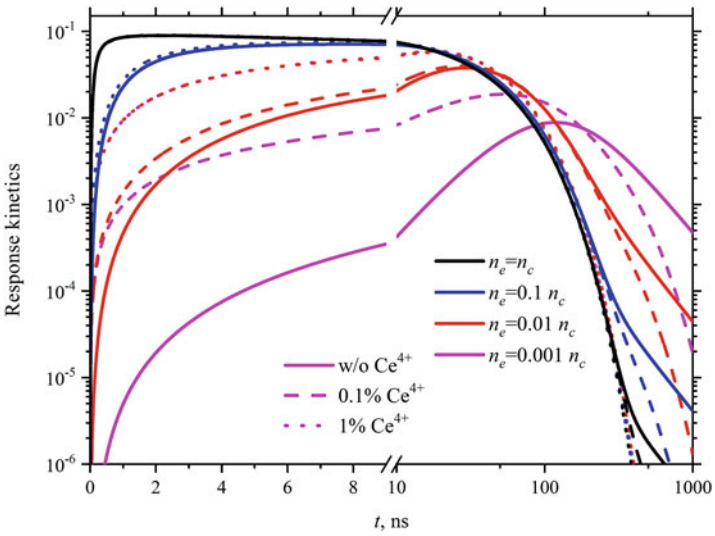

Fig. 3.32 Cerium response kinetics for different initial concentrations of electrons and holes (different colors) without presence of Ce^{4+} ions (solid curves) and with certain fraction of Ce^{3+} converted to Ce^{4+} (dashed and dotted curves)

addition of Ce^{4+} ions in the energy transfer from electron-hole pairs to cerium. In this case, one-step reaction $e + Ce^{4+} \rightarrow Ce^{3+*}$; $Ce^{3+*} \rightarrow Ce^{3+}+h\nu$ can result in the emergence of faster emission components. Cerium ionization according to reaction $STE + Ce^{3+} \rightarrow Ce^{4+}+e$ is an additional way for Ce^{4+} population to recover in the case when the system is co-doped by divalent ions (like Mg^{2+} and Ca^{2+}) [70]. Dashed and dotted curves show the modification of Ce^{3+*} kinetics with the conversion of 0.1% and 1% of Ce^{3+} ions to Ce^{4+} ions in non-excited crystal. The effect is strong for concentrations of electrons approximately equal to Ce^{4+} concentration or lower (magenta and red curves). In this case, the electrons in low concentration regions are captured rather by Ce^{4+} ions than by holes. The overall response becomes faster, and the rise time for emission from the low concentration regions is much faster than that in the case without Ce^{4+}. The shift of the balance between $e + Ce^{4+} \rightarrow Ce^{3+*}$ and $e + h \rightarrow ex$ also suppresses the long components, as shown experimentally. Again, this suppression is more pronounced in low-concentration parts of the track, which are responsible for the long decay components.

The curves presented in Fig. 3.32 demonstrate the kinetics from different parts of the track with different electron concentrations. The fast rise of scintillation response is caused by the regions with high concentration of excitations. These regions are near the central part of the track and at the tips of the track branches. The delayed non-exponential decay for times longer than the intrinsic radiation time of the activator is formed by peripheral parts of the track. The total response can be

obtained from these partial responses by weighting them with the distribution like that calculated for YAG [68] and shown in the left panel of Fig. 3.33 (compare with that depicted in Fig. 3.18 for CsI). A typical density distribution of the created excitations covers a wide range from 10^{10} to 10^{22} excitations per cm^3. We perform estimations of this distribution for two energies of ionizing electron, namely 10 keV (after the conversion of X-ray photon, magenta curve), and 662 keV (photoelectron from absorption of gamma from ^{137}Cs decay, blue curve). The distribution of the excitation densities generated by a 662 keV photoelectron is shifted to lower concentrations in comparison with that generated by a 10 keV photoelectron. This shift is equivalent to by a factor of 20 lower the concentration. Therefore, the decay for 10 keV excitation should have a faster leading edge of the response and a smaller contribution of slow components than in the case of gamma excitation. The corresponding experimental results are presented in Fig. 3 of [68].

The vertical lines in the Fig. 3.33 mark the concentrations of excitations equal to typical concentrations of Ce^{3+} and Ce^{4+} expressed in ppm (measured in units of yttrium concentration). Violet vertical line in the right panel in Fig. 3.33 corresponds to the distance between excitations equal to the dipole-dipole interaction radius. The excitons are strongly quenched, if their concentration is higher than n_{inter}.

The bottom panel of Fig. 3.33 shows the fraction of electrons participating in reactions $e + Ce^{4+} \rightarrow Ce^{3+*}$ (red curve) and $e + h \rightarrow ex$ (blue curve) followed by the energy transfer to Ce^{3+} ions for cerium concentration equal to 100 ppm and the concentration of Ce^{4+} ions equal to 10 ppm for excitation by 10 keV X-rays. The figure shows that approximately half of electrons recombine with Ce^{4+} ions rather than with holes. Thus, the additional intermediate reaction with production of excitons is excluded. The recombination with Ce^{4+} is still important even at Ce^{4+} concentration as low as 1 ppm. The result is the reduction of the rise time of the scintillation response, as it is shown in Fig. 3.32. For gamma excitation, the effect is even stronger, since the distribution of concentrations is shifted to lower concentrations.

The violet curve in the bottom panel of Fig. 3.33 shows schematically the fraction of excitons which are quenched due to dipole-dipole interaction. This quenching results in a decrease of excited cerium ions and reduces the light yield of scintillations crystals in comparison with the theoretical limit $E_\gamma/\beta E_g$. Moreover, additional quenching of excited cerium ions due to Auger-type reactions $e + Ce^{3+*} \rightarrow e + Ce^{3+}$, $h + Ce^{3+*} \rightarrow h + Ce^{3+}$, $ex + Ce^{3+*} \rightarrow e + h + Ce^{3+}$ is important at high concentrations of excitations. The schemes of such nonradiative deexcitations of cerium ions are presented in Fig. 6 of [68]. The result of these processes is the arising of the decay components in scintillation signal with the characteristic time faster than the characteristic decay time for activator.

The acceleration of cerium decay might have also other reasons, since bivalent ions in garnets modify also the number and the population of shallow defects, which can significantly reduce the mobility of electrons and holes in the system and, therefore, change the reaction constant even for capture process $e + h \rightarrow ex$.

The qualitative study of the example presented above on the energy transfer from host to cerium can be important for development of new fast scintillators.

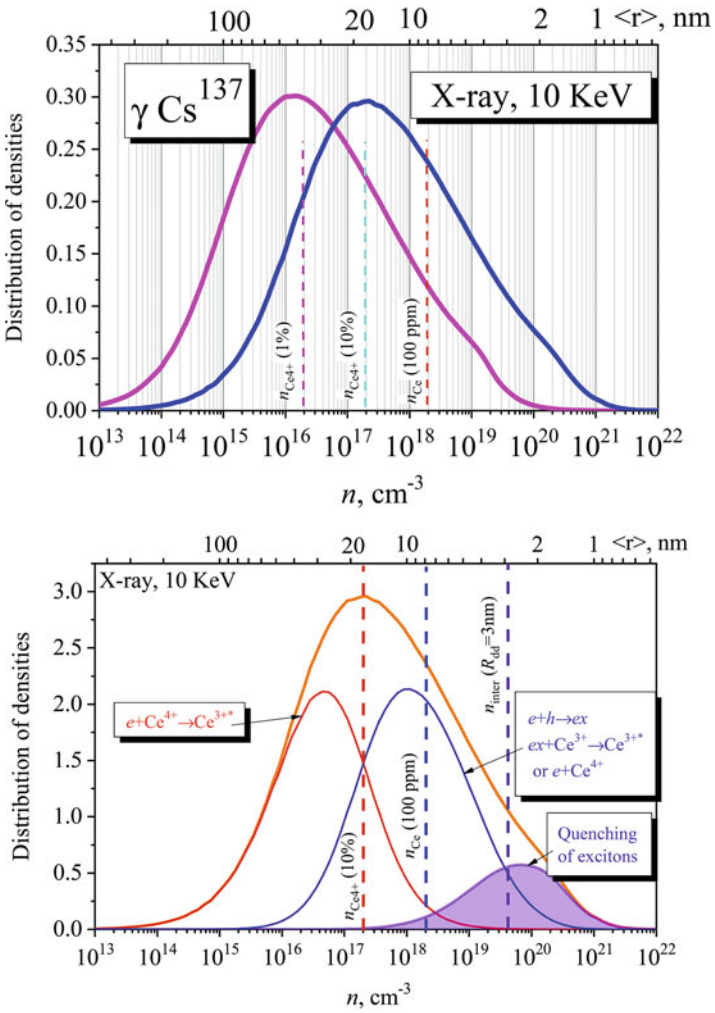

Fig. 3.33 Top panel: excitation density distribution functions $w(n;E)$ for electron densities in the track in YAG at 300 K after absorption of γ-quantum (magenta curve) and 10 keV X ray photon (blue curve). Vertical lines mark the cerium ion concentration of 100 ppm relative to Y and Ce^{4+} concentrations at 10% and 1% of Ce^{3+} converted to Ce^{4+} due to cooping by Mg^{2+}. Top axis provides the mean distances between excitations. Bottom panel: branching of electron capture by Ce^{4+} with creation of Ce^{3+*} and electron capture by holes with creation of excitons. Violet curve shows schematically the fraction of excitons, which are quenched rather than pass their energy to Ce^{3+}

3.11 Fast Nonlinear Luminescence in Crystals with Exciton-Like Luminescence

A number of scintillation crystals characterized by a fast emission have special properties. These are, in particular, crystals with intrinsic luminescence, which is certainly associated with excitons. They are of interest, since there are still no clear models for this luminescence. Such luminescence is observed in the pure crystals without activators, in particular, in CsI, $CsPbCl_3$, ZnO at room temperature. A common property of this type of luminescence is the substantially nonlinear dependence of luminescence efficiency on the intensity of interband excitation. Let us consider the features of such luminescence using pure CsI as an example.

The scintillation properties of pure CsI have been known for decades [71–73]. Ultraviolet luminescence at 4.1 eV exhibits non-exponential decay with the emission times ranging from subnanoseconds to a few nanoseconds. The room-temperature emission was interpreted by the recombination of self-trapped excitons, which are localized due to the redistribution of the population of different exciton states with increasing temperature [74]. Nevertheless, a number of properties of such luminescence are significantly different from those of typical exciton luminescence. In particular, this luminescence is effectively excited by photons with energies substantially larger than the band gap (above 40 eV), whereas its yield at lower energies is extremely small [75]. When excited by an intense femtosecond laser, the yield of this luminescence increases linearly with increasing excitation energy density [76] (in contrast to ordinary exciton luminescence [77], the yield of which does not change with increasing excitation density up to the quenching region). When excited by X-ray radiation, the luminescence yield experiences a positive jump at the X-ray absorption edges [76]; again, unlike the yield of most other types of luminescence, the intensity of which falls above the X-ray absorption edges. The interpretation of this luminescence behavior requires more complex dynamic models associated with exciton interaction. In particular, the model of fusion of self-trapped and free excitons was proposed for RbI [78]. This rate of this process is proportional to the square of exciton concentration. Unfortunately, a model explaining all the features of luminescence in pure CsI has not been developed yet.

The structure of the track of an ionizing particle described above shows that, in the case of a substantially inhomogeneous track, such luminescence occurs mainly from high-density regions (i.e., from excitation “clusters” produced by the Auger cascades of deep-core holes and the cascade of electrons with relatively low energy). Despite the relatively low yield, the luminescence of pure CsI may be a good candidate for a scintillator detector with a high time resolution.

Other non-activated inorganic crystals, in particular, ZnO [79] and some perovskites with heavy ions (in particular, $CsPbCl_3$) have a similar nonlinear dependence of luminescence intensity on excitation density. Investigations of such systems seem promising from the point of view of both fundamental research and practical applications.

3.12 Conclusions

In the present chapter, we discussed the relationship of the relaxation processes in scintillating crystals after the energy deposit of ionizing particles. From the point of view of developing the fast scintillators, it is important that the shape of the leading edge of the scintillator response is quick. The rising part of the response can consist of (i) rather fast stepwise increase of the signal due to prompt recombination, (ii) square root singularity due to geminate recombination of electron-hole pairs and (iii) linear in time contribution due to intermediate energy transfer. The relative contributions of these components forming the leading edge of the response strongly depend on the rates of corresponding reactions.

References

1. A. Khrutchinsky, M. Korzhik, P. Lecoq, A phenomenon of scintillation in solids. Nucl. Instrum. Methods Phys. Res. Sect. A **486**, 381–384 (2002)
2. E.R. Ilmas, G.G. Liidja, Ch.B. Lushchik, Photon multiplication in crystals. I. Luminescence excitation spectra of ionic crystals in region 4 to 21 eV. Opt. Spectrosc. (USSR) **18**, 255 (1965); Photon multiplication in crystals. 2. Mechanism of photon multiplication. Opt. Spectrosc. (USSR) **18**, 359 (1965)
3. A.N. Vasil'ev, V.N. Kolobanov, I.L. Kuusman, C.B. Lushchik, V.V. Mikhailin, Multiplication of electronic excitations in MgO crystals. Fizika Tverdogo Tela **27**, 2696–2702 (1985)
4. M. Kirm, E. Feldbach, T. Kärner, A. Lushchik, C. Lushchik, A. Maaroos, V. Nagirnyi, I. Martinson, Multiplication of electron–hole pairs in MgO crystals and ceramics. Nucl. Instrum. Methods Phys. Res. Sect. B **141**, 431–435 (1998)
5. Y.L. Klimontovich, *The Kinetic Theory of Electromagnetic Processes* (Springer, Berlin/Heidelberg/New York, 1983).
6. A.N. Vasil'ev, V.V. Mikhailin, *Introduction to Solid State Spectroscopy, Part 1* (KDU publishing house, Moscow, 2008)., in Russian)
7. A.N. Vasil'ev, Microtheory of scintillation in crystalline materials, in Engineering of Scintillation Materials and Radiation Technologies, ed. by A. Gektin and M. Korzhik (Springer, Cham, 2017), pp. 3–34
8. A.N. Vasil'ev, Polarization approximation for electron cascade in insulators after high-energy excitation. Nucl. Instrum. Methods Phys. Res. Sect. B: Beam Interact. Mater. Atoms. **107**, 165–171 (1996)
9. M. Inokuti, Inelastic collisions of fast charged particles with atoms and molecules—The Bethe theory revisited. Rev. Mod. Phys. **43**, 297–347 (1971)
10. https://physics.nist.gov/PhysRefData/Star/Text/ESTAR.html
11. A.N. Vasil'ev, Y. Fang, V.V. Mikhailin, Impact production of secondary electronic excitations in insulators: Multiple-parabolic-branch band model. Phys. Rev. B **60**, 5340–5347 (1999)
12. D.I. Vaisburd, K.E. Evdokimov, Creation of excitations and defects in insulating materials by high-current-density electron beams of nanosecond pulse duration. Phys. Status Solidi C **2**, 216–222 (2005)
13. R. Kirkin, V.V. Mikhailin, A.N. Vasil'ev, Recombination of correlated elec-tron-hole pairs with account of hot capture with emission of optical phonons. IEEE Trans. Nucl. Sci. **59**, 2057–2064 (2012)
14. Z. Wang, Y. Xie, B.D. Cannon, L.W. Campbell, F. Gao, S. Kerisit, Computer simulation of electron thermalization in CsI and CsI(Tl). J. Appl. Phys. **110**, 064903 (2011)

15. Z. Wang, Y. Xie, L.W. Campbell, F. Gao, S. Kerisit, Monte Carlo simula-tions of electron thermalization in alkali iodide and alkaline-earth fluoride scintillators. J. Appl. Phys. **112**, 014906 (2012)
16. D. Vaisburd, O. Koroleva, S. Kharitonova, Instantaneous spectrum of passively ionized electrons in a dielectric irradiated by a high-power electron beam. Russ. Phys. J. **39**(11), 1114–1121 (1996)
17. R.G. Deich, M. Karklina, L. Nagli, Intraband luminescence of CsI crystal. Solid State Commun. **71**(10), 859–862 (1989)
18. S.I. Omelkov, V. Nagirnyi, A.N. Vasil'ev, M. Kirm, New features of hot intraband luminescence for fast timing. J. Lumin. **176**, 309–317 (2016)
19. A.N. Vasil'ev, Relaxation of hot electronic excitations in scintillators: account for scattering, track effects, complicated electronic structure, in *Proceedings of The Fifth International Conference on Inorganic Scintillators and Their Applications*, (Faculty of Physics, Moscow State University, Moscow, 2000), pp. 43–52
20. A. Gektin, A. Vasil'ev, Scintillation, phonon and defect channel balance; the sources for fundamental yield increase. Funct. Mater. **23**, 183–190 (2016)
21. A.N. Belsky, R.A. Glukhov, P. Martin, V.V. Mikhailin, C. Pedrini, A.N. Vasil'ev, VUV excitation of intrinsic luminescence of ionic crystals with complicated band structure. Simulation. J. Lumin. **72–74**, 96–97 (1997)
22. A.N. Belsky, I.A. Kamenskikh, V.V. Mikhailin, C. Pedrini, A.N. Vasil'ev, Energy transfer in inorganic scintillators. Radiat. Eff. Defects Solids **150**, 1–10 (1999)
23. A.N. Vasil'ev, Final stages of inelastic electron scattering in insulators. Mater. Sci. Forum **239–241**, 235–240 (1997)
24. A.N. Belsky, R.A. Glukhov, I.A. Kamenskikh, P. Martin, V.V. Mikhailin, I.H. Munro, C. Pedrini, D.A. Shaw, I.N. Shpinkov, A.N. Vasilev, Luminescence quenching as a probe for the local density of electronic excitations in insulators. J. Electron Spectrosc. Relat. Phenom. **79**, 147–150 (1996)
25. M.A. Terekhin, A.N. Vasil'ev, M. Kamada, E. Nakamura, S. Kubota, Effect of quenching processes on decay of fast luminescence from barium fluoride excited by VUV synchrotron radiation. Phys. Rev. B **52**, 3117–3121 (1995)
26. R.A. Glukhov, M. Kamada, S. Kubota, E. Nakamura, S. Ohara, M.A. Terekhin, A.N. Vasil'ev, Effect of quenching processes on decay of fast luminescence from BaF_2, in *Proceedings, International Conference on Inorganic Scintillators and Their Applications SCINT95*, (Delft University Press, Delft, 1996), pp. 204–207
27. R.A. Glukhov, A.N. Vasil'ev, C. Pedrini, A. Yakunin, Track effects in crossluminescence, in *Proceedings of the Fifth International Conference on Inorganic Scintillators and Their Applications*, (Faculty of Physics, Moscow State University, Moscow, 2000), pp. 448–453
28. I.A. Markov, A.N. Vasil'ev, V.V. Veselova, Computer simulation of physical processes in scintillators, in *Proceedings of the 8th International Conference on Inorganic Scintillators and Their Use in Scientific and Industrial Applications*, (Alushta, Kharkov, 2005), pp. 7–10
29. A.N. Vasil'ev, V.V. Mikhailin, The role of relaxation through phonon emission in cascade process of multiplication of electronic excitations generated by X-ray quantum. Bull. Acad. Sci. USSR Phys. Ser. **50**, 113–116 (1986)
30. A.N. Vasil'ev, A.V. Gektin, Multiscale approach to estimation of scintillation characteristics. IEEE Trans. Nucl. Sci. **61**, 235–245 (2014)
31. Z. Wang, Y. Xie, B.D. Cannon, L.W. Campbell, F. Gao, S. Kerisit, Computer simulation of electron thermalization in CsI and CsI(Tl). J. Appl. Phys. **110**, 064903 (2011)
32. F. Gao, Y. Xie, S. Kerisit, L.W. Campbell, W.J. Weber, Yield, variance and spatial distribution of electron–hole pairs in CsI. Nucl. Inst. Methods Phys. Res. A **652**, 564–567 (2011)
33. Z. Wang, Y. Xie, L.W. Campbell, F. Gao, S. Kerisit, Monte Carlo simulations of electron thermalization in alkali iodide and alkaline-earth fluoride scintillators. J. Appl. Phys. **112**, 014906 (2012)

34. A.N. Vasil'ev, From luminescence non-linearity to scintillation nonproportionality. IEEE Trans. Nucl. Sci. **55**, 1054–1061 (2008)
35. S. Gridin, A. Belsky, C. Dujardin, A. Gektin, N. Shiran, A. Vasil'ev, Kinetic model of energy relaxation in CsI:A (A=Tl and In) scintillators. J. Phys. Chem. C **119**, 20578–20590 (2015)
36. S. Gridin, A.N. Vasil'ev, A. Belsky, N. Shiran, A. Gektin, Excitonic and activator recombination channels in binary halide scintillation crystals. Phys. Status Solidi B **251**, 942–949 (2014)
37. X. Lu, Q. Li, G.A. Bizarri, K. Yang, M.R. Mayhugh, P.R. Menge, R.T. Williams, Coupled rate and transport equations modeling proportionality of light yield in high-energy electron tracks: CsI at 295 K and 100 K; CsI: Tl at 295 K. Phys. Rev. B **92**, 115207 (2015)
38. R.T. Williams, K.B. Ucer, J.Q. Grim, K.C. Lipke, L.M. Trefilova, W.W. Moses, Picosecond studies of transient absorption induced by bandgap excitation of CsI and CsI:Tl at room temperature. IEEE Trans. Nucl. Sci. **57**, 1187–1192 (2010)
39. T.R. Waite, Theoretical treatment of the kinetics of diffusion-limited reactions. Phys. Rev. **107**, 463–470 (1957)
40. T.R. Waite, General theory of bimolecular reaction rates in solids and liquids. J. Chem. Phys. **28**, 463–470 (1958)
41. V.N. Kuzovkov, E.A. Kotomin, Kinetics of bimolecular reactions in condensed media. Rep. Prog. Phys. **51**, 1479–1524 (1988)
42. A.N. Vasil'ev, V.V. Mihailin, I.V. Ovchinnikova, Influence of electron-hole correlations on luminescence of crystalline phosphors with traps. Moscow Univ. Bulletin. Phys. Astron. **28**, 50–54 (1987). (in Russian)
43. R.T. Williams, J.Q. Grim, Q. Li, K.B. Ucer, W.W. Moses, Excitation density, diffusion-drift, and proportionality in scintillators. Phys. Status Solidi B **248**, 426–438 (2011)
44. Q. Li, J.Q. Grim, K.B. Ucer, A. Burger, G.A. Bizarri, W.W. Moses, R.T. Williams, Host structure dependence of light yield and proportionality in scintillators in terms of hot and thermalized carrier transport. Phys. Status Solidi (RRL) **6**, 346–348 (2012)
45. X. Lu, Q. Li, G.A. Bizarri, K. Yang, M.R. Mayhugh, P.R. Menge, R.T. Williams, Coupled rate and transport equations modeling proportionality of light yield in high-energy electron tracks: CsI at 295 K and 100 K; CsI: Tl at 295 K. Phys. Rev. B **92**, 115207 (2015)
46. G. Bizarri, W.W. Moses, J. Singh, A.N. Vasil'ev, R.T. Williams, An analytical model of nonproportional scintillator light yield in terms of recombination rates. J. Appl. Phys. **105**, 044507 (2009)
47. A. Belsky, K. Ivanovskikh, A. Vasil'ev, M.F. Joubert, C. Dujardin, Estimation of the electron thermalization length in ionic materials. J. Phys. Chem. Lett. **4**, 3534–3538 (2013)
48. V.M. Agranovich, M.D. Galanin, *Electronic Excitation Energy Transfer in Condensed Matter* (North-Holland Pub Co, Amsterdam/New York, 1983), p. 371
49. J.B. Birks, *The Theory and Practice of Scintillation Counting* (Pergamon, New York, 1967).
50. M. Kirm, V. Nagirnyi, E. Feldbach, M. De_Grazia, B. Carre, H. Merdji, S. Guizard, G. Geoffroy, J. Gaudin, N. Fedorov, P. Martin, A. Vasil'ev, A. Belsky, Exciton-exciton interactions in cdwo4 irradiated by intense femtosecond vacuum ultraviolet pulses. Phys. Rev. B **79**, 233103 (2009)
51. S. Chernov, R. Deych, L. Grigorjeva, D. Millers, Luminescence and Transient Optical Absorption in CdWO. Mater. Sci. Forum **239-241**, 299–302 (1997)
52. M. Yokota, O. Tanimoto, Effects of diffusion on energy transfer by resonance. J. Phys. Soc. Jpn. **22**, 779–784 (1967)
53. M.J. Weber, Multiphonon relaxation of rare-earth ions in yttrium Orthoaluminate. Phys. Rev. B **8**, 54–64 (1973)
54. Z. Onderisinova, M. Kucera, M. Hanus, M. Nikl, Temperature-dependent nonradiative energy transfer from Gd^{3+} to Ce^{3+} ions in co-doped LuAG:Ce,Gd garnet scintillators. J. Lumin. **167**, 106–113 (2015)
55. D. Spassky, A. Vasil'ev, A. Belsky, N. Fedorov, P. Martin, S. Markov, O. Buzanov, N. Kozlova, V. Shlegel, Excitation density effects in luminescence properties of $CaMoO_4$ and $ZnMoO_4$. Opt. Mater. **90**, 7–13 (2019)

56. A. Vedda, M. Fasoli, Tunneling recombinations in scintillators, phosphors, and dosimeters. Radiat. Meas. **118**, 86–97 (2018)
57. G. Bizarri, W.W. Moses, J. Singh, A.N. Vasil'ev, R.T. Williams, The role of different linear and non-linear channels of relaxation in scintillator non-proportionality. J. Lumin. **129**, 1790–1793 (2009)
58. W.W. Moses, G.A. Bizarri, R.T. Williams, S.A. Payne, A.N. Vasil'ev, J. Singh, Q. Li, J.Q. Grim, W.–.S. Choong, The origins of scintillator non-proportionality. IEEE Trans. Nucl. Sci. **59**, 2038–2044 (2012)
59. A.N. Belsky, private communication, 26 June 2019
60. S. Gundacker, E. Auffray, K. Pauwels, P. Lecoq, Measurement of intrinsic rise times for various L(Y)SO and LuAG scintillators with a general study of prompt photons to achieve 10 ps in TOF-PET. Phys. Med. Biol. **61**, 2802–2837 (2016)
61. E. Auffray, R. Augulis, A. Borisevich, V. Gulbinas, A. Fedorov, M. Korjik, M.T. Lucchini, V. Mechinsky, S. Nargelas, E. Songaila, G. Tamulaitis, A. Vaitkevičius, S. Zazubovich, Luminescence rise time in self-activated $PbWO_4$ and Ce-doped $Gd_3Al_2Ga_3O_{12}$ scintillation crystals. J. Lumin. **178**, 54–60 (2016)
62. G. Tamulaitis, A. Vaitkevi˘cius, S. Nargelas, R. Augulis, V. Gulbinas, P. Bohacek, M. Nikl, A. Borisevich, A. Fedorov, M. Korjik, E. Auffray, Subpicosecond luminescence rise time in magnesium codoped GAGG:Ce scintillator. Nucl. Instrum. Methods Phys. Res. Sect. A Accel. Spectrom. Detect. Assoc. Equip. **870**, 25–29 (2017)
63. M.H. Du, Chemical trends of electronic and optical properties of ns2 ions in halides. J. Mater. Chem. C **2**, 4784–4791 (2014)
64. P. Dorenbos, Modeling the chemical shift of lanthanide 4f electron binding energies. Phys. Rev. B **85**, 165107 (2012)
65. P. Dorenbos, Charge transfer bands in optical materials and related defect level location. Opt. Mater. **69**, 8–22 (2017)
66. C. Pedrini, C. Dujardin, J.C. Gâcon, A.N. Belsky, A.N. Vasil'ev, A.G. Petrosyan, Cerium-doped fluorescent and scintillating ionic crystals. Radiat. Eff. Defects Solids **154**, 277–286 (2007)
67. G. Tamulatis, A. Vasil'ev, M. Korzhik, A. Mazzi, A. Gola, S. Nargelas, A. Vaitkevičius, A. Fedorov, D. Kozlov, Improvement of the time resolution of radiation detectors based on $Gd_3Al_2Ga_3O_{12}$ scintillators with SIPM readout. IEEE Trans. Nucl. Sci. **66**, 1879–1888 (2019)
68. A. Belsky, K. Lebbou, V. Kononets, O. Sidletskiy, A. Gektin, E. Auffray, D. Spassky, A. Vasil'ev, Mechanisms of luminescence decay in YAG-Ce,Mg fibers excited by γ- and X-rays. Opt. Mater. **92**, 341–346 (2019)
69. M.T. Lucchini, V. Babin, P. Bohacek, S. Gundacker, K. Kamada, M. Nikl, A. Petrosyan, A. Yoshikawa, E. Auffray, Effect of Mg^{2+} ions co-doping on timing performance and radiation tolerance of Cerium doped $Gd_3Al_2Ga_3O_{12}$ crystals. Nucl. Instrum. Methods Phys. Res. Sect. A Accel. Spectrom. Detect. Assoc. Equip. **816**, 176–183 (2016)
70. Y. Wu, F. Meng, M. Qi Li, C.L. Koschan, Melcher, role of Ce^{4+} in the scintillation mechanism of Codoped $Gd_3Ga_3Al_2O_{12}$:Ce. Phys. Rev. Appl. **044009**, 2 (2014)
71. E. Sakai, Recent measurements on scintillator-photodetector systems. IEEE Trans. Nucl. Sci. **34**, 418–422 (1987)
72. A.N. Belsky, A.N. Vasilev, V.V. Mikhailin, A.V. Gektin, N.V. Shiran, A.L. Rogalev, E.I. Zinin, Time-resolved XEOL spectroscopy of new scintillators based on CsI. Rev. Sci. Instrum. **63**, 806–809 (1992)
73. A.V. Gektin, N.V. Shiran, A.N. Belskiy, A.N. Vasil'ev, Fast UV scintillations in CsI-type crystals. Nucl. Tracks Radiat. Meas. **21**, 11–13 (1993)
74. H. Nishimura, M. Sakata, T. Tsujimoto, M. Nakayama, Origin of the 4.1-eV luminescence in pure CsI scintillator. Phys. Rev. B **51**, 2167–2172 (1995)
75. A.N. Belsky, A.N. Vasilev, V.V. Mikhailin, A.V. Gektin, P. Martin, C. Pedrini, D. Bouttet, Experimental-study of the excitation threshold of fast intrinsic luminescence of CsI. Phys. Rev. B **49**, 13197–13200 (1994)

76. A. Belsky, N. Fedorov, S. Gridin, A. Gektin, P. Martin, D. Spassky, A. Vasil'ev, Time-resolved luminescence z-scan of CsI using power femtosecond laser pulses. Radiat. Meas. **124**, 1–8 (2019)
77. D. Spassky, A. Vasil'ev, A. Belsky, N. Fedorov, P. Martin, S. Markov, O. Buzanov, N. Kozlova, V. Shlegel, Excitation density effects in luminescence properties of $CaMoO_4$ and $ZnMoO_4$. Opt. Mater. **90**, 7–13 (2019)
78. K. Tanimura, N. Itoh, Relaxation of excitons perturbed by self-trapped excitons in RbI: Evidence for exciton fusion in inorganic solids with strong electron-phonon coupling. Phys. Rev. Lett. **64**, 1429–1432 (1990)
79. M. Patrick, N. Fedorov, A. Belsky, A.N. Vasil'ev, Free and bound excitons in ZnO at variable excitation density, in *Book of abstracts of the 2018 Europhysical Conference on Defects in Insulating Materials*, (EURODIM 2018, Bydgoszcz, 2018), p. 136

Chapter 4
Shallow Traps in Scintillation Materials

Abstract This chapter is focused on the shallow traps in scintillators with various crystal structures. Even in single crystals of scintillating materials, defects inevitably occur and play an important role in the excitation transfer phenomena. Special attention in this chapter is paid to the consequences of the modulation of the conduction band bottom due to random distribution of the ions in mixed crystals.

4.1 Trapping of Nonequilibrium Carriers in Crystal Matrix

Traps or trapping centers in crystalline material are crystal defects, which can capture nonequilibrium carriers and keep them localized certain time depending on trap properties and temperature. Carriers remain trapped until gaining thermal energy sufficient for escaping from the trap. The carriers can be retrapped, recombine by band-to-band recombination, or reach centers of radiative or nonradiative recombination. The spontaneous localization/delocalization or trapping/detrapping/retrapping processes occur with the participation of phonons in the material. Therefore, temperature is a crucial parameter, which determines the rate of the processes.

Traps are not necessarily associated with defects in the crystal. At low temperatures, trapping centers based on a regular crystal structure might be formed. A typical example is a polaronic centre in a self-activated scintillation material $PbWO_4$. The centre occurs due Jan-Teller distortion of an anionic WO_4^{2-} complex [1–3]. This trap can be as a local distortion defect. Its activation energy 50 meV, thus, it is actually depopulated at temperatures above 50 K.

In the following consideration, we focus on the traps which do not create stable colour centers. Long living color centers drive the crystalline system into a nonequilibrium state, as a fraction of electrons is localized above the Fermi level, and their distribution is nonequilibrium. However, spontaneous relaxation of the color centers by the thermal activation is a quite long process. Therefore, their contribution to the emission of scintillation photons within the time scale of the scintillation decay might be neglected. Though the spontaneous relaxation of colour centres can be accelerated by stimulation by optical photons or by heating of the material (see Ch. 6 in [15]), and the recovery might be reduced from days to

M. Korzhik et al., *Physics of Fast Processes in Scintillators*, Particle Acceleration and Detection, https://doi.org/10.1007/978-3-030-21966-6_4

seconds, the characteristic time constants still remain far from the durations of the processes under consideration below.

Shallow traps are of a particular interest. The term "shallow" requires a special comment. What does it mean in the view of our consideration? The key feature of the shallow trap is the ability for carrier localization for a time, which is short in comparison of the lifetime of the carrier. The time depends on the depth of the traps, which is usually characterized by activation energy E_{TA}. For electron traps, that's the energy separation between the trap level and the bottom of the conduction band and ranged up to several hundreds of meV. For hole trapping center, that's the energy between the energy of the trapping center and the top of the valence band. To be considered as shallow, the trap depth should be comparable with the energy of phonons, usually that of optical phonons in polar crystals, which facilitate the thermal detrapping. The trapping centers, having activation energy between the energy of shallow traps and metastable colour centers, i. e., approximately 0.6–0.7 eV, are responsible for persistent luminescence, which is observed up to hours after excitation [4]. In addition, persistent luminescence and phosphorescence can also occur due to tunneling of trapped carriers, which quite often occurs in crystalline materials [5].

Trap concentration is an important feature for their influence on the dynamics of nonequilibrium carriers. In general, as trapping centers might act various point defects in the crystal structure: ion vacancies, interstitials and their aggregates, isovalent substitution ions including antisite defects, impurity atoms or ions, radiation-induced defects including radioisotopes, etc. The technological efforts are usually targeted to make the trap concentration smaller than the concentration of emitting centers.

Finally, the stability of the traps under irradiation is important. Traps, when based on vacancies or Frenkel type defects (FTD) are subjected to diffusion under the influence of irradiation. In accordance with the profile of the absorbed dose along the detector element, a part of FTDs become recharged, what initiates their movement due to the concentration gradient. Vacancies can reach dislocations inside the crystals and be quenched in their vicinity. Impurity-based defects are less subjected to the diffusion, since a cation vacancy in the vicinity of carier localization is necessary for the diffusion. In addition, irradiation, particularly that by high-energy particles, introduces into the host matrix products of secondary interactions. Besides the knocking-out processes resulting in displacement of atoms from their sites, nuclear reactions generate nuclei fragments, including radioactive ones, which bombard the crystal matrix by their radiation. The cross section for these interactions depends on the energy of incident particle. The lighter the fragment is, the higher is the kinetic energy. The light fragments contribute mostly to the damage of the host matrix. The fragments and recoils create defects, which are similar to those created by incident particles. However, these defects are localized along the trajectories of the particles and fragments, have high local concentration and can interact with each other to produce more stable defects and their clusters. For instance, in PWO crystals, such clusters introduce a local symmetry change and modify the strength of the crystalline field [6]. The deformation of regular WO_4^{2-} oxy-complexes occurs

in the vicinity of the clusters. Since the bottom part of the conduction band of PWO is formed by *d*-orbitals of W^{6+} ion, which are very sensitive to the local crystalline field, the deformation of oxy-anionic complexes in the regular host leads to the removal of *d*-electronic level degeneration. This effect modifies the conduction band edge. At the microscopic level, it corresponds to a reduction of the band gap in the vicinity of clusters. As a consequence, shallow defects can be swept out in the surrounding as well. The same processes occur also in Y- and Lu-based crystals, for which the top of the valence band is mainly populated by oxygen 2*p* states, whereas the bottom of the conduction band is mainly composed of Y and Lu 3*d* and 5*d* states, respectively. Unfortunately, the damage imposed by fragments and knocking off the ions from their positions in the crystal matrix result in production of new vacancies, FTD and interstitials, which have much stronger deterioration effect on the overall scintillation properties.

4.2 Experimental Techniques to Reveal Shallow Traps

Traps activation by external energy input is the basis for the extensively used technique of Thermally Stimulated Luminescence (TSL). TSL is light produced by heating a solid to a temperature below that of incandescence [7]. To observe the light, irradiation of the cooled solid, preferably a transparent medium, by photons with certain energy, not necessarily larger than band gap, is required. Usually, external X-ray source is utilized for this purpose. The heating of the sample under investigation results in thermal ionization of traps with different activation energies, when the thermal energy reaches their activation energy. A practical application of TSL is in radiation dosimetry [8–12]. It has been shown for a few materials subjected to irradiation with ionizing radiation that the sum of the emitted light photons in thermal activation is proportional to the absorbed dose. Study of spectral distribution or integrated spectrum of the emitted photons with temperature is an extremely sensitive method to define the activation energies of traps in a wide range of activation energies.

Heating of the sample causes the release of the trapped nonequilibrium carriers. They have two ways: either the recombination of electrons and holes at a luminescent center or trapping by deeper traps followed by recombination at luminescent center at high temperatures. If the concentration of luminescence centers considerably exceeds the concentration of deep traps, the recombination resulting in luminescence dominates. The simplest model, nevertheless, describing the essential characteristics of TSL, takes into account only one type of luminescence centres. This situation usually occurs in doped scintillation materials, where one of commonly used activator ion (Ce^{3+}, Pr^{3+}, Eu^{2+}) is incorporated in the crystal to be a luminescent centre. The probability of releasing an electron from the trap per unit time p is described by the Arrhenius equation $p = s \cdot \exp.(-E_{TA}/kT)$, where s is the frequency factor, T is temperature, and k is the Bolzman constant. The frequency factor correlates with the mean phonon energy in the crystal and varies in the range

10^{12}–10^{13} s^{-1}. It is assumed that the carrier recombination is a first order process, though it occurs quite rarely. Usually, the carrier transport and recombination are more complicated processes, and an additional parameter reflecting the order of the kinetics is introduced.

The release of electrons to the conduction band is not a single process to observe TSL or change of its spectral distribution. The change of the recombination mechanism can be detected via the change of the spectrum of the photons emitted. A typical example is a trap based on anion vacancy V_o centre (WO_3) in PWO crystal. When an anion vacancy appears in anionic complex, the local symmetry of the new WO_3 complex is reduced from T_d to C_{3v}. The additional low-symmetry component of the crystalline field splits the lowest excited triplet term in two components: upper E_1 and lower $^1A_1$. The ground state is described by term $^1A_1$, so optical transitions are forbidden. At room temperature, both components of the triplet are populated, and green luminescence with maximum at 490 nm is observed due to radiative transition $E_1 \rightarrow {}^1A_1$ in WO_3 complex. At low temperatures, $^1A_1$ component of the $^3T_1$ state accumulates electrons as a trap. Note that due to a relatively narrow band gap, the F^+ centre based on anion vacancy is not stabilised in the $PbWO_4$ structure, thus, only F centres $(WO_3)^{2-}$ capturing an even number of electrons occur. When the temperature is increased, the release of the electrons from $^1A_1$ to upper E_1 state occurs, giving rise to the green luminescence. Contrary to other shallow traps in PWO [13], a few of them, having $E_{TA} = 0.21$, 0.23 and 0.27 eV, demonstrate only green emission after their thermal activation. A deeper trap occurs in the crystal as a result of the displacement of an oxygen ion into an intersite position (FTD). The V_o vacancy created by the Frenkel defect can also capture electrons forming the centre like $(WO_3)^{2-}$ but with stronger splitting of $^3T_1$ level. As a result, $E^1 \rightarrow {}^1A_1$ transition is shifted to the red part of the spectrum. This luminescence is observed at the thermal activation of this colour centre at the temperatures above 400 K.

In general, TSL spectroscopy does not enable distinguishing between the change of the trap concentration and the additional fast recombination channels for nonequilibrium carriers preventing trap population. The change of TSL spectra in GAGG:Ce crystal with a low concentration of codoping by aliovalent ion Mg^{2+} is a typical example. Figure 4.1 shows the comparison of TSL spectra measured in GAGG samples solely doped with Ce and codoped with Mg at the level of 8 ppm. The crystals were grown from the raw material obtained by Solid State Reaction (SSR) of initial charge. The codoping at low concentrations does not change the shape of TSL spectra but reduces TSL intensity by a factor five. As it is known [14], the aliovalent cooping by magnesium creates defect-centers, which introduce a very fast channel for nonradiative recombination. Therefore, the interpretation of the results of TSL measurements is slightly ambiguous: either codoping results in less efficient trapping at the initial stage defect population after irradiation, or it reduces the trap concentration.

Electron Paramagnetic Resonance (EPR) spectroscopy, sometimes also called Electron Spin Resonance, allows for characterization of trap vicinity after a single nonequilibrium carrier is captured by the trap. Combining TSL and EPR data enables more precise interpretation of the results, especially because of high

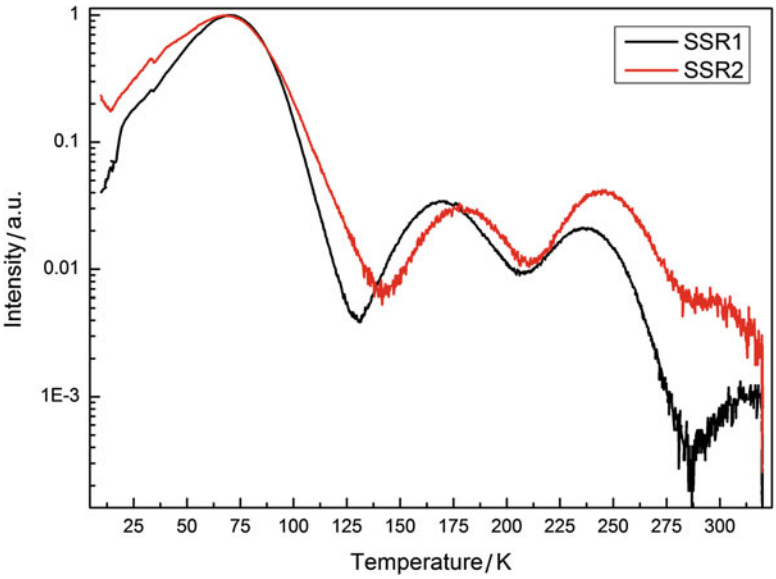

Fig. 4.1 Normalised TSL spectra measured in GAGG:Ce (SSR1), black curve, and GAGG:Ce,Mg (SSR2), red curve. Intensity of the red curve is multiplied by a factor of five. Intensity of luminescence spectrally integrated in the range 450–700 nm is presented

sensitivity of the spin-hamiltonian parameters to the symmetry of the location in the matrix at the position of electron or hole possessing a spin 1/2.

Combining the two methods enabled, for instance, the interpretation of shallow traps in PWO. As mentioned above, the shallowest traps were found to be the polaronic centres. This trap is emptied to the conduction band and finally results in blue intrinsic luminescence. In view of the contribution to the leading edge of scintillation, the most interesting is electron centre WO_4^{3-}, which is created on the basis of a regular tungstate anionic complex perturbed by a nearby rare-earth trivalent impurity ion, like La, Lu or Y [15] (See also Ch.5). It decays at ~97 K and has E_{TA} at ~100 meV.

In PWO crystals with La and Y codoping, the second trap centre is detected through TSL only with an activation energy of 130 meV. This centre is not paramagnetic but, most probably, is also a RE-$(WO_4)^{4-}$ centre. This conclusion is in agreement with the fact that RE-doped PWO crystals exhibit a larger TSL intensity in the vicinity of 100°K, compared to undoped PWO. Electron release from the 130 meV traps causes the simultaneous production of deeper electron centres by retrapping, as well as through the creation of RE-$(WO_4)^{3-}$ giving an increase in TSL intensity in that region.

Besides the defect identification, EPR allows for following the localisation conditions of a single electron. Authors of [16] investigated the localization of F^+ centre in binary garnet $Y_3Al_5O_{12}$ with temperature. The measurements showed that at $T < 50$ K, the EPR spectrum of the F^+ centre is anisotropic with g factors in the

range 1.999–1.988 and originates from three magnetically inequivalent positions of the center. As the temperature increases, the EPR spectrum becomes isotropic due to the motional averaging of the anisotropy: electron becomes sheared between neighboring oxygen vacancies. With further temperature increase above 200 K, delocalization of the F^+ centre electron to the conduction band with the activation energy of 0.4–0.5 eV occurs, what results in substantial spectral narrowing of the EPR line. Such temperature behavior of electron at the F^+ centre in YAG is similar to the behavior of a donor electron in semiconductors. It is supposed to be the first observation of a donor-like behavior of F^+ centre in a garnet crystal.

Nowadays, a direct probing of the shallow traps with infrared (IR) photons was found to be quite effective [17]. Optical stimulation using IR is known for a long time [18] as a useful way for the effective release of trapped electrons. In fact, the method has the same initial phase as in TSL measurements: the sample should be irradiated, and the traps have to be filled at low temperature. The IR stimulation causes the reduction of absorption bands associated with electron traps, results in luminescence and is convenient to probe hidden absorption bands that are caused by low-probability optical transitions. A high intensity, IR source with narrow band width becomes mandatory, since the number of traps, emptied by IR stimulation, depends on the intensity [19]. Fast progress in the development of compact free-electron laser IR sources made possible the visualization of hidden absorption bands due to the optical transitions from the electron trap levels to the conduction band. First results showed that the major trap in GAGG structure have the E_{TA} nearly 0.3 eV.

4.3 Antisite Defects and Related Traps

Another type of the defects, potentially capable to create shallow traps, are antisite defects [20]. In general, they can be expected in the compounds, where at least one of the cations has two localization sites with different coordination. Definitely, the antisite defects cannot occur in the crystals having oxyorthosilicate structure, where atoms of Si are strictly localized in oxygen tetrahedra, and RE ions, depending on their ionic radius, form the structure with possible localization in 6(O) and 7(O) or 7(O) and 8(O) oxygen coordination. On the contrary, garnets create conditions for Y and RE ions to be localized in both 8(O) and 6(O) coordinations. Similarly, perovskites allow the localization of these ions in 12(O) and 6(O) coordinations. Particularly, such distribution of cations is expected for Y and RE with the lowest ionic radii: Lu and Yb [21].

As an example, let us consider the garnet crystal structure YAG, which belongs to cubic space group Ia3d with the cations in spatial positions (on 16a, 24c and 24d sites) and oxygen anions in the general positions (on 96 h sites). Three cations have tetrahedral coordination (24d sites) and two cations have octahedral (16a sites) coordination formed by oxygen ions [22]. The eight-fold coordinate sites (dodecahedral, 24c sites) accommodate yttrium. There are eight formula units in the unit cell

with lattice parameter a = 12.01 Å at ambient conditions. The tetrahedra and octahedra are linked to each other by sharing all oxygen corners, whereas dodecahedra are linked by shared edges. When the crystal is grown from a stoichiometric mixture and part of the Y ions enter octahedral coordination, the cation vacancies in the Y site appear, and, distortion of the coordinating polyhedral occurs. Note, Al ions substitute Y ions in the garnet structure with lower probability.

The ionic radius of Y^{3+} is 1.02 Å for 8(O) coordination. Cerium ion usually replaces Y in the 24c site. The ionic radius of Al^{3+} is 0.53 and 0.39 Å for 6(O) and 4 (O) oxygen coordinations. Introducing the larger Y^{3+} cation into the 16a sites leads to the distortion of the initial crystal structure and modifies bond lengths and angles. The changes in the cation-oxygen interatomic distance and in the bond angle at the conditions of antisite substitution result in considerable lattice strain and lead to the distortion of the polyhedra and, as a consequence, cause the formation of shallow trapping centers. Antisite defects in YAG and LuAG facilitate autolocalization of holes [23]. LuAG single crystalline films demonstrate electron traps arising due to the presence of Lu ions in Al(6) positions. The trap with $E_{TA} = 0.29$ eV was associated with this center. In addition, shallow traps on a base of antisite detects cause tunneling phenomena in the radiative recombination processes in LuAG:Ce single crystals [24]. Antisite defects deteriorate both lasing and scintillation properties [25] and were detected by the existence of satellite 4f–4f emission lines of Er^{3+} and Nd^{3+} due to their localization in octahedral positions [26, 27].

4.4 Shallow Traps in Mixed Crystals

Up to now, we discussed low-concentration traps. At a low activator concentration, the traps located outside the Onsager spheres catch nonequilibrium carriers and slow down their diffusion. Inside the spheres, traps compete with activators for interaction with excitons and, in fact, deteriorate scintillation properties. From that point of view, any technological efforts to diminish the number of shallow traps based on point defects in crystal structure have positive consequences in the improvement of light yield and the decrease of the fraction of slow components in the scintillation.

The situation is drastically different in mixed crystal. Mixed crystals are the new generation of crystalline scintillation materials [15]. Increased diversity of anions and cations in the crystal matrix extends the capabilities for future improvement of the light yield and scintillation kinetics. Among novel materials, oxides, which are chemically stabile and easy for machining, are of particular interest.

The cation mixture in the crystal matrix introduces two important features.

The first feature is the compatible concentration of the mixed cations in the crystal. A typical example of mixed crystals is LYSO, containing, as a rule, 20% of Y and 80% of Lu in the composition. GAGG, having 40% of Al ions in 60% of Ga ions, which are distributed among the octahedral and tetrahedral positions in the garnet matrix, might serve as another example. In a mixed Al-Ga garnet structure, Ga^{3+} ions preferentially occupy tetrahedral rather than octahedral sites. For instance,

according to [22] composition occupancy of Ga^{3+} ions in $Y_3Al_2Ga_3O_{12}$ (YAGG) is 0.727 and 0.409 for tetrahedral and octahedral sites, respectively. In other words, 72.7% of Ga^{3+} ions occupy the tetrahedral sites, whereas 27.3% of them are in octahedral sites. Note that in the case of random distribution, these values should be 60% and 40%. In the gadolinium-gallium-aluminum garnet GGAG the Ga^{3+} ions have substantially greater preference for the tetrahedral site than the Al^{3+} ions in the YAGG garnet.

The ionic radius of Gd^{3+} and Ce^{3+} is 1.05 Å and 1.14 Å for 8(O) coordination, respectively. Ce ions usually replace Gd ions in *24c* site. The ionic radii of Ga^{3+} 0.62 and 0.47 Å for six-fold and four-fold coordination, respectively, are larger than those of Al^{3+}: 0.53 and 0.39, respectively. The introduction of larger Ga^{3+} cations into the YAG crystalline matrix leads to the distortion of the initial crystal structure and modifies bond lengths and angles. For example, cation-oxygen interatomic distance in YAG, 1.754 Å and 1.938 Å for tetrahedral and octahedral sites, respectively, changes to 1.814 Å and 1.955 Å in YAGG, whereas the Ga-O-Al bond angle changes from 130.65° to 128.65°. The crystal lattice becomes stressed, what leads to distortion of the polyhedra, and, as a consequence, to formation of shallow trapping centers.

The second important feature of mixed crystals is a random modulation of the bottom of the conduction band due to random distribution of the cations of different type leading to composition fluctuations.

For instance, in LYSO crystal, the substitution of Lu by Y introduces a minor change of the band structure. The most important change occurs in the bottom of the conduction band. Due to a smaller effective nuclear charge of Y, the band gap in pure Lu_2SiO_5 is smaller than that in Y_2SiO_5. Thus, in the locations containing Lu ions, the conduction band of LYSO has a dip, which might serve as a trapping center for electrons. The difference in the band gap of Y_2SiO_5 (6.4 eV) and Lu_2SiO_5 (6.2 eV) is ~0.2 eV [28, 29]. According to the composition and assuming a linear shift of the band gap with the concentration of the components, the band gap of $Lu_{1.6}Y_{0.4}SiO_5$ can be estimated as 6.24 eV.

The scale of the band gap fluctuations can be estimated as proposed for binary solid solutions in [30]. In this approach, the overlapping of 5d states of yttrium and lutetium with neighbor cations is taken into account. Figure 4.2 (left panel) shows the energy dependence of the density of states (DOS) in the conduction band without localized states created by the random distribution of the Y and Lu cations, the distribution of the bottom of the conduction band due to spatial fluctuations of the components, and the total DOS. The spatial profile of the bottom of the conduction band is illustrated on the right panel of Fig. 4.2. Ions Lu^{3+} and Y^{3+} are distributed randomly. Assuming that the percolation level for electrons (the energy sufficient to move through the crystal without tunneling through barriers) corresponds to the mean value of the bottom of the conduction band $<E_g>$, the typical depth of the traps due to random distribution of Y and Lu cations without any additional correlation is estimated to vary from 20 to 40 meV. Thus, the localized states might have a significant impact on the carrier migration in LYSO.

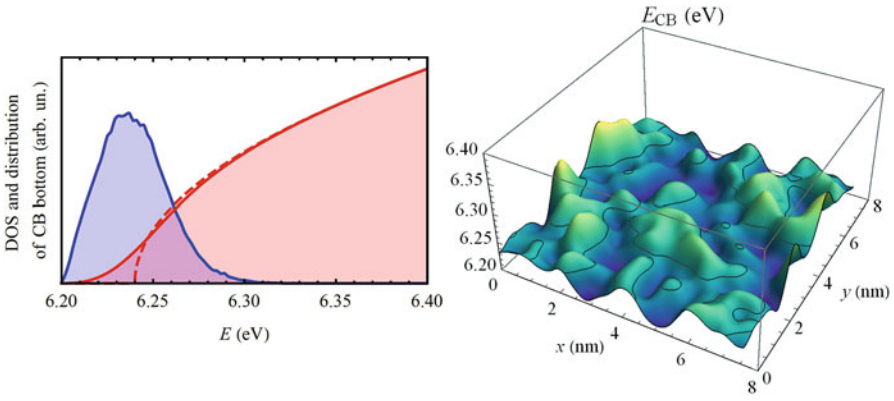

Fig. 4.2 Left panel: the energy dependence of the density of states (DOS) in the conduction band without localized states taken into account (green dashed curve), the distribution of the bottom of the conduction band due to spatial fluctuations of Lu and Y (grey solid line), and the total DOS (yellow solid line). Right panel: a typical profile of the spatial distribution of the bottom of the conduction band; the estimated percolation level is shown by the contour on this plot

Both, the lattice distortion and the band gap bottom modulation produce variety of shallow traps randomly distributed over the crystal matrix. Obviously, this imperfection cannot be removed in mixed crystals by any technological means, it is an intrinsic property of the mixed crystal.

Shallow traps in the mixed GAGG crystals solely doped with Ce and codoped with a small concentration of Mg were investigated in [31]. It was shown that the dominating TSL peak is formed by several traps, as seen in Fig. 4.3. The shape of the TSL band and structure of the traps are practically not changed after a small concentration of Mg is introduced into the matrix at the crystal growth. The intensity of a broad band with the complex structure and a peak in the vicinity of 75 K dominates over the other high temperature bands by a factor of ~50. The same dominating peak is observed in the samples produced from coprecipitated raw material. In addition, a set of weak TSL bands over 100 K with $E_{TA} = 0.13$ eV (175 K) and 0.18 eV (250 K) is detected in all samples, independently of the way the raw material is produced. Only the TSL glow peaks located above 300 K are affected by the peculiarities of growth technology [32]. Thus, the glow peaks with the maxima near 75, 175 and 250 K were concluded to be caused by intrinsic shallow traps.

The intentional selection of the composition of mixed crystal might be exploited to eliminate shallow traps based on point defects [33]. This approach is usually referred to as band gap engineering. However, the band gap engineering might introduce intrinsic shallow traps of another kind. The traps fill the Onsager spheres around activator ions and might have concentrations exceeding the cerium concentration in the crystal. On the one hand, as discussed in more detail in the next section, the intrinsic imperfections reduce the thermalization length of nonequilibrium carriers. This is in favor for keeping a larger fraction of geminate

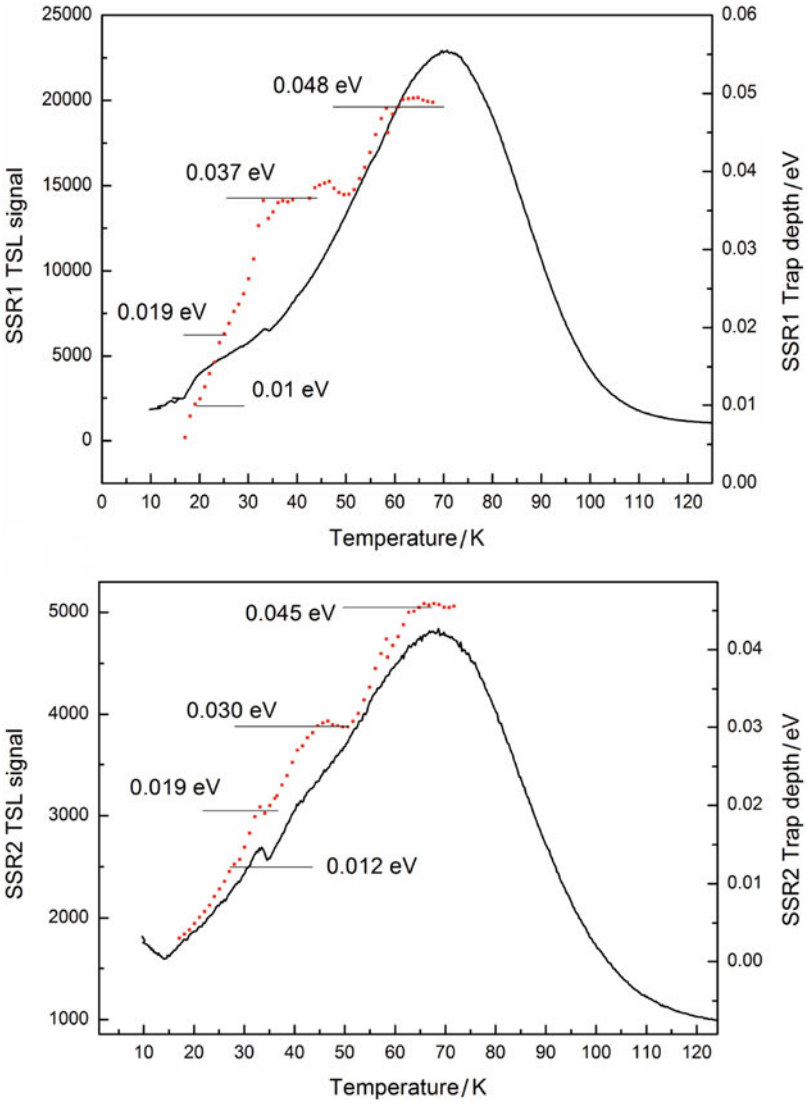

Fig. 4.3 TSL spectra measured with in GAGG:Ce (sample SSR1), upper panel, and GAGG:Ce,Mg (SSR2), lower panel. Intensity of luminescence spectrally integrated in the range 450–700 nm is presented. Red curves indicated E_{TA} points [31]

pairs together and, as consequence, creates conditions for light yield improvement. On the other hand, as will be shown in next Chapter, even short time trapping at the numerous imperfections leads to a less steep leading edge of scintillation response and results in deterioration of the time resolution of the detector. Capturing by

intrinsic shallow traps can be prevented by cooping in mixed crystals [34]. It is worth noting that in the temperature range studied, the TSL spectra of Mg -codoped GAGG:Ce crystal become hardly resolvable already at a Mg concentration of 50 ppm. This is an indication that the sample is overcodoped, resulting in effective prevention of nonequilibrium carrier trapping at shallow intrinsic traps. However, the codoping simultaneously reduces the light yield of the material and, consequently, deteriorates the detector time resolution, though in a different way. Therefore, the optimization of codoping concentration becomes a challenging technological task for each mixed material.

4.5 Thermalization Length of Nonequilibrium Carriers in Mixed Crystals

In previous sections, we pointed out that mixed crystals have substitutional disorder, i.e., the same sites can be occupied by matrix building ions of different types. In the case of substitutional solid solutions of two compounds which differ only in cations, this disorder effectively changes the potential experienced by the electrons moving in the conduction band. For simplicity, let us consider solid solution of two compounds of the same structural class AC and BC: $A_xB_{1-x}C$, where A and B are cations and C is anion or even an oxyanionic complex. Let us assume that the electronic structures of AC and BC differ from each other, and the difference exists for both core and conduction band states. It is well-known that the dependence of energy of electron in conduction band on wavevector strongly deviates from that in free electron parabolic band approximation. These deviations are due to the interaction of electron wave packets with potential of ions (including inner electrons). Assuming that AC and BC are ideal crystalline compounds, he elastic scattering of electrons on this regular periodic potential results in Bragg scattering of electrons from atomic surfaces, in formation of wavefunctions, whereas the energy dispersion law is different from that in empty lattice. In other words, the electron wavevector is a good quantum number in such ideal crystals, if the energy is described by complex dispersion law $E(\mathbf{k})$, and $\mathbf{k}$ is within the first Brillouin zone. If there is no disorder, $\mathbf{k}$ is conserved, and electron moves through the crystal with a constant velocity $\hbar^{-1} dE(\mathbf{k})/d\,\mathbf{k}$. If there is any disorder (for example, the presence of impurity ions), $\mathbf{k}$ changes in scattering events, thus, the transport mean free path due to this scattering has to be introduced. The scattering exists even in ideal crystals, if the thermal motion of the ions in the lattice is taken into account. The well-known electron phonon scattering is an example for this type of scattering on dynamic potential. The phonon scattering results in carrier thermalization as discussed in detail in Chap. 3. The stronger the scattering, the shorter the thermalization length for hot carriers. In disordered systems, where A and B ions are distributed over sites in a random way, the elastic scattering results in additional change of the electron wavevector $\mathbf{k}$ in the conduction band (and, therefore, the direction of its

motion). The electron energy is conserved in scattering of this type, so the thermalization rate is defined only by electron-phonon interaction, but the thermalization length becomes shorter.

Figure 4.2 in previous section demonstrates the result of simulation of the bottom of the conduction band in LYSO crystal. This calculation is performed taken account of only the smooth part of the difference between pseudopotentials of Lu and Y ions which spread over the nearest cation sites. The distribution of Lu and Y ions are supposed to be random. The bottom of the conduction band can be considered as modulated in space. This means that the kinetic energy of an electron moving through such potential is also not constant. Moreover, if the electron energy is small enough and falls into the region of conduction band bottom fluctuations, the motion is restricted in space and has features of percolation or even localization (trapping).

If we take into account that the energy of a cation depends on how many cations surround this cation, the distribution of different types of cations over sites becomes pseudorandom, instead of being purely random. Namely, if the energy of AA or BB pair formation (U_{AA} and U_{BB}, correspondingly) is smaller than the energy of AB pair formation U_{AB}, the presence of similar pairs in the close vicinity is preferable. On the one hand, minimization of free energy results in the possibility of formation of regions (clusters) enriched by cations of the same type. On the other hand, if the formation of AB pair is preferable, regions of regular superlattices like ABC_2 appears in the substitutional solid solutions [35]. The results of simulation of the conduction band bottom fluctuations is presented in Fig. 4.4. The simulation is performed for $W \equiv \exp(-U_{AA}/k_B T_{sim}) = 0.2$, 1, and 5 (from top to bottom), $U_{AA} = U_{BB} = -U_{AB}$ for two values of compound content $x = 0.125$ and $x = 0.5$. Here, T_{sim} is the 'temperature' used for simulation, the difference between band gaps of crystals AC and BC was used to be $\Delta E_g = 1$ eV. The middle row is for the case without the correlated incorporation of AA and BB pairs in the matrix, whereas the top row shows the case of AB correlation, and bottom row represent the results for strong AA and BB correlation. Figure 4.4 demonstrates, that for strong AA correlation, clusters of AC type appear, and the bottom of the conduction band fluctuates within $\Delta E_g = 1$ eV even for relatively low x. On the contrary, for strong AB correlation, the fluctuations have a low amplitude, the deviations of the bottom of the conduction band from the middle value $x\Delta E_g$ are also small.

The intensity of electron scattering at such fluctuations is obviously quite different in these three cases. For electrons with energy above the maximum of fluctuations, the transport mean free path can be calculated using Born approximation, and inverse value of it $\lambda^{-1}_{disorder,tr}$ is proportional to the integral of the structure factor for distribution of A ions over the sites and formfactor of the scattering potential of one A ion. The results of calculations of the inverse mean free path are presented in Fig. 4.5. The strongest scattering is observed evidently for the case of clusterization of solid solution $W = 5$, and $\lambda_{disorder,\,tr}$ can compete with the transport mean free path for phonon scattering on. The values presented in Fig. 4.5 are underestimated, since only the smooth part of the difference of pseudopotentials of A and B ions is used in

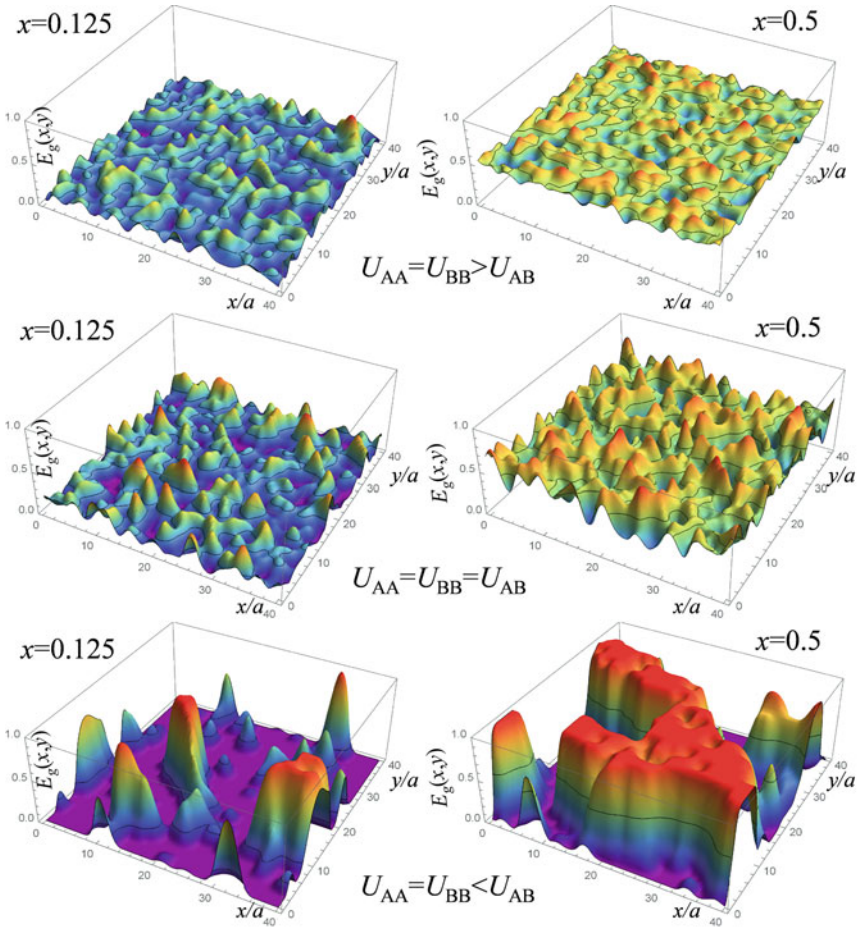

Fig. 4.4 2D cross-section of the pseudopotential profile of the bottom of the conduction band for different energies of formation of AA and AB pairs for $x = 0.125$ (left column) and $x = 0.5$ (right column) in substitutional solid solution $A_xB_{1-x}C$ at $\Delta E_g = 1$ eV. Solid lines correspond to the position of $x\Delta E_g$

the simulation. If the scattering due to the interaction with deeper electrons in the ion is taken into account, the scattering formfactor is much larger, and, consequently, the mean free path determined by disorder and, therefore, the thermalization length are significantly shorter. The dependence of $\lambda^{-1}_{disorder,tr}$ on crystal composition is close to $x(1 - x)$, except for the case of AB correlation.

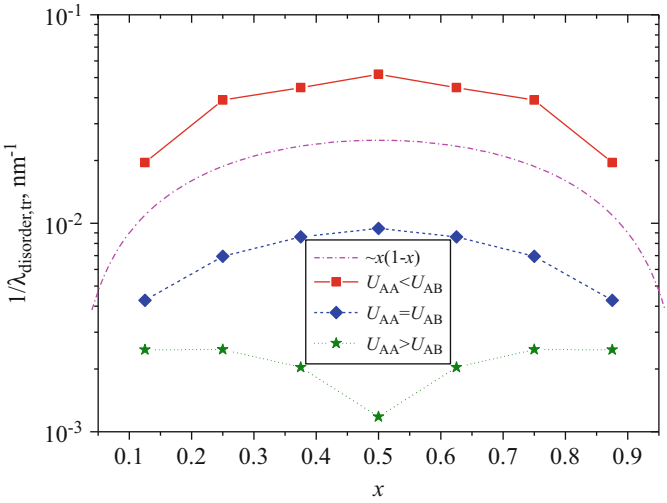

Fig. 4.5 Inverse mean free path for hot electrons with kinetic energy 0.5 eV for scattering on fluctuations of the pseudopotential in substitutional solid solutions as a function of the mixed crystal composition x for three values of affinity parameter $W \equiv \exp(-U_{AA}/k_BT_{sim})$: 5 (red), 1 (blue), and 0.2 (green). Dashed curve corresponds to the function proportional to $x(1-x)$

For small W (the lowest curve in Fig. 4.5) the inverse mean free path has even a peak at $x = 0.5$, since the ordered phase ABC_2 is formed in the substitutional solid solution.

For the electron energy smaller than the potential fluctuations, electrons can be captured within the potential wells formed by the fluctuations. The result can be twofold. In the case when the electron thermalization length is smaller than the average spatial size of the wells, the electrons cannot escape from the geminate holes and, therefore, the recombination is more probable and proceeds faster, since the electron diffusion is spatially restricted. On the other hand, for longer thermalization lengths, electron and hole can occur in different potential wells, and the returning of the electron to geminate hole is more complicated and, obviously, longer. This difficulty of the recombination reduces the light yield and simultaneously diminishes the contribution of the decay components with intermediate characteristic time (longer than the radiative recombination time at emission centers). Therefore, the role of disorder in the case of strong correlation can be controversial. It should be noted that, contrary to the scattering of electrons with higher energy, the concentration dependence of the confinement effects is not symmetric around $x = 0.5$. For instance, for the case of $x = 0.125$ and high W (bottom left panel in Fig. 4.4), the bottom of the conduction band is predominantly flat with a few peaks resulting in strong electron scattering. For the same W and $x = 0.875$, dips occur instead of the peaks, thus, producing a lot of traps. This asymmetry of the features of the conduction band bottom fluctuations is often revealed in the experimental observation that the light yield of scintillating solid solutions has its peak at $x = 0.3$ or $x = 0.7$, instead of $x =$ the 0.5 in symmetrical case [36].

4.6 Prospect for Composition Engineering in Scintillators Based on Mixed Crystals

The success with many mixed crystalline systems to develop better scintillation materials encourages attempts to increase the diversity of ions in such matrices. Are even more impressive scintillation properties in crystalline systems combining more than two ions in the matrix expected? As discussed in previous section, the optimal mixing should provide the modulation of the conduction band bottom without deep dips in the bottom landscape. This can be achieved by mixing both cations and anions.

The ion mixing in crystalline material and the resulting disorder introduces a positive effect, first of all, on the light yield of the scintillation material and on the light collection in the scintillation element.

First, we note a weaker self-absorption in the doped scintillation material. A variety of positions for localization of luminescent ions in the mixed crystals occurs. Geometrical and symmetrical nonequvalence for the localization positions is caused by distortions of the coordinating polyhedra and their bond angles. The variety causes an inhomogeneous broadening of spectral lines, results in widening of the luminescence bands and, in many cases, increases the Stokes shift. Particularly, this is important for Eu^{2+}-doped crystals. Mixing of Br and I in BaBrI:Eu crystal allows for increasing the Stokes shift up to 0.4 eV, i.e., just lightly less than the Stokes shift of Ce^{3+} emission in $LaBr_3$ crystal. These results ecourage the attempts to use Eu^{2+}-doped crystals with the same volume as lanthanum bromide but ensuring a better energy resolution.

Second, as discussed in Ch.2, high amplitude of the scintillation pulse is preferable for better timing properties of scintillation detector. Optimal combining of anions in the mixed crystals allows significant improvement of the light yield, while keeping the scintillation decay at the same level. Mixture of Br and I in BaBrI:Eu compound [37] enables reaching the light yield of up to 97,000 ph/MeV, whereas mixing of F and Cl with Br or I results in the light yield bellow 60,000 ph/MeV. On the contrary, Cl admixture in the well-known $LaBr_3$:Ce scintillator [38] at the content corresponding to 34% of $LaCl_3$ and 66% of $LaBr_3$ resulted in the increase of the light yield by 38%.

Moreover, the increase of the probability for electrons and hole to stay in geminate pairs and form excitons by appropriate ion mixing leads to a gain in the light yield in conventional scintillators used for decades. In ionic crystals [39], the substitution of I by Br accelerates the self-activated scintillator CsI decay kinetics and increases the light output of the mixed crystal. Due to the disorder in the mixed crystal, the luminescence band becomes broader and its peak is shifted to the long-wavelength side. Moreover, the scintillation decay becomes shorter than 5 ns, and the crystal exhibits the scintillation light yield substantially better than that in cross-luminescent crystal BaF_2.

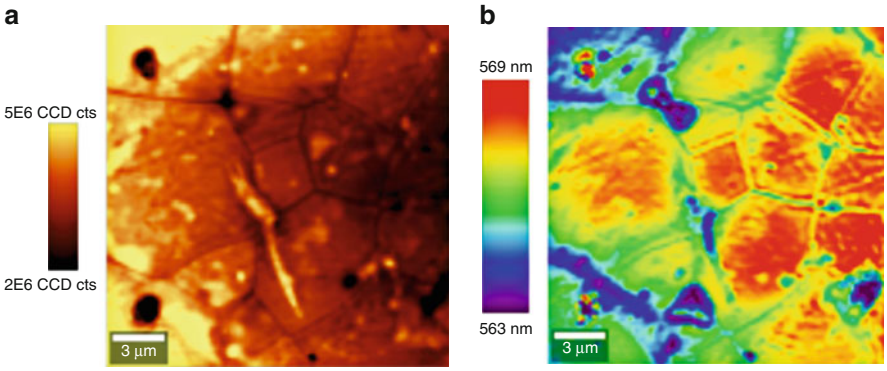

Fig. 4.6 Images of spatial distributions of the spectrally-integrated luminescence (**a**) and the peak position of luminescence band (**b**) in GdYAGG:Ce ceramics obtained with confocal microscope at excitation with He-Cd laser (442 nm). Measurements were performed at room temperature

Replacing a fraction of Gd by Y and Gd by Lu in garnet-structure ceramics in $(Gd_x\text{-}Y_{1\text{-}x})_3Al_2Ga_3O_{12}$ (GdYAGG) [40] and $(Gd,Lu)_2(Ga,Al)_5O_{12}$:Ce (GLuGAG) [41] results in increase of the light yield to 50,000 and 45,000 ph/MeV, respectively. However, no shortening of the scintillation kinetics was observed. Obviously, the dilution of Gd by Y or Lu in the crystalline material increases disorder and, consequently, decreases the average scattering length of nonequilibrium carriers, and results in an increase in the light yield. Meanwhile, the scintillation kinetics is practically not changed and has characteristic decay constants of ~100 ns. In codoped ceramic materials, a homogeneous distribution of aliovalent ions, which pretty good works in single crystals, is a hard technological task. There is a risk of segregation of the codoping ions at the crystallite boundaries in the ceramics. The pre boundary area of the crystallites is strongly stressed. The shape and peak position of the luminescence band due to ion emission is a good indicator for the lattice stress in the vicinity of the boundaries between grains. The radiating state of Ce^{3+} is a *d*-type electronic level, which is very sensitive to the strength of the local crystal field. Figure 4.6 shows images of the spatial distributions of spectrally-integrated luminescence (a) and the peak position of luminescence band in GdYAGG:Ce ceramics obtained with confocal microscope [42]. The grains and intergrain boundaries are evident in the images. The luminescence band is blueshifted from the areas near boundaries due to a change crystal field in their vicinity.

An increase in the codopant concentration to get a more homogeneous distribution in the volume of the ceramics might result in light yield deterioration, similarly to that in the single crystals. The migration of the nonequiliblium carriers and excitons through the intergrain space is still unexplored. Additional trapping is expected, so the gain in the light yield in such ceramics can be accompanied by expanding of the leading edge of the scintillation response. Technological efforts to obtain single crystalline GdYAGG and GdLuAGG to exploit improvements by codoping with a low concentration of aliovalent ions promises additional benefits to improve energy and time resolutions.

References

1. M. Bom, F. Henecker, A. Hofstaetter, et al., Shallow electron traps in the scintillator material PbWO4 to thermally stimulated luminescence, in *Proceedings of the International Workshop on Tungstate Crystals*, (Rome, 1998), pp. 139–146
2. M. Böhm, F. Henecker, A. Hofstaetter, et al., Electron traps in the scintillator material $PbWO_4$ and their correlation to the thermally stimulated luminescence. Radiat. Eff. Defects Solids **150**, 413–417 (1999)
3. V.V. Laguta, J. Rosa, M.I. Zaritski, et al., Polaronic WO_4^{3-} centers in $PbWO_4$ single crystals. J. Phys. Condens. Matter **10**, 7293–7302 (1998)
4. K.V. den Eechout, A. Bos, D. Poelman, P. Smet, Revealing trap depth distribution in persistent phosphors. Phys. Rev. B **87**, 045126 (2013)
5. A. Vedda, M. Nikl, M. Fasoli, E. Mihokova, J. Pejchal, M. Dusek, G. Ren, C.R. Stanek, K.J. McClellan, D.D. Byler, Thermally stimulated tunneling in rare-earth-doped oxyorthosilicates. Phys. Rev. B Condens. Matter Mater. Phys. **78**, 1–8 (2008)
6. E. Auffray, M. Korjik, Limits of inorganic crystalline materials to operate in a high dose rate irradiation environment at collider experiments. IEEE Trans. Nucl. Sci. **63**, 552–563 (2016)
7. A.J.J. Bos, Thermoluminescence as a research tool to investigate luminescence mechanisms. Materials **10**, 1357–1378 (2017)
8. K.V.R. Murthy, Thermoluminescence and its applications: A review. Defect Diffus. Forum **347**, 35–73 (2013)
9. F. Daniels, C. Boyd, D. Saunders, Thermoluminescence as a research tool. Science **117**, 343–349 (1953)
10. A.J.J. Bos, Theory of thermoluminescence. Radiat. Meas. **41**, 45–56 (2006)
11. S.W.S. McKeever, *Thermoluminescence of Solids* (Cambridge University Press, Cambridge, 1988)
12. R. Chen, V. Pagonis, J.L. Lawless, Evaluated thermoluminescence trapping parameters-What do they really mean? Radiat. Meas. **91**, 21–27 (2016)
13. A. Annenkov, M. Korzhik, P. Lecoq, Lead tungstate scintillation material. Nucl. Instrum. Meth. Phys. Res. A **490**, 30–50 (2002)
14. E. Auffray et al., Excitation transfer engineering in Ce-doped oxide crystalline scintillators by codoping with alkali-earth ions. Phys. Status Solidi A **215**, 1700798 (2018)
15. M. Korzhik, P. Lecoq, A. Gektin, *Inorganic Scintillators for Detector Systems* (Springer, Cham, 2016)
16. V. Laguta, M. Buryi, S. Tkachenko, P. Arhipov, I. Gerasymov, O. Sidletskiy, M. Nikl, Oxygen-vacancy centers in $Y_3Al_5O_{12}$ garnet crystals: Electron paramagnetic resonance and dielectric spectroscopy study, Arxiv:1812.11873
17. M. Kitara, H. Zen, K. Kamada, et al., Visualizing hidden electron trap levels in $Gd_3Al_2Ga_3O_{12}$: Ce using a mid-infrared free-electron laser. Appl. Phys. Lett. **112**, 031112 (2018)
18. W. Kuang, M. V. Fock, Luminescence Centers in Crystals, ed. by N.G. Basov (Consultants Bureau, New York/London, 1976), p. 40
19. M.V. Fok, Luminescence problem. J. Sov. Laser Res. **4**, 145–178 (1983)
20. M. Nikl, E. Mihokova, J. Pejchal, A. Vedda, Y. Zorenko, K. Nejezchleb, The antisite LuAl defect-related trap in $Lu_3Al_5O_{12}$: Ce single crystal. Phys. Status Solidi **242**, R119–R121 (2005)
21. R.D. Shannon, Revised effective ionic radii and systematic studies of interatomic distances in galides and chalcogenides. Acta Crystallogr. **32**, 751–767 (1976)
22. A. Nakatsuka, A. Yoshiasa, T. Yamanaka, Cation distribution and crystal chemistry of $Y_3Al_{5-x}Ga_xO_{12}$ ($0 \leq x \leq 5$) garnet solid solution. Acta Crystallogr. Sect. B: Struct. Sci. **55**, 266–272 (1999)
23. V. Laguta, M. Buryi, J. Pejchal, V. Babin, M. Nikl, Hole self-trapping in $Y_3Al_5O_{12}$ and $Lu_3Al_5O_{12}$ garnet crystals. Phys. Rev. Appl. **10**, 034058 (2018)
24. M. Nikl, A. Vedda, M. Fasoli, I. Fontana, V.V. Laguta, E. Mihokova, J. Pejchal, J. Rosa, K. Nejezchleb, Shallow traps and radiative recombination processes in $Lu_3Al_5O_{12}$: Ce single crystal scintillator. Phys. Rev. B **76**, 195121 (2007)

25. M. Nikl, V. Laguta, A. Vedda, Complex oxide scintillators: Material defects and scintillation performance. Phys. Status Solidi B **245**(9), 1701–1722 (2008)
26. M.K. Ashurov, Y.K. Voronko, V.V. Osiko, A.A. Sobol, M.I. Timoshechkin, Spectroscopic study of stoichiometry deviation in crystals with garnet structure. Phys. Status Solidi A **42**, 101–110 (1977)
27. V. Lupei, A. Lupei, C. Tiseanu, S. Georgescu, C. Stoicescu, P.M. Nanau, High-resolution optical spectroscopy of YAG:Nd: A test for structural and distribution models. Phys. Rev. B **51**, 8–17 (1995)
28. A. Lempicki, J. Glodo, Ce-doped scintillators: LSO and LuAP. Nucl. Inst. Methods Phys. Res. A **416**, 333–344 (1998)
29. V.V. Laguta, M. Nikl, S. Zazubovich, Photothermally stimulated creation of electron and hole centers in Ce^{3+}-doped Y_2SiO_5 single crystals. Opt. Mater. (Amst). **36**, 1636–1641 (2014)
30. A. Belsky, A. Gektin, S. Gridin, A.N. Vasil'ev, Electronic and optical properties of scintillators based on mixed ionic crystals, in *Engineering of Scintillation Materials and Radiation Technologies*, (Springer, Cham, 2017), pp. 63–82
31. M. Korzhik, V. Mechinsky, E. Tratsiak, G. Dosovitskiy, P. Sokolov, V. Alenkov, O. Buzanov, A. Fedorov, L. Grigorjeva, A. Zolotarjovs, V. Dormenev, A. Dosovitskiy, D. Agrawal, T. Anniyev, M. Vasilyev, V. Khabashesku, Nanoengineered $Gd_3Al_2Ga_3O_{12}$ scintillation materials with disordered garnet structure for novel detectors of ionizing radiation. Cryst. Res. Technol. **54**, 1800172 (2019)
32. E. Auffray, R. Augulis, A. Borisevich, V. Gulbinas, A. Fedorov, M. Korjik, M.T. Lucchini, V. Mechinsky, S. Nargelas, E. Songaila, G. Tamulaitis, A. Vaitkevičius, S. Zazubovich, Luminescence rise time in self-activated $PbWO_4$ and Ce-doped $Gd_3Al_2Ga_3O_{12}$ scintillation crystals. J. Lumin. **178**, 54–60 (2016)
33. M. Fasoli, A. Vedda, M. Nikl, C. Jiang, B.P. Uberuaga, D.A. Andersson, K.J. McClellan, C.R. Stanek, Band-gap engineering for removing shallow traps in rare-earth $Lu_3Al_5O_{12}$ garnet scintillators using Ga^{3+} doping. Phys. Rev. B: Condens. Matter Mater. Phys. **84**, 1–4 (2011)
34. G. Tamulaitis et al., Improvement of the time resolution of radiation detectors based on Gd3Al2Ga3O12 scintillators with SiPM readout. IEEE Trans. Nucl. Sci. **66**, 1879–1888 (2019)
35. A. Belsky, A. Gektin, A.N. Vasil'ev, Influence of disorder in scintillating solid solutions on thermalization and recombination of electronic excitations, Phys. Status Solidi B, submitted in 2019
36. A.V. Gektin, A.N. Belsky, A.N. Vasil'ev, Scintillation efficiency improvement by mixed crystal use. IEEE Trans. Nucl. Sci. **61**, 262–270 (2014)
37. Z. Yan, T. Shalapska, E.D. Bourret, Czochralski growth of the mixed halides BaBrCl and BaBrCl:Eu. J. Cryst. Growth **435**, 42–45 (2016)
38. U.S. Pat. No. 7,084,403 General Electric Company, Scintillator compositions, and related processes and articles of manufacture A.M. Srivastava
39. L. Swiderski, M. Moszynski, A. Nassalski, A. Syntfeld-Kazuch, W. Czarnacki, W. Klamra, V.A. Kozlov, Scintillation properties of undoped CsI and CsI doped with CsBr. IEEE Trans. Nucl. Sci. **55**, 1241–1245 (2008)
40. A. Giaz, G. Hull, V. Fossati, N. Cherepy, F. Camera, et al., Preliminary investigation of scintillator materials properties: SrI_2: Eu, $CeBr_3$ and GYGAG: Ce for gamma rays up to 9 MeV. Nucl. Inst. Methods Phys. Res. A **804**, 212–220 (2015)
41. J. Glodo, Y. Wang, R. Shawgo, C. Brecher, R.H. Hawrami, J. Tower, K.S. Shah, New developments in scintillators for security applications. Phys. Procedia **90**, 285–290 (2017)
42. A. Vaitkevicius, M. Korjik, E. Tretyak, E. Trusova, G. Tamulaitis, Photoluminescence of barium and lithium silicate glasses and glass ceramics doped with rare earth ions. Int. J. Mater. Metallurgical Eng. **10** (2016)

Chapter 5
Free Carrier Dynamics in Scintillation Materials

Abstract This chapter presents a review of the current results on the carrier dynamics in activated and self-activated scintillators, which are obtained by using time-resolved photoluminescence spectroscopy and differential optical absorption techniques with time resolution in picosecond and subpicosecond domains. The optical techniques ensuring a high time resolution are introduced. The formation of the luminescence response to a short-pulse excitation is in a special focus. The importance of carrier trapping, peculiarities of the trapping in mixed garnet- and orthosilicate-type scintillators, and the influence of codoping on excitation transfer are discussed in more detail.

5.1 Experimental Techniques

5.1.1 Time-Resolved Luminescence Spectroscopy

Time-resolved luminescence spectroscopy is the most straightforward way to study the kinetics of scintillator response. The simplest technique to measure the kinetics is direct measurement of the light emitted by the excited scintillator by using a fast photodetector (see reviews on photodetectors, e.g., in [1]). Photomultipliers (PMTs) can be exploited for such measurements. They are sensitive but need high voltages to ensure strong amplification and have to be vacuumed to avoid scattering of the electrons accelerated in the device. Avalanche photodiodes have also good time characteristics and are more compact solid-state devices. Recently, the development of silicon photomultipliers (SiMP) exhibits tremendous improvement of detecting properties [2–5]. Recently, the photodetection efficiency of SiPMs was substantially improved and the dark count rate and jittering were reduced by introduction of High Density (HD) [6] and Ultra High Density (UHD) [7] devices.

Streak camera is a convenient optoelectronic device for time-resolved luminescence spectroscopy. A sketch of the device is presented in Fig. 5.1. The light to be studied is transformed into photoelectrons, which are accelerated to fluorescent screen and deflected by applying a linearly increasing transversal electric field. The intensity of the fluorescence excited by the electrons reflects the intensity of

M. Korzhik et al., *Physics of Fast Processes in Scintillators*, Particle Acceleration and Detection, https://doi.org/10.1007/978-3-030-21966-6_5

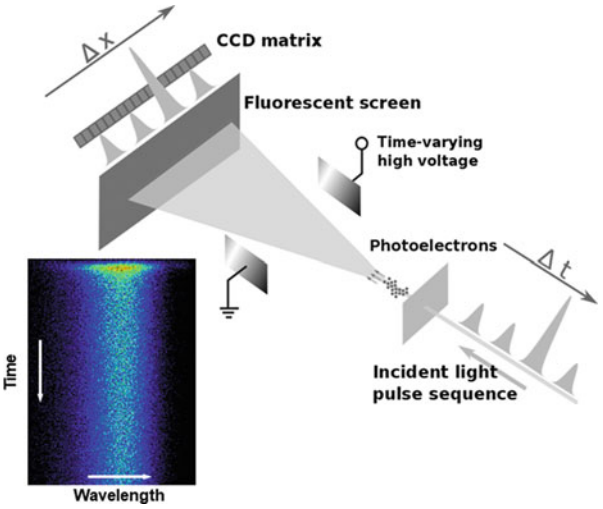

Fig. 5.1 Layout of the deflector transforming the evolution of the optical signal in time to a spatial intensity profile in streak camera. In the inset: a typical streak camera data image showing the intensity dependence on time and wavelength

initial light, whereas the variation of the light intensity in time is transformed into spatial profile of the fluorescence intensity. The profile is recorded by an array of photodetectors. Charge-coupled devices (CCDs) are usually exploited for the read-out. The system forming the spatial imaging of time profile is coupled in the streak camera with a spectrometer deflecting the incident light in perpendicular direction proportionally to its wavelength. As a result, the photoelectrons form a 2D image on the fluorescence screen. The image is red out by a 2D CCD matrix. The intensity distribution of the image provides the distribution of the luminescence signal studied both in time and in wavelength. A typical streak camera image is presented in Fig. 5.1.

Streak cameras can be operated in two modes: single sweep and synchroscan. In single sweep mode, the optical signal triggers the ramp voltage on the deflection electrodes. Thus, the camera can operate in a single shot regime or at frequencies up to 10^5 Hz. The high frequencies are good for averaging the signal repeatedly collected from many pulses. A typical time range in the measurement is from tens of picoseconds to tens of miliseconds. The time resolution in this regime is limited predominantly by the jitter of the trigger pulse. In synchoscan mode, a high-frequency sine-wave voltage is synchronized with the optical signal and is permanently applied to the deflection electrodes. This mode is useful for measurements with a high signal-to-noise ratio in a measurement time range from several hundreds of picoseconds to a few nanoseconds. This operation mode ensures a higher, subpicosecond time resolution.

The time resolution of the streak camera is limited by the instrumental function, which depends on the design and operation mode of the camera. In time-resolved photoluminescence measurements, the net time resolution might be also limited by the pulse duration of the laser used for photoexcitation. Usually, a laser emitting pulses shorter than the instrumental function of the camera is exploited.

A subpicosecond time resolution can be achieved in the systems for time-resolved photoluminescence spectroscopy based on up-conversion. Sum-frequency generation in nonlinear crystal is exploited in such system. The luminescence light under study and a high-power short laser pulse are directed to an appropriate nonlinear crystal. When both pulses coincide in space and time, a signal at the sum-frequency is generated in the crystal. As the delay between the light pulse under study and the laser pulse is changed, the intensity of the sum-frequency signal reflects the time evolution of the light pulse. The intensity of the sum-frequency signal depends on the crystal properties and the product of powers of both pulses. Thus, the up-conversion efficiency might be enhanced by increasing the pulse energy of the laser used for probing. Nonlinear barium boron oxide (BBO) crystals are currently most frequently exploited in the up-converters for time-resolved spectroscopy and high-power femtosecond pulses are used for probing. However, the conversion efficiency in such systems does not exceed a few percent.

The devices for time-resolved luminescence measurements based on the time-correlated single photon counting (TCSPC) technique are less complicated and user-friendly though have a worse time resolution than that of other devices discussed above. In TCSPC device, the delay between the moment of the short-pulse excitation of the sample studied and the moment of detection of the first photon from the excited sample is measured. The measurements are repeated shot by shot, and the dependence of the frequency of the detection events on the delay is accumulated. Coupling of the TCSPC device with a spectrometer enables time-resolved measuring of luminescence spectra. The TCSPC devices are relatively inexpensive, especially those with laser diodes or light-emitting diodes used as the short-pulse excitation source. Currently, the commercially available LDs and LEDs deliver pulses with duration down to ~50 ps and operate at the repetition rates of up to 100 MHz ensuring relatively fast data collection. In study of scintillating materials, the technique is usually exploited for measuring decay of slow luminescence components.

Studying scintillators by photoluminescence spectroscopy has an advantage in capability of selective excitation by tuning the excitation photon energy. However, the variation of the photon energy of laser sources is practically limited at ~6 eV by generation of the fifth harmonic of the laser radiation. Higher harmonics are rarely used in conventional spectroscopic setups. Therefore, the photon energies delivered by conventional laser systems are insufficient for band-to-band excitation of certain scintillators.

Vacuum ultraviolet (VUV) radiation is used for excitation by photons of energy above ~6 eV. The most convenient sources of such radiation are synchrotrons and storage rings, which are commonly used as specialized sources of synchrotron radiation. The spectrum of such sources is wide and ranges from visible to X-rays. Special devices as undulators and wigglers are designed to increase the intensity of

synchrotron radiation in different spectral regions. The usage of monochromators enables excitation by photons with selected energies. The synchrotron radiation sources are very convenient for time-resolved measurements, since it can be delivered in extremely stable pulses with duration down to 50 ps at a repetition rate of hundreds of nanoseconds [8]. The stability is achieved in a one-bunch operation mode, when the same electron bunch circulates over the synchrotron ring during hours and, therefore, produces such stabile pulses. The emission of the samples under study is usually registered by PMTs, PMTs with microchannel plates, or other devices with the time resolution of approximately a hundred of picoseconds. The highly stable pulses allow for using dissectors, which are analogues of streak cameras with a secondary electronic multiplier instead of CCD [9]. This detection technique ensures the time resolution of a few picoseconds. The time-resolved luminescence spectroscopy with synchrotron radiation was developed at many large synchrotron facilities at DESY, Hamburg, Germany (see, e.g., [10–14]), at SRS in Daresbury, UK (e.g., [15, 16]), at SuperACO and DCI in Orsay, France (e.g., [14, 16, 17]), at UVSOR in Japan (e.g., [18, 19]), in Novosibirsk (e.g., [9]) and Moscow in Russia, in Lund, Sweeden, in Triest, Italy (e.g., [20]), and many other places. One of the best stations for VUV time-resolved spectroscopy was SUPERLUMI in HASYLAB, DESY [10], where the results for more than 500 scientific papers were obtained. The pulse duration at this station was ~120 ps [21]. The next generation of high-quantum-energy short-pulsed sources are free electron lasers (FEL). For example, the FEL at the FLASH facility of HASYLAB at DESY (Hamburg, Germany) delivers 25 fs pulses in extreme UV region, which can be used to excite scintillators [22]. In laboratory conditions, laser-driven X-ray tubes also provide picosecond pulses useful for luminescence spectroscopy with high time resolution [23].

5.1.2 Optical Pump and Probe Technique

The time evolution of scintillation response to excitation depends on the processes important in basically five stages of the transformation of the excitation energy to luminescence of the scintillating material. For scintillators, the five stages are: (i) generation of electron-hole pairs and relaxation of their energy, (ii) migration of the nonequilibrium carriers to the emitting centres, (iii) excitation of the emitting centres, (iv) radiative recombination with photon emission, (v) escape of the photons out of the crystal. For self-activated scintillators, stages (ii) and (iii) corresponds to formation of free or localized excitons. Luminescence spectroscopy reveals just the cumulative effect of the processes in all these stages. Meanwhile, the nonlinear optical techniques provide a deeper insight into the specific processes in the system of the nonequilibrium carriers.

The dynamics of nonequilibrium carriers can be studied by measuring the time evolution of the spectrum of the optical absorption induced by a pump pulse. In optical pump and probe configuration, the pump pulse is used to generate

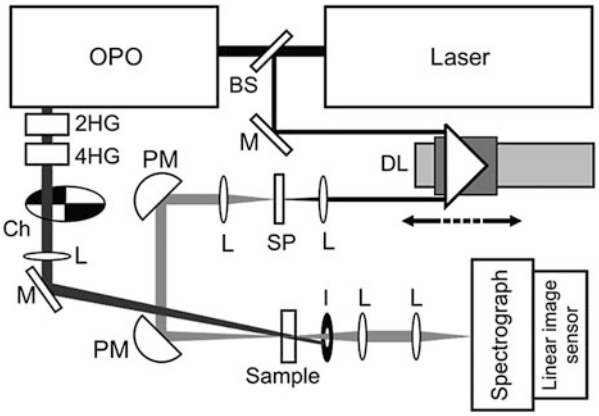

Fig. 5.2 Layout of a setup for study of time-resolved differential absorption in pump and probe configuration, consisting of femtosecond laser, beam splitter (BS), optical parametric oscillator (OPO), harmonic generators (HG), delay line (DL), chopper (Ch), flat (M) and parabolic (PM) mirrors, lenses (L), sapphire plate (SP) for generation of white light continuum, spectrograph and CCD camera for readout of probe spectrum. (After Ref. [24])

nonequilibrium carriers, whereas the changes in optical absorption are probed by a probe pulse delivered to the sample with a variable delay. The measured signal of the differential absorption (DA) is recorded as

$$DA(\lambda) = \ln\left(\frac{\mathrm{I}(\lambda)_{unexc}}{\mathrm{I}(\lambda)_{\mathrm{exc}}}\right). \tag{5.1}$$

Here, $I(\lambda)_{unexc}$ and $I(\lambda)_{exc}$ are the intensities of probe beam, recorded when the sample is unexcited and excited, respectively. By probing the sample with a broad-spectrum pulse, DA in a wide spectral range might be recorded for each probe pulse. The variable delay of the probe pulse enables step by step measurements of the time evolution of the DA spectrum.

A typical layout of a setup for studying the time-resolved DA in pump and probe configuration is presented in Fig. 5.2.

The setup is based on a pulsed laser. The time resolution of the measurement depends on the pulse duration of the laser used. Lasers emitting femtosecond or picosecond pulses are usually exploited. The output of the laser is split into two beams by a beam splitter. The major part of the initial pulse energy is directed to the pump beam. Harmonics generators based on nonlinear crystals are used to increase the photon energy of the pump beam. To continuously tune the photon energy, optical parametric oscillators are exploited. The probe beam passes an optomechanical delay line, where the length of the pulse path is variably changed by moving a retroreflector on a motorized translation stage. The maximal delay between the pump and probe pulses is limited by the length of the delay line and is typically of the order of 10 ns. After the delay line, the probe pulse is focused on a

plate of transparent material to generate a quasi-white light continuum. Sapphire is often the material of choice to generate the pump pulse with a quite flat spectrum. The probe light is focused by parabolic mirrors on the sample surface into a spot overlapping with the pump beam spot. To ensure a good overlap, the pump spot is usually larger (typically ~300 μm) than the probe spot (~100 μm). The probe light transmitted through the sample is dispersed by a spectrograph and recorded using an image sensor matrix, usually, a CCD camera. The pump beam is equipped with a chopper to periodically open and block the pump pulses. Thus, the probe light transmitted when the sample is excited and unexcited is recorded, and the DA is calculated according to Eq. (5.1). The final measurement result is a matrix of DA values recorded at different spectral positions and time delays. Cross-sections of the matrix provide either the DA spectrum at a fixed delay or the DA kinetics at a fixed spectral position.

The DA occurs due to the light absorption by any kind of nonequilibrium electrons and holes, whether they are free, trapped or in the excited states of activator ions. The DA efficiency depends on the absorption cross-section and the density of final states and, most importantly, is directly proportional to the density of the absorbing carriers. Thus, the DA intensity reflects the density of certain kind of nonequilibrium carriers, provided that the type of the carriers responsible for the DA is known. In DA experiments, the simultaneous measurement of spectral and kinetic features facilitates identification of the origin of the feature. Another degree of freedom in the DA experiments is the capability to tune the photon energy of the pump beam and perform selective excitation. Finally, the time resolution in these measurements is limited only by the duration of the laser used. Thus, by using a femtosecond laser, the time resolution in femtosecond domain is achieved.

The technique of time-resolved DA measurements is a quite common tool for studying semiconductor materials and was recently exploited for investigation of fast carrier dynamics in several extensively used scintillators: CsI:Tl, NaI:Tl, SrI_2:Eu [25], $LaBr_3$:Ce [26], GAGG:Ce [27, 28], YAG and LuAG [29], YAP-LuAP [30], and $CeBr_3$ [31].

5.2 Ce-Doped Oxyorthosilicates

Lutetium oxyorthosilicate Lu_2SiO_5:Ce (LSO:Ce) was initially introduced as a scintillator ensuring a better count rate to substitute BGO for well-logging applications [32]. However, the performance deterioration at the high temperatures typical of deep wells limited the application of LSO:Ce in oil field exploration, though LSO:Ce response is by a factor of 7 faster and its light output is by a factor of 3 higher than those of BGO [33]. Meanwhile, LSO:Ce turned out to be the scintillator of choice in positron emission tomography (PET) [34], especially, in PET devices operated in time-of-flight (TOF) mode [35]. In line with a good combination of scintillation properties, fast scintillation response is the key advantage of LSO:Ce in PET applications. First of all, the fast response enables increasing the signal to noise

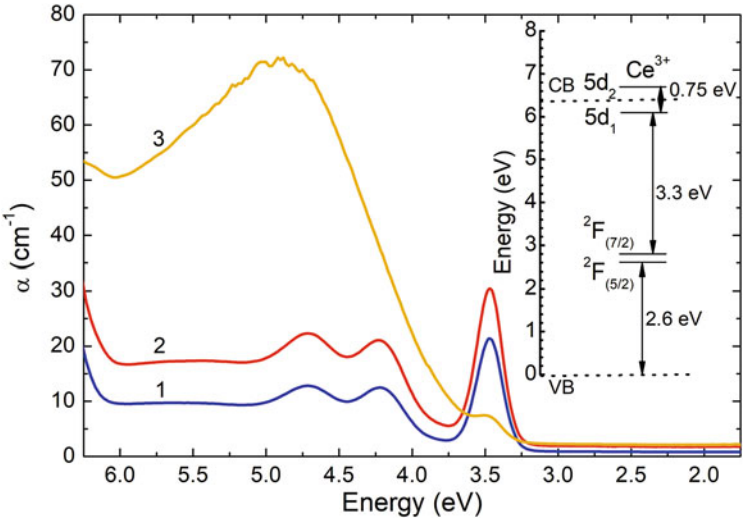

Fig. 5.3 Absorption spectra of LSO:Ce (1) and LYSO:Ce without codoping (2) and codoped with Ca (3). In the inset: the energy states of Ce^{3+} ion are schematically depicted in respect to the energies of the valence and conduction bands

ratio and improving the spatial resolution of PET images. Moreover, the faster signal readout followed by fast signal processing ensures the observation of accumulation events during the PET image acquisition in real time, enables observation-based selection of the acquisition time instead of the predetermined time, and, consequently, optimizes the radiation dose obtained by a patient.

Substitution of a part of lutetium by yttrium in the crystal matrix to fabricate multicomponent oxyorthosilicate $(Lu_x\text{-}Y_{1\text{-}x})_2SiO_5$ (LYSO) not only reduced the cost of the material and the crystallization temperature but also diminished the scintillation afterglow and improved the light yield of the material. Moreover, annealing of LYSO in oxidizing atmosphere heals oxygen vacancies and improves the response time of oxyorthosilicate scintillators [36].

The scintillation properties of LYSO:Ce can be improved by aliovalent codoping of the crystals: codoping with divalent calcium improves the light yield, shortens the luminescence decay time and suppresses the afterglow [37–40].

Typical spectra of optical absorption of LSO and LYSO with different doping are presented in Fig. 5.3. In the spectral range from 2 to 6 eV, the absorption spectrum of LSO:Ce has three distinct bands due to optical transitions from the ground state 4*f* to three lowest excited 5*d* states of the activator ion Ce^{3+}. The three lowest 5*d* states $5d_{1,2,3}$ are a result of splitting due to a low-symmetry crystal field. The crystal system of LSO is monoclinic [32] and Ce ions occupy in the crystal lattice two nonequivalent sites, Ce(1) and Ce(2) with 7- and sixfold oxygen coordination, respectively. As a result, the relative intensity of the bands in the optical absorption spectrum of LSO:Ce slightly depends on the polarization of light in respect to the

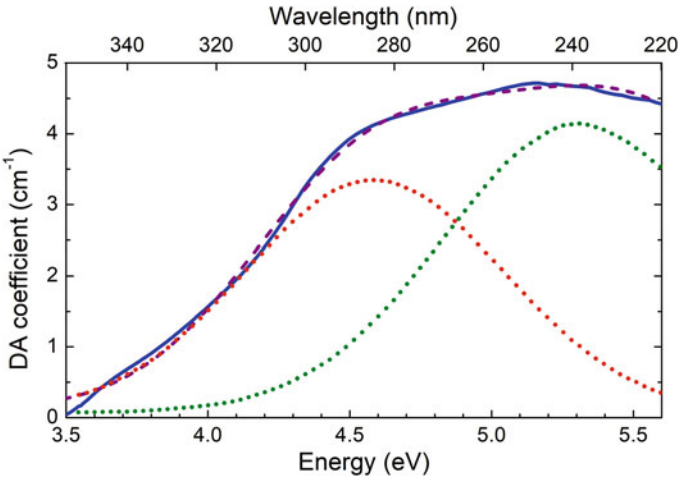

Fig. 5.4 Spectra of difference in absorption coefficients in LSO:Ce with and without Ca-codoping (solid line) and the best fit (dashed line) with two Gaussian-shaped bands (dotted lines). (After Ref. [42])

crystallographic orientation of the sample. The bands due to absorption of Ce^{3+} in positions Ce(1) and Ce(2) strongly overlap and are unresolvable at room temperature. Moreover, the ground state of Ce^{3+} ion is split into two sublevels $^4F_{5/2}$ and $^4F_{7/2}$ [41]. However, the upper sublevel is by 0.24 eV above the lower one and is not populated at room temperature. Thus, only the absorption due to transitions from the lower spin-orbital sublevel is important.

As evidenced by the spectra of LSO:Ce and LYSO:Ce (see Fig. 5.3), substitution of 10–20% of lutetium in LSO matrix by yttrium does not significantly affect the spectral positions of the absorption bands due to Ce ions.

The introduction of calcium results in formation of an additional absorption band [38], which is traceable already at a Ca content of a few ppm and is distinct in LYSO:Ce,Ca at the calcium content of 30 ppm. The band is peaked at 4.9 eV [38] and has the full width at half maximum, FWHM, of 1.66 eV. The formation of this band has been attributed to the absorption via charge transfer transitions from oxygen to Ce^{4+} ions. This interpretation is based on the increasing part of Ce ions in Ce^{4+} charge state, which has been observed in Ca-codoped LSO:Ce by X-ray Absorption Near Edge Spectroscopy (XANES) [40], however, the contribution of other emission centers formed due to the incorporation of Ca impurities are also feasible. The spectrum of differential absorption of LSO:Ce and LSO:Ce,Ca is presented in Fig. 5.4. The spectrum of the difference in the absorption coefficient of LSO:Ce with and without Ca-codoping can be well fitted by two Gaussian-shaped bands peaked at 270 and 235 nm. This is an indication that the absorption induced by introduction of calcium has two spectrally separated components, possibly of different origin. The differential spectrum in YSO:Ce and YSO:Ce,Cd can also be similarly fitted by taken into account two components; in this case, peaked at

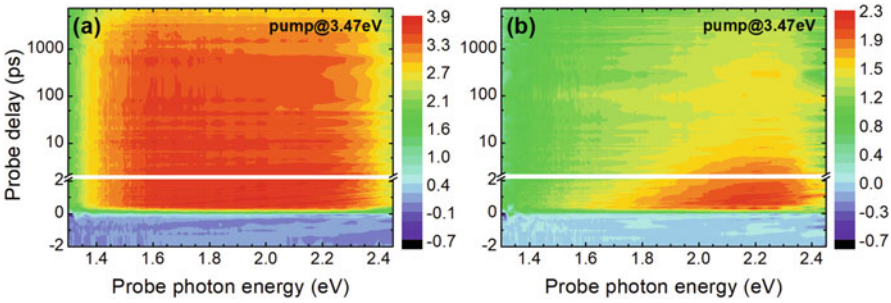

Fig. 5.5 Differential absorption (color-coded as indicated by sidebar) dependence on probe photon energy and delay between pump and probe pulses for LYSO:Ce with low (**a**) and (**b**) high level of Ca-codoping

275 and 240 nm, in contrast to the aliovalently-doped garnet-type scintillators, where only one band is observed. The two absorption subbands in oxyorthosilicates might be related with two possible positions of Ca^{2+} ion in the oxyorthosilicate host matrix: 6(O) and 7(O). Instead, only a single position 8(O) is possible for Ca^{2+} ion in a garnet structure.

The capability of tuning the excitation photon energy in the pump and probe experiments enables selective excitation of Ce^{3+} ion to the first and second excited states and initiate the optical transitions from the valence band to the tail of the conduction band, which is formed, in addition to the phonon-assisted sub-band-gap absorption, predominantly by shallow defect-related states acting as trapping centres for electrons.

The excitation photon energy of 3.47 eV corresponds to the energy separating the ground state and the first excited state of Ce^{3+} ion. In addition, these photons can also excite Ce^{4+} ions via charge transfer (CT) transitions from the oxygen orbitals building the top of the valence band to the unoccupied electron state of Ce^{4+} ion. In uncodoped LSO:Ce or LYSO:Ce, just a negligible part of Ce ions are in the state Ce^{4+}; however, the part increases with increasing Ca-codoping [43].

Application of pump and probe technique enables obtaining the differential absorption intensity as a function of the time and spectral position of probe photon. An example of the corresponding data carpets is presented in Fig. 5.5. The DA kinetics, which is obtained as a cross-section of the data carpet at certain probe photon energy is presented in Fig. 5.6.

Two DA components are evident in the data carpets and the kinetics of the DA signal at two typical probe photon energies. The spectrum of the first feature, which is well pronounced in the LYSO:Ce with low Ca codoping, is approximately flat. This DA component decays with a characteristic decay time of ~40 ns coinciding with the luminescence decay time. Therefore, this component is attributed to the absorption by an electron occupying the first excited level of Ce^{3+}. The characteristic decay time of the fast DA decay component is ~5 ps, whereas this component is most strongly pronounced at the probe photon energies in the vicinity of ~2.3 eV. This component is more pronounced in LYSO:Ce codoped with Ca, whereas its time-

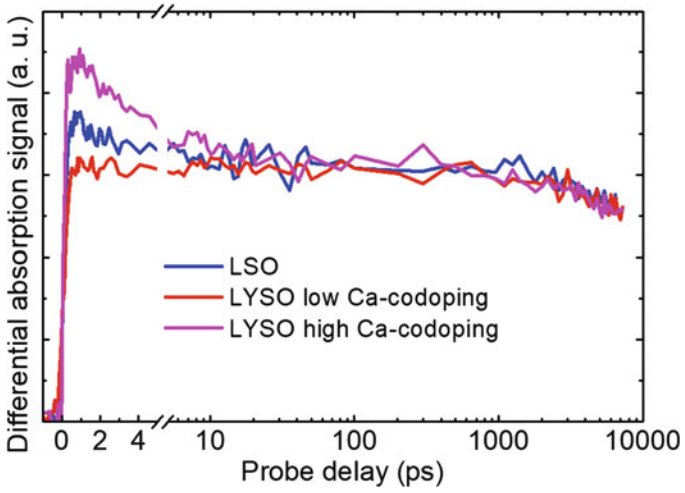

Fig. 5.6 Kinetics of differential absorption at a probe energy of 1.4 eV for LSO:Ce samples (indicated) after pumping with 3.47 eV photons. The arbitrary units are normalized for all the samples by taking into account their thicknesses and absorption coefficients

integrated contribution is by orders of magnitude smaller than that of the slow component. This DA component is tentatively attributed to the absorption by free holes generated due to pump-induced CT transitions from the valence band to Ce^{4+} ground state. The enhancement of the fast component by codoping is explained by increasing share of Ce ions in Ce^{4+} state in the codoped crystal, as observed in [40].

The pump photon energy of 4.82 eV corresponds to the transition from the ground to the third excited state in Ce^{3+} ion. The energy of this state is above the bottom of the conduction band. The electron excited to this state has two routes of energy relaxation: (i) intracentre relaxation down to the lowest excited state of Ce^{3+} ion and radiative recombination afterwards (as at the 3.47 eV resonant excitation to the lowest excited state), or (ii) leaving the Ce^{3+} ion to become a free electron in the conduction band.

The conditions of CT excitation of electrons from the oxygen orbitals in the valence band to the ground state of Ce^{4+} are similar to those at the excitation with 3.47 eV photons. Moreover, the pump photon energy of 4.82 eV corresponds to the peak of the broad absorption band, which becomes more pronounced in the absorption of Ca-codoped LYSO:Ce (see Fig. 5.3). The origin of this band is still debated, however, it is reasonable to assume that this absorption band is at least partially caused by optical transitions from the valence band to codoping-induced defect centres. Consequently, additional holes are expected to be generated by excitation of electrons from the valence band to the Ca-related states a few hundreds of meV below the bottom of the conduction band. This interpretation is in line with the observation that the free hole absorption peaked at 2.2 eV in the DA spectra is stronger at the excitation at the pump photon energy of 4.82 eV than that at 3.47 eV excitation.

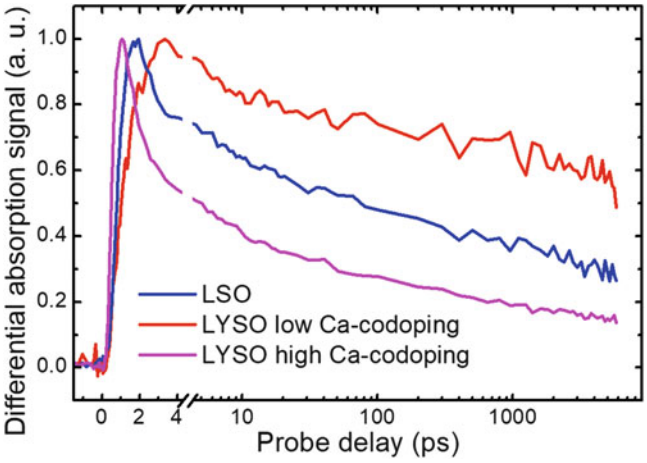

Fig. 5.7 Kinetics of differential absorption at 1.4 eV in LSO:Ce and LYSO:Ce with low and high Ca content after pumping with 4.82 eV photons. All kinetics are normalized to their peak values

The DA kinetics at 1.4 eV probe photon energy have two distinct features: a delayed rise in the DA response and a fast decay component, which is more pronounced in the kinetics of the LYSO:Ce with high level of Ca codoping. The fast decay component is attributed to the generation of free electrons, which are not generated by pump photon with energy of 3.84 eV. It is also assumed that the generation of free electrons results also in a slower rise of the DA response. The rise time is of the order of 1 ps in LSO:Ce, is longer in LYSO:Ce, and is at least below the 1 ps in LYSO:Ce,Ca (see Fig. 5.7).

The delayed DA rise and the fast decay component are better pronounced at pump photon energy of 5.91 eV. This photon energy is still smaller than the LYSO band gap but already high enough to excite electrons from the valence band to the states, which occur in the band gap close to the bottom of the conduction band. The pump photons with energy of 5.91 eV excite Ce^{3+} to high excited states or create free electrons in the conduction band due to charge transfer (CT) transitions to the 5*d* states of matrix-building Lu forming the conduction band [44]. The DA kinetics at 5.91 eV pump photon energy and several probe photon energies are compared in LSO:Ce and LYSO:Ce in Fig. 5.8.

All three components in the DA kinetics are evident also at these excitation conditions. The initial part of the kinetics in the low-energy part of the probing spectrum is dominated by the fast decay component attributed to free electron absorption. The kinetics at all probe photon energies converge to the same decay rate towards the nanosecond time domain. This behaviour is in line with the assumption that this decay component is caused by radiative recombination at excited Ce^{3+} centres. The slow rise component in DA kinetics is better pronounced for probe photons above 2 eV and is substantially stronger in LYSO:Ce than in LSO:Ce.

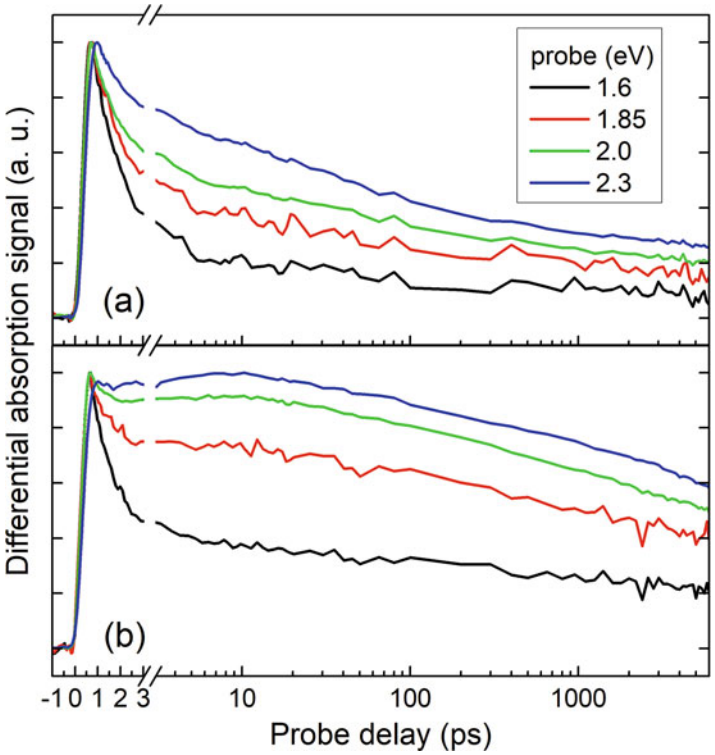

Fig. 5.8 Time evolution of normalized differential absorption in LSO:Ce (**a**) and LYSO:Ce (**b**) at 5.91 eV pump photon energy and probe photon energies indicated

The DA results obtained at different pump photon energies show that the free electrons exists before relaxing down to the first Ce^{3+} excited state or getting trapped with a characteristic decay time of ~1 ps, as evidenced by the fast decay component in the DA response. The additional population of the lowest excited Ce^{3+} state by electrons occurs in uncodoped LSO:Ce with a delay of the order of ~5 ps, which is longer than the decay time of free electron component. This delay in population of the lowest excited state of Ce^{3+} ion is attributed to the migration of electrons trapped on shallow traps. Such interpretation of the delay in DA response was suggested earlier in GAGG:Ce and GAGG:Ce,Mg [27]. The trapped electrons have certain probability to be thermally detrapped and to migrate to the radiative Ce^{3+} centres experiencing multiple trapping and detrapping. It is reported that oxygen vacancies are the main electronic defects in LYSO [45]. The density of the oxygen vacancies can be reduced by oxygen in the growth [46] and annealing [47] atmospheres. It is also reported that the density of oxygen vacancies might be reduced by introduction of lithium [48]. The delay in population of Ce^{3+} level $5d_1$ in LYSO:Ce is more pronounced than that in LSO:Ce. This peculiarity is interpreted by electron trapping

at the centres formed due to composition fluctuations in the multicomponent garnet LYSO. Even statistical fluctuations in the local density of Lu and Y atoms modulate the bottom of the conduction band, and the minima of the potential profile experienced by electrons serve for their trapping. Note that the energy necessary for electrons to move to the neighbouring localized states by hopping might be substantially lower than the depth of the state in respect to the conduction band. Therefore, the electrons can move in the crystal by hoping through localized states without being thermally excited to the conduction band and reach the Ce^{3+} this way.

Summing up the results on carrier dynamics in orthosilicates it is reasonable to conclude that the slow rise component in the population of Ce^{3+} level $5d_1$ is the most sensitive feature of DA prospective to be exploited for characterization of LSO:Ce and LYSO:Ce.

It is worth noting that Ca-codoping of LYSO:Ce practically completely eliminates the slow rise component at low codoping levels, even as low as 5 ppm. Such a strong effect might hardly be explained by conversion of a substantial part of Ce^{3+} to Ce^{4+}, i.e., the effect, which is often pointed out as the origin of the improvement of the light yield and the response time of Ce-doped LSO/LYSO and other oxyorthosilicate- and garnet-type scintillators. However, such a small amount of calcium ions can hardly affect the distribution of valence states of Ce ions. The change in valency is feasible for the crystal growth in conditions, which are favourable for coherent doping, i.e., the incorporation of the dopant in close vicinity of the emitting ion. Therefore, the stabilization of cerium ions in Ce^{4+} state might be expected at high levels of Ca-codoping. The measurements using XANES technique show that Ce^{4+} content in LSO:Ce is negligible [43]. Only 35% of Ce ions are in the state Ce^{4+} in LYSO:Ce,Ca with 30–40 ppm of Ca [40]. Thus, no substantial change in the valency of Ce ions might be expected at the codoping at the level of 5 ppm, which is sufficient to improve the response time of LSO/LYSO scintillators substantially. The faster population of emitting Ce-centres and the improvement of scintillation properties of LSO/LYSO at low aliovalent codoping levels cannot be explained by the increasing contribution of Ce^{4+}, which is being pointed out as the major effect in the current discussions of aliovalent codoping (see, e.g., the review [49] and references therein). These improvements must have a different origin. The faster response is interpreted by diminished carrier trapping or faster nonradiative recombination of the trapped carriers. As mentioned above, the dominant electron traps in LSO/LYSO are most probably caused by oxygen vacancies. The Ca^{2+} ions in codoped crystals compensate the oxygen vacancies [37]. The decrease in trap concentration was observed with increasing content of Ca in thermoluminescence measurements of YSO:Ce [39] and LSO:Ce [38]. This decrease is caused by two competing effects of aliovalent codoping: (i) co-dopants are introduced in the initial charge in excess to its stoichiometric composition, thus, the co-dopants decrease simultaneously the concentrations of cation and anion vacancies during the crystal growth [50], (ii) the substitution of a trivalent ion by a divalent one increases the anion vacancy concentration in the host matrix.

5.3 Ce-Doped Garnets

Technology for growing single crystals of yttrium aluminum garnet $Y_3Al_5O_{12}$ (YAG) was developed in the sixties, first of all, due to application of neodymium-doped YAG as active medium in solid state lasers [51], whereas YAG:Ce was proven to be prospective scintillator material (see, e.g., a review [52]). Substitution of yttrium by lutetium in the garnet structure resulted in a higher density and effective atomic number and expanded applicability of $Lu_3Al_5O_{12}$:Ce (LuAG:Ce) for detection of hard X-rays and γ-quanta. Moreover, LuAG:Ce exhibited a better luminescence time response. YAG:Ce scintillators suffer from strong afterglow due to the contribution of trapped carriers. At least partially, this drawback was successfully eliminated by engineering the garnet composition [49, 53]. In particular, a properly balanced introduction of Ga and Gd in the GAGG:Ce garnet shifts the bottom of the conduction band down in energy to bury the impurities-related levels in the conduction band. Moreover, the GAGG:Ce single crystals exhibit a higher light yield than that of binary garnets. Though being slightly lower in the single crystals grown in other research groups and companies producing scintillators, the light yield of GAGG:Ce is reported to be as high as ~60,000 photons/MeV [49].

The luminosity expected in many future high-energy physics experiments puts forward new challenges for the fast timing of scintillators in subnanosecond domain. Therefore, the leading edge of the luminescence response of the prospective GAGG:Ce becomes an issue. The optical pump and probe technique was shown to be an informative technique for studying the fast nonequilibrium carrier dynamics in GAGG:Ce.

It is demonstrated that co-doping of GAGG:Ce by Mg significantly improves the response time [54] and enabled decreasing the coincidence time resolution down to 233 ps [24, 55] and even bellow 50 ps in thin crystals GAGG:Ce,Mg at the excitation with a high-energy charged pion beam [56].

5.3.1 Leading Edge of Luminescence Response in GAGG Scintillators

To study the luminescence response kinetics with high time resolution, time-resolved photoluminescence spectroscopy by using a streak camera with 3 ps FWHM of the instrumental response function was applied [28]. The initial part of the photoluminescence kinetics after excitation with a short, 200 fs, laser pulse at a photon energy of 4.88 eV (254 nm) is presented in Fig. 5.9. The photons excite the electrons from the ground state of Ce^{3+} ions into their high excited levels or to the conduction band via charge transfer (CT) transitions. The front edge of the luminescence response has two rise components. The first component is below 1 ps, whereas the slower one has a characteristic time of a few nanoseconds. The slow component disappears in the crystal with Mg codoping. The front part of the

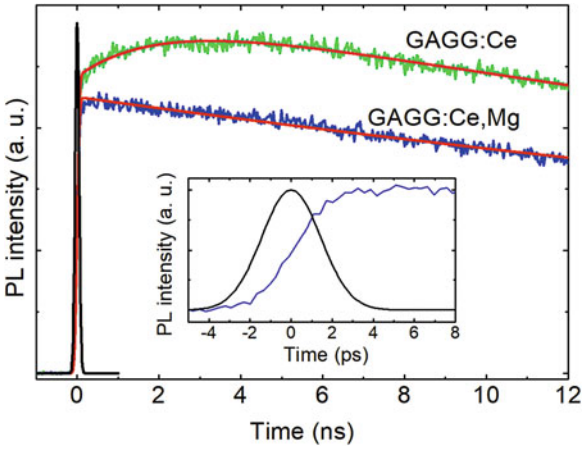

Fig. 5.9 Photoluminescence response of GAGG:Ce and GAGG:Ce,Mg to a 200-fs excitation pulse with a photon energy of 4.88 eV. Instrumental response function is presented by black solid line. In the inset: the front part of the luminescence response in GAGG:Ce,Mg. (After Ref. [28])

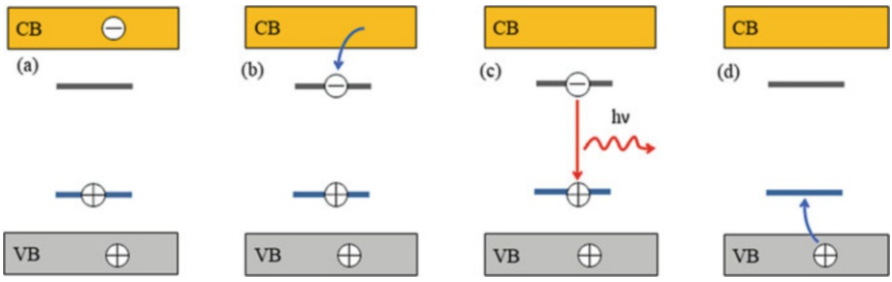

Fig. 5.10 Schematical explanation of processes going on at Ce^{4+} ion involved in luminescence in scintillators: initial state with a hole in the ground state and free electrons and holes (**a**), capture of free electron (**b**), radiative electron-hole recombination by photon emission (**c**), capture of free hole (**d**)

luminescence response in GAGG:Ce,Mg is presented in the inset of Fig. 5.9 together with the instrumental response function of the TRPL setup based on a streak camera. It is evident that the rise time of GAGG:Ce,Mg has no slow component, whereas the characteristic rise time of the fast component is below 1 ps.

The shorter luminescence response time in aliovalently codoped GAGG:Ce and many other Ce-doped scintillators is usually attributed to increasing influence of Ce ions in tetravalent state. The mechanism was suggested decades ago [57]. Basically the same mechanism has been exploited to interpret the improvement of timing properties of LSO:Ce, as mentioned above, and many other Ce-doped scintillators [58, 59]. The mechanism is schematically explained in Fig. 5.10. The Ce ions are

supposed to have a large cross-section to capture a hole and to be stable in tetravalent state, as depicted in Fig. 5.10a. The hole occupies the ground state, whereas the first excited state, which is located by ~200 meV below the bottom of the valence band of GAGG matrix, is empty. Due to the hole on the ground state, the first excited state of Ce^{4+} is effective to attract an electron from the conduction band. This state (Fig. 5.10b) is identical with the state of excited ion Ce^{3+*}. The electron and hole recombine by emitting a photon and leaving the Ce ion in trivalent state Ce^{3+} (Fig. 5.10c). Subsequently, the ion Ce^{3+} captures a hole and transforms to Ce^{4+} again (Fig. 5.10d). The gain in luminescence response time is caused by capability of Ce^{4+} to effectively compete with trapping centres in capturing the nonequilibrium electrons.

The mechanism explains well the faster luminescence response and the higher light yield in Ce-doped materials with a higher ratio of Ce ions in tetravalent and trivalent states observed experimentally. The correlation between the shorter luminescence response and the higher share of cerium in Ce^{4+} state observed in Ca-codoped LSO:Ce by XANES technique [40] is usually considered as a strong experimental evidence of the importance of this mechanism. However, no experimental data or theoretical estimates of the limits of this importance are still available. Moreover, the model has a few features waiting for deeper understanding. First of all, the simplified scheme provided in Fig. 5.10 and similar schemes provided in literature are drawn assuming that the capture of a hole by ion Ce^{3+} does not shift the state of the ion on the energy scale in respect to the band gap of the matrix. This issue was addressed in more detail in Chap. 3. Secondly, the mechanism of the hole capturing is not clear: the ground state of Ce^{3+} is 3.35 eV above the top of the valence band, the transition is not radiative, thus, the question of the mechanism for the hole to lose such a large energy is still not clear. Finally, the effect of aliovalent codoping is strong even at small amounts of the codoping ions, e.g., at 5 ppm of Ca in LYSO:Ce or 10 ppm of Mg in GAGG:Ce [24]. The doping of GAGG:Ce at a level such low as 10 ppm should not significantly affect the ratio between the concentrations of Ce^{3+} and Ce^{4+}. At 10 ppm, the Mg concentration corresponds to one magnesium ion in a volume of 2700 nm^3 containing ~1400 unit cells of GAGG, provided that the magnesium distribution in the crystal is homogeneous. The concentration of ~500 ppm of homogeneously distributed cerium corresponds to one Ce ion per volume of ~60 nm^3 (corresponding to less than 40 of GAGG unit cells). Therefore, the probability for Mg and Ce ions for pairing to form a charge-balanced link between Mg^{2+} and Ce^{4+} is low. Moreover, to estimate the probability of such pairing, the localization of Mg and Ce ions in suitable sites of the garnet-type host matrix has to be taken into account. Garnet-type crystal structure belongs to the cubic space group Ia3d (#230) with cations at special positions (on 16a, 24c and 24d sites) and oxygen anions at general positions (on 96 h sites). Three cations have tetrahedral coordination (24d sites) and two cations have octahedral (16a sites) coordination formed by oxygen ions [60]. The eighth coordinate sites (dodecahedral, 24c sites) accommodate Gd ions. There are eight formula units in a unit cell.

It is reasonable to assume that the Ce-Mg pairing occurs when Ce and Mg ions are within a distance at least equal to the radius of the second cation coordination sphere.

For a cation in position *24d*, there are four atoms in position *16a* in the first coordination sphere, whereas for a cation in position *16a*, there are six atoms in position *24d* in the first coordination sphere. In two cation coordination spheres, Mg ion has 34 positions suitable for Ce stabilization. Therefore, only nearly 1 per cent of Ce^{3+} ions have a chance to be located within the first two coordination spheres around Mg ion. Consequently, the formation of Ce^{4+} due to pairing of Ce ion with Mg^{2+} might be considerable at high codoping concentration but is insignificant at the aliovalent codoping of GAGG:Ce with Mg at the level of 10 ppm.

An important point is that the fast and slow rise components in the population of the emitting level of Ce ion occur even at the direct excitation of cerium ions. In this case, the Ce^{4+} ions are actually excluded from the active participation in the dynamics of nonequilibrium carriers. Furthermore, the slow rise component occurs only at the excitation of Ce^{3+} ion to the second excited state, which is above the bottom of the conduction band [24].

5.3.2 *Dynamics of Ce^{3+} Ion Population in GAGG:Ce*

All the experimental data on the influence of aliovalent doping on improving the scintillation properties can be explained by assuming that the codopants decrease the density of shallow traps, which substantially affect the excitation migration to the emitting Ce ions. This assumption is strongly supported by the experimental results obtained by exploiting the measurements of differential optical absorption in pump and probe configuration. As discussed above, this technique has an advantage of selective excitation.

Typical spectra of linear optical absorption of GAGG-based scintillators are presented in Fig. 5.11.

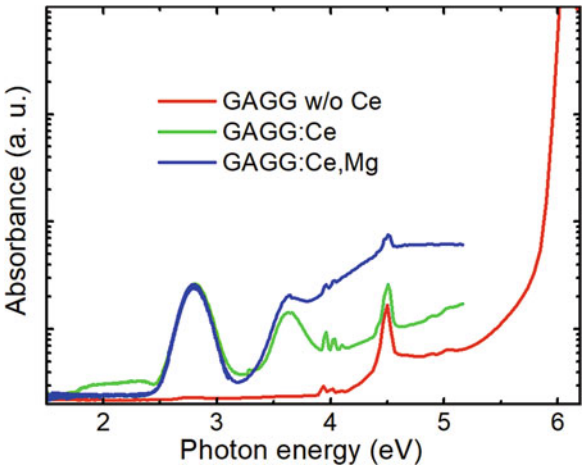

Fig. 5.11 Optical absorption spectra of GAGG, GAGG:Ce, and GAGG:Ce, Mg. (After Ref. [27])

The absorption spectrum of nominally undoped GAGG is also presented in Fig. 5.11. Below the Urbach's tail of band-to-band absorption, the absorption spectrum of undoped GAGG has no other absorption bands except of the narrow lines attributed to the *f-f* absorption bands of matrix-building gadolinium ions. The spectrum of GAGG:Ce has the usual two distinct absorption lines due to optical transition from the ground state of Ce^{3+} to two lowest excited states, one by ~200 meV below the bottom of the conduction band, another above the bottom of the conduction band. The incorporation of magnesium introduces a broad absorption band in the near UV region. The band can be attributed either to the absorption by Ce^{4+} or to the CT transitions from the valence band to shallow traps formed under the influence of aliovalent codoping.

Two typical data carpets depicting the DA signal as a function of probe photon energy and delay between pump and probe pulses in uncodoped GAGG:Ce are presented in Fig. 5.12 for two pump photon energies. The pump with photon energy of 2.8 eV excites electrons at Ce^{3+} from the ground to the first excited state $5d_1$ lying below the bottom of the conduction band. The DA feature spectrally peaked at 1.4 eV, which is absent in nominally undoped GAGG, is attributed to DA due to the absorption of the nonequilibrium electrons occupying the level $5d_1$. As expected, the decay of this DA proceeds at the same rate as the luminescence decay.

The front edge of the DA response in GAGG:Ce without codoping has two rise components: the first component is instantaneous on a picosecond scale, the second one has a characteristic rise time of ~10 ps (see Fig. 5.13). The introduction of Mg codopant eliminates the slow rise component. Note that Mg-codoping even at the level as small as 10 ppm results in a substantial decrease of the contribution of the slow rise component. The carrier trapping is pointed out as the most probable origin of the slow rise component. The electrons generated into the second excited level $5d_2$ (at 3.63 eV pump) have two routes of relaxation to the first excited state $5d_1$: (i) intracentre relaxation and (ii) relaxation via the states in the conduction band. In the latter case, the electron leaves the Ce^{3+} ion, relaxes to the bottom of the band in the vicinity of the Ce^{3+} ion and returns back to the ion to its lowest excited state $5d_1$. During the last stage, the electrons have also certain probability to be trapped at shallow levels caused by impurities or structural defects of the crystal matrix or captured by deeper defect-related states acting as the centres of nonradiative recombination. Electron trapping-detrapping results in certain delay in the population of $5d_1$ level via this relaxation route. Meanwhile, the nonradiative recombination competes with the return of the nonequilibrium electrons back to Ce^{3+} and decreases the contribution of the slow component in the population of $5d_1$ level of Ce^{3+}. However, the nonradiative recombination also decreases the light yield and, consequently, deteriorates the timing capability of the scintillator. The influence of aliovalent doping on the formation of defects in GAGG is still not clarified. The introduction of aliovalent dopants into GAGG:Ce seems to decrease the density of trapping centres as well as to increase the density of nonradiative recombination centres. Shifting the effect of the aliovalent doping on the defect formation in GAGG in favour of suppressing the trapping centres is an important challenge in further development of codoped GAGG:Ce scintillators.

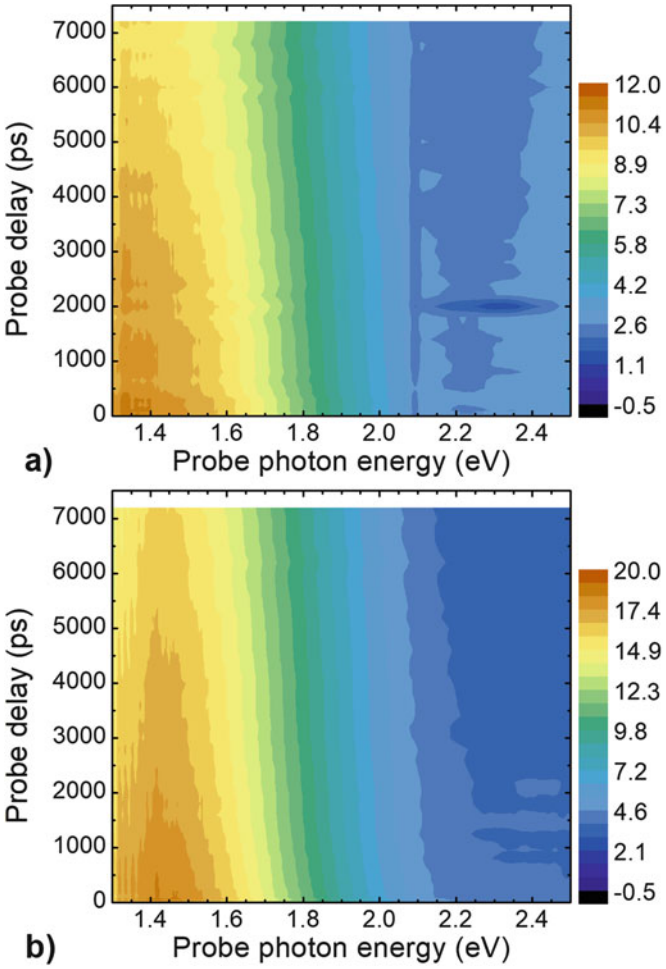

Fig. 5.12 Differential absorption of GAGG:Ce as a function of probe photon energy and delay between pump and probe pulses at two pump photon energies: 2.8 eV (**a**) and 3.63 eV (**b**). (Reprinted with permission from Ref. [24])

The experimentally observed dynamics of nonequilibrium electrons might be described by a set of rate equations for population of two excited states of Ce^{3+} and a trapping level.

$$\frac{dN_{5d2}}{dt} = G(t) - \frac{N_{5d2}}{\tau_{21}} - \frac{N_{5d2}}{\tau_{2T}} \tag{5.2}$$

$$\frac{dN_T}{dt} = \frac{N_{5d2}}{\tau_{2T}} - \frac{N_T}{\tau_{T1}} \tag{5.3}$$

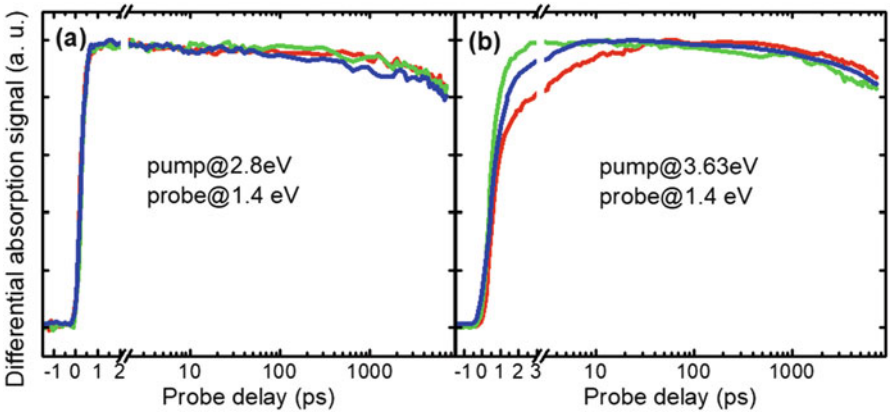

Fig. 5.13 Differential absorption kinetics at a probe photon energy of 1.4 eV in GAGG:Ce (red curve) and GAGG:Ce,Mg with a Mg content of 10 ppm (green curve) and 7 ppm (blue curve). Pump photon energies: 2.8 eV (**a**) and 3.63 eV (**b**). (After Ref. [24])

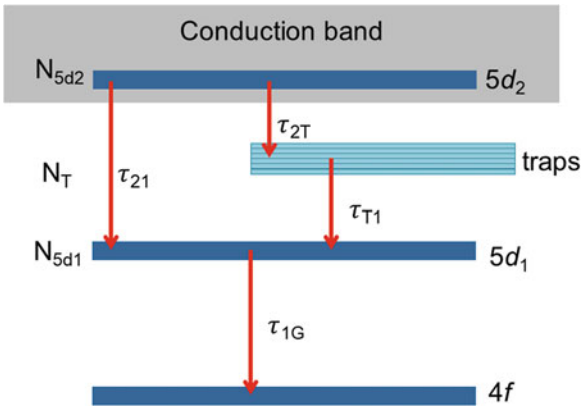

Fig. 5.14 Energy levels in GAGG:Ce (not to scale) with their populations and characteristic times of the optical transitions taken into account in the simulation described below indicated

$$\frac{dN_{5d1}}{dt} = \frac{N_{5d2}}{\tau_{21}} + \frac{N_T}{\tau_{T1}} - \frac{N_{5d1}}{\tau_{1G}} \tag{5.4}$$

The populations of the involved levels and characteristic transition times are indicated in Fig. 5.14 presenting the schematic picture of the levels on energy scale. The populations of the first (N_{5d1}) and second (N_{5d2}) excited states of Ce^{3+} ion and the population of generalized electron traps N_T are involved. The time constants for relaxation transitions from state $5d_2$ to $5d_1$, from state $5d_2$ to trapping level, from trapping level to state $5d_1$, and from $5d_1$ to ground state are denoted as τ_{21}, τ_{2T}, τ_{T1}, and τ_{1G}, respectively. The pump laser pulse is described by a Gaussian $G(t)$.

Solving the equation set (5.2) provided the time evolution of the population of level $5d_1$, which is directly probed in DA experiments. The results of the fitting of the

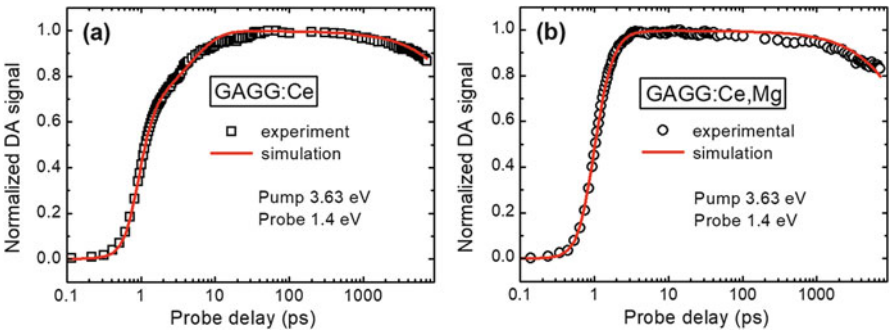

Fig. 5.15 Fits of experimentally obtained kinetics of DA (points) reflecting the population of $5d_1$ and of the population simulated by solving equation set (5.2, 5.3, and 5.4) (lines) in uncodoped (**a**) and Mg-codoped (**b**) GAGG:Ce. (After Ref. [27])

kinetics of the simulated population of N_{5d1} and the DA signal for probe photon energy at 1.4 eV, which is directly proportional to N_{5d1}, are illustrated in Fig. 5.15. The time of relaxation from the second to the lowest excited state (τ_{21}) was maintained constant in the fittings with the experimental results obtained at excitation to both $5d_1$ and $5d_2$ levels. The fitting enabled the estimation of the time of intracentre electron relaxation from $5d_2$ to $5d_1$. The time equals ~500 fs.

The correlation between the codoping level and the time constant for transitions between the trapping level and the $5d_1$ level of Ce^{3+} is another important conclusion of the simulation and fitting. The time constant decreases as the Mg-codoping level is increased, what is in line with the assumption that the codoping decreases the influence of trapping centres.

At pump photon energy of 4.8 eV the excitation of Ce^{3+} ions to the conduction band is also possible; however, this energy corresponds to the energy of electronic transitions $^8S_{7/2}$-^6I_j of Gd^{3+} ions. Thus, holes at Gd^{3+} ions are expected and might be observed by probe pulse. A typical DA data carpet at this pump photon energy is presented in Fig. 5.16a. The carpet is dominated by a new feature spectrally peaked at 2.2 eV. The contribution to DA by absorption of electrons at $5d_1$ level of Ce^{3+} is also observed with rising and decay component (see Fig. 5.16b).

The fast DA component decays within a few picoseconds and is attributed to the absorption due to the excitation of gadolinium ions. Analysis of anticipated energy diagram leads to conclusion that this DA component is caused by absorption of holes generated via excitation of gadolinium. The distinct absorption line peaked at ~4.5 eV (see, e.g [61]) is usually attributed to the absorption by Gd^{3+}, which is a matrix-building ion. Theoretical calculations show that the ground state of Gd^{3+} ion in the GAGG matrix is within the valence band [62]. Since the band gap of GAGG $E_g = 6.2$ eV, the distance between the first excited state of Gd^{3+} and the bottom of the conduction band is above $E_g - 4.5$ eV $= 1.7$ eV. Meanwhile, the DA is observed also for the probe photon energies well below 1 eV (see Fig. 5.17) and might not be attributed to optical transitions of electrons from the excited states of Gd^{3+} ion.

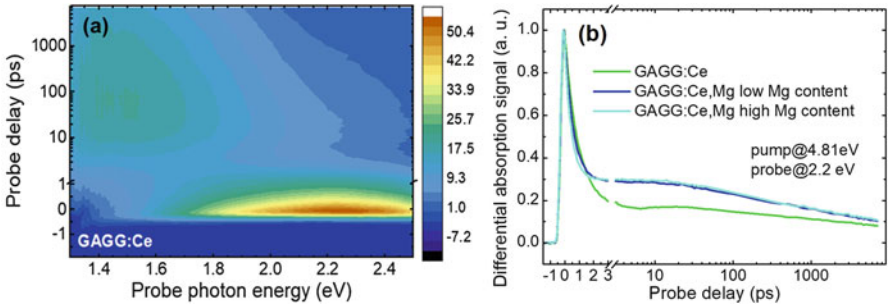

Fig. 5.16 Differential absorption of GAGG:Ce as a function of probe photon energy and delay between pump and probe pulses (**a**) and kinetics of differential absorption at 2.2 eV in GAGG:Ce without codoping (green line) and Mg-codoped (blue) at pump photon energy of 4.81 eV (**b**). (After Ref. [27])

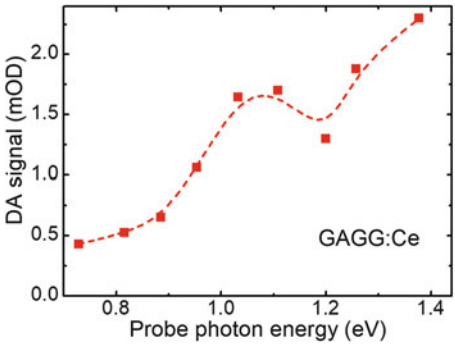

Fig. 5.17 Probe photon energy dependence of differential absorption in GAGG:Ce. (Reprinted with permission from Ref. [42])

The dependence of DA on probe photon energy is nonmonotoneous and has a band peaked at ~1 eV. Under assumption that the band is caused by absorption by free holes from the top of the valence band to the ground state of gadolinium, the ground state is by ~1 eV lower than the top of the valence band. The presence of the distinct absorption band in the DA spectrum correlates with the transformation observed in the DA kinetics. The DA signal rises with characteristic time constant of 1.5 ps exhibiting no significant spectral dependence. This is determined by the relaxation of holes from the ground level of Gd^{3+} to the top of the valence band.

As an update of the energy diagrams in Gd-based crystals [63, 64], a sketch of GAGG:Ce,Mg energy level diagram is presented in Fig. 5.18. For simplicity, only the positions of zero-phonon states are indicated there. The energy level diagram of Ce^{3+} in GAGG has been already described in [65]. The energy positions of Ce^{3+} ion depends on the band gap. It was taken to be 6.8 eV in [65], whereas different band gap values are also reported [66]. The energy differences between Ce^{3+} levels used in the diagram are based on the positions of the absorption bands [61] depicted by taking into account that the lowest zero-phonon radiating level of Ce^{3+} is located by 0.3 eV below the bottom of the conduction band. The level f_1 turns out to be by ~3.35 eV above the top of the valence band.

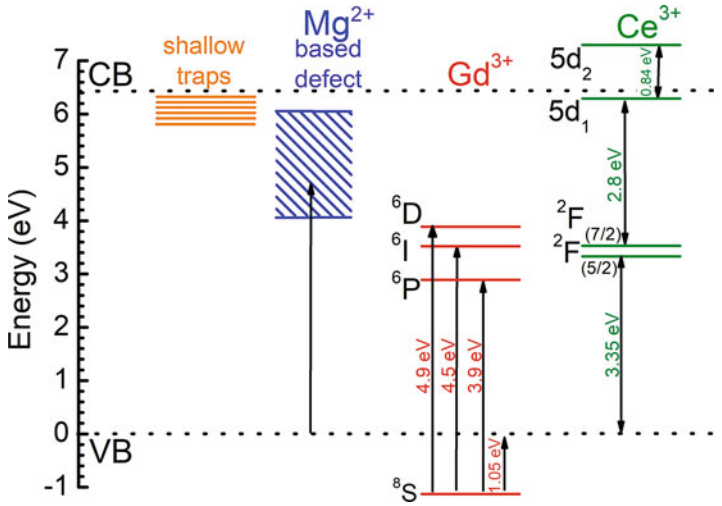

Fig. 5.18 Energy-level diagram for GAGG:Ce,Mg. (After Ref. [42])

5.3.3 Correlation Between the Front Edge in Activator Population and the Time Resolution of Scintillators

According to eq. (2.30), the time stamp $\langle t_{st} \rangle$ in the case of instantaneous population of the luminescence centres is proportional to τ_{em}. Therefore, the timing properties of the scintillators of this type are mainly determined by the time of luminescence decay. Meanwhile, $\langle t_{st} \rangle$ depends also on the ratio N_{th}/N_{em}, where N_{th} is determined by the detecting system and the irradiation environment. The ratio is proportional to the light yield of scintillator material. This situation, which is indicated as case (i) in Chap. 2, corresponds well to that in cross-luminescence scintillators [33].

The situation described in case (ii) (see Chap. 2) is close to that in the detectors based on self-activated scintillators. For example, the luminescence rise time of lead tungstate $PbWO_4$ (PWO) single crystals is in subpicosecond domain, whereas τ_{em} at room temperature is of the order of 10 ns [28]. Therefore, the time resolution of PWO scintillators in measurements at high energy deposit is proportional to $N_{em}{}^{-1/2}$ and can be as short as 100 ps [67, 68].

Case (iii) is typical of activated scintillators, where the excitation migration to the radiative recombination centres takes the time long enough to substantially influence the leading edge of the luminescence response.

The scintillation kinetics calculated for the three cases discussed above are compared in Fig. 5.19. The calculations were performed using the parameters, which are typical of Ce-doped scintillators: $N_{em} = 10{,}000$, $\tau_{em} = 30$ ns, $\tau_{rise} = 20$ ps, $\tau_{ex} = 100$ ns, and $q = 60$.

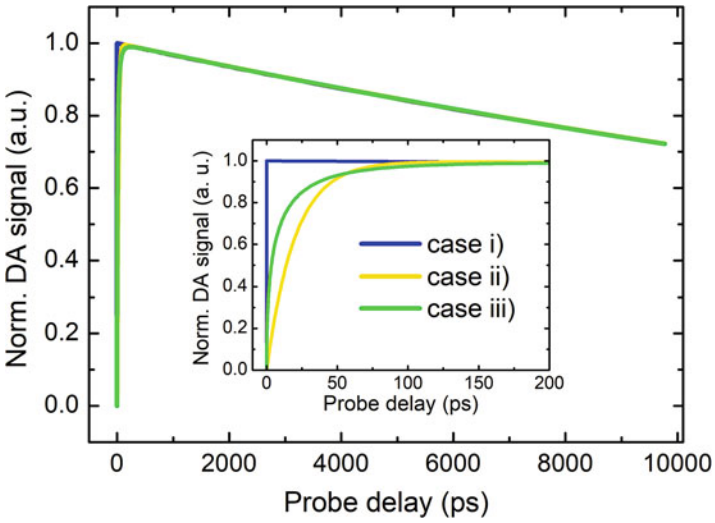

Fig. 5.19 Scintillation kinetics and the initial part of it (in the inset) for three cases of luminescence response discussed in the text: (i) blue line, (ii) yellow line, and (iii) green line. (After Ref. [24])

Note that the rise slope might be steeper in case (iii) than that in case (ii) even at $\tau_{ex} \gg \tau_{rise}$, though the time to reach the peak value is longer in case (iii). The scintillation response decays at the same rate for all the cases studied.

The study of the timestamps for different shapes of the front edge in luminescence response to fast excitation shows that the time resolution limits imposed by scintillation crystals have to be treated by taking into account the rise time of the response. The commonly used description of the time resolution is valid only in the case when the leading edge can be assumed to be instantaneous in comparison with the decay time. The correlation between the time resolution and the rise time in population of Ce^{3+} emitting level was analyzed in uncodoped and codoped GAGG:Ce by comparing the results of differential optical absorption, CTR measurements and the calculations using the model described above as case (iii).

Variable photon energy of excitation pulses in DA experiments enables selective excitation. The excitation by a 3.63 eV photon results in the transfer of an electron from level 4*f* to level $5d_2$ of Ce^{3+} ion in GAGG:Ce. The level $5d_2$ is already in the conduction band of GAGG host. Thus, the electron excited by a 3.63 eV photon might either remain at Ce^{3+} ion or leave the Ce ion. In the latter case, a Ce^{4+} ion and a free electron are result of the excitation: $h\nu + Ce^{3+} \rightarrow Ce^{4+} + e$. The electron is attracted to the geminate Ce^{4+} ion by Coulomb interaction and might be recaptured. However, there is certain probability for the electron to escape from the geminate ion in the process of thermalization [13]. The thermalization distance $l_e(E_{kin})$ depends on the electron kinetic energy E_{kin}. It is reasonable to assume that the distance r in real space between the endpoint of electron thermalization and the position of the geminate Ce ion is distributed according to a 3D Gaussian distribution function:

$$f(r, l_e, (E_{\text{kin}})) = \frac{3\sqrt{6}r^2}{\sqrt{\pi}l_e^3(E_{\text{kin}})} \exp\left(-\frac{3r^2}{2l_e^2(E_{\text{kin}})}\right). \tag{5.5}$$

The return of the electron to the geminate Ce^{4+} ion via the electron diffusion in the Coulomb field can be described by a time-dependent equation, which has no analytical solution. Instead, this process can be described by exploiting the model of the black sphere of recombination. According to this model, it is assumed that all electrons within this black sphere around the geminate Ce ion are captured by this ion to occupy the lowest excited $5d_1$ state of it. Meanwhile, the electron diffusion outside the black sphere proceeds with a negligible influence of the electric field. The radius of the black sphere R_{BS} depends on the temperature T and can be taken equal to the Onsager radius:

$$R_{\text{BS}} = \frac{e^2}{4\pi\varepsilon\varepsilon_0 k_{\text{b}} T}. \tag{5.6}$$

The electrostatic potential within this sphere is strong enough to prevent the electron from escaping the sphere due to thermal energy $k_{\text{B}}T$. Consequently, the electron returns to Ce^{4+} ion and recombines radiatively afterwards. Meanwhile, the attractive potential is assumed to be negligible outside this sphere. The fraction of electrons thermalized within the capture sphere

$$p(0) = \text{erf}\left(\sqrt{\frac{3}{2}}\frac{R_{\text{c}}}{l_e}\right) - \sqrt{\frac{6}{\pi}}\frac{R_{\text{c}}}{l_e} \exp\left(-\frac{3R_{\text{c}}^2}{2l_e^2}\right). \tag{5.7}$$

The fraction increases with time as

$$p(t) = \text{erf}\left(\sqrt{\frac{3}{2}}\frac{R_{\text{c}}}{l_e}\right) - \sqrt{\frac{6}{\pi}}\frac{R_{\text{c}}}{\sqrt{l_e^2 + 6D_e t}} \exp\left(-\frac{3R_{\text{c}}^2}{2(l_e^2 + 6D_e t)}\right) \times \left(1 - \text{erf}\left(\frac{3R_c}{l_e}\sqrt{\frac{D_e t}{l_e^2 + 6D_e t}}\right)\right) \tag{5.8}$$

where, D_e is the electron diffusion coefficient.

The probability for an electron to return to geminate Ce^{4+} ion approaches the limit $p(\infty) = \text{erf}\left(\sqrt{\frac{3}{2}}\frac{R_c}{l_e}\right)$ for $t \gg {l_e}^2/D_e$. Consequently, a fraction 1 – $p(\infty)$ of the nonequilibrium electrons leave the geminate Ce^{4+} ion forever. These electrons move through the crystal matrix possibly experiencing trapping and detrapping and finally recombine radiatively at Ce^{4+} centres created due to the absorption of other pump photons or nonradiatively. These processes cause hyperbolic decay tails in the electron population kinetics.

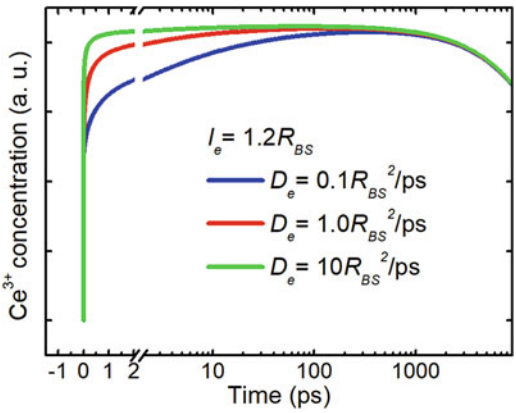

Fig. 5.20 Kinetics of Ce^{3+} $5d_1$ level population calculated at three electron diffusion coefficients (indicated) and a thermalization length of $1.2R_{BS}$

The time evolution of the population of Ce^{3+} excited state $5d_1$ for three values of the diffusion coefficient at the population decay time of 40 ns is presented in Fig. 5.20. For the black sphere radius $R_{BS} = 10$ nm, which is a typical value of the Onsager radius at 300 K, the diffusion coefficient $D_e = {R_{BS}}^2/\text{ps} = 1$ cm^2/s. Thus, the kinetics in Fig. 5.20 were calculated in the vicinity of this value: for 0.1, 1, and 10 cm^2/s. This diffusion coefficient is of the same order of magnitude as the $D_e = 0.21$ cm^2/s in CsI calculated using the Einstein formula $\mu = qD/k_BT$ and the value of the room-temperature electron mobility of 8 cm^2/(V·s) reported in [64].

The simulated kinetics presented in Fig. 5.20 are similar to those obtained experimentally (see Fig. 5.13). This result shows that the rise time is sensitive to the electron diffusion coefficient, which is predominantly determined by the shallow trap concentration, which, in turn, strongly depends on the codoping level.

As seen in Fig. 5.21, the measured and calculated kinetics of the population of Ce^{3+} level $5d_1$ are similar, however, the rising part of the simulated kinetics is more extensive than that of the experimental DA kinetics. This discrepancy is interpreted by the contribution of the electrons escaped beyond the black sphere from their geminate Ce ions. The experimental data on DA kinetics for three samples and the calculated curves are compared in Fig. 5.21. The calculated curves are presented as the convolution of the simulated population kinetics and the instrumental function with a Gaussian shape $\frac{1}{\sqrt{2\pi\sigma^2}} e^{\left(\frac{-t^2}{2\sigma^2}\right)}$ at $\sigma = 400$ fs. The simulations were performed for $l_e = 1.25R_{BS}$ and three values of D_e. The response on a step function is also presented in Fig. 5.21. The simulated kinetics fit the experimental data quite well, in spite of the application of the model of a black sphere, which is a simplification in comparison with more complicated models accounting for a more realistic shape of the Coulomb attractive potential. The diffusion coefficients used to simulate the red, blue, and green solid curves in Fig. 5.21 are 0.08, 0.25 and 1 cm^2/s, respectively.

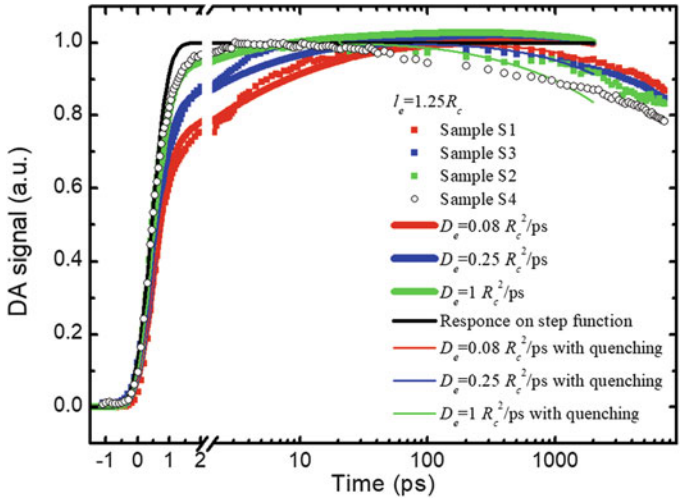

Fig. 5.21 Kinetics of differential absorption at 1.4 eV in four GAGG scintillators pumped at 3.63 eV (points) and simulated at different diffusion coefficients without (thick solid lines) and with (thin solid lines) quenching taken into account for the parameters indicated. The kinetics as a response to a step function is also presented. The diffusion coefficients used in the simulation are 0.08, 0.25, and 1 cm^2/s for red, blue, and green curves, respectively. (Reprinted with permission from Ref. [24])

As seen on Fig. 5.21, the increasing part in the experimental kinetics is substantially shorter than that in the simulated kinetics. The decrease in the experimental kinetics depends on the crystal. In certain crystals, the peak DA is reached a few picoseconds after excitation, whereas the rising part of the kinetics might continue up to ~100 ps. This additional contribution to the delayed DA response is interpreted by the influence of the electrons escaped outside the black spheres around their geminate cerium ions. These electrons can initiate a nonradiative Auger-type reaction

$$Ce^{3+*} + e \rightarrow Ce^{3+} + \text{high-energy e} \tag{5.9}$$

and, consequently, quench the radiative recombination at the Ce ions. The quenching rate depends on the density of free electrons escaped from their geminate Ce ions, the concentration of excited cerium ions Ce^{3+*}, and the electron diffusion coefficient. At the initial stages after excitation, the density of excited Ce ions depends on the rate of the radiative decay with a characteristic time τ_r (~60 ns in GAGG:Ce) and the rate of Auger processes, which depends on the electron diffusion coefficient. The density depends on time as $e^{\left(-\frac{t}{\tau_r} - a\sqrt{D_e t}\right)}$, where a is a parameter depending on the electron density, the concentration of Ce^{3+*} ions, and the Auger

interaction coefficient. Therefore, the influence of the nonradiative Auger recombination increases with increasing electron diffusion coefficient. The kinetics simulated with the quenching due to the Auger recombination taken into account are depicted by thin lines in Fig. 5.21. The fit of the simulated curves to the measured ones is improved.

The description presented above enables matching the experimental results obtained by exploiting the differential optical absorption with the data obtained in the experiments using excitation with a large excess energy (excitation by X-rays, γ-quanta or ionizing particles). The selective optical excitation of a Ce^{3+} ion results in the generation of an excited ion Ce^{3+*} or a pair of Ce^{4+} ion and electron. The kinetic energy E_{kin} of the electron produced in the latter process equals the difference between the photon energy and the energy distance between Ce^{3+} ground state $4f$ and the bottom of the conduction band (about 0.2–0.4 eV). Meanwhile, the energy transfer to Ce^{3+} ion under excitation by ionizing radiation has additional stages of excitation relaxation with the generation of electron-hole pairs and the transfer of the excitation to the Ce^{3+} ions.

Though the excitation transfer in Gd-based materials is addressed in many studies since the pioneering attempts reported in [27, 40, 44], these processes are not well understood up to now. The transfer has different routes. One of them is the route facilitated by the Coulomb dipole-dipole interaction via the Gd sublattice [27, 45]. However, the transfer time from Gd sublattice to the excited state of Ce^{3+} $5d_1$ is in the domain of microseconds or even milliseconds [45, 46]. Another route is the transfer by self-trapped excitons (STEs), which are formed by the oxygen-based valence band and the conduction band. The formation of STEs was found to be quite efficient in the crystals containing no gadolinium. Quite often, the STEs are optically inactive and can't be observed in the absorption and emission spectra, though they might transfer the energy to cerium ions. This is a dipole-dipole energy transfer, which is accomplished after exciton diffusion to Ce ions. The mean distance, which an exciton should pass to reach a Ce^{3+} ion, is proportional to the concentration of Ce ions as $n_{Ce}^{-1/3}$. Therefore, the exciton transition time is proportional to $\frac{1}{n_{Ce}^{2/3} D_{ex}}$. The final stage of the energy transfer is a bimolecular-type reaction between an exciton and a cerium ion. The rate of the energy transfer from an exciton to a Ce^{3+} ion is proportional to the exciton density. The result of the energy transfer from the exciton to excite a Ce^{3+} ion or to generate a pair of Ce^{4+} and electron is similar to the excitation of Ce ion by a photon. However, the energy of the excitons generated by ionizing radiation is higher than the photon energy at selective photoexcitation of Ce^{3+} ions. Therefore, the radiation-generated electrons have a larger kinetic energy E_{kin}. The thermalization length of these electrons is larger than that at photoexcitation. Consequently, the irradiation-induced population of Ce ions should proceed substantially slower than after photoexcitation.

The data on the processes forming the response of GAGG:Ce scintillator are still scarce and fragmental. Thus, sketching the main processes responsible for the response is still quite schematic. First of all, the excitation density is different along the excitation track in a wide range from 10^{14} to 10^{21} cm^{-3}, according to the

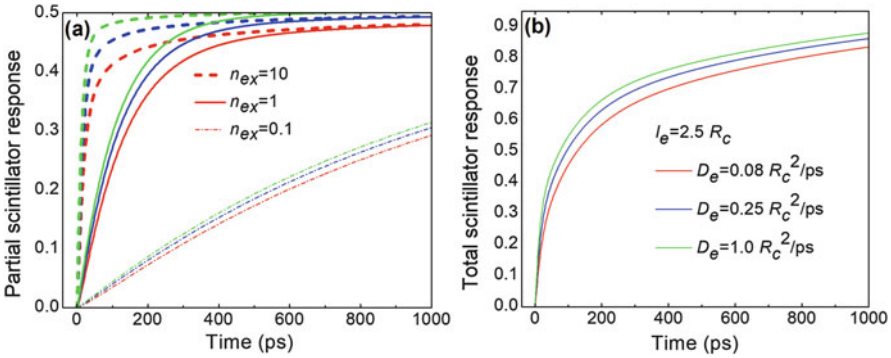

Fig. 5.22 Time evolution of partial (**a**) and total (**b**) concentration of excited cerium ions simulated at three relative exciton densities (indicated by line type) and three values of electron diffusion coefficient (indicated by colour). (Reprinted with permission from Ref. [24])

estimates for CsI [69]. In Fig. 5.22a, the time evolution of the density of excited cerium centres is presented for three exciton densities and three diffusion coefficients, which were extracted for three typical GAGG-based scintillators by fitting of the simulated results and DA kinetics. Furthermore, the curves were integrated over the distribution of the excitations (see Fig. 5.22b) assuming that the average distance between free electron and Ce^{4+} at the excitonic energy transfer is larger than that after the laser excitation and that $l_e = 2.5R_c$. Since the lifetime of the excited cerium ions Ce^{3+*} is substantially longer (~60 ns in GAGG:Ce), the rise time of the total scintillator response presented in Fig. 5.22b reflects the rate of the increase in the concentration of excited ions. The time evolution of the response is qualitatively similar to that observed in the measurements of the leading edge of Ce emission in other garnet crystals [70].

The time evolution of the number of emitted photons is presented in Fig. 5.23. The dependences presented there were calculated for three values of D_e extracted by fitting the experimental data on DA kinetics. The photon count rate of 340 ph/ns used in the calculations was estimated for a light yield of 40,000 ph/MeV (a typical value for 511 keV excitation of GAGG:Ce) and a luminescence decay time of 60 ns. For the detection of a γ-quantum by a photodetector coupled to the scintillator, the number of photoelectrons generated in the photodetector should exceed a certain threshold. The threshold of 5 photoelectrons is taken for the following estimates. Not every photon generates a photoelectron: a part of the photons is lost on the border coupling the scintillator crystal with the photodetector, whereas the quantum efficiency of the photodetector is well below 100%. Therefore, it is estimated that 15 photons are necessary to generate the 5 photoelectrons corresponding the detection threshold. Therefore, the time resolution in the detection of a 511 keV γ-quantum corresponds to the time necessary to emit 15 photons (see horizontal line in Fig. 5.23). Three values of the time resolution corresponding to the three experimentally estimated values of D_e are 108 ps, 116 ps, and 128 ps (see vertical lines in Fig. 5.23). The same time resolutions Δt can be calculated using the

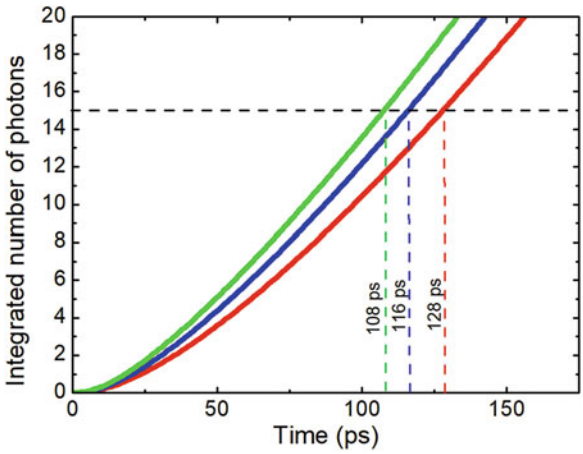

Fig. 5.23 Time evolution of the number of emitted photons calculated for three values of electron diffusion coefficients (indicated), which were used in fitting the experimentally obtained differential absorption kinetics. (After Ref. [24])

characteristic times Δt_{CTR} in CTR experiments: $\Delta t = \Delta t_{CTR}/\sqrt{2}$. The Δt values calculated using Δt_{CTR} measured for the same three samples are 117 ps, 129 ps, and 136 ps, in good correspondence with those estimated from Fig. 5.23. The estimate is obtained under several quite rough assumptions, however, the key result is in the observation that the rise time in DA kinetics observed in GAGG:Ce scintillators and varying on the time scale of 10 ps correlates well with the time resolution of the order of 150 ps extracted for the crystals in CTR experiments. The origin of the correlation is the dependence of both the time characteristics on the electron diffusion coefficient. The study described above evidences that the differential absorption measurements, which are contactless and ensure subpicosecond time resolution, is a prospective method to study the time resolution of scintillators to be exploited in fast radiation detectors.

5.3.4 Bi-Cation Garnets Doped with Ce

The non-equilibrium carrier dynamics has been tested also in binary garnets $Y_3Al_5O_{12}$ and $Lu_3Al_5O_{12}$ solely doped with Ce and codoped with Mg. Binary garnets have no compositional nonuniformity like $Gd_3Al_2Ga_3O_{12}$:Ce, in which Al and Ga ions are inhomogeneously distributed in the crystal matrices. However, the binary garnets have certain structural inhomogeneity: the small-ionic-radius ions Y^{3+} and Lu^{3+} might occupy not only the positions with an eightfold oxygen coordination but also the positions with octahedral coordination [55, 71]. The probability to take the location with octahedral coordination is quite substantial due to the high crystallization temperature of the garnet-type materials, which results in high ion mobility at the crystallization front. Such structural nonuniformity might also cause carrier trapping. These traps are formed by the isovalent exchange of trivalent ions in the matrix, thus, they should be shallow. Therefore, the influence of the traps on the

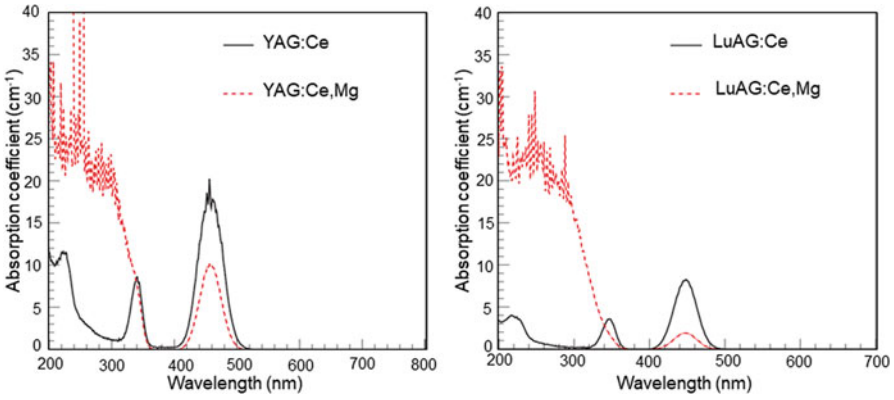

Fig. 5.24 Absorption spectra of YAG (**a**) and LuAG (**b**) solely doped with Ce (black) and codoped with Ce and Mg (red). (After Ref. [15])

process of populating the Ce^{3+} radiating state should be similar to the influence of the traps due to the compositional nonuniformity in GAGG. Moreover, the impact of codoping on the contribution of these traps should be the same.

The light yield of the binary Ce-doped garnet-type scintillators is quite high, though smaller than that of GAGG:Ce [33]. Their luminescence decay time is shorter than 100 ns, and their emission band peaks in the range 520–560 nm. An essential difference between YAG/LuAG and GAGG crystals is the absence of numerous *f* levels in the band gap. The absorption spectra of Ce-doped YAG and LuAG crystals with and without Mg codoping at the level of 20 ppm are presented in Fig. 5.24.

Uncodoped YAG:Ce and LuAG:Ce crystals exhibit 4*f*-5*d* absorption bands corresponding to inter-configurational transitions of Ce^{3+} ions. In addition, the absorption spectra of Mg-codoped crystals contain a broad absorption band peaking at 4.7 eV (265 nm). This band is better pronounced in the LuAG:Ce crystal having a lower concentration of Ce^{3+} ions. Supposedly, this absorption band is caused by charge transfer (CT) transitions from the valence band to the defect, which is stabilized by Mg^{2+}, as in GAGG:Ce,Mg.

The kinetics of differential absorption for two probe wavelengths [29] are presented in Figs. 5.25 and 5.26 for YAG and LuAG, respectively.

The pump at a wavelength of 263 nm excites Ce^{3+} ions in a long-wavelength shoulder of the third component of $4f_1$-$5d_1 4f_0$ transition. This excited level is located in the conduction band. Thus, the delocalization of the excited electrons into the conduction band and their capture by traps might be expected. Moreover, the pump might also cause CT transitions from the valence band to the defect centres introduced by the codoping with divalent impurities and, as a result, create holes in the valence band.

Contrary to GAGG, both YAG:Ce and LuAG:Ce without codoping exhibit no fast component in the DA decay. The initial parts of ΔD kinetics for probe photons in

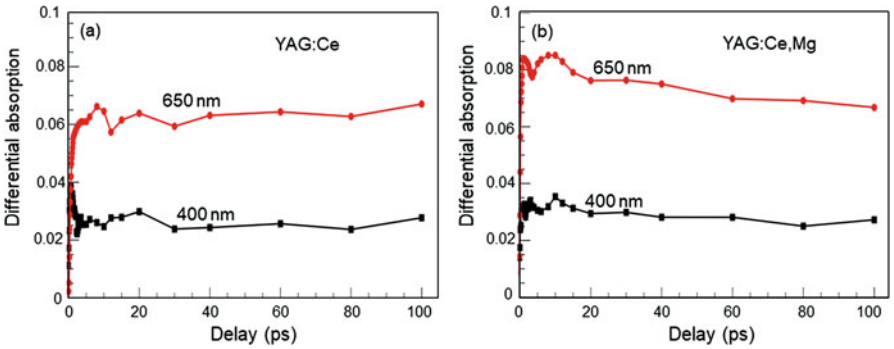

Fig. 5.25 Kinetics of differential absorption at two probe wavelengths (indicated) after excitation at 263 nm (4.75 eV) in YAG:Ce (**a**) and YAG:Ce,Mg (**b**). (After Ref. [29])

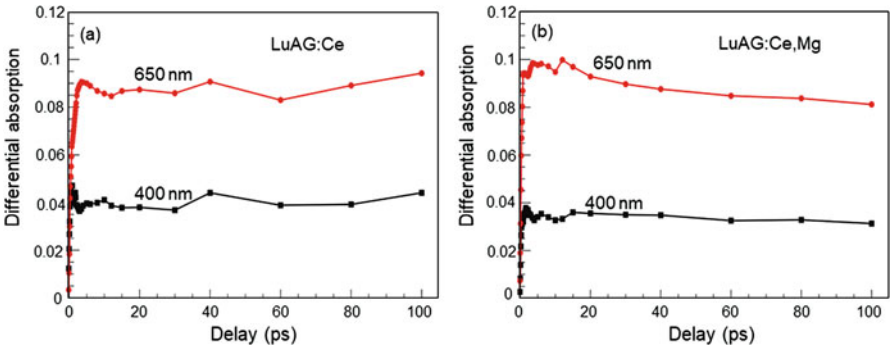

Fig. 5.26 Kinetics of differential absorption at two probe wavelength after excitation at 263 nm (4.75 eV) in LuAG:Ce (**a**) and LuAG:Ce,Mg (**b**). (After Ref. [29])

blue-green and red spectral ranges are compared in Fig. 5.27. The most indicative result is the change of the DA kinetics due to the absorption from $5d_1$ level of Ce^{3+}. In both garnets, the absorption exhibits opposite behaviour in uncodoped and codoped crystals. Free electrons are generated via the absorption of the probe photons by Ce^{3+} and the subsequent transfer of the electrons to the conduction band. In the uncodoped crystal, a part of the electrons are captured and reside on traps. The electrons on shallow traps have a high probability for thermal excitation and returning to Ce^{4+} to form an excited state Ce^{3+*}. This process causes the increase of DA in the time range up to 100 ps, indicating a delayed build-up of the population of Ce^{3+*}. Mg-codoping introduces the defects, which provide a fast channel for the nonradiative recombination of trapped electrons, which prevails over the thermally-induced detrapping. As a result, the slow component in the leading edge of DA response is diminished.

Meanwhile, the additional channel of nonradiative recombination, which is introduced by Mg codoping, reduces the light yield of garnet crystals. This is a general effect of aliovalent codoping in garnet-type scintillation crystals, which is

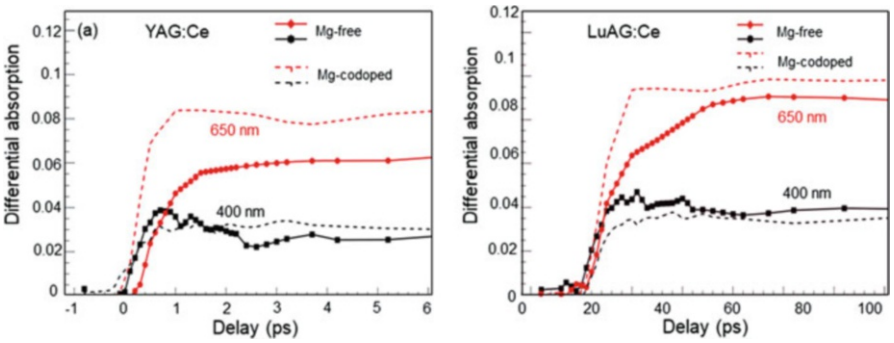

Fig. 5.27 The leading edge of the DA response after excitation at 263 nm for two probe wavelengths (indicated) in YAG:Ce (**a**) and LuYAG:Ce (**b**) without and with Mg-codoping. (After Ref. [29])

caused by effective blocking of the participation of shallow traps in the formation of the population of Ce^{3+} ions by draining of nonequilibrium electrons via the channel of nonradiative recombination involving the nonradiative recombination centres introduced due to Mg-doping. Therefore, the improvement of the scintillation pulse leading edge by codoping should be accomplished by taking into account the trade-off between a shorter rise time and a lower scintillation yield.

5.4 Ce-Doped Perovskites

Perovskite-type crystals $(Y_x\text{-}Lu_{1\text{-}x})AlO_3$ doped with Ce or Pr are prospective scintillators for fast radiation detectors [33]. $YAlO_3$:Ce (YAP:Ce) has a linear scintillation response for γ-quanta with energy down to a few keV and a high energy resolution, which is important for precision spectrometry in X-ray range. The development of the technology for production of YAP:Ce with a high light yield (20,000 ph/MeV) enabled large-scale applications [72–74], whereas the short luminescence decay time of 28 ns is attractive for fast detectors. YAP:Pr scintillators were introduced later [72] and exhibit even shorter luminescence decay time (13 ns [75]) but a lower light yield (7000 ph/MeV) [33]. The spectral position of YAP:Ce and YAP:Pr luminescence bands in UV (peaked at 260 and 295 nm, respectively) is a drawback for coupling the scintillators with conventional photodetectors.

High mechanical hardness, weak dependence of the light yield on temperature and exclusive resistance to fast temperature changes of YAP [76] enable application of YAP-based scintillators in detectors for oil well logging [77]. The YAP-based detectors exhibit a good energy resolution of 4.38% FWHM for 661.6 keV emission of ^{137}Cs [78], though have a low efficiency to detect γ-quanta in MeV range. YAP scintillators are also suitable for α particle detection [79] and are used in pulsed neutron generators [80].

Substitution of Y in YAP by Lu in $LuAlO_3$ (LuAP) increases the crystal density from 5.35 g/cm^3 to 8.34 g/cm^3 and the effective atomic number from 33.5 to 64.9. The luminescence decay time of LuAP:Ce is short, 17 ns, however, growth of high quality transparent single crystals of this scintillator is difficult and the crystals are expensive. LuYAP crystal, $(Lu_{1-x}\text{-}Y_x)AlO_3$, is considered to be a better choice (see, e.g., [33]). The contents of Y and Lu in LuYAP is varied to mitigate the technological difficulties encountered in the production of LuAP crystals and to optimize the scintillation properties [47, 81]. The highest light yield is found to be in the crystal containing equal parts of Lu and Y cations: $Lu_{0.5}Y_{0.5}AlO_3$ [58]. An increase of Lu/Y atomic ratio from 1:1 to 0.7:0.3 in the composition of LuYAP:Ce results in a decrease of the light yield from 14,000 ph/MeV to 12,000 ph/MeV and deterioration of CTR FWHM from 405 ± 6 ps to 438 ± 6 ps [30].

The data carpets of the measurements of differential absorption in $YAlO_3$, $Lu_{0.5}Y_{0.5}AlO_3$, and $Lu_{0.7}Y_{0.3}AlO_3$ are presented in Fig. 5.28 for two pump photon energies: 4.35 eV and 5.91 eV.

The ground *f* state of Ce^{3+} ion is 1.8 eV above the top of the valence band [30], whereas the band gap of YAP equals 7.8 eV and does not change significantly with the substitution of Y with Lu [82]. Therefore, the 4.35 eV photons resonantly excite Ce^{3+} ions from their ground state to the first excited level $5d_1$. The level is well below the bottom of the conduction band, so that no thermally excited exchange between the level and the conduction band is expected. The DA data carpet has one feature spectrally centered in the vicinity of 2.1 eV, which is due to the absorption by the electrons occupying level $5d_1$.

The pump photon energy of 5.91 eV resonantly excites the Ce^{3+} ion to its level $5d_2$, which is expected to be in the conduction band. The nonequilibrium electrons have two relaxation routes to the first excited level $5d_1$ acting as an emitting level. The first route is intracenter relaxation from $5d_2$ to $5d_1$. The second one involves the extended states in the conduction band. The electron relaxes to the bottom of the conduction band, migrates through the crystal and might be captured by trapping centers. Subsequently, the electron might either return to the initial Ce^{3+} ion (to its lowest excited state $5d_1$), or move to the next Ce ion, or relax down to a center of nonradiative recombination.

The DA kinetics obtained by making cross-sections of the data carpets presented in Fig. 5.28 are presented in Fig. 5.29. At excitation to the lowest excited state, the rise time is in subpicosecond domain in all the samples. In YAP:Ce, the kinetics is similar also at excitation to the second excited state at 5.9 eV, though certain delay in DA response is observed. The delay at 5.9 eV excitation is much longer in LuYAP:Ce and is more pronounced with increasing Lu content. Moreover, the decay after the DA response reached its maximum proceeds faster than that at 4.35 eV pump. This behaviour is explained by carrier trapping. The trapping is enhanced by introducing Lu, since additional electron trapping due to composition fluctuations is expected, as in other multicomponent scintillators like LYSO:Ce and GAGG:Ce discussed above.

Lutetium ions have the smallest ionic radius among all the rare earth elements, thus, the perovskite crystals containing lutetium, like the garnets consisting of the

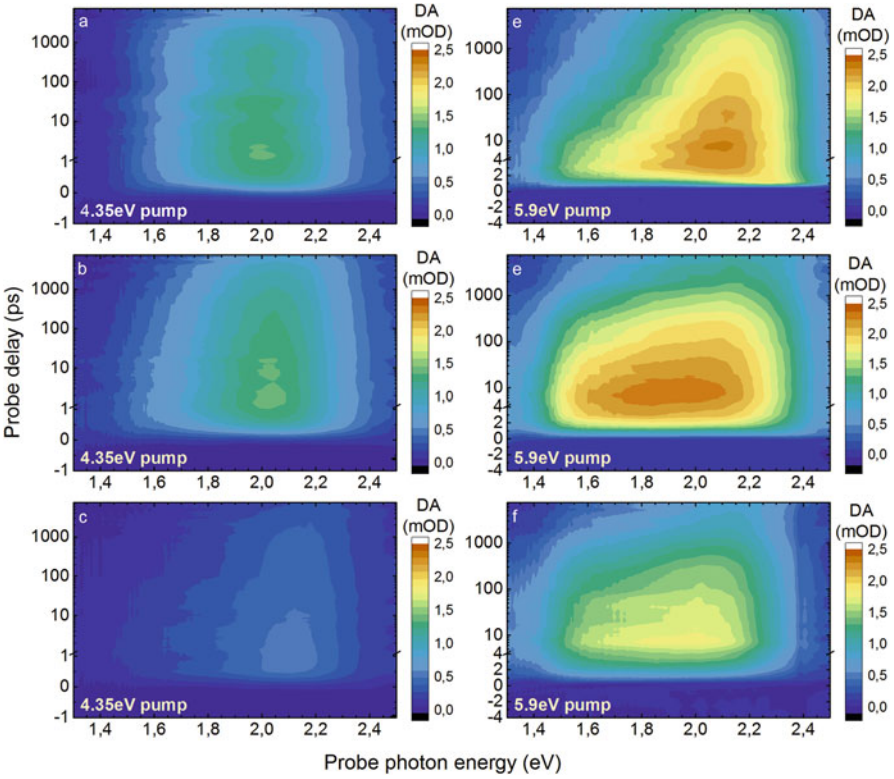

Fig. 5.28 Differential absorption (color scale) as a function of probe photon energy and delay between pump and probe pulses at pump photon energy of 4.35 eV (left column) and 5.91 eV (right column) in samples $YAlO_3$ (**a**, **d**), $Lu_{0.5}Y_{0.5}AlO_3$ (**b**, **e**), and $Lu_{0.7}Y_{0.3}AlO_3$ (**c**, **f**). (Reprinted with permission from Ref. [30])

same chemical elements, are prone to antisite defects Lu_{Al} [71], which might serve for additional carrier localization. The radius of Lu ion varies from 0.86 Å in sixfold to 1.03 Å in ninefold oxygen coordination. In the orthorhombic structure, nine oxygen O^{2-} ions are located closer than three additional ones. Thus, the ionic radius of lutetium in 12(O)-fold coordination is close to that in 9(O)-fold coordination. A fraction of Lu ions might form trapping centers by occupying sites in oxygen octahedra. In the garnet structure, such traps have activation energy of ~0.2 eV [83], i.e., are deeper than the traps due to composition fluctuations. A similar situation is observed in perovskite-structure crystals [47, 84]. Therefore, the antisite defects Lu_{Al} slow down the population of Ce^{3+} radiative level. The effect is expected to be more pronounced in perovskites than that in multicomponent oxyorthosilicates like LYSO having the host matrix formed by silicon tetrahedra, where Lu cannot be localized. Thus, the content of Lu_{Al} antisite defects in LYSO:Ce is lower, and the scintillator exhibits a better time resolution [85].

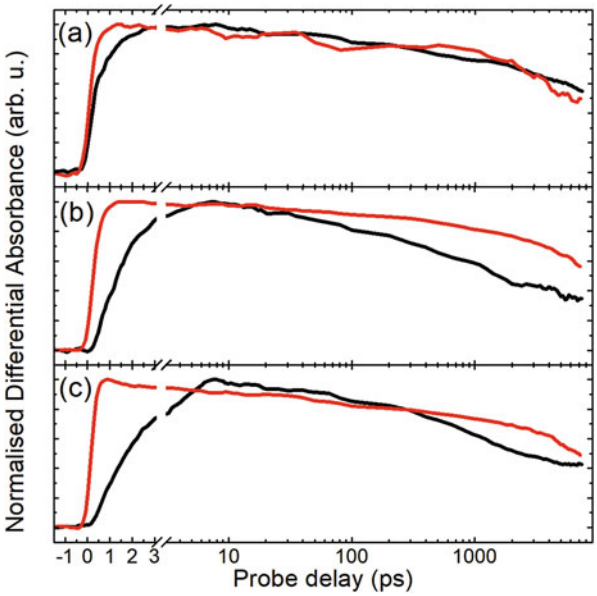

Fig. 5.29 Differential absorption kinetics in $YAlO_3$ (**a**), $Lu_{0.5}Y_{0.5}AlO_3$ (**b**), and $Lu_{0.7}Y_{0.3}AlO_3$ (**c**) excited at 4.35 eV (red line) and 5.91 eV (black) and probed at energies indicated. (After Ref. [30])

Summing up, the study of nonequilibrium carrier dynamics in Ce-doped YAP shows that the introduction of Lu results in delayed electron transfer to the lowest excited Ce^{3+} level. As in other multicomponent scintillators, the trapping in LuYAP:Ce is enhanced by localization in the minima of the spatial potential fluctuations due to composition fluctuations. The formation of antisite defects Lu_{Al}, which has a high probability in this crystal, also serves for electron trapping. Though introduction of Lu substantially increases the crystal density, what is beneficial for many applications in radiation detectors, the high Lu content results in decreased light yield and increased luminescence response time.

5.5 Doped Halides

5.5.1 Doped Iodides NaI, CsI, SrI_2

The study of nonequilibrium carriers by using differential optical absorption has been performed also in classical metal iodide scintillators. NaI:Tl and CsI:Tl were the first bulk single crystal materials to be used as scintillators on a wide scale. In spite of the expanding variety of applications demanding specific properties of

scintillation detectors, NaI:Tl remains the dominant scintillation material with world-wide production volume by far outweighing that of all other scintillating materials. CsI:Tl is also extensively exploited as scintillator. Undoped CsI exhibits STE luminescence, which is peaked at 4.1 eV and has a short decay time of 15 ns at room temperature [86], or fast intrinsic luminescence [87]. Introduction of Tl increases the light yield. However, a high afterglow level is an important drawback of CsI-based scintillators and limits their suitability for certain applications.

The DA amplitude as a function of the probe photon energy and the delay between pump and probe pulses is presented on a pseudo-3D display in Fig. 5.30 for CsI and CsI:Tl with different Tl contents [25]. Pump pulses of 500 fs in duration were used for band-to-band excitation of the crystal via two photon excitation.

Three signatures in spectrum and time were observed in the DA response of CsI. The first two signatures are attributed to absorption by STE. The signatures spectrally peaked at 0.5 eV and 0.7 eV are attributed to type-I (with on-center configuration) and type-II (with off-center configuration) STEs, respectively. Both these signatures have a rising part with a characteristic rise time of 4 ps, which reflects the time necessary to form a STE. The time increases with increasing excess energy of photoexcited electron-hole pair. The spectrum of the third signature is broader. The DA in this signature rises in subpicosecond domain and decays with a characteristic time of 1–2 ps. It is assigned to the absorption of free carriers. The decay of this signature reflects trapping of the free carriers.

As seen in Fig. 5.31, the introduction of Tl decreases the intensity of the DA caused by STE. This is expected due to excitation transfer from STE to tellurium ion.

The differential absorption of NaI:Tl and SrI_2:Eu contains the same signatures of STE and free carriers, though not so clearly pronounced, as in the DA of CsI:Tl. Moreover, the study of DA in SrI_2:Eu revealed an interesting feature: the introduction of Eu in SrI_2 results in substantial shortening of free carrier decay down to a characteristic decay time of ~400 ps in SrI_2 with 3% of Eu. The fast excitation transfer from SrI_2 host to activator correlates with a substantially higher light yield of SrI_2:Eu, compared to that of CsI:Tl or NaI:Tl, where the transfer is slower [25].

5.5.2 *Cerium and Lanthanum Bromides: $CeBr_3$, $LaBr_3$:Ce, $La_{1-x}Ce_xBr_3$*

The contribution of STE in differential optical absorption induced by band-to-band excitation is also identified in $LaBr_3$ [26]. This observation is in line with the STE luminescence observed in this material [88] and EPR spectra of similar chalcogenide $LaCl_3$ [89]. Data on the DA as a function of probe photon energy and delay between pump and probe pulses in $LaBr_3$:Ce with different Ce content are presented in Fig. 5.32.

The time of STE formation in $LaBr_3$ is in subpicosecon domain even at the excess energy of photoexcited electron-hole pair of ~3 eV. DA signatures due to absorption

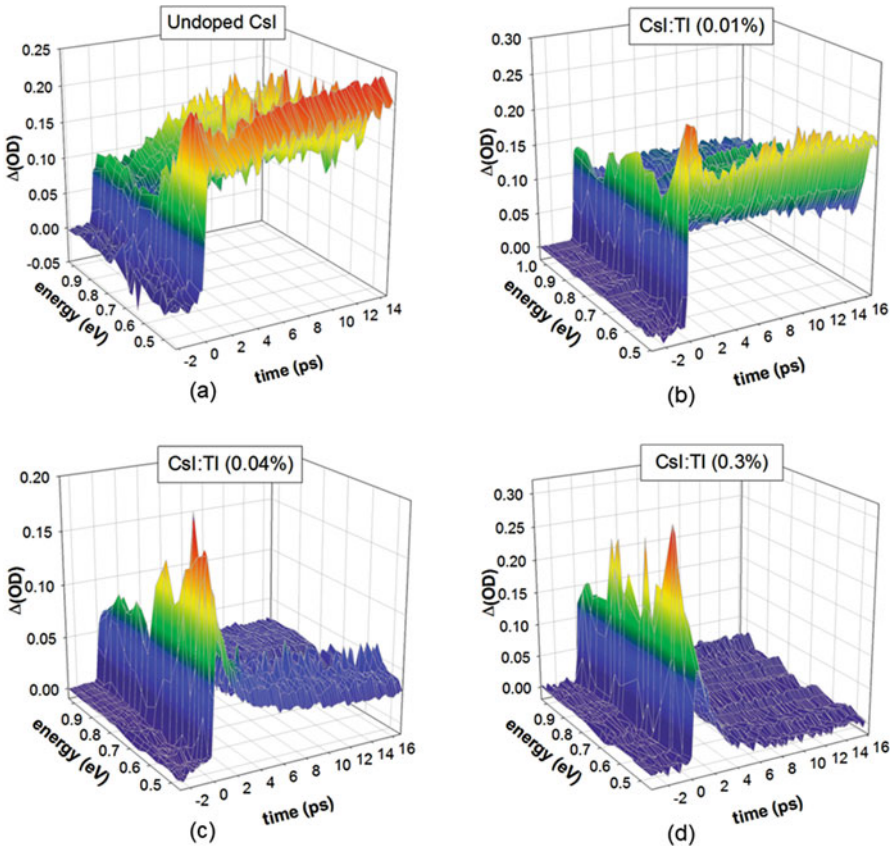

Fig. 5.30 Time evolution of the spectra of photoexcitation-induced change in optical density in CsI:Tl single crystals with different Tl content (indicated). 500-fs laser pump pulses with photon energy of 2.95 eV were used for excitation via two-photon absorption. (Reprinted with permission from Ref. [25])

by electron (in IR and red spectral regions) and hole (in UV region) in STE have been observed. The contributions of STEs in on-center (type I), weakly off-center (type II) and strongly off-center (type III) configurations have been identified.

At resonant excitation of Ce^{3+} ions, an additional DA signature spectrally peaked at 2.1 eV becomes progressively evident with increasing level of Ce-doping. The introduction of Ce suppresses the DA due to STE and decreases its decay time down to 1 ps (at band to band excitation). The excitation transfer from the host to the activator ion Ce^{3+} acting as an emitting centre in $LaBr_3$:Ce might proceed via two routes: subsequent capture of nonequilibrium hole and electron or dipole-dipole transfer from STE. The results on DA study [26] evidence the excitonic transfer mechanism.

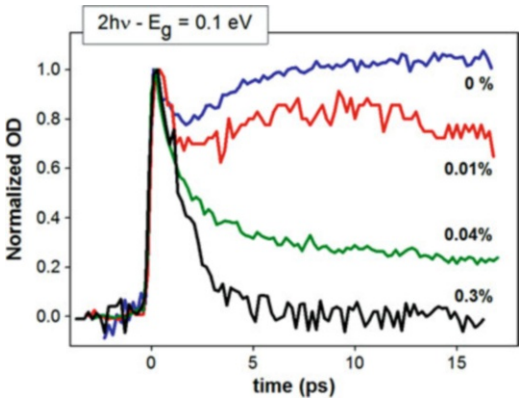

Fig. 5.31 Normalized differential absorption at probe photon energy of 0.5 eV in CsI:Tl with different Tl doping levels (indicated). (Reprinted with permission from Ref. [25])

Cerium bromide $CeBr_3$ is currently the fastest and brightest self-activated Ce-based scintillator material exhibiting the scintillation decay time of 17 ns and having no slow rise component of the scintillation response [90], in contrary to that in the response front in $LaBr_3$:Ce [90–92]. The comparison of the differential absorption of $CeBr_3$ and $La_{1-x}Ce_xBr$ is recently reported in [31]. In Fig. 5.33, the data carpets of the DA measurements performed by two-photon band-to-band absorption are presented for a few compositions of $La_{1-x}Ce_xBr$ covering the entire range from $LaBr_3$ to $CeBr_3$.

As discussed in [31], DA signatures due to the transitions of electron from the excited state 5*d* to the conduction band and from the valence band to the hole at the ground state 4*f* of excited ion Ce^{3+*} are observed. Both the signatures reflect the formation and decay of cerium ion in its emitting state Ce^{3+*}. The population of Ce^{3+*} increases from 10% to 90% within ~1 ps after band-to-band excitation of nonequilibrium electrons and holes. The DA kinetics is in consistence with the assumption that the excitation is transferred to the emitting Ce ion from the bromine-based STE via dipole-dipole interaction. The STE formation time is well in subpicosecond domain. A similar excitation transfer, though at a slower rate, has been observed in $LaBr_3$:Ce, as discussed above. The difference in the transfer rate is caused by different dipole-dipole spacing in these materials. In $CeBr_3$, the transfer occurs to the nearest-neighbour ion at a distance of 0.3 nm, whereas the transfer in $LaBr_3$:Ce occurs over different spacings with their average value of ~3 nm, i.e., by a factor of 10 larger than the spacing in $CeBr_3$. No DA signatures of Ce^{4+} was observed. Therefore, the DA study shows that the extremely fast population of the emitting states of Ce ions in $CeBr_3$ is caused by an efficient excitation transfer from bromine-based STEs to Ce^{3+}.

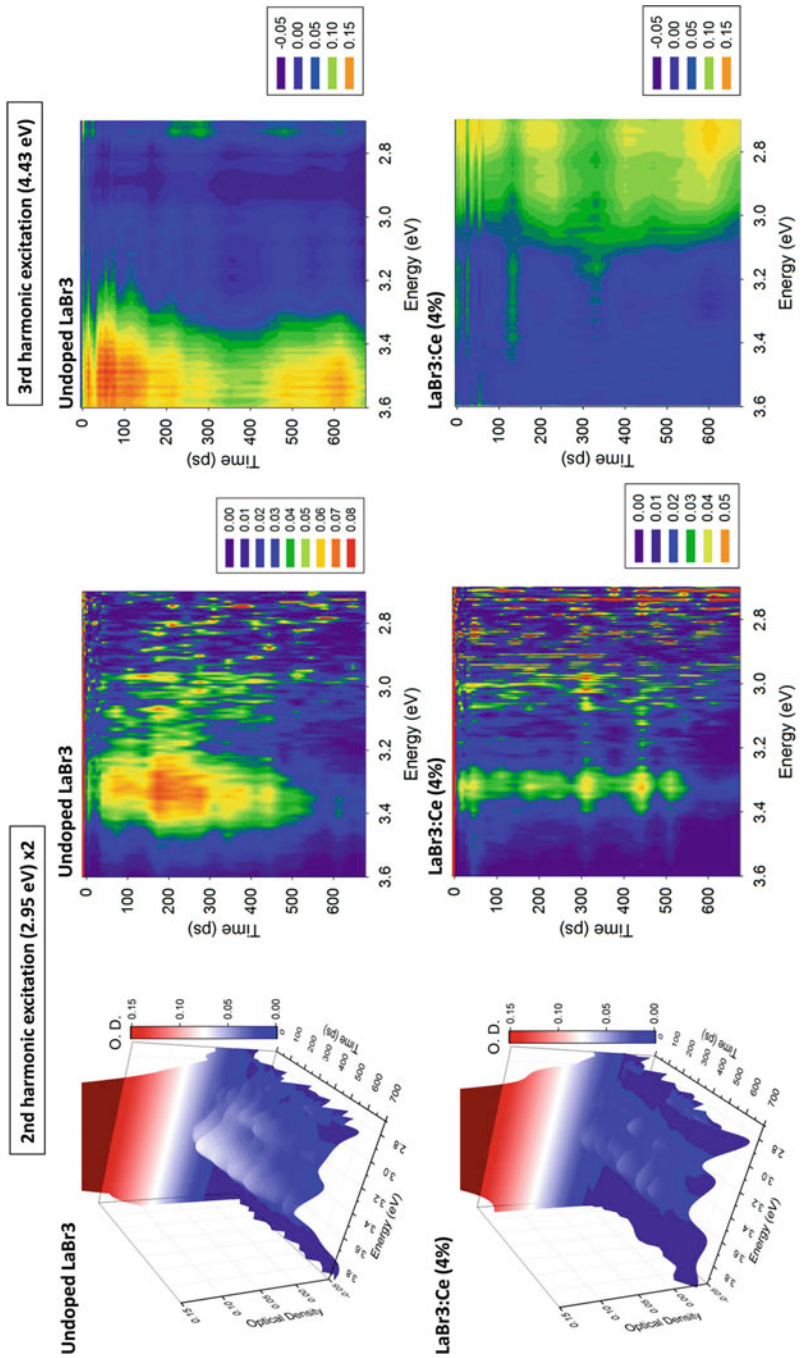

Fig. 5.32 Differential absorption (color scale) as a function of probe photon energy and delay between pump and probe pulses in $LaBr_3$ without intentional doping (upper row) and doped with 4% of Ce (lower row). Pump photon energies are indicated above the columns. (Reprinted with permission from Ref. [261])

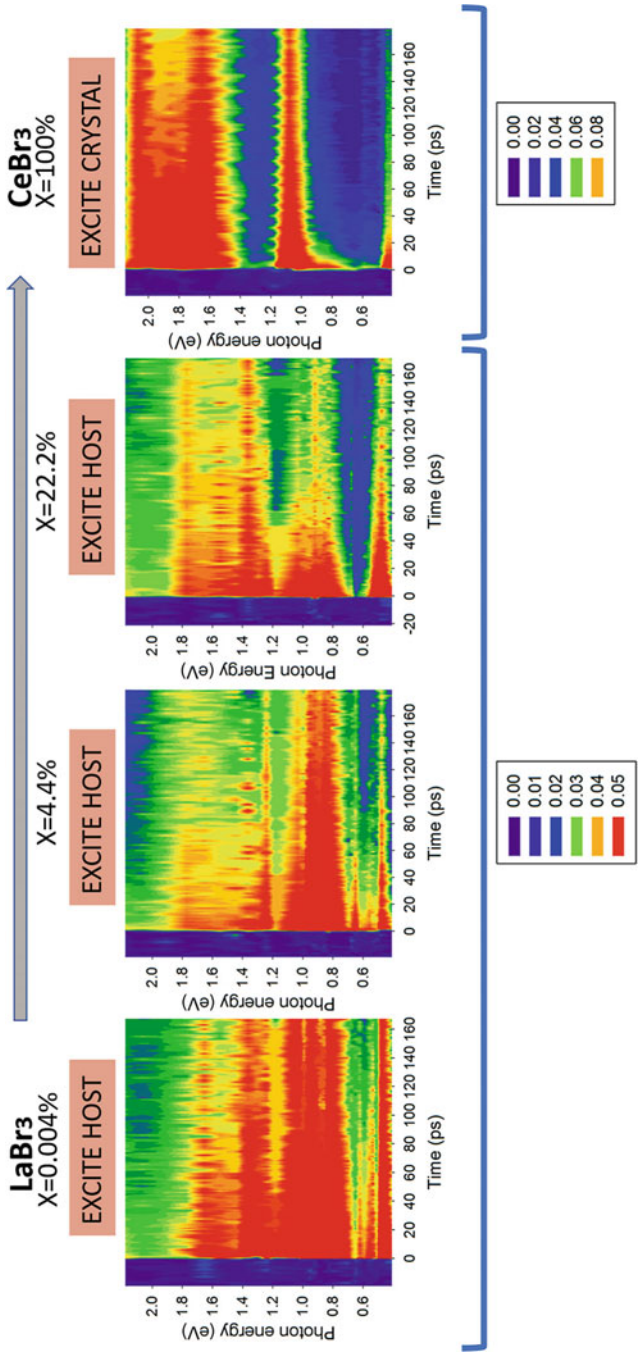

Fig. 5.33 Differential absorption (color scale) as a function of pump photon energy and delay between probe pulse and pump pulse exciting $La_{1-x}Ce_xBr$ with different x (indicated) via two-photon absorption of 2.95 eV pump photons. (Reprinted with permission from Ref. [31])

5.6 Heavy Self-Activated Scintillators

5.6.1 Lead Tungstate (PWO) Scintillator

Lead tungstate $PbWO_4$ (PWO) is a self-activated scintillator. Thus, a short rise time in luminescence response of this material is expected. The PWO luminescence decay time is also comparatively short, approximately 10 ns. Both these features are attractive in view of application of this material in fast scintillation detectors. However, a low light yield (by two orders of magnitude lower than that in high-light-yield scintillators like LYSO:Ce) deteriorates the timing properties of PWO. From the point of view of application in high-energy physics experiments, it is important that this material exhibits high radiation tolerance (see, e.g., [93]). PWO single crystals are nonhighroscopic, mechanically strong. Large, comparatively homogeneous ingots of PWO can be fabricated by the Czochralski technique, and the material properties can be improved by appropriate annealing [94]. The combination of all the properties put forward this material as the scintillator of choice in several large high-energy physics experiments, such as CMS and ALICE at LHC [95] and PANDA at GSI [96]. The comparatively low light yield limits the expectations to use PWO-based radiation detectors in the applications, where the fast timing is of the key importance. However, there are applications, where the PWO response time is sufficient, thus, a reinvestigation of the excitation dynamics in PWO with a better time resolution is currently on demand.

5.6.2 Kinetics of PWO Luminescence

Figure 5.34 presents typical photoluminescence spectra of lead tungstate of quality PWO-II, as usually referred to the PWO crystals of the second generation meeting certain quality standards [67]. The spectra consist of two spectrally overlapping bands [97]. The dominant band is peaked in blue region at ~420 nm and is usually attributed to the recombination at the regular host oxy-anionic complexes WO_4^{2-} [98, 99]. The second, green luminescence band is peaked in the vicinity of 550 nm and is attributed to recombination at oxygen-deficient oxy-anionic complexes WO_3 [98, 100]. The green luminescence is weak at band to band excitation (green line in Fig. 5.34) and becomes more pronounced at excitation with 3.61 eV photons below the band gap of PWO (4.33 eV at room temperature [33].

The initial part of PL kinetics is presented in Fig. 5.35. As expected for a self-activated material, the front edge of the luminescence response recorded after a short-pulse excitation follows the shape of the instrumental response function having a FWHM of 4.7 ps in the time-resolved photoluminescence measurements of the kinetics presented in Fig. 5.35. Thus, the PL rise time of PWO is in subpicosecond domain. The subpicosecond luminescence rise time of PWO is an indication that the

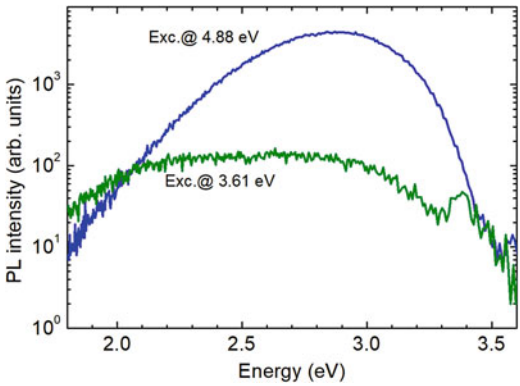

Fig. 5.34 Time-integrated PWO luminescence spectra after excitation at the wavelength of 254 nm (blue line) and 343 nm (green line). (After Ref. [101])

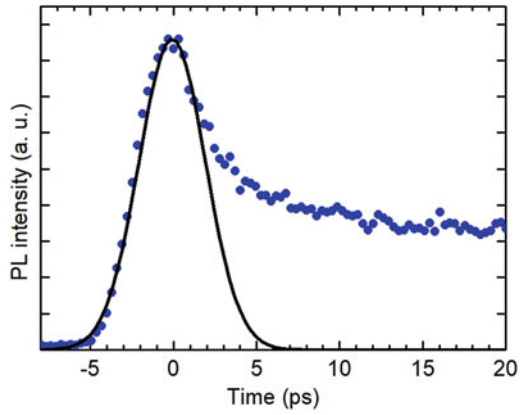

Fig. 5.35 Initial part of spectrally-integrated photoluminescence kinetics in PWO (blue dots) and the shape of the instrumental function (black solid line). (After Ref. [101])

relaxation of nonequilibrium carriers is an intrinsic process and is not significantly affected by crystal defects, at least at the quality of a standard PWO II crystal.

The short rise time at the 4.9 eV excitation of electron-hole pairs with excess energy of 0.6 eV above the band gap is consistent with the model of relaxation of germinal carrier pairs to the radiating states at oxy-complexes WO_4^{2-}.

Under excitation of the nonequilibrium electron-hole pairs by ionizing radiation, the germinal pairs are most probably disconnected in the thermalization process. However, no substantial increase in the rise time of the scintillation response is expected, since the thermalization occurs via the emission of phonons on the time scale of picoseconds or even shorter. Moreover, the energy deposit to the PWO detectors in the high-energy physics experiments like those in LHC experiments occurs within a time period of less than 1 ns by interaction with high-energy particles having energies of hundreds of GeV. Thus, the density of free carriers is high enough to prompt coupling of electrons and holes.

The rise time in subpicosecond domain is also observed at excitation with 3.64 eV photons, which are below the band gap. This is an indication of a fast establishing of the equilibrium between regular and oxygen-deficient tungsten octahedra.

As evidenced in many investigations, the characteristic luminescence decay time in PWO single crystals is 8–10 ns. PWO exhibits thermally quenched luminescence, i.e. the luminescence decay time in this material is determined not by the rate of radiative recombination but rather by nonradiative recombination of thermally activated carriers. The recent measurements of the luminescence decay with picosecond time resolution using a streak camera [101] revealed two more decay components. The fastest component decays with a characteristic decay time of 3.8 ps at 3.61 eV selective excitation or 5.9 ps at 4.88 eV band-to-band excitation. This decay component is more pronounced after below-band-gap excitation at 3.61 eV. This component was attributed to radiative decay of F^+ centers. The intermediate PL decay component decays with the decay time of approximately 800 ps (683 ps or 824 ps extracted by fitting the PL decay kinetics after short-pulse excitation at 3.61 eV and 4.88 eV, respectively). The existence of this decay component was observed but not numerically characterized in the early work of Nikl et al. [102]. The intermediate decay component might be interpreted by the luminescence originating from the thermally quenched luminescence of complexes WO_4^{2-} + RE^{3+}, where RE^{3+} stands for La^{3+} or Y^{3+}, which are introduced in scintillation crystals PWO II, which are currently in use for applications [98]. A positive impact of the intermediate component on the leading edge of the scintillation pulse in PWO is discussed in Chap. 2.

From the practical point of view, it is important that both spectral components, blue and green, decay at the same rate. Moreover, the decay rate does not depend on the density of nonequilibrium carriers, as evidenced by the study of PWO PL kinetics at different excitation intensities. This feature is important for proportionality of the scintillator response.

5.6.3 Differential Absorption in PWO

Typical kinetics of differential optical absorption in PWO at pump photon energy of 4.88 eV, probe photon energy of 1.2 eV and different excitation pulse energy densities are presented in Fig. 5.36. At low excitation intensities, the pump pulse induces certain differential absorption relaxing with characteristic time substantially exceeding the measurement time window of 7 ns. At elevated excitation intensities, the DA signal with a faster decay is observed. The decay can be fitted by a biexponential decay with two decay constants of approximately 200 ps and 2 ns. The two time constants do not match with the two time constants of the fast decaying part of luminescence (4–6 ns and ~800 ps, see above). The luminescence intensity reflects the density of the excited complexes WO_4^{2-} acting as the emitting centers. The DA might have contributions of all nonequilibrium carriers, including free electrons and holes and those on the complexes WO_4^{2-} located in the regular matrix

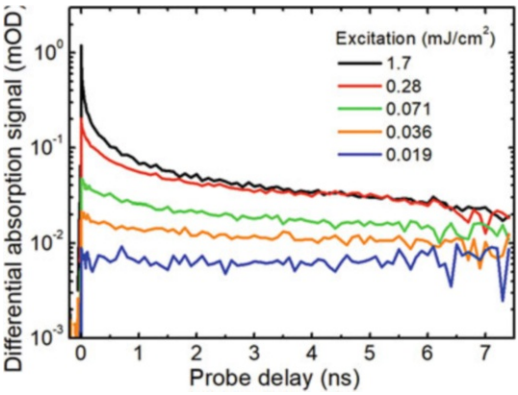

Fig. 5.36 Kinetics of differential optical absorption of PWO at pump photon energy of 4.88 eV, probe photon energy of 1.2 eV and different excitation pulse energy densities (indicated). (After Ref. [61])

and near La^{3+} or Y^{3+} ions, which are routinely introduced in PWO II crystals, and defect centers. The discrepancy in the decay constants reflecting the mechanisms of DA and PL might be interpreted by assuming that a part of excitations are captured at the complexes WO_4^{2-} faster than the other part of the excitations, like the fast and slow formation of STEs in metal bromides [26].

The excitation intensity dependence of the DA response is presented in Fig. 5.37. The dependence for the fast component is linear, whereas the intensity of the slow component tends to saturation.

5.6.4 Differential Absorption in Bismuth Germanate (BGO)

Bismuth germanate $Bi_4Ge_3O_{12}$ (BGO) is another self-activated scintillator quite extensively used on a comparatively large scale in several applications. The abbreviation BGO is sometimes also used for bismuth and germanium oxide $Bi_{12}GeO_{20}$, which is prospective for applications in optoelectronics [103]. The luminescence properties of $Bi_4Ge_3O_{12}$ (thereafter BGO) are being studied since the 1970-ties [104, 105], however, the luminescence peculiarities are not clear up to now. BGO has a high density of 7.13 g/cm^3 and a large effective atomic number (76) resulting in a high efficiency in stopping the ionizing radiation and high-energy particles to be detected. These features enabled exploitation of BGO in PET devices, in spite of a comparatively low light yield of this scintillator (~13% of the light yield of the conventional scintillator NaI:Tl). BGO is nonhigroscopic and chemically stabile, single crystals of BGO can be grown on industrial scale by using Czochralski technique. However, the increasing demand on the time resolution in PET scanners is in favour of LSO crystals against BGO [34, 106]. Therefore, the current competition with LSO [107] urges revival of BGO studies to possibly improve the scintillation properties, especially the timing properties of BGO.

The leading edge of luminescence response of BGO is fast, as expected for a self-activated scintillator. A data carpet of differential absorption measurements after

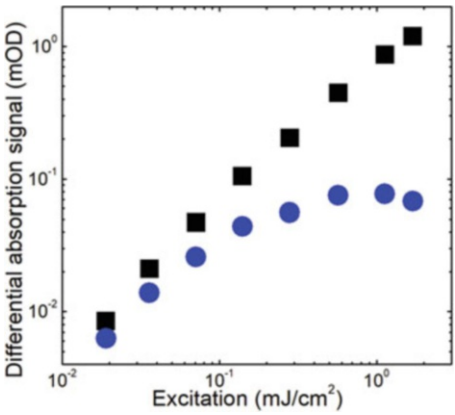

Fig. 5.37 Induced optical density of PWO at 1.2 eV probe photon energy at delays of 0.3 ps (black squares) and 1 ns (blue dots) after 200 fs pump pulse at 4.88 eV as a function of pump pulse energy density. (After Ref. [61])

excitation of BGO by 200 fs-long pulses of 4.82 eV photons is presented in Fig. 5.38. The DA signal has no distinct spectral features within the entire probing range from 1.4 eV to 3 eV. The emission in BGO is caused by self-trapped excitons, thus, the DA signal reflects the density of the excitons. In principle, certain contribution in DA might also be expected from the free carriers, which occur in the conduction and valence bands as a result of thermal excitation of the excitons. However, this contribution should not be high at room temperature due to a large activation energy. The decay of the DA signal is nonexponential; the intensity of the DA signal decreases to 30% of its initial value during the first 1 ns.

Figure 5.39 presents the kinetics of the DA signal for BGO without intentional doping and doped crystals BGO:Ca, BGO:Ti, BGO:Mg, and BGO:La,Y. None of these dopants have any significant influence on the DA decay kinetics of these single crystals.

The insensibility of the population of the self-trapped excitons, the density of which is monitored by the DA signal, might be explained by a large Stokes shift of BGO luminescence. The large Stokes shift evidences a large activation energy for the thermal ionization of a self-trapped exciton. Thus, trapping to and detrapping from the comparatively shallow traps expected due to BGO doping occurs at a substantially shorter time scale than the thermal ionization of excitons.

5.6.5 Cerium Fluoride Scintillator

Cerium fluoride, CeF_3, has two important features different from those of other two self-activated scintillators, PWO and BGO, discussed above. The bottom of the conduction band in CeF_3 is formed by *d* orbitals of Ce^{3+} ions with certain admixture

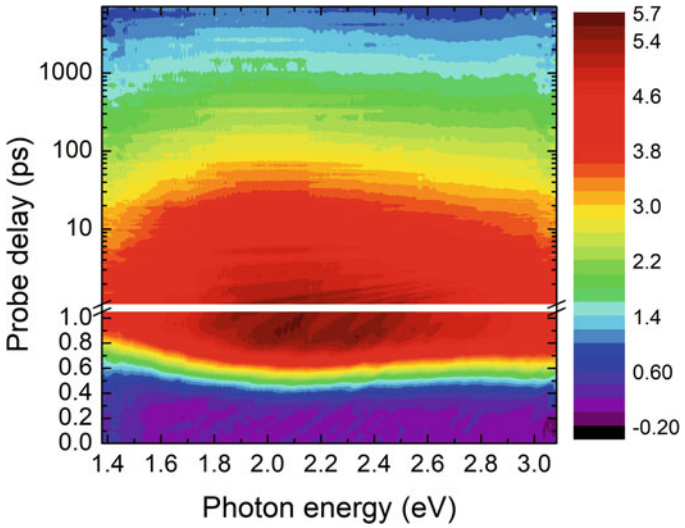

Fig. 5.38 Differential absorption of BGO as a function of probe photon energy and delay between pump and probe pulses at pump photon energy of 4.82 eV. Note the scale change from linear to logarithmic at 1 ps

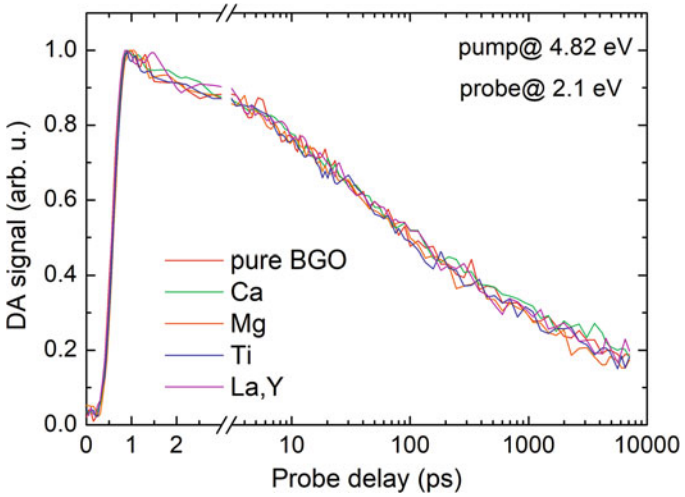

Fig. 5.39 Differential absorption kinetics at 2.1 eV of nominally pure BGO, BGO:Ca, BGO:Mg, BGO:Ti, and BGO:La,Y crystals pumped at 4.82 eV. The kinetic in each crystal is normalized to its peak value

of *f* and *s* states of Ce^{3+}. The partially filled *f* orbital of Ce^{3+} is ~0.5 eV higher than the top of the valence band formed by the filled *p* states of F^-. Ion Ce^{3+} is the luminescence center instead of oxyanionic complex in other self-activated scintillators. As a result, the Stokes shift of the luminescence is small, so that the luminescence band partly overlaps with the absorption spectrum. The gaps between the *5d* Ce^{3+} electronic levels and other bands in the upper part of the conduction band was determined by measurements of optical absorption in a crystalline film of CeF_3 [108]. A set of five absorption bands in the range from 247 to 194 nm was identified. An absorption band peaked at 172 nm was also observed and attributed to an interconfiguration transition *4f-6 s* [109]. The energy of allowed *d-s* transition from the lowest excited *d* state of Ce^{3+} is estimated to be in the range from 400 to 420 nm. The crystal was also studied using optical pump-probe technique with pumping by 140 fs pulses at 263 nm and probing by supercontinuum radiation in the range of 390–720 nm [110]. Three wide bands of induced absorption were observed in the spectral range from 390 to 700 nm (see Fig. 5.40).

All the bands have the leading edge, which coincides with the front of excitation pulse and is shorter than 1 ps. The short-wavelength band peaked at 420 nm corresponds to fast population of the lowest *d* level of Ce^{3+} ions, and the induced absorption in this band is caused by transitions between *d* and *s* states of Ce^{3+}.

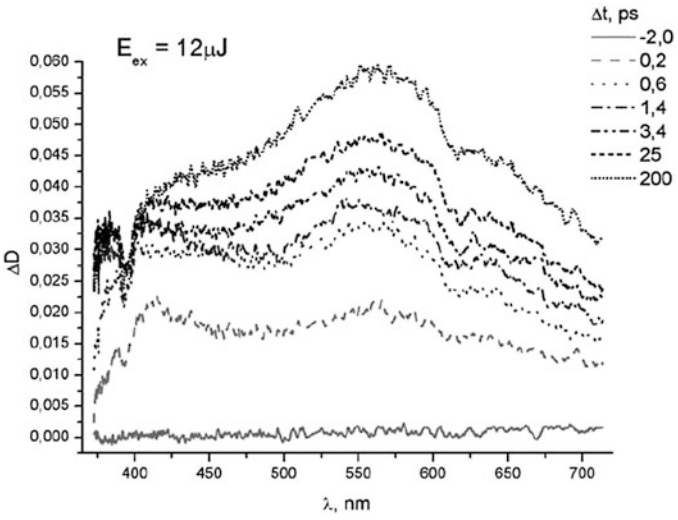

Fig. 5.40 Induced absorption spectra of CeF_3 single crystal for different time delays between pump and probe pulses (indicated). (Reprinted with permission from Ref. [110])

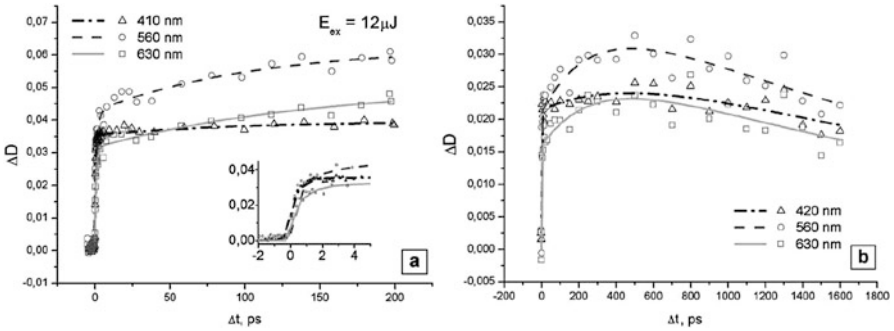

Fig. 5.41 Kinetics of transient absorption of CeF_3 single crystal obtained at different wavelength of probe pulse (indicated) on (**a**) short (0–200 ps) and (**b**) long (0–2000 ps) time ranges. The time scale is expanded in the inset in (**a**) to demonstrate the coincidence of the leading edge of differential absorption. (Reprinted with permission from Ref. [110])

Figure 5.41 shows the kinetics of the transient absorption on short (0–200 ps) and long (0–2000 ps) time scales.

Two long-wavelength bands peaked at 560 and 630 nm exhibit slower intensity increase after excitation with a rise time of 200–300 ps, whereas the short-wavelength band intensity reaches a plateau in subpicosecond domain. The bands peaked at 560 and 630 nm occur due to trapping–retrapping of the electrons escaped from excited Ce^{3+*} ions: $Ce^{3+*} \rightarrow Ce^{4+} + e$. This process is facilitated in CeF_3 by a high diffusion coefficient for excitations via the Ce^{3+} subsystem due to a strong overlap of emission and excitation spectra in this crystal. The capture of electron by Ce^{4+} has an almost instantaneous component due to geminate recombination, whereas a delayed component is caused by the diffusion of the electron to an ionized center. After the capture of electron by ionized Ce^{4+}, all 5*d* levels are populated, producing the delayed induced absorption in the long-wavelength range. In addition, similarly to the situation in other Ce-containing scintillators, the rising part of long-wavelength components is caused by trapping at shallow traps. Such shallow traps might be created by the mixture of *d-f* states with the dominant *f* density component. Assuming the thermal activation energy of the traps to be ~0.2 eV, the two observed long-wavelength bands correspond to the electron transfer from the trap state to two upper Stark components of 5*d* level of Ce^{3+} ions. Approximation of the experimentally obtained kinetics by a sum of exponents showed that the induced optical density in all bands decays on a long time range with a time constant of ~2.5 ns, indicating the rate of decrease in the population of the corresponding level. The decay correlates well with the time profile of the depopulation of the lowest Ce^{3+}conduction band level related to the inter-configurational *d-f* luminescence transition. It is well known that the initial stage of the luminescence decay kinetics of CeF_3 crystals contains a short component with a decay constant at the level of 3–5 ns. The results

obtained on CeF_3 show that, in spite the peculiarities of the DOS, the population of the radiating states follows the same trends as in other self-activated scintillators, and shallow traps play a similar role as in other scintillators.

5.7 Peculiarities of Excitation Transfer in Ce-Doped Scintillators

As illustrated above, the combination of time-resolved photoluminescence spectroscopy and spectrally-resolved nonlinear optical absorption in pump and probe configuration with picosecond and subpicosecond time resolution enables a deeper insight in the dynamics of nonequilibrium carriers in scintillating material, which is important to better understand the processes of excitation transfer and peculiarities of carrier recombination, which are important for the time resolution of scintillating detectors.

The optical pump and probe technique is less productive in self-activated scintillators, where binding of nonequilibrium electrons and holes to excitons and their self-trapping proceed instantaneously even on the picosecond time scale. Consequently, the rise time of the luminescence response is negligible in comparison with the luminescence decay time, and the time resolution of these scintillators depends on the light yield and luminescence decay time, as described in Chap. 2. Usually, the luminescence of self-activated scintillators is thermally quenched. The rate of thermal activation depends on the exciton binding energy, whereas the rate of nonradiative recombination of the thermally activated electrons and holes, which determines both the luminescence decay time and the light yield, depends on the rate of their capture to the centers of nonradiative recombination.

The current studies of fast scintillators, which are prospective for applications in the coming high-energy physics experiments and the high-spatial-resolution medical imaging devices with TOF capability, are predominantly focused on Ce-doped materials, mainly garnet-type crystals or oxyorthosilicates. As shown in Sect. 5.3.3, both excitation transfer after excitation of a scintillator with a high-energy photon, as in radiation detectors, and the front edge in the population of the emitting level of Ce^{3+} depend on the electron diffusion coefficient. Therefore, the results on the response rise time after optical pumping correlate with the time resolution of radiation detectors, in particular, in the coincidence resolution time measurements after excitation with annihilation of 511 keV γ-quanta.

The cerium ions in most of Ce-doped scintillators can be stable in two valence states: as Ce^{3+} and Ce^{4+} ions. Moreover, the ions interact with the host crystal lattice. The energy states of the ions, with the interaction with the lattice taken into account, are usually considered using configuration diagrams. The corresponding diagrams for Ce^{3+} and Ce^{4+} ions presenting excited and ionized states (as in [111]) are

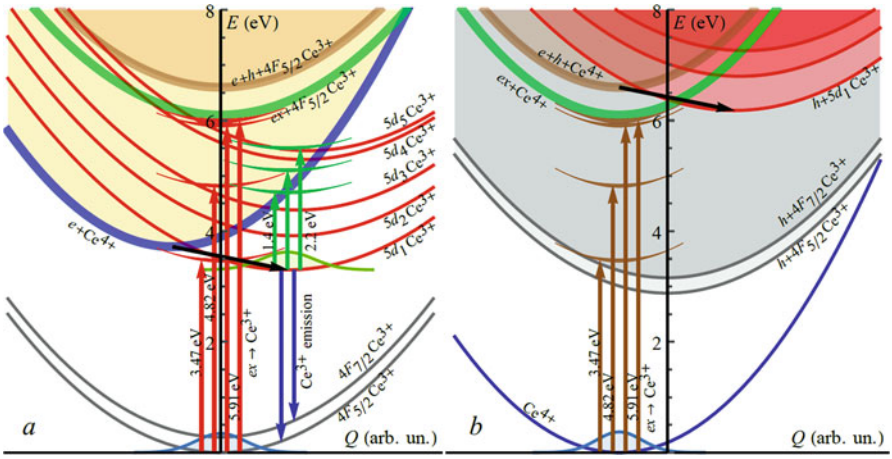

Fig. 5.42 Configuration diagrams for Ce^{3+} (**a**) and Ce^{4+} (**b**) ions

presented in Fig. 5.42. The ground state of Ce^{3+} is split into two levels, $4F_{5/2}$ and $4F_{7/2}$. The Gaussians depicted in grey display the thermal distribution functions of the electrons in the ground state. The energy distances between the ground and excited states are indicated by vertical arrows. The optical transitions resulting in photon emission are indicated by downwards blue arrows. The processes of electron capture by relaxed Ce^{4+} ions resulting in formation of excited state of Ce^{3+} ion are indicated by black arrows. The influence of fluctuations of the bottom of the conduction band is reflected by the width of the lines depicting the parabolas in the configuration diagrams.

The red parabolas depict the excited states, whereas the parabolas with shaded regions above correspond to ionized sates. The parabolas for ground and excited Ce^{3+} states were positioned in accordance with the absorption and emission spectra observed experimentally. The absorption spectrum calculated on the basis of the configuration diagram depicted in Fig. 5.42 is presented in Fig. 5.43 and is similar to the experimental absorption spectrum. Local phonon energies of 50 meV and 40 meV were taken for ground and excited states of Ce^{3+}, respectively, as estimated for Ce^{3+} in LSO [112]. The local phonon frequency for Ce^{4+} is taken 70 meV, slightly larger than that for the excited state of Ce^{3+}. Since the radius of the excited Ce^{3+} ion is larger than that of the ground state, the equilibrium position (the vertex of the corresponding parabola) of the excited Ce^{3+} state reflects the shift of a ligand ion off the initial position. Meanwhile, the parabola for Ce^{4+} is shifted to the opposite direction, since the radius of ionized cerium is less than that of the ground Ce^{3+} state, and, consequently, the Coulomb interaction between ligands and Ce^{4+} is stronger than that with Ce^{3+}. Therefore, the increase in the rigidity of the bonds between cerium and ligands with decreasing distance between them results in the increase in the local phonon frequency from the excited Ce^{3+} ion to Ce^{3+} in ground state to Ce^{4+}. As evident in the absorption spectra, the optical transitions involving Ce^{4+} ions do

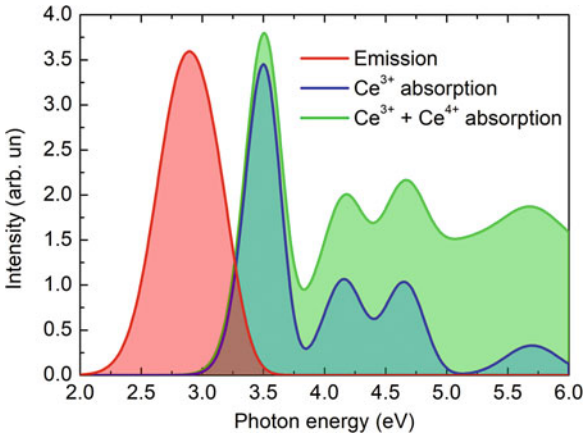

Fig. 5.43 Emission (red line) and absorption spectra for Ce^{3+} absorption (blue) and Ce^{3+} with contribution of charge transfer absorption by Ce^{4+} (green). The line positions correspond to the arrows in Fig. 5.42a, b

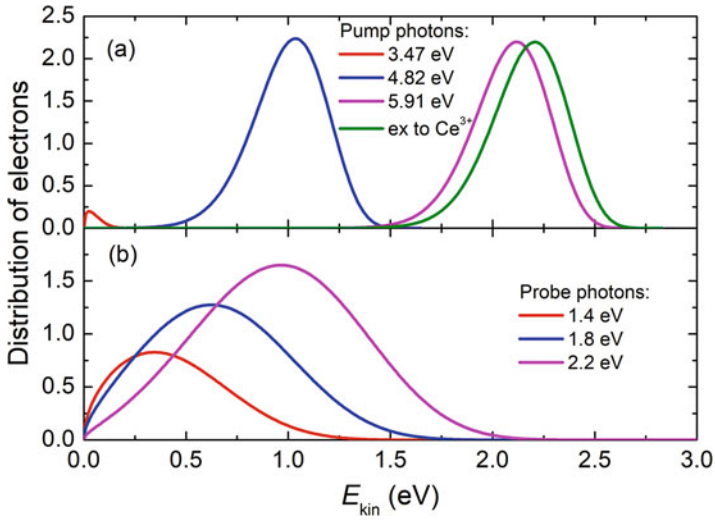

Fig. 5.44 The number of electrons as a function of their kinetic energy after absorption of pump (**a**) and probe (**b**) photons with energies indicated

not results in new absorption band, but rather result in broad-band enhancement of the absorption in UV region.

The distributions of the kinetic energies of the electrons generated by the absorption of pump photons of different energy by Ce^{3+} are presented in Fig. 5.44a. The

kinetic energy distribution after the absorption of probe photons of different energy by Ce^{3+} excited in the lowest $5d_1$ state is shown in Fig. 5.44b, whereas the distribution after a dipole-dipole energy transfer to Ce^{3+} by an exciton is shown in Fig. 5.44a by a red line.

The nonequilibrium electrons excited with excess energy lose their kinetic energy E_{kin} predominantly by the emission of phonons. The emission of longitudinal optical phonons is the most important mechanism for energy relaxation in ionic crystals. According to [113] the thermalization distance as a function of the kinetic energy can be described as:

$$l^2_{e,LO}(E_{kin}) = \frac{a_B^2}{24}\left(\frac{\widetilde{\varepsilon} m_0}{m_e}\right)^2 \tanh\left(\frac{\hbar\Omega_{LO}}{2k_BT}\right)\mathrm{Ei}\left(3\ln\left(\frac{4E_{kin}}{\hbar\Omega_{LO}}\right)\right), \tag{5.10}$$

where a_B is the Bohr radius, m_0 and m_e are free and effective electron masses, respectively, $\hbar\Omega_{LO}$ is the LO-phonon energy, $\widetilde{\varepsilon} = \left(\varepsilon_\infty^{-1} - \varepsilon_{st}^{-1}\right)^{-1}$ is the effective dielectric permittivity expressed in terms of high-frequency ε_∞ and static ε_{st} dielectric permittivities, and $\mathrm{Ei}(x)$ is the exponential integral function. The electron effective mass can be estimated as $m_e = 0.6m_0$ using the dispersion law at the bottom of the conduction band available in AFLOW database [114, 115] for YSO, which is a structural analogue of LSO. The value of 4.56–4.73 for $\widetilde{\varepsilon}$ is estimated by taking the refraction index as $n = 1.78$–1.80 and the static dielectric permittivity ε_{st}= 9.6–11.2 [116]. The bulk phonon energy for LYSO can be taken as $\hbar\Omega_{LO} = 40$ meV, equal to the local phonon energy for Ce^{3+} estimated in [111].

The kinetic energy dependence of the thermalization length estimated according to Eq. 5.10, which is valid for a parabolic dispersion law, is shown by a blue line in the inset of Fig. 5.45. Actually, the dispersion is nonparabolic, especially for energies more than ~1 eV above the bottom of the conduction band. Therefore, a restricted velocity model assuming that the mean electron velocity and the electron-phonon scattering rate are constant for electron kinetic energies >1 eV might be exploited similarly to the approach used in [117, 118]. According to this approximation,

$$l^2_{e,LO}(E_{kin} > 1\text{ eV}) = l^2_{e,LO}(1\text{ eV}) + A(E_{kin} - 1\text{ eV}) \tag{5.11}$$

where, for $E_{kin} = 1$ eV, the constant $A = dl^2_{e,LO}(E_{kin})/dE_{kin}$. The corresponding dependence for the restricted velocity model is shown in Fig. 5.45 by a red line and is used in the further considerations in this section.

The distribution of the spatial positions r of the electrons from their birthplaces can be described by

$$f(r, l_e(E_{\mathrm{kin}})) = \frac{3\sqrt{6}r^2}{\sqrt{\pi}l_e^3(E_{\mathrm{kin}})}\exp\left(-\frac{3r^2}{2l_e^2(E_{\mathrm{kin}})}\right). \tag{5.12}$$

The function has to be normalized: $\int_0^\infty f(r)dr = 1$.

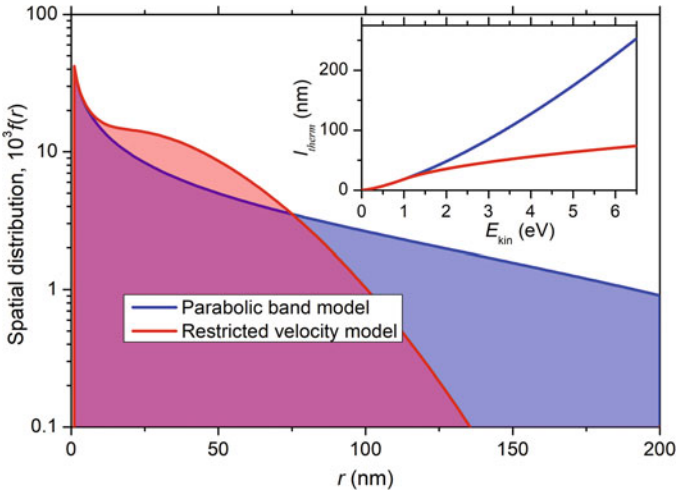

Fig. 5.45 Spatial distribution of electrons $f(r)$ thermalized by cascading down after their generation by a high-energy excitation for parabolic band model (blue line) and according to the model assuming a constant velocity for $E_{\text{kin}} > 1$ eV (red). In the inset: the thermalization length as a function of electron kinetic energy

To obtain the spatial distribution for the electrons created by photon absorption, the distribution described by

$$(r, l_e(E_{kin})) = \frac{3\sqrt{6}r^2}{\sqrt{\pi}l_e^3(E_{kin})} \exp\left(-\frac{3r^2}{2l_e^2(E_{kin})}\right). \tag{5.13}$$

has to be convoluted with the distribution of the electrons over their initial energies. This convolution is shown in Fig. 5.46.

A part of the thermalized electrons return back to the geminate Ce^{4+} ion to occupy the excited $5d_1$ state of Ce^{3+}. This transition is indicated by black arrows for Ce^{3+} in Fig. 5.42a and for Ce^{4+} ion in Fig. 5.42b. Similar processes occur also in Ce-doped GAGG scintillators, as described in [24]. Only the electrons thermalized closer to the geminate Ce^{4+} ion than the Onsager radius, i.e., the distance at which the energy due to Coulomb interaction between electron and Ce^{4+} ion equals thermal energy, can be captured without migrating out of the range of the effective Coulomb interaction. Therefore, only electrons with $r < R_{Ons}$ return to the geminate Ce^{4+} ions (a part of them are captured by the centers of nonradiative recombination).

The spatial distribution of nonequilibrium carriers after their thermalization is also important at the excitation with high-energy quanta initiating scintillation. After losing most of their energy by cascading down in the conduction band, the electrons have the distribution of their kinetic energy ranging from zero to the band gap energy E_g, since the electrons with a higher kinetic energy are able to produce electron-hole pairs and lose their energy this way until below $\sim E_g$. This distribution of electron

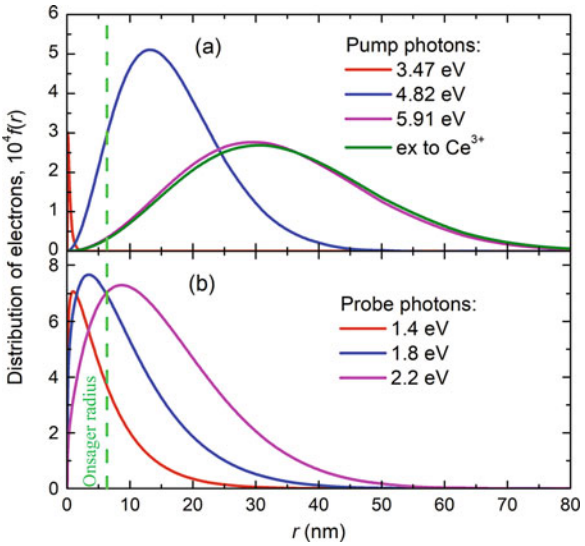

Fig. 5.46 Spatial distribution of thermalized electrons $f(r)$ after ionization of Ce^{3+} ion by 3.47 eV, 4.82 eV, and 5.91 eV pump photons (**a**) and by 1.4 eV, 1.8 eV, and 2.2 eV probe photons (**b**). The Onsager radius is indicated by a vertical line

kinetic energy smoothly decreases from its peak value at low energy [119]. This distribution controls the formation of excitons. The excitons, after migrating to the vicinity of Ce^{3+} ions, can transfer their energy to the Ce^{3+} ion. The exciton energy substantially exceeds the energy of the lowest *f-d* transition of Ce^{3+}. Thus, the energy transfer might also result in the ionization of Ce^{3+} ion. Therefore, the final stage of energy transfer from exciton to Ce^{3+} ion is similar to the processes important for energy relaxation after photoexcitation of the ion. The time evolution of the leading edge of scintillation response, which has a strong influence on time resolution of a fast scintillation detector, depends on three key processes: formation of excitons, ionization of Ce^{3+} ions, and return of electrons to their geminate ions to form an excited ion Ce^{3+*}. The differential optical absorption technique is capable to reveal the peculiarities of the last process and is a useful tool for characterization of timing properties of activated scintillators.

References

1. D. Renker, E. Lorenz, Advances in solid state photon detectors. J. Instrum. **4**(4), P04004–P04004 (2009)
2. C. Piemonte, A. Ferri, A. Gola, T. Pro, N. Serra, A. Tarolli, N. Zorzi, Characterization of the first FBK high-density cell silicon photomultiplier technology. IEEE Trans. Electron Devices **60**(8), 2567–2573 (2013)
3. C. Piemonte, F. Acerbi, A. Ferri, A. Gola, G. Paternoster, V. Regazzoni, G. Zappala, N. Zorzi, Performance of NUV-HD silicon photomultiplier technology. IEEE Trans. Electron Devices **63**(3), 1111–1116 (2016)

4. N. D'Ascenzo, W. Brockherde, S. Dreiner, A. Schwinger, A. Schmidt, Q. Xie, Design and characterization of a silicon photomultiplier in 0.35-um CMOS. IEEE J. Electron Devices Soc. **6**, 74–80 (2018)
5. A. Bornheim, M.H. Hassanshahi, M. Griffioen, J. Mao, A. Mangu, C. Peña, M. Spiropulu, S. Xie, Z. Zhang, LYSO-based precision timing detectors with SiPM readout. Nucl. Instrum. Methods Phys. Res. Sect. A **896**, 75–81 (2018)
6. A. Gola, C. Piemonte, A. Tarolli, Analog circuit for timing measurements with large area SiPMs coupled to LYSO crystals. IEEE Trans. Nucl. Sci. **60**(2), 1296–1302 (2013)
7. F. Acerbi, G. Paternoster, A. Gola, V. Regazzoni, N. Zorzi, C. Piemonte, High-density silicon photomultipliers: Performance and linearity evaluation for high efficiency and dynamic-range spplications. IEEE J. Quantum Electron. **54**(2), 1–7 (2018)
8. M. Kirm, V. Babin, E. Feldbach, S. Guizard, M. De Grazia, V. Nagirnyi, A. Vasil'ev, S. Vielhauer, Behaviour of scintillators under XUV free electron laser radiation. J. Lumin. **128**(5–6), 732–734 (2008)
9. P.-A. Douissard, T. Martin, F. Riva, E. Mathieu, Y. Zorenko, V. Savchyn, T. Zorenko, A. Fedorov, Scintillating screens for micro-imaging based on the Ce-Tb doped LuAP single crystal films. IEEE Trans. Nucl. Sci. **61**(1), 433–438 (2014)
10. G. Tamulaitis, A. Vasil'ev, M. Korzhik, A. Gola, S. Nargelas, V. Vaitkevicius, A. Fedorov, D. Kozlov, Improvement of the time resolution of radiation detectors based on Gd3Al2Ga3O12 scintillators with SiPM readout. IEEE Trans. Nucl. Sci. **66**(7), 1879–1888 (2019)
11. K.B. Ucer, G. Bizarri, A. Burger, A. Gektin, L. Trefilova, R.T. Williams, Electron thermalization and trapping rates in pure and doped alkali and alkaline-earth iodide crystals studied by picosecond optical absorption. Phys. Rev. B **89**(16), 1–15 (2014)
12. V.N. Makhov, Vacuum ultraviolet luminescence of wide band-gap solids studied using time-resolved spectroscopy with synchrotron radiation. Phys. Scr. **89**(4), 044010 (2014)
13. A. Belsky, K. Ivanovskikh, A. Vasil'ev, M.-F. Joubert, C. Dujardin, Estimation of the electron thermalization length in ionic materials. J. Phys. Chem. Lett. **4**(20), 3534–3538 (2013)
14. J. Becker et al., Time resolved luminescence spectroscopy of wide bandgap insulators. J. Electron Spectros. Relat. Phenom. **79**, 99–102 (1996)
15. I.A. Kamenskikh, V.V. Mikhailin, I.H. Munro, D.A. Shaw, I.N. Shpinkov, A.N. Vasil'ev, Decay of core holes in cesium chloride studied by the luminescence spectroscopy. J. Lumin. **72–74**, 930–932 (1997)
16. A.N. Belsky et al., Luminescence quenching as a probe for the local density of electronic excitations in insulators. J. Electron Spectrosc. Relat. Phenomena **79**, 147–150 (1996)
17. A.N. Belsky et al., Fast luminescence of undoped PbWO4 crystal. Chem. Phys. Lett. **243**(5–6), 552–558 (1995)
18. M. Itoh, M. Kamada, N. Ohno, Temperature dependence of auger-free luminescence in alkali and alkaline-earth halides. J. Phys. Soc. Jpn. **66**(8), 2502–2512 (1997)
19. M.A. Terekhin, A.N. Vasil'ev, M. Kamada, E. Nakamura, S. Kubota, Effect of quenching processes on the decay of fast luminescence from barium fluoride excited by VUV synchrotron radiation. Phys. Rev. B **52**(5), 3117–3121 (1995)
20. E. Meltchakov et al., Soft X-ray excitation of luminescence in wide bandgap crystals doped with rare-earth ions. Phys. Status Solidi **4**(3), 1092–1095 (2007)
21. P.-A. Douissard et al., Scintillating screens for micro-imaging based on the Ce-Tb doped LuAP single crystal films. IEEE Trans. Nucl. Sci. **61**(1), 433–438 (2014)
22. M. Kirm et al., Behaviour of scintillators under XUV free electron laser radiation. J. Lumin. **128**(5–6), 732–734 (2008)
23. R.M. Turtos et al., Ultrafast emission from colloidal nanocrystals under pulsed X-ray excitation. J. Instrum. **11**(10), P10015–P10015 (2016)
24. G. Tamulaitis et al., Improvement of the time resolution of radiation detectors based on Gd3Al2Ga3O12 scintillators with SiPM readout. IEEE Trans. Nucl. Sci. **66**(7), 1879–1888 (2019)

25. K.B. Ucer, G. Bizarri, A. Burger, A. Gektin, L. Trefilova, R.T. Williams, Electron thermalization and trapping rates in pure and doped alkali and alkaline-earth iodide crystals studied by picosecond optical absorption. Phys. Rev. B **89**(16), 1–15 (2014)
26. P. Li, S. Gridin, K.B. Ucer, R.T. Williams, P.R. Menge, Picosecond absorption spectroscopy of self-trapped excitons and transient Ce states in LaBr3 and LaBr3:Ce. Phys. Rev. B **97**(14), 1–18 (2018)
27. G. Tamulatis et al., Improvement of response time in GAGG:Ce scintillation crystals by magnesium codoping. J. Appl. Phys. **124**(21), 215907 (2018)
28. G. Tamulaitis et al., Subpicosecond luminescence rise time in magnesium codoped GAGG:Ce scintillator. Nucl. Instrum. Methods Phys. Res. Sect. A **870**, 25–29 (2017)
29. M.T. Lucchini et al., Measurement of non-equilibrium carriers dynamics in Ce-doped YAG, LuAG and GAGG crystals with and without Mg-codoping. J. Lumin. **194**, 1–7 (2018)
30. M. Korzhik et al., Timing properties of Ce-doped YAP and LuYAP scintillation crystals. Nucl. Instrum. Methods Phys. Res. Sect. A **927**, 169–173 (2019)
31. P. Li, S. Gridin, K.B. Ucer, R.T. Williams, P.R. Menge, Picosecond absorption spectroscopy of self-trapped excitons and Ce excited states in CeBr3 and La1-xCexBr3. Phys. Rev. B **99** (10), 1–9 (2019)
32. C.L. Melcher, J.S. Schweitzer, Cerium-doped lutetium oxyorthosilicate: A fast, efficient new scintillator. IEEE Trans. Nucl. Sci. **39**(4), 502–505 (1992)
33. P. Lecoq, A. Gektin, M. Korzhik, *Inorganic Scintillators for Detector Systems* (Springer, Cham, 2017)
34. C.L. Melcher, Scintillation crystals for PET. J. Nucl. Med. **41**, 1051–1055 (2000)
35. D.L. Bailey, D.W. Townsend, P.E. Valk, M.N. Maisey, *Positron Emission Tomography* (Springer, Secaucus, 2005)
36. B. H. T. Chai, Method of enhancing performance of cerium doped lutetium yttrium orthosilicate crystals and crystals produced thereby. U.S. Patent 7166845 B1, 2007
37. M.A. Spurrier, P. Szupryczynski, K. Yang, A.A. Carey, C.L. Melcher, Effects of Ca2+co-doping on the scintillation properties of LSO:Ce. IEEE Trans. Nucl. Sci. **55**(3), 1178–1182 (2008)
38. K. Yang, C.L. Melcher, P.D. Rack, L.A. Eriksson, Effects of calcium codoping on charge traps in LSO:Ce crystals. IEEE Trans. Nucl. Sci. **56**(5), 2960–2965 (2009)
39. H.E. Rothfuss, C.L. Melcher, L.A. Eriksson, M.A. Spurrier Koschan, The effect of Ca2+ codoping on shallow traps in YSO:Ce scintillators. IEEE Trans. Nucl. Sci. **56**(3), 958–961 (2009)
40. S. Blahuta, A. Bessiere, B. Viana, P. Dorenbos, V. Ouspenski, Evidence and consequences of Ce4+ in LYSO:Ce,Ca and LYSO:Ce,Mg single crystals for medical imaging applications. IEEE Trans. Nucl. Sci. **60**(4), 3134–3141 (2013)
41. D. Ding, B. Liu, Y. Wu, J. Yang, G. Ren, J. Chen, Effect of yttrium on electron–phonon coupling strength of 5d state of Ce3+ ion in LYSO:Ce crystals. J. Lumin. **154**, 260–266 (2014)
42. E. Auffray et al., Excitation transfer engineering in Ce-doped oxide crystalline scintillators by codoping with alkali-earth ions. Phys. Status Solidi **215**(7), 1700798 (2018)
43. C.L. Melcher, S. Friedrich, S.P. Cramer, M.A. Spurrier, P. Szupryczynski, R. Nutt, Cerium oxidation state in LSO:Ce scintillators. IEEE Trans. Nucl. Sci. **52**(5), 1809–1812 (2005)
44. L. Ning et al., Electronic properties and 4f → 5d transitions in Ce-doped Lu2SiO5: A theoretical investigation. J. Mater. Chem. **22**(27), 13723–13731 (2012)
45. S. Blahuta et al., Defects identification and effects of annealing on Lu2(1-x)Y2xSiO5 (LYSO) single crystals for scintillation application. Materials (Basel) **4**(7), 1224–1237 (2011)
46. E. Auffray et al., Radiation damage of LSO crystals under γ- and 24GeV protons irradiation. Nucl. Instrum. Methods Phys. Res. Sect. A **721**, 76–82 (2013)
47. A.N. Belsky et al., Progress in the development of LuAlO3-based scintillators. IEEE Trans. Nucl. Sci. **48**(4), 1095–1100 (2001)

48. Y. Wu et al., On the role of Li + codoping in simultaneous improvement of light yield, decay time, and afterglow of Lu2SiO5:Ce3+ scintillation detectors. Phys. Status Solidi – Rapid Res. Lett. **13**(2), 1800472 (2019)
49. K. Kamada et al., Composition engineering in cerium-doped (Lu,Gd)3(Ga,Al)5O12 single-crystal scintillators. Cryst. Growth Des. **11**(10), 4484–4490 (2011)
50. M.V. Korzhik, A general approach to increasing the radiation hardness of complex structure oxide scintillation crystals. Nucl. Instrum. Methods Phys. Res. Sect. A **500**(1–3), 116–120 (2003)
51. C.D. Brandle, Czochralski growth of oxides. J. Cryst. Growth **264**(4), 593–604 (2004)
52. M. Moszyński, T. Ludziejewski, D. Wolski, W. Klamra, L.O. Norlin, Properties of the YAG: Ce scintillator. Nucl. Instrum. Methods Phys. Res. Sect. A **345**(3), 461–467 (1994)
53. K. Kamada et al., Scintillator-oriented combinatorial search in Ce-doped (Y,Gd)3(Ga,Al) 5O12 multicomponent garnet compounds. J. Phys. D. Appl. Phys. **44**(50), 505104 (2011)
54. K. Kamada et al., Alkali earth co-doping effects on luminescence and scintillation properties of Ce doped Gd3Al2Ga3O12 scintillator. Opt. Mater. (Amst) **41**, 63–66 (2015)
55. M.T. Lucchini et al., Effect of Mg2+ ions co-doping on timing performance and radiation tolerance of cerium doped Gd3Al2Ga3O12 crystals. Nucl. Instrum. Methods Phys. Res. Sect. A **816**, 176–183 (2016)
56. M.T. Lucchini et al., Timing capabilities of garnet crystals for detection of high energy charged particles. Nucl. Instrum. Methods Phys. Res. Sect. A **852**, 1–9 (2017)
57. V.V. Averkiev, J.A. Valbis, *Luminescence Crystals and Convertors of Ionizing Radiation* (Nauka, Novosibirsk, 1985)
58. M. Nikl et al., Defect engineering in Ce-doped aluminum garnet single crystal scintillators. Cryst. Growth Des. **14**(9), 4827–4833 (2014)
59. M. Nikl, A. Yoshikawa, Recent R&D trends in inorganic single-crystal scintillator materials for radiation detection. Adv. Opt. Mater. **3**(4), 463–481 (2015)
60. A. Nakatsuka, A. Yoshiasa, T. Yamanaka, Cation distribution and crystal chemistry of Y3Al5−xGaxO12 ($0 \leq x \leq 5$) garnet solid solutions. Acta Crystallogr. Sect. B **55**(3), 266–272 (1999)
61. E. Auffray et al., Free carrier absorption in self-activated PbWO4 and Ce-doped Y3 (Al0.25Ga0.75)3O12 and Gd3Al2Ga3O12 garnet scintillators. Opt. Mater. (Amst) **58**, 461–465 (2016)
62. P. Dorenbos, A review on how lanthanide impurity levels change with chemistry and structure of inorganic compounds. ECS J. Solid State Sci. Technol. **2**(2), R3001–R3011 (2013)
63. H. Suzuki, T.A. Tombrello, C.L. Melcher, C.A. Peterson, J.S. Schweitzer, The role of gadolinium in the scintillation processes of cerium-doped gadolinium oxyorthosilicate. Nucl. Instrum. Methods Phys. Res. Sect. A **346**(3), 510–521 (1994)
64. H. Suzuki, T.A. Tombrello, C.L. Melcher, J.S. Schweitzer, Energy transfer from Gd to Ce in Gd2(SiO4)O:Ce. J. Lumin. **60–61**, 963–966 (1994)
65. F. Meng, M. Koschan, Y. Wu, C.L. Melcher, Relationship between Ca2+ concentration and the properties of codoped Gd3Ga3Al2O12:Ce scintillators. Nucl. Instrum. Methods Phys. Res. Sect. A **797**, 138–143 (2015)
66. J.M. Ogieglo, *Luminescence and Energy Transfer in Garnet Scintillators* (Utrecht University, Utrecht, 2012)
67. M. Kavatsyuk et al., Performance of the prototype of the electromagnetic calorimeter for PANDA. Nucl. Instrum. Methods Phys. Res. Sect. A **648**(1), 77–91 (2011)
68. D. del Re, Timing performance of the CMS ECAL and prospects for the future. J. Phys. Conf. Ser. **587**, 012003 (2015)
69. A.N. Vasil, ev, microtheory of scintillation in crystalline materials, in *Engineering of Scintillation Materials and Radiation Technologies*, (Belarus CNUM, Minsk, 2017), pp. 3–34
70. S. Gundacker, E. Auffray, K. Pauwels, P. Lecoq, Measurement of intrinsic rise times for various L(Y)SO and LuAG scintillators with a general study of prompt photons to achieve 10 ps in TOF-PET. Phys. Med. Biol. **61**(7), 2802–2837 (2016)

71. M. Nikl, E. Mihokova, J. Pejchal, A. Vedda, Y. Zorenko, K. Nejezchleb, The antisite LuAl defect-related trap in Lu3Al5O12:Ce single crystal. Phys. Status Solidi **242**(14), R119–R121 (2005)
72. V.G. Baryshevsky et al., YAlO3:Ce-fast-acting scintillators for detection of ionizing radiation. Nucl. Instrum. Methods Phys. Res. Sect. A **58**(2), 291–293 (1991)
73. M.V. Korzhik, O.V. Misevich, A.A. Fyodorov, YAlO3:Ce scintillators: Application for X- and soft γ-ray detection. Nucl. Instrum. Methods Phys. Res. Sect. B **72**(3–4), 499–501 (1992)
74. M. Kobayashi et al., YAlO3:Ce-Am light pulsers as a gain monitor for undoped CsI detectors in a magnetic field. Nucl. Instrum. Methods Phys. Res. Sect. A **337**(2–3), 355–361 (1994)
75. M. Zhuravleva et al., Crystal growth and scintillating properties of Zr/Si-codoped YAlO3:Pr3 +. IEEE Trans. Nucl. Sci. **55**(3), 1476–1479 (2008)
76. J.A. Mareš, M. Nikl, C. Pédrini, B. Moine, K. Blažek, A study of fluorescence emission of Ce3 + ions in YAlO3 crystals by the influence of doping concentration and codoping with Nd3+ and Cr3+. Mater. Chem. Phys. **32**(4), 342–348 (1992)
77. S. Petrovic, A. Kepic, M. Carson, Scintillators for PGNAA in mineral exploration. ASEG Ext. Abstr. **1**, 1–6 (2018)
78. M. Moszyński, Inorganic scintillation detectors in γ-ray spectrometry. Nucl. Instrum. Methods Phys. Res. Sect. A **505**(1–2), 101–110 (2003)
79. V.A. Kachanov et al., Light source for energy stabilization of calorimetric detectors based on photodetectors. Nucl. Instrum. Methods Phys. Res. Sect. A **314**(1), 215–218 (1992)
80. S. Pesente et al., Detection of hidden explosives by using tagged neutron beams with sub-nanosecond time resolution. Nucl. Instrum. Methods Phys. Res. Sect. A **531**(3), 657–667 (2004)
81. A. Annenkov et al., Industrial growth of LuYAP scintillation crystals. Nucl. Instrum. Methods Phys. Res. Sect. A **537**(1–2), 182–184 (2005)
82. M. Korzhik, *Physics of scintillation in oxide crystals* (Belarussian State University, Minsk, 2003)
83. M. Nikl et al., Shallow traps and radiative recombination processes in Lu3Al5O12:Ce single crystal scintillator. Phys. Rev. B **76**(19), 195121 (2007)
84. C.R. Stanek, K.J. McClellan, M.R. Levy, R.W. Grimes, Defect behavior in rare earth REAlO3 scintillators. J. Appl. Phys. **99**(11), 113518 (2006)
85. S. Gundacker et al., State of the art timing in TOF-PET detectors with LuAG, GAGG and L(Y) SO scintillators of various sizes coupled to FBK-SiPMs. J. Instrum. **11**(8), P08008–P08008 (2016)
86. H. Nishimura, M. Sakata, T. Tsujimoto, M. Nakayama, Origin of the 4.1-eV luminescence in pure CsI scintillator. Phys. Rev. B **51**(4), 2167–2172 (1995)
87. A.N. Belsky et al., Experimental study of the excitation threshold of fast intrinsic luminescence of CsI. Phys. Rev. B **49**(18), 13197–13200 (1994)
88. G. Bizarri, P. Dorenbos, Charge carrier and exciton dynamics in LaBr3:Ce3+ scintillators: Experiment and model. Phys. Rev. B **75**(18), 184302 (2007)
89. U. Rogulis et al., Magnetic resonance investigations of LaCl3:Ce3+ scintillators. Radiat. Eff. Defects Solids **157**(6–12), 951–955 (2002)
90. D.N. ter Weele, D.R. Schaart, P. Dorenbos, Intrinsic scintillation pulse shape measurements by means of picosecond x-ray excitation for fast timing applications. Nucl. Instrum. Methods Phys. Res. Sect. A **767**, 206–211 (2014)
91. J. Glodo et al., Effects of Ce concentration on scintillation properties of LaBr3:Ce. IEEE Trans. Nucl. Sci. **52**(5), 1805–1808 (2005)
92. S. Seifert, J.H.L. Steenbergen, H.T. van Dam, D.R. Schaart, Accurate measurement of the rise and decay times of fast scintillators with solid state photon counters. J. Instrum. **7**(9), P09004–P09004 (2012)
93. R.W. Novotny et al., Radiation hardness and recovery processes of PWO crystals at -25degC. IEEE Trans. Nucl. Sci. **55**(3), 1283–1288 (2008)

94. S. Burachas et al., Lead tungstate crystals for the ALICE/CERN experiment. Nucl. Instrum. Methods Phys. Res. Sect. A **486**(1–2), 83–88 (2002)
95. A. Breskin, *The CERN Large Hadron Collider: Accelerator and Experiments* (CERN, Geneva, 2009)
96. R.W. Novotny, Fast and compact lead tungstate-based electromagnetic calorimeter for the PANDA detector at GSI. IEEE Trans. Nucl. Sci. **51**(6), 3076–3080 (2004)
97. M. Nikl, Wide band gap scintillation materials: Progress in the technology and material understanding. Phys. Status Solidi **178**(2), 595–620 (2000)
98. A. Annenkov, M. Korzhik, P. Lecoq, Lead tungstate scintillation material. Nucl. Instrum. Methods Phys. Res. Sect. A **490**(1–2), 30–50 (2002)
99. W. van Loo, Phys. Stat. Sol. (a) **27**, 565 (1979); **28**, 227 (1979)
100. J.A. Groenink, G. Blasse, Some new observations on the luminescence of PbMoO4 and PbWO4. J. Solid State Chem. **32**(1), 9–20 (1980)
101. E. Auffray et al., Luminescence rise time in self-activated PbWO4 and Ce-doped Gd3Al2Ga3O12 scintillation crystals. J. Lumin. **178**, 54–60 (2016)
102. M. Nikl et al., Excitonic emission of scheelite tungstates AWO4 (A=Pb, Ca, Ba, Sr). J. Lumin. **87–89**, 1136–1139 (2000)
103. M. Itoh, T. Katagiri, Intrinsic luminescence from self-trapped excitons in Bi4Ge3O12 and Bi12GeO20: Decay kinetics and multiplication of electronic excitations. J. Phys. Soc. Jpn. **79** (7), 074717 (2010)
104. M.J. Weber, R.R. Monchamp, Luminescence of Bi4Ge3O12 : Spectral and decay properties. J. Appl. Phys. **44**(12), 5495–5499 (1973)
105. R. Moncorge, B. Jacquier, G. Boulon, F. Gaume-Mahn, J. Janin, Electronic structure and photoluminescence processes in Bi4Ge3O12 single crystal. J. Lumin. **12–13**, 467–472 (1976)
106. W.W. Moses, Time of flight in pet revisited. IEEE Trans. Nucl. Sci. **50**(5), 1325–1330 (2003)
107. S. Vandenberghe, E. Mikhaylova, E. D'Hoe, P. Mollet, J.S. Karp, Recent developments in time-of-flight PET. EJNMMI Phys. **3**(1), 3 (2016)
108. C. Dujardin et al., Spectroscopic properties of CeF3 and LuF3:Ce3+ thin films grown by molecular beam epitaxy. Opt. Mater. (Amst) **16**(1–2), 69–76 (2001)
109. C. Pedrini, B. Moine, J.C. Gacon, B. Jacquier, One- and two-photon spectroscopy of Ce3+ ions in LaF3-CeF3 mixed crystals. J. Phys. Condens. Matter **4**(24), 5461–5470 (1992)
110. E. Auffray et al., Picosecond transient absorption rise time for ultrafast tagging of the interaction of ionizing radiation with scintillating crystals in high energy physics experiments. J. Instrum. **9**(7), P07017–P07017 (2014)
111. C. Pedrini, C. Dujardin, J.C. Gâcon, A.N. Belsky, A.N. Vasil'ev, A.G. Petrosyan, Cerium-doped fluorescent and scintillating ionic crystals. Radiat. Eff. Defects Solids **154**(3–4), 277–286 (2001)
112. I.A. Kamenskikh et al., LSO-Ce fluorescence spectra and kinetics for UV, VUV and X-ray excitation. Radiat. Eff. Defects Solids **135**(1–4), 391–396 (1995)
113. R. Kirkin, V.V. Mikhailin, A.N. Vasil'ev, Recombination of correlated electron–hole pairs with account of hot capture with emission of optical phonons. IEEE Trans. Nucl. Sci. **59**(5), 2057–2064 (2012)
114. S. Curtarolo, G.L.W. Hart, M.B. Nardelli, N. Mingo, S. Sanvito, O. Levy, The high-throughput highway to computational materials design. Nat. Mater. **12**(3), 191–201 (2013)
115. S. Curtarolo et al., AFLOWLIB.ORG: A distributed materials properties repository from high-throughput ab initio calculations. Comput. Mater. Sci. **58**, 227–235 (2012)
116. N.C. Carvalho, J.-M. Le Floch, J. Krupka, M.E. Tobar, Multi-mode technique for the determination of the biaxial Y2SiO5 permittivity tensor from 300 to 6K. Appl. Phys. Lett. **106**(19), 192904 (2015)
117. H. Huang, Q. Li, X. Lu, Y. Qian, Y. Wu, R.T. Williams, Role of hot electron transport in scintillators: A theoretical study. Phys. Status Solidi – Rapid Res. Lett. **10**(10), 762–768 (2016)

118. M.P. Prange, Y. Xie, L.W. Campbell, F. Gao, S. Kerisit, Monte Carlo simulation of electron thermalization in scintillator materials: Implications for scintillator nonproportionality. J. Appl. Phys. **122**(23), 234504 (2017)
119. A.N. Vasil'ev, A.V. Gektin, Multiscale approach to estimation of scintillation characteristics. IEEE Trans. Nucl. Sci. **61**(1), 235–245 (2014)

Chapter 6
Transient Phenomena in Scintillators

Abstract This chapter describes the fastest processes during the propagation of electronic excitations through the media, Cherenkov radiation, intraband luminescence, cross-luminescence, elastic polarization, and their relaxation. The spectral features and time profiles of these types of emission are discussed.

6.1 Radiation Processes During Thermalization

The hot luminescence emitted during thermalization of electronic excitations can improve the time resolution to low values [1]. The general scheme of energy losses during the propagation of charged particles and electronic excitations through the crystal is discussed in Chap. 3 in terms of electromagnetic interaction of the charged particle with media. Formula (3.4) describes the probability of the emission of electromagnetic quanta by a fast electron as an integral over all possible energies and momenta of these emitted excitations. The core part of this formula is the imaginary part of the sum which describes the emission of longitudinal (first term) and transversal (second term) photons:

$$\begin{aligned} w^e(E_e) = &-\frac{4}{(2\pi)^4}\int\limits_{-\infty}^{\infty}\frac{d\omega}{1-e^{-\hbar\omega/k_BT}}\int d^3q\left[\mathrm{Im}\left(-\frac{1}{\varepsilon(\omega,\mathbf{q})}\right)M^e_{\parallel}(E_e,E_e-\hbar\omega,\mathbf{q})\right. \\ &\left.+\mathrm{Im}\left(-\frac{2}{\varepsilon(\omega,\mathbf{q})-c^2q^2/\omega^2}\right)M^e_{\perp}(E_e,E_e-\hbar\omega,\mathbf{q})\right]G_e(E_e-\hbar\omega) \\ &\equiv w^e_e(E_e)+w^e_{ph}(E_e)+w^e_r(E_e). \end{aligned} \tag{6.1}$$

Here, $M^e_{\parallel}(E_e,E_e-\hbar\omega,\mathbf{q})$ is the mean value of the square of the longitudinal component of dipole momentum matrix element (the unit polarization vector $\mathbf{e}$ is parallel to $\mathbf{q}$) for transition between states $\{E_e,\mathbf{k}\}$ and $\{E_e-\hbar\omega,\mathbf{k}-\mathbf{q}\}$; averaging is performed over $\mathbf{k}$ within the first Brillouin zone. $M^e_{\perp}$ is the analogous mean value for the transversal component ($\mathbf{e}\perp\mathbf{q}$); E_e is the electron energy, $G_e(E_e)$ is the electron

M. Korzhik et al., *Physics of Fast Processes in Scintillators*, Particle Acceleration and Detection, https://doi.org/10.1007/978-3-030-21966-6_6

density of states. The integration over ω is limited by the region where the density of final states $G_e(E_e - \hbar\omega)$ is not zero. Please note that the Bose statistical factor is included into the integrand of (6.1) in order to taking account of both absorption and emission processes. This factor is important mostly for phonon energy region, and we can separate it taking the integral over phonon region $w^e_{ph}(E_e) = \int\limits_{-\Omega_{LO}}^{\Omega_{LO}} \cdots d\omega$, where Ω_{LO} is the frequency of longitudinal photon. Note that the imaginary part of the dielectric permittivity is an odd function of ω, and the denominator in the Bose statistical factor also changes its sign when ω becomes negative. So, the integral over negative ω is positive and describes the phonon absorption processes (the final energy of electron $E_e + |\hbar\omega|$ is higher than the initial one E_e). The rest part of this integral can be further subdivided in two parts according to the terms in the square brackets. The first term is the emission of virtual longitudinal photons which are immediately absorbed by the media with creation of electron-hole pairs. Therefore, this term defines the rate of strongly inelastic electron-electron scattering $w^e_e(E_e)$. The second term in the square brackets corresponds to the emission of transversal photons, and the resulting rate can be denoted as $w^e_r(E_e)$. The transversal photons can escape the crystal only if their energy falls into the transparency range. For crystals with low defect concentration, this range is $\hbar\Omega_{LO} < \hbar\omega < E_{ex}$. Other photons are absorbed in the crystal with production of additional excitations, and the corresponding part of the transversal integral can be included in the term $w^e_e(E_e)$.

In transparency region, the fraction $1/(\varepsilon(\omega, q) - c^2q^2/\omega^2 + i0)$ has a pole when the wavevector q approaches the solution of wave equation $q = \omega n(\omega)/c$, where $n(\omega) \equiv \mathrm{Re}\sqrt{\varepsilon(\omega, 0)}$ is the refractive index of the crystal. In this case, the integral over $\mathbf{q}$ can be calculated and the rate of emission equals:

$$w^e_r(E_e) = \frac{1}{\pi^2} \int\limits_{\Omega_{LO}}^{E_e/\hbar} d\omega \, \frac{\omega^3}{c^3} \, n(\omega) M^e_\perp(E_e, E_e - \hbar\omega, 0) \, G_e(E_e - \hbar\omega), \tag{6.2}$$

where the integration is performed over the transparency range.

The same equations can be written for holes (with exchange of indexes $e \leftrightarrow h$). In this case, the hole energy is also positive and increases from the top of the valence band to deeper core levels. The principal difference between electrons and of holes is that the density of states for holes $G_h(E_h)$ is non-zero only within the allowed valence and core bands, whereas for electrons, gaps in the conduction band are observed only for a few crystals.

The electron-electron scattering and the radiation process result in rather big change of the carrier energy. On the contrary, the phonon scattering changes the energy only by optical phonon energy, which is typically less than 100 meV. Therefore, this change can be assumed to be small, and smooth behavior of $n_e(E_e, t)$ on this energy scale might be supposed. Thus, the rate equation for the population of hot electrons $n_e(E_e, t)$ and holes $n_h(E_h, t)$ for the energies corresponding to the final

stages of the cascade of electron-hole pair multiplication can be written as a diffusion equation over energy. For electrons, it has a form:

$$\begin{aligned}\frac{\partial n_e(E_e,t)}{\partial t} =& - w_e^e(E_e)n_e(E_e,t) - w_r^e(E_e)n_e(E_e,t)\\ &+ \frac{\partial}{\partial E_e}\left(D_e^E(E_e)G_e(E_e)e^{-E_e/k_BT}\frac{\partial}{\partial E_e}\left(\frac{n_e(E_e,t)}{G_e(E_e)}e^{E_e/k_BT}\right)\right).\end{aligned} \tag{6.3}$$

where the energy diffusion coefficient equals

$$\begin{aligned}D_e^E(E_e) =& \frac{\hbar^2}{2\pi^2}\int_0^{\Omega_{LO}} d\omega \int d^3q\,\mathrm{Im}\left(-\frac{1}{\varepsilon(\omega,\mathbf{q})}\right)\\ &\times \omega^2\Big((n_\omega+1)M_\parallel^e(E_e,E_e-\hbar\omega,\mathbf{q})G_e(E_e-\hbar\omega)\\ &+ n_\omega M_\parallel^e(E_e,E_e+\hbar\omega,\mathbf{q})G_e(E_e+\hbar\omega)\Big).\end{aligned} \tag{6.4}$$

Here, $n_\omega = 1/\left(e^{\hbar\omega/k_BT}-1\right)$ is the phonon population at temperature T. For interaction of electrons with one branch of longitudinal optical phonons and a parabolic band with effective mass m^*, the diffusion coefficient is

$$D_e^E(E_e) = (2n_{\Omega_{LO}}+1)\frac{\hbar^3\Omega_{LO}^3}{a_B\widetilde{\varepsilon}\sqrt{2E_em^*}}\ln\frac{4E_e}{\hbar\Omega_{LO}}. \tag{6.5}$$

Equation (6.3) describes the carrier thermalization together with possible photon emission and electron scattering processes. For holes, the latter two processes are usually referred to as Auger processes. If the energy of the carrier is well above energy k_BT from the boundary of the corresponding band (bottom of the conduction band, top of the valence band or top of the outermost core band), Eq. (6.3) can be simplified and written in the form of energy drift rather than diffusion [2]:

$$\frac{\partial n_e(E_e,t)}{\partial t} = -w_e^e(E_e)n_e(E_e,t) - w_r^e(E_e)n_e(E_e,t) - \frac{\partial}{\partial E_e}\left(S_e^E(E_e)n_e(E_e,t)\right). \tag{6.6}$$

Here, $S_e^E(E_e) = D_e^E(E_e)/k_BT$ is the energy relaxation rate, if LO phonon energy is less than k_BT, and

$$S_e^E(E_e) = D_e^E(E_e)/\left(\frac{\hbar\Omega_{LO}}{2}\coth\left(\frac{\hbar\Omega_{LO}}{2k_BT}\right)\right) = \frac{\hbar^2\Omega_{LO}^2}{a_B\widetilde{\varepsilon}\sqrt{2E_em^*}}\ln\frac{4E_e}{\hbar\Omega_{LO}} \tag{6.7}$$

in case of one LO phonon mode. The initial conditions for Eqs. (6.3) and (6.6) are the electron and hole concentrations, $n_e(E_e,0) = g_e(E_e)$ and $n_h(E_h,0) = g_h(E_h)$, after the

main stage of the energy relaxation cascade, which is described in Sect. 3.5 (Eqs. (3.6) and (3.7)).

The solution of Eq. (6.6) can be found in general way:

$$n_e(E_e,t) = \frac{1}{S_e^E(E_e)} \int_{E_e}^{E_{th}} \exp\left(- \int_{E_e}^{E_1} \frac{w_e^e(E_2)}{S_e^E(E_2)} dE_2 \right) n_e(E_1,0)\delta\left(t - \int_{E_e}^{E_1} \frac{dE_2}{S_e^E(E_2)} \right) dE_1. \tag{6.8}$$

In this integral, we neglect the term describing the population reduction due to radiation processes, since the radiation rate is approximately equal or less than 10^9 s^{-1}, whereas the thermalization duration is $\sim 10^{-12}$ s, and the input of this term in the exponent is negligible. The meaning of this equation is rather straightforward. The δ-function in Eq. (6.8) describes the electron energy descent from initial energy E_1 to E_e, and the time of this descent is $\int_{E_e}^{E_1} dE_2/S_e^E(E_2)$. The exponential function describes the reduction of electron number due to scattering (or Auger process for holes). The electron concentration is inversely proportional to the rate of energy relaxation $S_e^E(E_e)$, which, in turn, is proportional to the density of states in the vicinity of energy E_e. This means that the energy distribution of thermalizing electrons has its maximum slightly above the energy corresponding to the minimum of the density of states.

The spectrum of photons emitted by an electron with energy E_e is just the integrand of Eq. (6.2). Therefore, the time dependence of the spectrum is the integral of this integrand multiplied by the electron distribution $n_e(E_e,t)$:

$$I^e(\hbar\omega,t) = \frac{1}{\hbar\pi^2} \frac{\omega^3}{c^3} n(\omega) \int_{\hbar\Omega_{LO}}^{E_{th}} M_\perp^e(E_e, E_e - \hbar\omega, 0)\, G_e(E_e - \hbar\omega) n_e(E_e,t) dE_e. \tag{6.9}$$

The properties of emission which occur during the relaxation of electronic excitations strongly depend on the continuity of the density of states. If the density of states is a continuous function or has either certain dips to non-zero level or gaps with a relatively small energy width (below 1 eV), the corresponding emission is often referred to as electronic or hole intraband luminescence (IBL). Its properties are discussed in Sect. 6.2. If the density of states contains rather wide gaps, the emission is known as cross-luminescence, Auger-free luminescence, or core-valence transitions. All three terms mean the same phenomenon. In this book (Sect. 6.3), we use the term cross-luminescence.

6.2 Intraband Luminescence

The transient emission accompanying the relaxation of hot electrons and holes within continuous conduction band is known as intraband luminescence (IBL) [3, 4]. Recently, the study of this effect was renovated using contemporary experimental basis [5, 6], since this emission is considered to be a candidate for fast registration of ionizing particles [1]. Figure 6.1 shows the scheme of the processes described in the previous section in a continuous conduction band. The thermalization process is dominated by the phonon emission. The phonon emission rate is 10^{14}–10^{15} s^{-1}. For longitudinal optical phonons, this rate nearly linearly increases with the phonon energy. In case of a parabolic conduction band, the net rate of energy relaxation, which takes into account both phonon emission and absorption, is described by Eq. (6.7) and quadratically increases with LO phonon energy. The typical values of $S_e^E(E_e)$ are ~10^{14} eV/s for $\hbar\Omega_{LO} \approx 100$ meV (for the case of crystal consisting of light ions like oxygen) and ~10^{12} eV/s for $\hbar\Omega_{LO} \approx 10$ meV (in the case of crystal consisting only of heavy ions like CsI) (see also Fig. 3.15). Therefore, hot electrons exist in the conduction band during only a few tens of femtoseconds (for the case of high-energy phonons) or few picoseconds (in case of low-energy phonon energy). The typical radiative recombination rate is ~10^9 s^{-1} for the emission of photon with energy of ~5 eV, and ~10^8 s^{-1} for photons in red region (corresponding to an approximately quadratic dependence on photon energy). Therefore, in case of

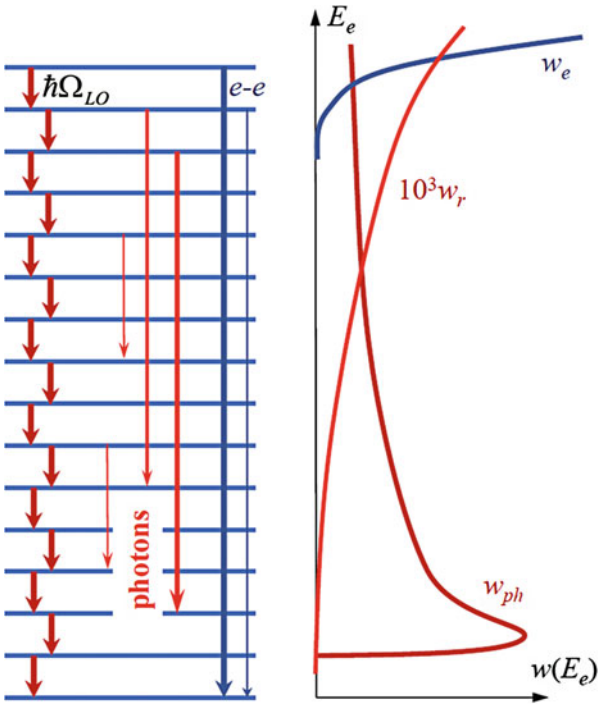

Fig. 6.1 Scheme of the processes influencing the IBL (left panel) and the electron energy dependences of the rates of inelastic electron-electron scattering w_e, phonon scattering w_{ph}, and radiative recombination w_r

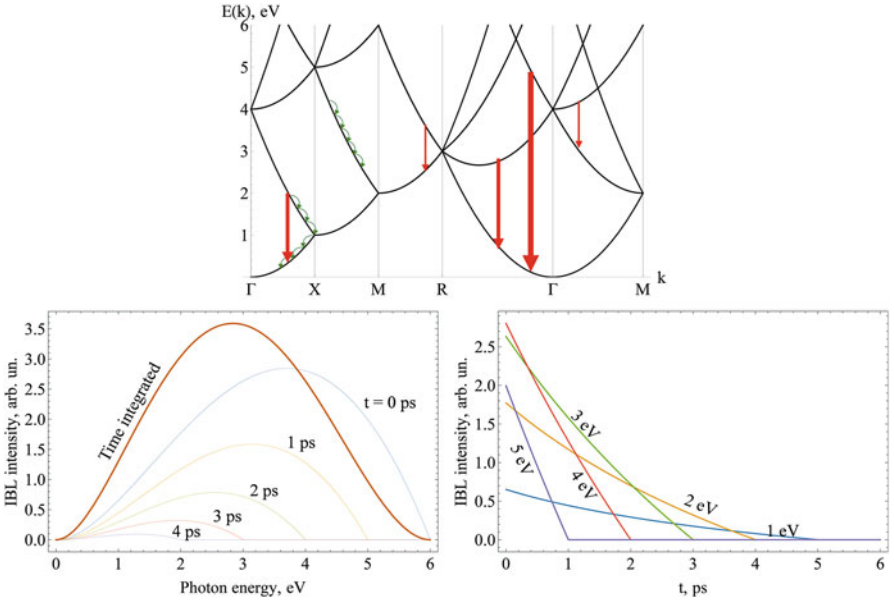

Fig. 6.2 Top panel: Band structure for the model of nearly free electrons. Red arrows illustrate direct radiative transitions, relaxation with phonon emission is indicated in olive. Bottom: Typical evolution of IBL spectrum in time, delay times are indicated, (bottom left panel) and typical IBL decay kinetics (bottom right) for different spectral components of the emission (indicated). The calculation parameters were close to those of CsI crystal (band gap width 6 eV, phonon energy ~10 meV)

continuous density of states, the yield of hot luminescence during the relaxation is very small, from 10^{-5} to 10^{-3} photons per one electron. For the interaction with a 662 keV electron, the number of produced electron-hole pairs is $\sim 10^5$, thus, the maximal yield of such emission is not higher than 30 photons per event. This estimation takes into account that the initial energy distribution of secondary electrons after cascading down is non-uniform in energy and shifted to the low energy side (see Fig. 3.14 and the corresponding part of Sect. 3.5).

The typical IBL spectrum and the decay kinetics of spectral components for a continuous parabolic band reflect the dynamics of electrons during their relaxation (see Fig. 6.2). The matrix elements, which are in the integrands of Eqs. (6.2) and (6.9), are taken for zero momentum transfer ($\mathbf{q} = 0$), since the wavevector of the photon with energy in the transparency region is much smaller than the electron wavevector. So, the radiative transitions are "vertical", and the electron momentum is conserved during this transition. The top panel of Fig. 6.2 shows the dispersion law in the model of nearly free electrons in a crystal (multiple parabolic bands model, MPB) with parameters of CsI (simple cubic lattice with the lattice constant and the electron effective mass equal to that of CsI). The transitions can occur only between the branches of the energy dispersion law. Possible radiative transitions are

shown by red arrows, phonon transitions resulting in relaxation are indicated in olive.

Bottom panels show schematically the evolution of spectrum of IBL for MPB approximation. The high-energy components of the emission spectrum decay faster than low-energy ones. The decay is strongly non-exponential and has a finite duration until the hot electron relaxation is finished. These curves are calculated in the approximation of energy descent (Eq. (6.6) and (6.8)). Taking the energy diffusion into account results in slowing of the final thermalization steps, when the electron energy approaches k_BT. This part of thermalization has no substantial influence on the decay in the systems with a smooth density of states. These estimations show that IBL is fast and week process, which could be exploited in real applications, provided that a way to increase the light yield is found.

The IBL emission spectrum for a continuous density of states is rather smooth due to integration over all initial states and has the upper limit equal to the threshold of inelastic electron-electron scattering. The weakness of the IBL intensity is a result of the electron momentum conservation law for direct optical transitions. Taking indirect radiative transitions (phonon-assisted transitions, which appear in the second order of perturbation) modifies the low-energy part of the IBL spectrum. For the indirect transitions, the radiative emission is a reverse process to the Drude absorption, which allows the transitions without electron momentum conservation even in a single parabolic band. In this case, the emission intensity increases with decreasing photon energy [5, 6]. The infrared peculiarities observed in the IBL spectrum can be attributed to such second order processes [7].

The situation changes, when the density of states has dips or gaps. Figure 6.3 illustrates the modification of the hot carrier population in these cases. The energy relaxation rate has its minimum at energies slightly above the minimum of the density of states (see Fig. 6.3, left panel). According to Eq. (6.8), the hot carrier population increases at these energies due to a pile-up effect, since the relaxation across the dip is slower. The hot carrier accumulation above the dip can result in the emission spectrum modification, since, for a large fraction of carriers, the energy relaxation is slower just above the dip and makes the relaxation longer with evident increase in the hot carrier lifetime and, correspondingly, in the increase of the intraband luminescence intensity.

If the dip in the density of states drops to zero and a gap between two sub-bands is formed (as depicted in the middle panel of Fig. 6.3), the carrier accumulation above the gap results in a temporal formation of Boltzmann energy distributions of electrons or holes. The lifetime of such "thermalized" excitations above the gap is determined by the processes facilitating the jump of the carriers across the gap. The main process of this type is the process of a multi-phonon transition across the gap. The rate of this transition depends on the ratio between the gap width and the phonon energy. As mentioned in Sect. 3.3, this rate exponentially decreases with the increase of the gap ΔE as $\exp(-p\Delta E/\hbar\Omega_{LO})$, where p is a dimensionless parameter with a value close to 1. Therefore, the systems with gaps in the density of states of ~1 eV are prospective for generation of IBL with increased yield and longer decay (tens of picoseconds).

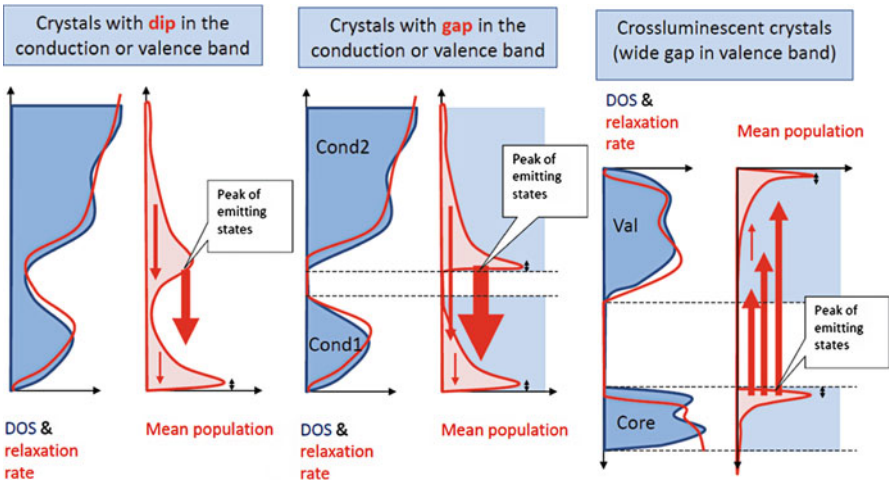

Fig. 6.3 Density of states (blue lines) and relaxation time (red lines, both on the left part of each panel) and the mean hot carrier population (right part of each panel) for the densities of states containing dips (left panel), relatively small (middle panel) and large (crossluminescent crystals, right panel) gaps

The gaps within the conduction band can occur in the crystals containing ions with *d*-electrons forming the bottom of the conduction band. If the upper part of the conduction band is formed by, e.g., *s* states, the gap might exist, and the dipole matrix element of the transition over the gap can be rather large. The crystals containing oxyanionic groups like WO_4 and MoO_4 might be pointed out as examples of the crystals with gaps in the conduction band. The further search for such crystals demands further experimental and theoretical investigations.

Other candidates for the systems with band gaps are the systems with a strong spin-orbit splitting resulting in the subdivision of the valence band into several sub-bands. Unfortunately, it is hardly to expect significant dipole transition matrix element for transition between sub-bands from the levels of the same type (*s-, p-, d-*) but, of different *J* value. The same situation occurs, e.g., for the systems where the valence band is split into sub-bands due to crystal field (for instance, K_2SiF_6, for which the valence band is split into four narrow sub-bands of the same 2*p*F origin).

6.3 Cross-Luminescence

As the gap between the sub-bands increases, the excitation relaxation qualitatively changes, when the multi-phonon relaxation rate across the gap becomes smaller than the rate of radiative recombination. In this case, it is more adequate to speak about bands instead of sub-bands, since the origins of the two bands can be different. The radiation transition is called cross-luminescence (CL), since it is luminescence

originated from the transition between the bands formed by the states of different ions, like 5*p*Ba and 2 *p*F states in the case of BaF_2, the first crystal, in which the fast nanosecond emission was proved to be caused by a transition of this kind [8]. Another name of this emission is core-valence transitions, which underlines the origin of the bands involved in the radiation transition. The third name of this effect, Auger-free emission, reflects another feature of such transitions. A rather detailed table of cross-luminescent crystals with references is presented in [9].

As mentioned above, the radiative transition should be the fastest process resulting in the transition of the core hole to the valence band. The energy conservation demands that the maximal energy, which can be released in this transition process, should be smaller than the minimal energy, which can be absorbed by electronic system of the media. Namely, the difference between the tops of the valence band E_{v1} and the uppermost core band E_{core1} should be smaller than the exciton energy: $|E_{v1} - E_{core1}| < E_{ex}$. In such crystals, the holes can be created in the uppermost core band then thermalized at the top of the core band and passed to the valence band via photon emission with the energy between $|E_{v2} - E_{core1}|$ and $|E_{v1} - E_{core1}|$, where E_{v2} is the bottom of the valence band (Fig. 6.4). If the threshold of the Auger processes is within the uppermost core band, only a part of the holes created during the electron-electron scattering cascade and Auger processes from deeper core levels can survive and participate in CL emission. This part depends on temperature due to the Urbach absorption tail described by $\mathrm{Im}(-1/\varepsilon)$. In the case of, e.g., CsBr, CL is quenched due to the proximity of the Auger threshold to the top of the 5pCs core band and strongly depends on temperature. The temperature dependence differs from Mott-type quenching and is determined by the parameter σ of the Urbach absorption tail $\varepsilon_2(\omega) \sim \exp(\sigma(\hbar\omega - E_0)/k_BT)$ [2]. In most of other CL crystals, the intensity slightly depends on temperature up to the melting point.

The most reliable method of attributing fast emission to the CL type is the excitation spectrum, the threshold of which corresponds to the energy slightly above the core exciton peak [10] (see also Fig. 6.5). CL is only slightly excited in the range of direct creation of core exciton, since, due to Fano effect, the exciton states based on the hole in the core band are mixed with the hot electron states and a hole in the valence band, and the density of such interfering states is much higher than the density of core exciton states (see Sect. 3.2). This type of Auger effect results in fast non-radiative decay of core holes, and the yield of CL in the core exciton region is small (see the inset in Fig.6.5).

Such high sensitivity of CL intensity and decay kinetics on the surrounding excitations is one of the specific features of this effect. Even weak absorption in the transparency region results in strong quenching of CL. Impurities with absorption band peaked below E_{ex} might be an example of such quenching. If the concentration of such defects is low, the main quenching effect occurs within close pairs of core hole and defect and is due to dipole-dipole energy transfer from the core hole to the defect. If the core hole is immobile, the kinetics of CL is described by Eq. (3.36), whereas the decay for mobile holes becomes controlled by diffusion (Eq. (3.42)). Core holes are easily quenched by surface defects as well [12], and the modification of excitation spectra due to the changes of absorption

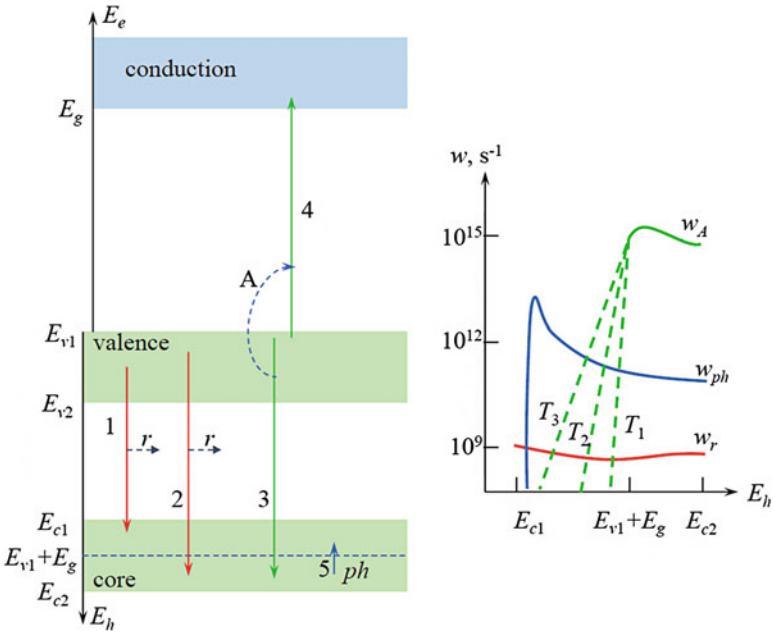

Fig. 6.4 Left panel: scheme of the processes involving holes from the outermost core band: radiative recombination (1, 2), Auger recombination (3) resulting in creation of a new electron-hole pair (4), thermalization with phonon emission (5). Auger processes are allowed due to energy conservation only below the dashed line. Right panel: schematic dependence of the probability of Auger process (w_A), thermalization with phonon emission (w_{ph}), and radiative recombination (w_r) on the core hole energy. Dashed lines indicate the Urbach tail of w_A ($T_3 > T_2 > T_1$)

coefficient allows one to estimate the core hole mobility [13] (the "surface quenching" effect). The same quenching describes the dependence of CL yield and decay kinetics in BaF_2 nanoparticles [14].

The quenching of CL by neighboring impurities is an "extrinsic" effect. This type of emission is very sensitive for all types of neighboring electronic excitations, especially to the spatially correlated excitations produced by the same VUV photon absorption or in the same track of ionizing particle. Such type of quenching on correlated excitations is easily observed for VUV photons, which produce clusters of electronic excitations. For instance, a 100 eV photon creates 4–6 electron-hole pairs around 5pBa core hole at the thermalization distance, and this core hole is easily quenched with significant decrease of the decay time and the deviation from exponential decay (see left panel of Fig. 6.6).

The sensitivity of the CL to the neighboring excitations has two consequences. The "positive" one is that, due to the CL dependence, on the density of excitations in the track, the emission of this type is sensitive to the type of ionizing particles. For

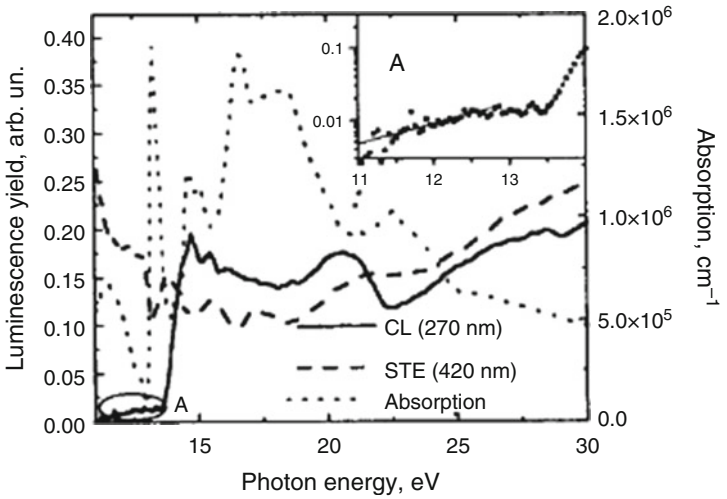

Fig. 6.5 Excitation spectra of CsCl CL (solid curve) and self-trapped exciton emission (dashed curve) and absorption spectrum (dotted curve). In the inset, CL yield as a function of excitation photon energy in the pre-threshold region on semi-logarithmic scale. (Reprinted from Ref. [11] with permission)

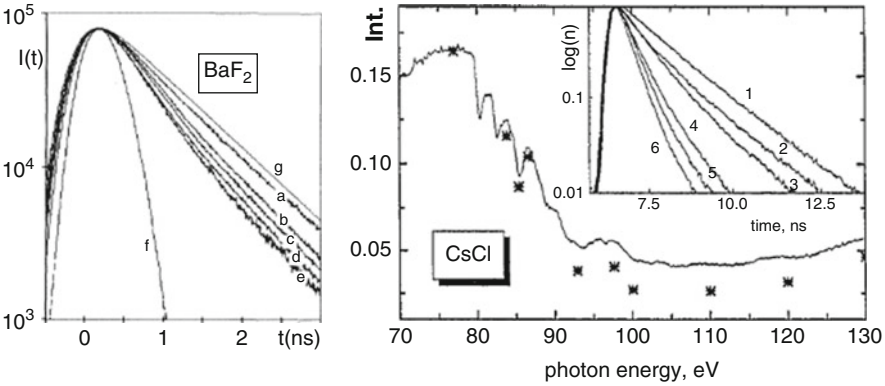

Fig. 6.6 Left panel: BaF_2 fluorescence decay curves for different excitation energies: 30 (**a**), 40 (**b**), 52 (**c**), 70 (**d**), and 90 eV (**e**), UVSOR synchrotron radiation excitation profile (**f**), and the convolution of single exponential decay with characteristic decay time 0.92 ns with excitation profile (**g**). Right panel: CsCl CL excitation spectrum at 150 K. Stars show CL intensity normalized to the peak value 1.5 ns after the excitation pulse. In the inset: CL decay curves at 150 K for excitation energies of 77 eV (curve 2), 140 eV (4), 130 eV (5), and 100 eV (6) and at 10 K for excitation energies of 80 eV (1) and 100 eV (3). (Reprinted from Refs. [12, 15] with permission)

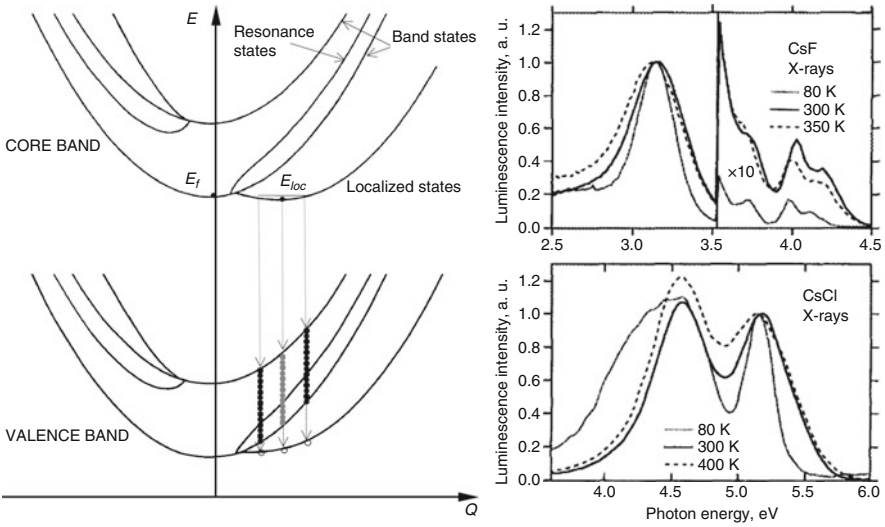

Fig. 6.7 Left panel: configuration diagram of a crossluminescent crystal in the case of core hole localization. The scheme is plotted for the total energy of the system. The system with core hole has higher energy than the system with valence hole, therefore, the core band is above the valence band. Simulation parameters are from [18]. Right panel: CL spectra of CsF (top) and CsCl (bottom) for X-ray excitation. (Reprinted from Ref. [20] with permission)

instance, BaF_2 has two types of emissions: CL with typical room-temperature decay time of ~0.9 ns ("fast") and spectrally separated STE emission with the decay time of ~600 ns ("slow"). For dense tracks of α-particles, there is practically no fast emission. The ratio between fast and slow components enables discrimination of events produced by electrons, mesons, and protons [16].

The "negative" effect of this sensitivity is that the CL yield for ionizing radiation is low (~2000 photons per MeV for BaF_2). The fraction of the uppermost core holes created by ionizing radiation is rather high (~10% of all holes in BaF_2), thus, the yield of $\sim 10^4$ photons per MeV might be expected. Nevertheless, the quenching of the core holes by neighboring excitations substantially reduces the yield (see right panel of Fig. 6.6 for CsCl CL excited by XUV photons of synchrotron radiation).

Relatively long lifetime of the core hole at the top of the outermost core band results in deformation of the lattice around the hole (like around self-trapped hole and self-trapped exciton). This deformation influences not only directly the core holes but also the electrons from the valence band. In this case, the Green function approach [17, 18] shows the formation of resonant states from the valence band (Fig. 6.7, left panel). The transitions from the localized state of the core hole to these resonance states result in the Stokes shift and the temperature dependence of the width of the corresponding CL bands. The broadening of the bands with temperature varies from band to band [19, 20], since the curvature of the final states in coordination diagram is different.

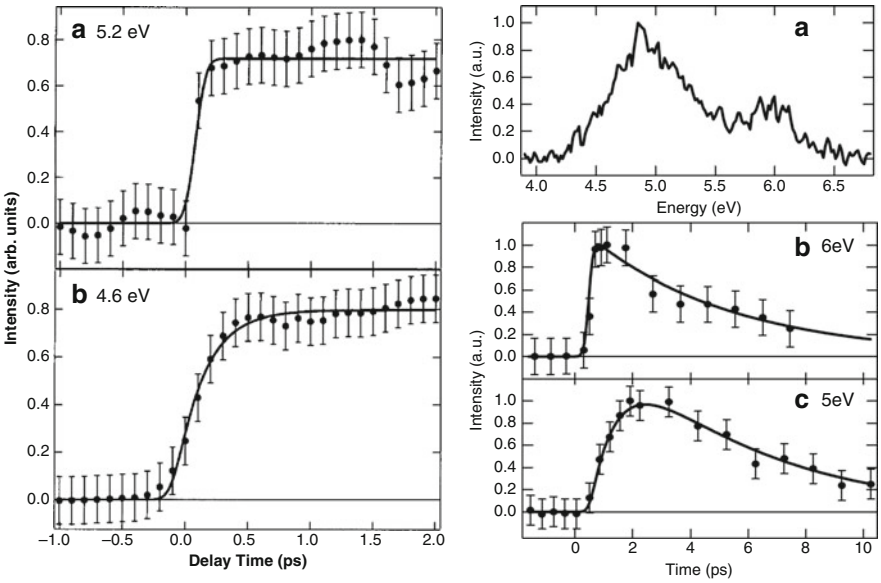

Fig. 6.8 Left panels: time dependence of CL intensity at 5.2 (**a**) and 4.6 eV (**b**). Solid curves represent the fitting results taking account of a response function with temporal width of 140 fs convolved. The rise time at 4.6 eV was 220 ± 50 fs. Right panels: luminescence spectrum of CsBr excited by high harmonics of laser radiation at 300 K (**a**), and the decay kinetics of the luminescence detected at 5.0 eV (**b**) and at 6.0 eV (**c**) at 300 K. Solid lines indicate the best fits. The decay times are 5.0 ± 0.5 ps in both cases. The high-energy band rises instantaneously, whereas the low-energy band emerges with a rise time of 950 ± 100 fs. (Reprinted from Ref. [21, 22] with permission)

The CL decay time is within nanosecond range: ~0.9 ns for BaF_2 and a few nanoseconds for crystals with lower energy emission. The rise time of this emission is very fast and corresponds to the time of the formation of core holes in the cascade process. The time was measured experimentally using the excitation by high harmonics of femtosecond laser radiation generated in gases [21, 22]. The femtosecond detection of CL was performed using the frequency mixing of the luminescence with variably delayed infrared first harmonic of the laser radiation. The rise time is about hundreds of femtoseconds for typical CL crystals (Fig. 6.8). The decay time is 1.8 ns for CsCl crystal and ~5 ps for quenched CL of CsBr crystal.

CL has an additional drawback: this type of emission in most of CL crystals is in UV or even in VUV region and does not fit the spectral sensitivity of most commonly used photodetectors like SiPMs. There is a crystal with CL in the visible range (CsF), but it is highly hygroscopic and hardly useable in most applications.

6.4 Cherenkov Radiation

Here, we have to mention a classical fast emission which is produced by ionizing particles at the very beginning of the cascade when the velocity of the primary electron or fast delta-electron is higher than the phase velocity of the light in the media with certain refraction index. The rate of Cherenkov photon emission is also determined by the second term in Eq. (3.4) and can be expressed as in Eq. (6.2). The properties of Cherenkov emission are well known. The intensity of this emission is unfortunately low, however, this is really "prompt" emission, since the photons are generated before the main part of the cascade and thermalization occur. Cherenkov emission has a wide spectrum which is limited only by the crystal transparency region. The number of emitted photons increases to the short-wavelength edge of the emission spectrum, so the problem of spectral coupling with the detector also arises like in the case of cross-luminescence.

6.5 Elastic Polarization Due to Ionization in Scintillation Crystal

A few phenomena occur in parallel with the carrier relaxation within the very first picoseconds after the ionization starts. One of the phenomena is the elastic polarization [23] due to the local lattice distortion caused by additional electric field due to the displacements of electrons and holes generated by the ionization. This local lattice distortion results in redistribution of the density of states (DOS) of electron in the conduction band in the ionization track. The key feature of the elastic polarization is its short response time, which makes it prospective for using as an optically detectable time mark. Thus, the combination of the detection of scintillation in a conventional energy measurement mode with the detection of a high precision timestamp for interaction promises better capabilities for the detection in collider experiments. Nonlinear optical absorption of femtosecond light pulses at appropriate wavelength is considered to be a tool to form the mark [24, 25]. The effect of elastic polarization should be observed in many crystalline compounds. The strongest effect should be observed in compounds with the bottom of the conduction band formed by *nd* orbitals of the lattice cations. According to the crystal field theory, these orbitals are most sensitive to distortions of the crystal field in the vicinity of emitting centers. Thus, the crystals with lattice cations having strong contribution of *d* orbitals in conduction band (tungstates, molybdates, rare-earth and yttrium garnets, perovskites, oxy-orthosilicates, etc.) might be good candidates.

To estimate the electric field generated due to the non-isotropic distribution of electrons e^- and holes h in the track after thermalization, we use the radial distribution of nonequilibrium carriers in the track in CsI crystal doped by 0.3% of Tl (see details in Chap. 3 and [26]). To simplify the evaluation, let us assume that the track is straight, and the electron energy loss is uniformly distributed along the length of the

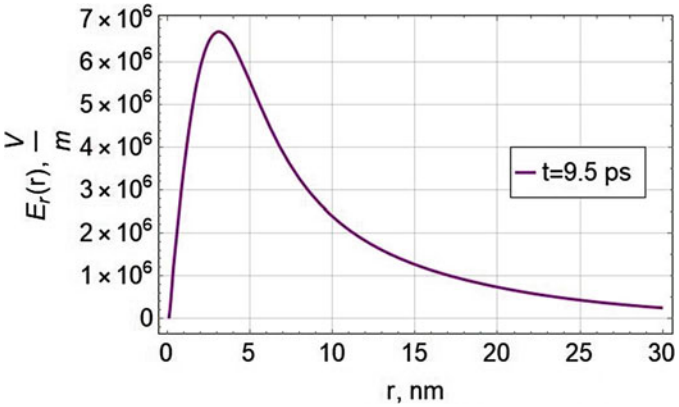

Fig. 6.9 The radial component of the electric field generated by the nonisotropic distribution of electrons and holes in CsI crystal after thermalization of nonequlibrium carriers. The carrier distribution is taken from Ref. [26]

track. Moreover, we suppose that the track length is substantially longer than its radius, so that the edge electric field effects can be neglected. Similarly to [26], we introduce a cylindrical coordinate system, in which Z axis coincides with the central track line of the primary particle. We estimate the field at a point located at a distance r from the track axis, which is much smaller than the distances to the start and end points of the track. Therefore, the dependence of the electric field at the certain point in the track on coordinate z can be neglected. Moreover, due to the axial symmetry of the distribution of electrons and holes relative to the track line, the electric field does not depend on the azimuthal angle φ. The electric field $\overrightarrow{E}(\overrightarrow{r},t) = (E_r(r,t),0,0)$ will satisfy to the following equation:

$$\overrightarrow{\nabla}\cdot\overrightarrow{E}(\overrightarrow{r},t) = \frac{\rho(r,t)}{\varepsilon\varepsilon_0} => \frac{dE_r(r,t)}{dr} + \frac{1}{r}E_r(r,t) = \frac{\rho(r,t)}{\varepsilon\varepsilon_0}, \tag{6.10}$$

where $\rho(r,t) = \frac{e}{2\pi L r}(N_h(r,t) - N_e(r,t))$, $N_h(r,t)$ is radial hole density, $N_h(r, t) \approx N_e(r,0)$, and e is the elementary charge.

The results of the numerical solution of differential equation (6.10) with the boundary condition $E_r(0,t) = 0$ for the time moment $t = 9.5$ ps are presented in Fig. 6.9 for CsI crystal with permittivity ε =5.65.

It is worth noting that this estimation is performed without taking account of screening by surrounding anions, cations, and non-equilibrium charge carriers. Screening might reduce the expansion of the electric field. However, the electric field is slightly smaller than the crystal field, which appears at interatomic distances in ionic crystals. Such crystal fields are of the order of 10^7–10^8 V/m or even higher. Additional microscopic fields occur due to non-uniform distribution of carriers like in plasma. The distribution of microscopic fields is described by Holtsmark distribution [27]. Such additional macroscopic electric field due to the separation of

electrons and holes, together with the microscopic fields due to the distribution of charge carriers in the track region, cause the Stark effect, distorts crystal-forming polyhedra, what results in the redistribution of DOS, particularly in the conduction band, inside and outside the track volume. This effect was measured in [28] at the irradiation of PWO crystal with γ-source and probing by ultrashort laser pulses. The electric field in one track covers thousands of unit cells. The lifetime of the elastic deformation is limited by the relaxation of free carriers. Therefore, fast scintillators like PWO, in which the relaxation occurs via radiative recombination with a time constant of ~10 ns, are preferable for exploitation of the electric field for fast timing. This technique can be useful not only for the registration of high energy particles in scintillation detectors with quite high ionization density, but also for the registration of short high-intensity X-ray pulses creating even larger density of nonequilibrium carriers, as was recently demonstrated in [29].

6.6 Conclusions

The transient luminescence produced during thermalization process is a good candidate for fast timing mainly due to its femtosecond rise time. The intensity of this emission increases in crystals with slow relaxation rate for hot electrons and holes. Electron-phonon relaxation rate is lower in crystals with low-energy optical phonons. An additional increase of the hot carrier lifetime is observed in the crystals with gaps in the conduction or valence bands. Therefore, engineering of composition and structure of such crystals can improve the yield of intraband emission. Cross-luminescent crystals are the limiting case of such slowing of the relaxation, since the gap in this case equals several electron-volts, and the lifetime of the hole before radiative recombination can be as high as a few nanoseconds. The fast emission of this type has its own drawbacks. e.g., emission in UV, but the development of new semiconductor detectors with a wider spectral range could facilitate the application of these cross-luminescent systems for fast timing.

References

1. P. Lecoq, M. Korzhik, A. Vasil'ev, Can transient phenomena help improving time resolution in scintillators. IEEE Trans. Nucl. Sci. **61**, 229–234 (2014)
2. I. Davoli, V.V. Mikhailin, S. Stizza, A.N. Vasilev, Urbach effects in the kinetics of core holes for excitation of cross-luminescence. J. Lumin. **51**, 275–282 (1992)
3. D. Vaisburd, O. Koroleva, S. Kharitonova, Instantaneous spectrum of passively ionized electrons in a dielectric irradiated by a high-power electron beam. Russ. Phys. J. **39**, 1114–1121 (1996)
4. R.G. Deich, M. Karklina, L. Nagli, Intraband luminescence of CsI crystal. Solid State Commun. **71**, 859–862 (1989)

5. S.I. Omelkov, V. Nagirnyi, A.N. Vasil'ev, M. Kirm, New features of hot intraband luminescence for fast timing. J. Lumin. **176**, 309–317 (2016)
6. S.I. Omelkov, V. Nagirnyi, S. Gundacker, D.A. Spassky, E. Auffray, P. Lecoq, M. Kirm, Scintillation yield of hot intraband luminescence. J. Lumin. **198**, 260–271 (2018)
7. A.N. Vasil'ev, R.V. Kirkin, Emission spectrum of intraband luminescence for single parabolic band under excitation of wide-band-gap insulators by ionizing radiation and particles. Phys. Wave Phenom. **23**, 186–191 (2015)
8. Y.M. Aleksandrov, V.N. Makhov, P.A. Rodnyi, T.I. Syreishchikova, M.N. Yakimenko, Intrinsic luminescence of BaF_2 at pulse excitation by synchrotron radiation. Sov. Phys. Solid State **26**, 1734 (1984)
9. C.W.E. van Eijk, Cross-luminescence. J. Lumin. **60&61**, 936–941 (1994)
10. V.N. Makhov, Investigations of fast luminescence in ionic crystals under pulsed synchrotron radiation excitation at the S-60 electron synchrotron. Nucl. Inst. Methods Phys. Res. A **308**, 187–189 (1991)
11. A.N. Belsky, I.A. Kamenskikh, V.V. Mikhailin, A.N. Vasilev, Crossluminescence in ionic crystals. J Electron. Spectrosc. Relat. Phenom. B **79**, 111–116 (1996)
12. M.A. Terekhin, A.N. Vasil'ev, M. Kamada, E. Nakamura, S. Kubota, Effect of quenching processes on decay of fast luminescence from barium fluoride excited by VUV synchrotron radiation. Phys. Rev. B **52**, 3117–3121 (1995)
13. N.Y. Kirikova, V.N. Makhov, Simulation of cross-luminescence excitation spectra of BaF_2 and CsBr crystals. Nucl. Inst. Methods Phys. Res. A **359**, 354–356 (1995)
14. M. Chylii, T. Malyi, I. Rovetskyi, T. Demkiv, V. Vistovskyy, P. Rodnyi, A. Gektin, A. Vasil'ev, A. Voloshinovskii, Diffusion of 5p-holes in BaF_2 nanoparticles. Opt. Mater. **91**, 115–119 (2019)
15. A.N. Belsky, R.A. Glukhov, I.A. Kamenskikh, P. Martin, V.V. Mikhailin, I.H. Munro, C. Pedrini, D.A. Shaw, I.N. Shpinkov, A.N. Vasilev, Luminescence quenching as a probe for the local density of electronic excitations in insulators. J. Electron Spectrosc. Relat. Phenom. **79**, 147–150 (1996)
16. R. Novotny, *Proceedings, International Conference on Inorganic Scintillators and their Applications SCINT95* (Delft University Press, Delft, 1996), pp. 70–73
17. Y. Kayanuma, A. Kotani, Lattice relaxation in Auger decay-free core luminescence. J. Electron Spectrosc. Relat. Phenom. **79**, 219–222 (1996)
18. O.I. Baum, A.N. Vasil'ev, Modification of crossluminescence spectra due to localization of core hole: tight-binding approximation, in *Proceedings, International Conference on Inorganic Scintillators and their Applications SCINT99* (Moscow, 2000), pp. 453–457
19. V.N. Makhov, I. Kuusmann, J. Becker, M. Runne, G. Zimmerer, Crossluminescence at high temperatures. J. Electron Spectrosc. Relat. Phenom. **101-103**, 817–820 (1999)
20. A. Belsky, I. Kamenskikh, V. Mikhailin, A. Vasil'ev, Crossluminescence in ionic crystals. J. Electron. Spectrosc. Relat. Phenom. **79**, 111–116 (1996)
21. T. Sekikawa, T. Yamazaki, Y. Nabekawa, S. Watanabe, Femtosecond lattice relaxation induced by inner-shell excitation. J. Opt. Soc. Am. B **19**, 1941–1945 (2002)
22. T. Shimizu, T. Sekikawa, T. Kanai, S. Watanabe, M. Itoh, Time-resolved Auger decay in CsBr using high harmonics. Phys. Rev. Lett. **91**, 017401 (2003)
23. V.I. Baryshnikov, T.A. Kolesnikova, Femtosecond mechanisms of electronic excitations in crystalline materials. Phys. Solid State **47**, 1847–1851 (2005)
24. E. Auffray, M. Korjik, O. Buganov, A. Fedorov, I. Emelianchik, E. Griesmayer, others, Non-linear optical phenomena in detecting materials as a possibility for fast timing in detectors of ionizing radiation. IEEE Trans. Nucl. Sci. **63**, 2979–2984 (2016)
25. E. Auffray et al., New detecting techniques for a future calorimetry. J. Phys. Conf. Ser. **587**, 012056 (2015)
26. R.T. Williams, J.Q. Grim, Q. Li, K.B. Ucer, W.W. Moses, Excitation density, diffusion-drift, and proportionality in scintillators. Phys. Status Solidi B **248**, 426–438 (2011)

27. M. Baranger, B. Mozer, Electric field distributions in an ionized gas. Phys. Rev. **115**, 521–525 (1959)
28. E. Auffray et al., Application of two-photon absorption in PWO scintillator for fast timing of interaction with ionizing radiation. Nucl. Inst. Methods Phys. Res. A **804**, 194–200 (2015)
29. N. Hartman et al., Sub-femtosecond precision measurement of X-ray arrival time for free-electron lasers. Nat. Photonics **8**, 706–709 (2014)

Chapter 7
Wide-Band-Gap Semiconductor Scintillators

Abstract Conductive semiconductor radiation detectors are successfully used in many applications. This chapter is focused on exploitation of semiconductors, especially wide-band-gap semiconductors, as scintillators. The semiconductor scintillators are prospective for fast radiation detectors. Attempts to use bulk and nanostructured semiconductor scintillators are reviewed. The prospective of using diamonds for fast timing applications is especially addressed.

7.1 Exploitation of Semiconductors in Radiation Detection

Semiconductors are used in the detection of ionizing radiation in two ways: by direct electrical readout of the carriers generated by irradiation or in a scintillator mode, when the light emitted by the irradiated semiconductor is detected by a photodetector.

7.1.1 Conductive Semiconductor Detectors

The direct electrical readout of the carriers generated by irradiation is extensively exploited in many types of semiconductor detectors of ionizing radiation. The detection is based on the measurement of electric current or voltage, which occur due to the separation of nonequilibrium electrons and holes at a p-n or a semiconductor-metal junction and are proportional to the density of the nonequilibrium carriers generated by irradiation. Many books and reviews are devoted for various types of semiconductor detectors of ionizing radiation (see, e.g., [1]) and this topic is out of the scope of the current book. Most of the semiconductor detectors are based on silicon. Their fabrication technology is mature and indirectly supported by the developments in silicon-based electronics and photovoltaics. Unfortunately, the silicon atomic number is too low to ensure sufficient stopping power for certain applications. The atomic number and material density of germanium are more than twice as high as those of silicon, thus, the

M. Korzhik et al., *Physics of Fast Processes in Scintillators*, Particle Acceleration and Detection, https://doi.org/10.1007/978-3-030-21966-6_7

stopping power of Ge is substantially better than that of Si. However, Ge has a narrow band gap (0.67 eV at room temperature, in contrast to 1.12 eV for Si), so that germanium detectors work well, but at cryogenic cooling. CdTe and CdZnTe have approximately the same density and substantially larger effective atomic number than those of Ge, whereas their band gaps are above 1.5 eV. Therefore, these compound semiconductors are the most popular substitutes for Si in the room-temperature-operating semiconductor detectors requiring high stopping power in nuclear radiation detectors (see, e.g., [2, 3]) or for astrophysical and medical applications [4, 5]. Many applications require high radiation tolerance of the detector material. The high radiation hardness might be ensured by exploiting GaN [6–9]. GaN and other III-nitride semiconductors are usually grown as heteroepitaxial layers using MOCVD technique, thus, a typical thickness of the epilayers is below 1 μm, what is insufficient for efficient detection of X-rays, γ-rays, and other uncharged and charged particles. Current progress in the fabrication of bulk or bulk-like GaN offers new chances for developing GaN-based detectors of ionizing radiation. III-nitride-based light emitting diodes, many other optoelectronic devices, and diodes for power electronics are already produced on a large industrial scale and are still being substantially improved. Thus, a significant spillover effect to the field of the radiation detectors based on GaN or other III-nitrides might be expected.

Recently, quite strong defect-related luminescence under excitation by 1.6 MeV protons is observed in GaN [10, 11] and AlGaN [12] and a concept of double-response sensors consisting of III-nitride structures acting both as conductive detectors and scintillators is suggested and implemented for proton detection [10–12].

Silicon carbide is another radiation-tolerant wide-band-gap material prospective to be used in ionizing radiation detectors [13]. SiC-based conductive detectors coupled with scintillators might be used to separate fast component of Cherenkov light from slower component due to scintillation light, which propagates unabsorbed due to wide bandgap of SiC [14]. This approach might turn out to be prospective for fast timing in radiation detection.

The development of SiC-based radiation detectors might benefit from the development of SiC diodes and transistors for power electronics.

7.1.2 Bulk Semiconductor Scintillators

Semiconducting materials might also serve as scintillators, i.e., by emitting scintillation light, which is further detected by photodetectors. Opportunity to design a device matching the scintillator and photodetector in the same semiconductor crystal has been pointed out as a distinct advantage of semiconductor scintillators. Band-to-band radiative recombination in a direct-band-gap semiconductor is usually quite efficient, however, hardly suitable to directly exploiting in scintillation detector, because of the strong reabsorption due to a small Stokes shift between the band-to-band emission and absorption. Therefore, the emission involving defect-related states in the band gap of semiconductors is usually exploited in semiconductor scintillators.

Though not so efficient as the band-to-band recombination, the light emission due to donor-acceptor pair (DAP) recombination or radiative transitions between a donor state and the valence band or the conduction band and an acceptor state might exhibit quite high light yield. This efficiency might be intentionally increased by growth technology and/or annealing. Zinc selenide isovalently doped by tellurium to introduce defect centers serving for efficient DAP recombination might be pointed out as one of the quite efficient semiconductor scintillators (see [15, 16] and recent review [17]). However, the scintillation decay time in ZnSe:Te is of the order of microseconds [18].

Near-band-edge luminescence involving shallow donors and acceptors as well as exciton emission have also been studied in several wide-band-gap semiconductors in view of their exploitation as scintillators. Near-band-edge emission under X-ray excitation has been observed in intentionally doped ZnO:Ga and CdS:In and nominally undoped CuI, PbI_2, HgI_2 [19]. Substantial efforts in the field of semiconductor scintillators have been focused on ZnO:Ga scintillators [20, 21]. However, the emission efficiency of these materials is quite low. The emission bands of these semiconductor scintillators are near the band edge. Therefore, the quantum efficiency of the emission decreases strongly with increasing temperature due to thermally activated transfer of nonequilibrium carriers from light emission centers to nonradiative recombination centers.

Semiconductor scintillators ZnO:Ga and CdS:In exhibit extremely short scintillation decay times of the order of 1 ns, however, their light yield is low, whereas ZnO:Zn, CdS:Ag,Cl, ZnS:Ag have a high light yield but a substantially longer decay time [22]. Since the short decay time in semiconductor scintillators at room temperature is usually caused predominantly by enhanced nonradiative recombination, a high emission efficiency and a short scintillation decay time are simultaneously achieved only at low temperatures.

Semiconductor scintillators suffer from strong reabsorption of the near-band-edge emission. However, the reabsorption does not significantly deteriorate the performance of thin scintillators to detect the radiation with a short absorption length, e.g., α-particles [23]. Moreover, many semiconductor scintillators have a strong stopping power, since they contain heavy stabile elements Tl, Hg, Pb, and Bi as the constituents in their crystal lattice.

7.1.3 Nanostructured Semiconductor Scintillators

The scintillation properties of semiconductors are currently being attempted to improve by exploiting semiconductor nanostructures, where the nonequilibrium carriers experience quantum confinement. The nanostructures with quantum confinement in all three directions are usually referred to as semiconductor 0D structures, quantum dots (QDs) or nanocrystals (NCs).

For centuries, semiconductor nanocrystals have been used to color stained glass. Colored glasses for the magnificent stained-glass windows of churches in Europe

and worldwide have been produced by varying the composition of the ingredients to form nanocrystals of CdSe, CdSSe and other semiconductors and by selecting appropriate fabrication conditions to monitor the size of the semiconductor nanoparticles. The semiconductor-doped glasses became the object for physical studies and, later on, for applications, after the technologies to fabricate the semiconductor-doped glasses with nanocrystals of a small size dispersion were demonstrated [24, 25]. Later on, colloidal QDs were introduced [26, 27], have already three decades of development history [28] and are being fabricated on commercial scale.

When the size of a semiconductor nanocrystal is of the same order of magnitude as the exciton Bohr radius or the characteristic length describing the extension of the wave functions of electrons and holes, the quasiparticles in the nanocrystal experience quantum confinement, and the continuous spectrum of the density of states of bulk semiconductor transforms to a discrete spectrum, like in atoms or molecules. Within the effective mass approximation, which works well even for small QDs, the discrete energy spectrum $E_n(L)$ of a particle with mass m confined within the length L in one direction can be expressed as

$$E_n(L) = E_g + \frac{n^2\hbar^2\pi^2}{2mL^2}. \tag{7.1}$$

Here, E_g is the band gap of bulk semiconductor, n is the number of the energy level, and $\hbar$ is the reduced Planck constant. For the spectrum in a spherical QD, the ratio $\hbar^2\pi^2/L^2$ in (7.1) is substituted by nodes of appropriate Bessel functions with the QD radius as their argument. As the QD radius is of the order of the exciton Bohr radius, the exciton is confined as a composite quasiparticle, and the mass m in (7.1) or similar expressions equals the exciton mass $m_e + m_h$, where m_e and m_h are the electron and hole effective masses, respectively. For smaller QD radii, in a strong confinement regime when the confinement-related energy is larger than the exciton binding energy due to Coulomb interaction between electron and hole, electrons and holes experience the quantum confinement individually. In this case, m in (7.1) equals m_e or m_h for electrons and holes, respectively, whereas the energies of the optical transitions between the quantized states of electrons and holes with the same number n can be calculated using (7.1) with the reduced mass $\mu\left(\frac{1}{\mu} = \frac{1}{m_e} + \frac{1}{m_h}\right)$. The term exciton is sometimes used also for the pair of individually confined electron and hole in a nanocrystal.

More detailed calculations of the spectral features of light absorption and emission show that the Stokes shift between emission and absorption bands in QDs is slightly larger than that in bulk crystal of the same semiconductor. The calculation results are supported by experimental evidences obtained by photoluminescence excitation and fluorescence line narrowing technique. Though much smaller in many other semiconductor QDs, the resonant Stokes shift observed using size-selective techniques in CdS QDs is reported to be 20–70 meV [29]. Though not large in comparison with the emission band width at room temperature, such larger Stokes

shift is definitely desired for better light extraction from scintillation medium. The Stokes shift engineering is also important for application of semiconductor nanostructures in photovoltaics [30], so synergy of the research in these two directions might be expected.

Exploiting semiconductor nanoparticles instead of bulk semiconductors to develop fast scintillating material attracted recently considerable attention due to expectations that the radiative recombination in nanoparticles is accelerated due to quantum confinement effects. Actually, the oscillator strength per volume for optical transitions in a QD with radius a increases proportionally to $1/a^3$, i.e., at the same rate as the volume of the QD decreases. Consequently, in the first approach, the oscillator strength per QD is constant [31]. However, the dependence of the radiative recombination rate on the emission photon energy, which increases with decreasing size of a QD, and the redistribution of oscillator strength in favor of the lowest optical transition have to be taken into account [32] for a more detailed calculation of the rate of radiative recombination in QDs. Moreover, the radiative recombination rate in QDs depends also on the surrounding medium, as observed, e.g., in CdSe and CdTe QDs embedded in various solvents [33]. The influence of the local field on the spontaneous emission rate in QDs is difficult to estimate, since the typical size of QDs is on the intermediate length scale between the lengths appropriate for the description using the microscopic polarizability and the macroscopic description in terms of the refractive index [34].

Many papers report on very fast luminescence decay experimentally observed in QDs and other nanoparticles of various semiconductors. The problem is that the extraction of the radiative recombination time from the study of luminescence decay in the nanostructures is complicated due to strong nonradiative recombination. QDs have a very large surface to volume ratio, whereas the surface facilitates nonradiative recombination due to nonradiative recombination centers caused by dangling bonds and foreign atoms abundant on the surface. As a result, the luminescence decay is fast but at the expense of efficiency. The surface recombination is substantially diminished by covering the QD with a shell of a structurally compatible semiconductor with a wider band gap. In such a core-shell QD, the carriers are confined in the core of a lower-band-gap semiconductor and experience a spherical potential barrier due to the shell of a wider-band-gap semiconductor. CdSe/CdS or CdS/ZnSe systems might be examples of commercially available core-shell QDs. Both the luminescence efficiency and the decay time increase with the deposition of an appropriate shell. For example, photoluminescence decay time in CdSe/CdS core-shell QDs with 3–4 monolayers of CdS shell was reported to be ~17 ns [35], even longer than that usually observed in bulk CdS. See more on lifetimes in QDs in [36].

Semiconductor nanocrystals offer great freedom for their purposeful design. Several design approaches to improve scintillation properties are already suggested. Fast emission decay under X-ray excitation has been reported in giant-shell QDs [37], i.e., QDs with a thick shell, where the absorption predominantly occurs, and a relatively small core, where the ligh is emitted, though efficiency of this scintillator has still to be improved [38]. Another approach is to use semiconductor nanoplatelets, i.e. plate-like nanostructures with the in-plane dimensions large

enough to neglect the quantum confinement, whereas the thickness of the plate is small enough to cause quantum confinement [38]. The structure intends exploiting the combination of quantum-confinement-enhanced oscillator strength of optical transitions and macroscopically large volume of the plate ensuring collective phasing of dipoles over many unit cells resulting in a giant oscillator strength [39].

Attempts to exploit the benefits of quantum confinement for improving scintillation properties are also being exercised in extended 2D structures, in InGaN/GaN multiple quantum wells (MQWs), which are shown to be prospective for fast detection of soft X-rays [40]. The efficiency of the InGaN/GaN MQW structures is recently improved by depositing a large number of quantum wells [41].The luminescence rise time of at least <10 ps has been observed after photoexcitation with 200 fs pulses [42].

Many possibilities to shift the luminescence decay time in semiconductor nanostructures to picosecond domain [43, 44] are still unexplored.

Exploitation of compactly packed semiconductor QDs as scintillation medium is hardly feasible, first of all, due to the difficulties in absorption of a high-energy quantum and subsequent multiplication of electron-hole pairs within one QD (see, e.g., the studies of excitation clusters in bulk scintillators [45, 46]). It is shown that the fraction of X-ray quantum energy deposited directly in a nanoparticle drops rapidly with X-ray quantum energy even for the nanoparticles 50 nm in size [47]. Moreover, the nonequilibrium carriers efficiently escape the QDs with more than one electron-hole pair due to nonradiative Auger recombination, when the energy of the recombining electron-hole pair is transferred to the third quasiparticle (electron or hole) [48]. The third quasiparticle acquires energy of the order of the effective band gap and has a high probability to escape from the QD. Both the nonradiative Auger recombination and the escape of nonequilibrium carriers out of a QD deteriorate the performance of the QD as a radiation absorber. Meanwhile, the emission properties of QDs have no significant gross favor. Though the rate of radiative recombination in QDs might be higher than that in bulk semiconductors, the gain is depreciated by the problems with nonradiative recombination and lower effective material density, whereas the problem with the tradeoff between the active thickness and the influence of reabsorption remains similar to that in bulk semiconductors.

Exploitation of QDs as light emitters in a matrix acting as radiation absorber seems to be substantially more prospective. In this case, the scintillating medium is similar to the conventional activated scintillators like Ce-doped scintillators. The most important issues in such QD-doped scintillators are the rate and efficiency of excitation transfer from matrix to QDs. Several composite QD containing media have been already demonstrated as prospective scintillators.

Scintillator consisting of CdSe/ZnSe core-shell QDs introduced into porous VYCOR glass by the diffusion from toluene solution is demonstrated to be

prospective for the detection of α-particles [49] and γ irradiation [50]. It is shown that the energy resolution of this composite scintillator is by a factor 2 better than that in a standard NaI crystal, when the 59 keV line of an americium γ-source is used.

A high scintillation efficiency is demonstrated in the composite scintillators fabricated by dispersion of ZnO:Ga powder in polystyrene. Nonradiative energy transfer from polystyrene host to ZnO:Ga scintillating microcrystals is evidenced for X-ray excitation. Scintillation rise time below 18 ps (time resolution of the experiment performed) and a single-exponential decay with a decay time of ~500 ps were observed [51]. A high time resolution of ZnO:Ga nanopowder is observed in coincidence time resolution experiments using a 511 keV gamma source [52].

Scintillators consisting of nanoplatelets of perovskite-type semiconductor CsPbBr3, which had previously been suggested for conductive X- and γ-ray detectors [53], dispersed in a polystyrene host matrix, are demonstrated to be also prospective [54]. Excitonic emission in $CsPbBr_3$ nanoplatelets with several luminescence components decaying with the characteristic times of a few nanoseconds was observed, whereas it was concluded that the loading of the nanoplatelets in polystyrene should be substantially higher than the 0.1 wt.% in the samples studied to ensure efficient energy transfer from the polystyrene matrix to the $CsPbBr_3$ nanoplatelets [54].

In view of practical exploitation of the composite scintillators consisting of semiconductor nanoparticles in an absorbing matrix, the composition of the matrix is of especial importance. The matrixes consisting of light elements suite better for detection of X-rays and soft γ-quanta. However, for γ-quanta with energy above ~100 keV, Compton scattering is the dominating absorption mechanism, and energy deposit becomes strongly delocalized (see Chap. 1). The spatial spreading of the energy deposit is also important for high energy neutrons knocking out protons in media containing hydrogen. In applications requiring good time resolution, the key problem of the energy deposit in a large volume of scintillator is a large dispersion in distances, which the scintillation photons travel from their emission place to photodetector.

Scintillators based on semiconductor nanostructures might be prospective in view of the development of fast detecting systems of hybrid functional pixels consisting of conventional scintillation detectors and scintillation detectors optimized for fast timing. CdSe-based semiconductor nanoplatelets combined with standard scintillator technology are recently demonstrated to achieve 80 ps coincidence time resolution of such a hybrid functional pixel [55].

In conclusion, scintillators based on semiconductor nanostructures offer a wide variety and rich flexibility in their design. They are promising for fast radiation detectors but still in an early development stage in comparison with other scintillating materials prospective for fast timing applications (see, e.g., the recent reviews [56, 57]).

7.2 Detection of Ionizing Radiation with Diamond

7.2.1 Exploitation of Semiconductor Properties

Diamond is one of the first multi-purpose materials in our civilization. Diamond history starts from worshiping diamond jewelry attributing mystical properties and admiration for the look of this crystal and proceeds to routine use of diamond powder for processing other materials. Gradually, especially in the last century, other amazing properties of this material were discovered. Nowadays, it is hard to surprise anyone with artificial diamonds, which are obtained predominantly by high-pressure high-temperature (HPHT) process or by chemical vapor deposition (CVD). In view of many properties (electron and hole mobilities, breakdown voltage, thermal conductivity, etc.), diamond is the best semiconducting material. Diamond as a semiconductor has been tried to exploit in detection of ionizing radiation, particularly neutrons [58–60].

Since diamond is very robust, versatile and radiation tolerant material, it is a favorable candidate for instrumentation for diagnostics of beams of various particles. Diamond has a unique combination of properties: high chemical stability, large heat conductivity, low Z, fast charge transport, durability in the sun light and tolerance to other kinds of irradiation. In a 0.5 mm-thick diamond plate, a 7 TeV proton deposits 645 keV, whereas a 100 GeV electron deposits nearly the same energy, 412 keV.

In spite of a low detecting efficiency, the diamond-based radiation detectors are quite often used to measure fast neutrons exploiting direct interaction with carbon nuclei in the material. The nuclear reactions $^{12}C(n,\alpha)^{9}Be$ and $^{13}C(n,\alpha)^{10}Be$ occur under diamond interaction with neutrons possessing energy above certain threshold. For instance, for the neutrons with energy of 14 MeV, as those provided by a tritium neutron gun, the energy deposit by α-particles due to the process $^{13}C(n,\alpha_0)^{10}Be$ is peaked at 10.5 MeV, whereas the deposit due to $^{12}C(n,\alpha_0)^{9}Be$ reaction has the peak in the vicinity of 8.6 MeV. Moreover, the contribution from $^{12}C(n,3\alpha)$ reaction results in the energy deposition between 5.0 MeV and 7.2 MeV. The ionization by the α-particles emitted in these reactions is very fast and localized in the material (see Chap. 1). Thus, thin detectors are preferable. The detectors based on CVD diamonds show a sub-nanosecond time response [61, 62] and high tolerance to different kinds of irradiation [63, 64] and enable an effective discrimination from other interaction events in the detection material [65, 66]. The diamond-based detectors are a good tool for monitoring fast neutron flux and high-precision neutron spectroscopy [67, 68].

7.2.2 Diamond-Based Scintillators

Besides the crystalline diamond, nanostructured diamond structures gain significant interest, particularly for X-ray beam monitors [69]. The currently extensive research

efforts in this field are focused on the study of structural defects and impurity-related luminescence centers of different origin, which are actually well-known for a long time, e.g., complexes of carbon vacancies with nitrogen, silicon, and germanium. The luminescence centers show fast decaying on a nanosecond range and spectrally narrow, a few nanometers broad at room temperature, lines in their emission. The luminescence of synthetic diamonds is well reviewed in [70, 71]. The luminescence is caused by the defect-related centers, which are formed in the crystal due to peculiarities of technology. The green luminescence is caused by complex defects containing nickel and nitrogen. These luminescence centers can be introduced in the process of CVD deposition or by ion implantation in crystalline diamond but seem to be not important for scintillations.

Another approach to introduce the scintillation centers is the attempt to incorporate into diamond the luminescence ions traditionally used as activators in scintillation materials [72]. It should be emphasized that the incorporation of the rare-earth ions into monoatomic material is a hard technological task. Even after successful introduction, the luminescent properties of the ions in diamond are quite poor. One of novel approaches is to grow a composite material consisting of EuF_3 nanoparticles embedded in microcrystalline diamond films. The system shows a strong Eu^{3+} photoluminescence [73].

There are two types of HPHT diamond samples. Both of them are yellowish in color, however, a part of the samples exhibits a strong green luminescence, whereas the others show only a week shining at the same conditions of photoexcitation. The luminescent properties of the diamond samples are caused by the defects of different kind; most of them are nitrogen-related centers. As a rule, the samples have a luminescence band peaked at ~530 nm and a broad luminescence excitation band peaked at ~340 nm. Luminescent HPHT-diamond samples show a clear scintillation effect under excitation by *a*-particles [74]. Figure 7.1 shows the room temperature amplitude spectra of ^{238}Pu α-particles measured with 0.3 mm-thick diamond crystal

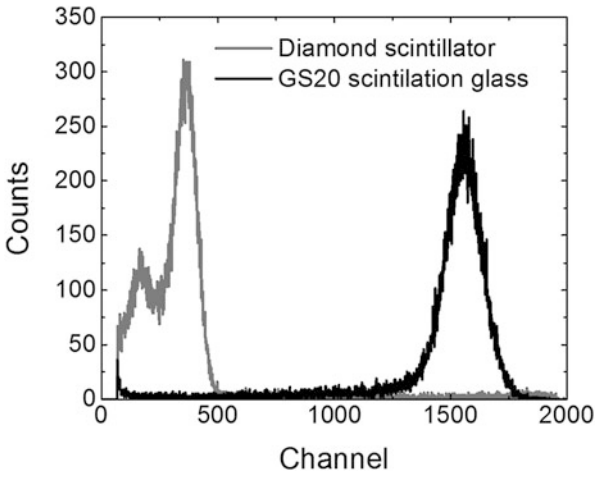

Fig. 7.1 ^{239}Pu alpha-particle amplitude spectra measured with HPHT diamond sample (grey) and GS20 scintillation glass (black). (Reprinted with permission from Ref. [73])

and a reference spectrum obtained with light scintillation glass GS20. CVD diamond also shows scintillations suitable for the detection of α-particles, however, its light output was found to be three times smaller than that of HPHT diamond.

7.3 Nonlinear Optical Absorption and Non-equilibrium Carrier Dynamics in Diamonds Produced Using Different Technologies

In contrary to the complex oxide crystals based on oxy-anionic complexes, diamond is a wide-band-gap indirect semiconductor having a relatively simple electronic band structure due to its monoatomic network. Two-photon absorption in nitrogen-free diamond is studied in detail for different reasons [75]. The lowest two-photon absorption band was observed to peak at the total energy of the two photons of 5.5 eV. This energy corresponds to the indirect transition from valence band to conduction band. Direct two-photon absorption was found to occur at 6.5 eV. Figure 7.2 shows the spectrum of differential absorption at different delays between pump at 3.16 eV (395 nm) and probe pulses in HPHT diamond sample exhibiting no scintillations. The pump photon energies were smaller than a half of the 6.5 eV to prevent direct two-photon absorption. Variation of the probe in a range of 3–1.6 eV (410–750 nm) allows for examining by two-photon absorption the energy interval where possible defects and traps have energy levels and indirect transitions might occur. This variation of the pump-probe method targets not only the nonequilibrium carrier dynamics, as described in Chap. 5. In addition, it enables probing the energy levels in diamond, particularly in the HPHT-samples having the cutoff of transmis-

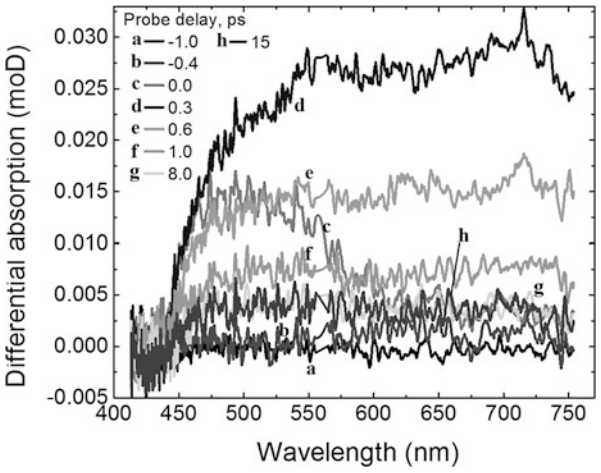

Fig. 7.2 Differential absorption spectra of HPHT diamond pumped with 3.16 eV at different delays between pump and probe indicated. (Reprinted with permission from Ref. [74])

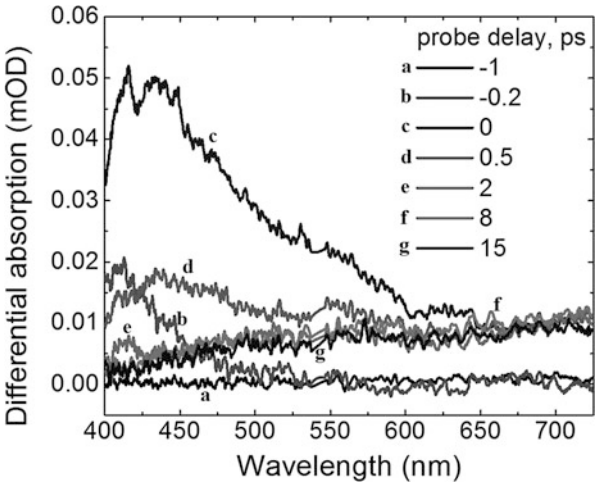

Fig. 7.3 Spectra of differential absorption in CVD diamond pumped at 264 nm (4.73 eV) and probed at different delays between pump and probe (indicated). (Reprinted with permission from Ref. [74])

sion spectrum at ~3.2 eV, i.e., in the spectral region above the limit for single-photon spectroscopy. At a negative delay between pump and probe pulses, when probe pulse enters the sample before pump pulse, no DA signal is observed in the entire spectral range studied. At zero delay, a combined spectrum due to nonlinear absorption of two photons with different energies and to absorption by nonequilibrium carriers is observed. When the delay is positive but still shorter than 1 ps, a contribution to DA from trapped carriers is detected.

The band peaked at ~465 nm (2.6 eV) on the short wavelength shoulder of the band peaked at ~550 nm corresponds quite good the energy of the indirect transition to conduction band. Another, third, band observed in the samples is peaked at ~700 nm.

CVD diamond sample, which, due to technological reasons, has a smaller defect concentration, did not show similar DA spectra at 395 nm pump: only a weak band peaked at ~465 nm was detected. A stronger DA signal was observed for pump at 4.73 eV (264 nm), as seen in Fig. 7.3. A strong band peaked in blue range at 430 nm and two weak bands having maxima at ~550 and 700 nm were detected. Due to a small concentration of defects, the signal is weak when probed with 550 nm. A two-photon transition corresponding to the direct band-to-band transition is observed as a weak shoulder to the band peaked at ~550 nm. A strong band corresponding to the total energy of pump and probe photons of 7.58 eV is observed, in line with the data reported in [75].

All the DA bands in the not scintillating HPHT diamond decay fast and no slow decay components are practically observed (see Fig. 7.4). The total energy of pump and probe photons for the bands peaked at 550 and 700 nm was considerably smaller than the band gap of diamond. Thus, defect centers were claimed to be responsible

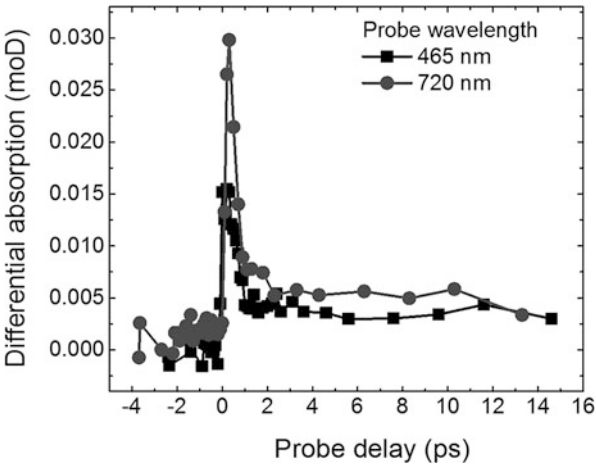

Fig. 7.4 Kinetics of differential absorption in HPHT diamond at 3.16 eV pump and two probe wavelengths: 465 nm (2.7 eV) and 720 nm (1.74 eV). (Reprinted with permission from Ref. [74])

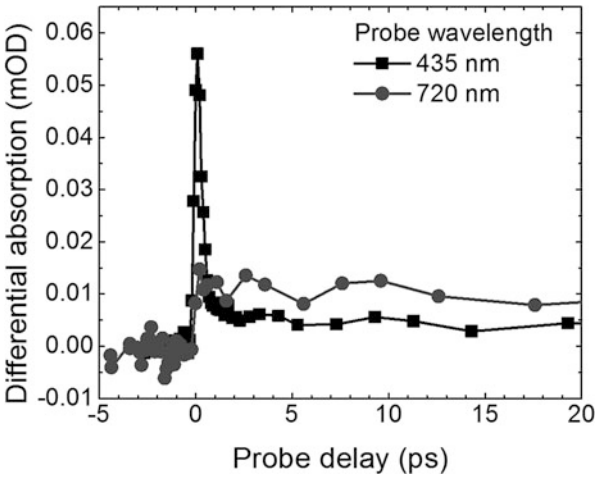

Fig. 7.5 Kinetics of differential absorption in CVD diamond at 4.73 eV pump and two probe wavelengths: 435 nm (2.9 eV) and 720 nm (1.74 eV). (Reprinted with permission from Ref. [74])

for the two-photon absorption in this spectral region. DA signals in CVD diamond are quite fast too (Fig. 7.5).

When the scintillating HPHT diamond sample is probed at 700 nm, the kinetics of differential absorption completely changes its shape, as seen in Fig. 7.6.

Besides the components due to two-photon absorption process, the DA kinetics contains also a rising component attributed to the population of luminescent centers. The rise constant of this component is estimated to be 4 ps.

As demonstrated also for other scintillators, the pump-probe technique can be applied to diamond for the future improvement of its scintillation properties.

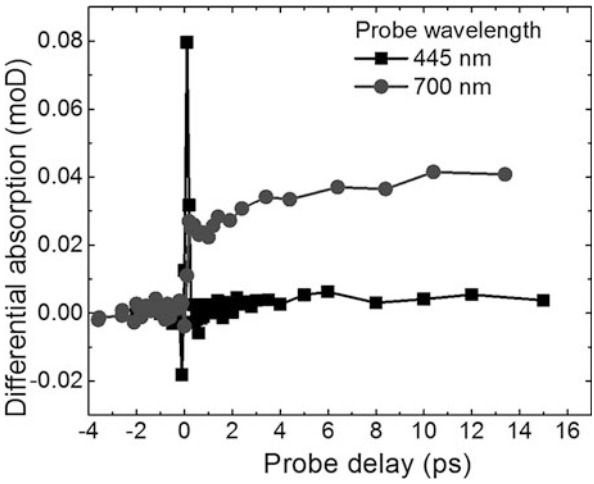

Fig. 7.6 Kinetics of differential absorption of scintillating HPHT diamond at 3.16 eV pump and two probe wavelengths: 465 nm (2.7 eV) and 700 nm (1.7 eV). (Reprinted with permission from Ref. [74])

References

1. G. Lutz, *Semiconductor Radiation Detectors: Device Physics* (Springer, Berlin, 2007)
2. T. Schlesinger et al., Cadmium zinc telluride and its use as a nuclear radiation detector material. Mater. Sci. Eng. R. Rep. **32**(4–5), 103–189 (2001)
3. T. Takahashi, S. Watanabe, Recent progress in CdTe and CdZnTe detectors. IEEE Trans. Nucl. Sci. **48**(4), 950–959 (2001)
4. S. Del Sordo, L. Abbene, E. Caroli, A.M. Mancini, A. Zappettini, P. Ubertini, Progress in the development of CdTe and CdZnTe semiconductor radiation detectors for astrophysical and medical applications. Sensors **9**(5), 3491–3526 (2009)
5. W.C. Barber, J.C. Wessel, E. Nygard, J.S. Iwanczyk, Energy dispersive CdTe and CdZnTe detectors for spectral clinical CT and NDT applications. Nucl. Instrum. Methods Phys. Res. Sect. **784**, 531–537 (2015)
6. J. Grant et al., Wide bandgap semiconductor detectors for harsh radiation environments. Nucl. Instrum. Methods Phys. Res. Sect. A **546**(1–2), 213–217 (2005)
7. P.J. Sellin, J. Vaitkus, New materials for radiation hard semiconductor dectectors. Nucl. Instrum. Methods Phys. Res. Sect. **557**(2), 479–489 (2006)
8. J. Grant et al., GaN as a radiation hard particle detector. Nucl. Instrum. Methods Phys. Res. Sect. A **576**(1), 60–65 (2007)
9. J. Wang, P. Mulligan, L. Brillson, L.R. Cao, Review of using gallium nitride for ionizing radiation detection. Appl. Phys. Rev. **2**(3), 031102 (2015)
10. E. Gaubas et al., In situ characterization of radiation sensors based on GaN LED structure by pulsed capacitance technique and luminescence spectroscopy. Sensors Actuators A Phys. **267**, 194–199 (2017)
11. E. Gaubas et al., Pulsed photo-ionization spectroscopy of traps in as-grown and neutron irradiated ammonothermally synthesized GaN. Sci. Rep. **9**(1), 1473 (2019)
12. Ceponis et al., Evolution of scintillation and electrical characteristics of AlGaN double-response sensors during proton irradiation. Sensors **19**(15), 3388 (2019)
13. F. Nava, G. Bertuccio, A. Cavallini, E. Vittone, Silicon carbide and its use as a radiation detector material. Meas. Sci. Technol. **19**(10), 102001 (2008)
14. O. Adriani et al., CLASSiC: Cherenkov light detection with silicon carbide. Nucl. Instrum. Methods Phys. Res. Sect. **845**, 439–442 (2017)

15. V. Ryzhikov, N. Starzhinskiy, L. Gal'chinetskii, P. Gashin, D. Kozin, E. Danshin, New semiconductor scintillators ZnSe(Te,O) and integrated radiation detectors based thereon. IEEE Trans. Nucl. Sci. **48**(3), 356–359 (2001)
16. W.G. Lee et al., Particularities of ZnSe-based scintillators for a spectrometry of charged particles and gamma quanta. J. Korean Phys. Soc. **48**(1), 47–50 (2006)
17. S. Jagtap, P. Chopade, S. Tadepalli, A. Bhalerao, S. Gosavi, A review on the progress of ZnSe as inorganic scintillator. Opto-Electron. Rev. **27**(1), 90–103 (2019)
18. V. Ryzhikov, G. Tamulaitis, N. Starzhinskiy, L. Gal'chinetskii, A. Novickovas, K. Kazlauskas, Luminescence dynamics in ZnSeTe scintillators. J. Lumin. **101**(1–2), 45–53 (2003)
19. S.E. Derenzo, M.J. Weber, M.K. Klintenberg, Temperature dependence of the fast, near-band-edge scintillation from CuI, HgI2, PbI2, ZnO:Ga and CdS:In. Nucl. Instrum. Methods Phys. Res. Sect. **486**(1–2), 214–219 (2002)
20. J.S. Neal, L.A. Boatner, N.C. Giles, L.E. Halliburton, S.E. Derenzo, E.D. Bourret-Courchesne, Comparative investigation of the performance of ZnO-based scintillators for use as α-particle detectors. Nucl. Instrum. Methods Phys. Res. Sect. A **568**(2), 803–809 (2006)
21. E.D. Bourret-Courchesne, S.E. Derenzo, M.J. Weber, Development of ZnO:Ga as an ultra-fast scintillator. Nucl. Instrum. Methods Phys. Res. Sect. A **601**(3), 358–363 (2009)
22. S.E. Derenzo, E. Bourret-Courshesne, G. Bizarri, A. Canning, Bright and ultra-fast scintillation from a semiconductor? Nucl. Instrum. Methods Phys. Res. Sect. A **805**, 36–40 (2016)
23. Z.I. Kolar, W. den Hollander, 2003: A centennial of spinthariscope and scintillation counting. Appl. Radiat. Isot. **61**(2–3), 261–266 (2004)
24. A.I. Ekimov, A.A. Onushchenko, Quantum size effect in three-dimensional microscopic semiconductor crystals. JETP Lett. **34**(6), 345–349 (1981)
25. A.I. Ekimov, A.I. Efros, A.L. Onushchenko, Quantum size effect in semiconductor microcrystals. Solid State Commun. **56**(11), 921–924 (1985)
26. A.P. Alivisatos, A.L. Harris, N.J. Levinos, M.L. Steigerwald, L.E. Brus, Electronic states of semiconductor clusters: Homogeneous and inhomogeneous broadening of the optical spectrum. J. Chem. Phys. **89**(7), 4001–4011 (1988)
27. M.G. Bawendi, M.L. Steigerwald, L.E. Brus, The quantum mechanics of larger semiconductor clusters ('quantum dots'). Annu. Rev. Phys. Chem. **41**(1), 477–496 (1990)
28. J.Y. Kim, O. Voznyy, D. Zhitomirsky, E.H. Sargent, 25th anniversary article: Colloidal quantum dot materials and devices: A quarter-century of advances. Adv. Mater. **25**(36), 4986–5010 (2013)
29. Z. Yu, J. Li, D.B. O'Connor, L.-W. Wang, P.F. Barbara, Large resonant stokes shift in CdS nanocrystals. J. Phys. Chem. B **107**(24), 5670–5674 (2003)
30. F. Meinardi et al., Large-area luminescent solar concentrators based on 'stokes-shift-engineered' nanocrystals in a mass-polymerized PMMA matrix. Nat. Photonics **8**(5), 392–399 (2014)
31. T. Vossmeyer et al., CdS nanoclusters: Synthesis, characterization, size dependent oscillator strength, temperature shift of the excitonic transition energy, and reversible absorbance shift. J. Phys. Chem. **98**(31), 7665–7673 (1994)
32. C. de Mello Donegá, R. Koole, Size dependence of the spontaneous emission rate and absorption cross section of CdSe and CdTe quantum dots. J. Phys. Chem. C **113**(16), 6511–6520 (2009)
33. S.F. Wuister, C. de Mello Donegá, A. Meijerink, Local-field effects on the spontaneous emission rate of CdTe and CdSe quantum dots in dielectric media. J. Chem. Phys. **121**(9), 4310–4315 (2004)
34. C. Dujardin, D. Amans, A. Belsky, F. Chaput, G. Ledoux, A. Pillonnet, Luminescence and scintillation properties at the nanoscale. IEEE Trans. Nucl. Sci. **57**(3), 1348–1354 (2010)
35. W. Nan et al., Crystal structure control of zinc-blende CdSe/CdS core/shell nanocrystals: Synthesis and structure-dependent optical properties. J. Am. Chem. Soc. **134**(48), 19685–19693 (2012)

36. L.-Y. Chena, H.-L. Chou, C.-H. Chenc, C.-H. Tseng, Surface modification of CdSe and CdS quantum dots-experimental and density function theory investigation, in *Nanocrystals – Synthesis, Characterization and Applications*, (InTech, Rijeka, 2012)
37. Y. Chen et al., 'Giant' multishell CdSe nanocrystal quantum dots with suppressed blinking. J. Am. Chem. Soc. **130**(15), 5026–5027 (2008)
38. R.M. Turtos et al., Ultrafast emission from colloidal nanocrystals under pulsed X-ray excitation. J. Instrum. **11**(10), P10015–P10015 (2016)
39. S. Ithurria, M.D. Tessier, B. Mahler, R.P.S.M. Lobo, B. Dubertret, A.L. Efros, Colloidal nanoplatelets with two-dimensional electronic structure. Nat. Mater. **10**(12), 936–941 (2011)
40. A. Hospodková et al., InGaN/GaN multiple quantum well for fast scintillation application: Radioluminescence and photoluminescence study. Nanotechnology **25**(45), 455501 (2014)
41. T. Hubáček et al., Advancement toward ultra-thick and bright InGaN/GaN structures with a high number of QWs. CrystEngComm **21**(2), 356–362 (2019)
42. G. Toci et al., InGaN/GaN multiple quantum well for superfast scintillation application: Photoluminescence measurements of the picosecond rise time and excitation density effect. J. Lumin. **208**, 119–124 (2019)
43. J. Wilkinson, K.B. Ucer, R.T. Williams, Picosecond excitonic luminescence in ZnO and other wide-gap semiconductors. Radiat. Meas. **38**(4–6), 501–505 (2004)
44. G. Xiong, J. Wilkinson, K.B. Ucer, R.T. Williams, Giant oscillator strength of excitons in bulk and nanostructured systems. J. Lumin. **112**, 1–4), 1–6 (2005)
45. A.N. Vasil'ev, Y. Fang, V.V. Mikhailin, Impact production of secondary electronic excitations in insulators: Multiple-parabolic-branch band model. Phys. Rev. B **60**(8), 5340–5347 (1999)
46. G. Bizarri, W.W. Moses, J. Singh, A.N. Vasil'ev, R.T. Williams, An analytical model of nonproportional scintillator light yield in terms of recombination rates. J. Appl. Phys. **105**(4), 044507 (2009)
47. A.-L. Bulin, A. Vasil'ev, A. Belsky, D. Amans, G. Ledoux, C. Dujardin, Modelling energy deposition in nanoscintillators to predict the efficiency of the x-ray-induced photodynamic effect. Nanoscale **7**(13), 5744–5751 (2015)
48. V.I. Klimov, A.A. Mikhailovsky, D.W. McBranch, C.A. Leatherdale, M.G. Bawendi, Quantization of multiparticle auger rates in semiconductor quantum dots. *Science (80-.)* **28**, 1011–1013 (2000)
49. S.E. Létant, T.-F. Wang, Study of porous glass doped with quantum dots or laser dyes under alpha irradiation. Appl. Phys. Lett. **88**(10), 103110 (2006)
50. S.E. Létant, T.-F. Wang, Semiconductor quantum dot scintillation under γ-ray irradiation. Nano Lett. **6**(12), 2877–2880 (2006)
51. H. Burešová et al., Preparation and luminescence properties of ZnO:Ga – Polystyrene composite scintillator. Opt. Express **24**(14), 15298 (2016)
52. R.M. Turtos et al., Timing performance of ZnO:Ga nanopowder composite scintillators. Phys. Status Solidi Rapid Res. Lett. **10**(11), 843–847 (2016)
53. C.C. Stoumpos et al., Crystal growth of the perovskite semiconductor CsPbBr 3: A new material for high-energy radiation detection. Cryst. Growth Des. **13**(7), 2722–2727 (2013)
54. K. Tomanová et al., On the structure, synthesis, and characterization of ultrafast blue-emitting CsPbBr 3 nanoplatelets. *APL Mater.* **7**(1), 011104 (2019)
55. R.M. Turtos et al., On the use of CdSe scintillating nanoplatelets as time taggers for high-energy gamma detection. npj 2D Mater. Appl. **3**, 1–10 (2019)
56. C. Dujardin et al., Needs, trends, and advances in inorganic scintillators. IEEE Trans. Nucl. Sci. **65**(8), 1977–1997 (2018)
57. F. Maddalena et al., Inorganic, organic, and perovskite halides with nanotechnology for high–light yield X- and γ-ray scintillators. Crystals **9**(2), 88 (2019)
58. H. Kagan, Diamond radiation detectors may be forever! Nucl. Instrum. Methods Phys. Res. Sect. A **546**(1–2), 222–227 (2005)
59. M. Pomorski et al., Development of single-crystal CVD-diamond detectors for spectroscopy and timing. Phys. Status Solidi **203**(12), 3152–3160 (2006)

60. M. Ciobanu et al., In-beam diamond start detectors. IEEE Trans. Nucl. Sci. **58**(4), 2073–2083 (2011)
61. H. Frais-Kolbl, E. Griesmayer, H. Kagan, H. Pernegger, A fast low-noise charged-particle CVD diamond detector. IEEE Trans. Nucl. Sci. **51**(6), 3833–3837 (2004)
62. H. Pernegger et al., Charge-carrier properties in synthetic single-crystal diamond measured with the transient-current technique. J. Appl. Phys. **97**(7), 073704 (2005)
63. D. Husson et al., Neutron irradiation of CVD diamond samples for tracking detectors. Nucl. Instrum. Methods Phys. Res. Sect. **388**(3), 421–426 (1997)
64. D. Meier et al., Proton irradiation of CVD diamond detectors for high-luminosity experiments at the LHC. Nucl. Instrum. Methods Phys. Res. Sect. A **426**(1), 173–180 (1999)
65. P. Kavrigin, P. Finocchiaro, E. Griesmayer, E. Jericha, A. Pappalardo, C. Weiss, Pulse-shape analysis for gamma background rejection in thermal neutron radiation using CVD diamond detectors. Nucl. Instrum. Methods Phys. Res. Sect. A **795**, 88–91 (2015)
66. M. Pillon, M. Angelone, A. Krása, A.J.M. Plompen, P. Schillebeeckx, M.L. Sergi, Experimental response functions of a single-crystal diamond detector for 5–20.5MeV neutrons. Nucl. Instrum. Methods Phys. Res. Sect. A **640**(1), 185–191 (2011)
67. C. Weiss et al., A new CVD Diamond Mosaic-Detector for (n,α) Cross-Section Measurements at the n_TOF Experiment at CERN. Nucl. Instrum. Methods Phys. Res. Sect. A **732**, 190–194 (2013)
68. C. Weiss, H. Frais-Kölbl, E. Griesmayer, P. Kavrigin, Ionization signals from diamond detectors in fast-neutron fields. Eur. Phys. J. A **52**(9), 269 (2016)
69. M. Makita et al., High-resolution single-shot spectral monitoring of hard x-ray free-electron laser radiation. Optica **2**(10), 912 (2015)
70. J. Lindblom, Luminescence study of defects in synthetic as-grown and HPHT diamonds compared to natural diamonds. Am. Mineral. **90**(2–3), 428–440 (2005)
71. A.T. Collins, The characterisation of point defects in diamond by luminescence spectroscopy. Diam. Relat. Mater. **1**(5–6), 457–469 (1992)
72. P. Lecoq, A. Gektin, M. Korzhik, *Inorganic Scintillators for Detector Systems* (Springer, Berlin, 2017)
73. V.S. Sedov et al., Diamond-EuF 3 nanocomposites with bright orange photoluminescence. Diam. Relat. Mater. **72**, 47–52 (2017)
74. M.V. Korjik et al., Non-linear optical phenomena in detecting materials as a possibility for fast timing in detectors of ionizing radiation. IEEE Trans. Nucl. Sci. **63**(6), 2979–2984 (2016)
75. T. Roth, R. Laenen, Absorption of free carriers in diamond determined from the visible to the mid-infrared by femtosecond two-photon absorption spectroscopy. Opt. Commun. **189**(4–6), 289–296 (2001)

Chapter 8
Coincidence Time Resolution Measurements with Scintillators

Abstract This chapter reviews the technique of coincidence time resolution (CTR) using scintillators as the primary detectors of γ-quanta exploited in these measurements, which are quite often used to characterize the timing capabilities of scintillating materials. The contributions of different factors affecting the measurements are analyzed. The recent results obtained by using the CTR technique for studying the currently prospective scintillators are presented.

8.1 Coincidence Time Resolution Technique

8.1.1 Coincidence Time Resolution in a Thin Scintillator

Timing properties of scintillation detectors are under study since the discovery of alkali halide scintillators and their exploitation in radiation detectors. The theoretical results of pioneering studies [1–4] set a way for the description of timing properties, which is actually in use up to now. Further development of the theoretical framework came through accounting for the scintillation pulse shape [5] and other effects caused predominantly by photo-receivers and electronic detection circuits [6–8]. In the last two decades, quite a few papers analyzed more in detail the role of the rise time [9], the influence of light transport [10], the depth of interaction [11], the rise time of the luminescence response, and the capabilities of new photo-receivers, particularly SiPMs [12]. The study in this direction has been further stimulated by the discrepancies in experiential results and the need to understand the fundamental limits for timing measurements with scintillators. In this chapter, we focus on the Coincidence Time Resolution (CTR) [13] measurements and the analysis of physical and instrumental factors affecting the CTR results. The CTR method is quite often used to characterise the time resolution capabilities of scintillation materials. However, the results of the CTR measurements obtained in different laboratories are quite different, even when the same scintillation material produced by the same vendor is exploited. For instance, the CTR FWHM of LSO:Ce and LYSO:Ce crystals reported in recent publications [14–16] vary in a wide range from 85 to 197 ps. The absolute values of the FWHM observed in CTR measurements are strongly affected by

M. Korzhik et al., *Physics of Fast Processes in Scintillators*, Particle Acceleration and Detection, https://doi.org/10.1007/978-3-030-21966-6_8

sample shape and size, experiment geometry, coupling of the samples to SiPMs, the SiPM type and the readout electronics. Since there are no standards for performing the CTR experiments and reporting the experiment conditions, the comparison of the absolute values obtained and reported by different research groups should be exercised cautiously.

As the first step, let us consider two identical thin scintillators used for CTR measurements. The scintillator is assumed to be thin, if the probability to absorb a 511 keV γ-quantum is equal along the length of the sample and does not depend on the energy deposit point. To simplify the evaluation process, similarly as in [5, 17], we approximate our scintillation pulse entering a photo-receiver in a single detector by two exponents with rise and decay components τ_r, τ_d, respectively:

$$f(t,t_0) = \frac{exp\left(-\frac{t-t_0}{\tau_d}\right) - exp\left(-\frac{t-t_0}{\tau_r}\right)}{\tau_d - \tau_r}\theta(t-to), \tag{8.1}$$

where t_0 is the moment of energy deposit in the crystal, $\theta(t - t_0)$ is a Heaviside step function. Here and afterwards, we exploit the first approach for timing with scintillation pulse: the detection of the first photons (see Sect. 2.2). The detection chain consisting of a photo-receiver and electronic circuits can be characterized by a Gaussian-type response to a single-pulse excitation:

$$g(t) = \frac{1}{\sigma_t\sqrt{2\pi}}\exp\left(-\frac{(t-\Delta_t)^2}{2{\sigma_t}^2}\right), \tag{8.2}$$

where σ_t includes the terms reflecting the clock, digitization, electronic jitters, and the noise term of photo-sensor, as described by (1.7), Δ_t is the mean time delay due to electronics. Thus, the change of the scintillation pulse after the registration chain is described by the convolution of $f(t)$ with the response function $g(t)$:

$$\begin{aligned} S(t,t_0) &= \int_{-\infty}^{+\infty} f(\tau)g(t-\tau)d\tau \\ &= \frac{1}{2(\tau_d-\tau_r)}\mathrm{e}^{-t\left(\frac{1}{\tau_d}+\frac{1}{\tau_r}\right)}\left(\mathrm{e}^{\frac{\sigma_\mathrm{t}^2+2(t_0+\Delta_\mathrm{t})\tau_d}{2\tau_d^2}+\frac{1}{\tau_r}}\left(1-\mathrm{Erf}\left[\frac{\sigma_\mathrm{t}^2+(-t+t_0+\Delta_\mathrm{t})\tau_d}{\sqrt{2}\sigma_\mathrm{t}\tau_d}\right]\right)\right. \\ &\quad \left.-\mathrm{e}^{\frac{t}{\tau_d}+\frac{\sigma_\mathrm{t}^2+2(t_0+\Delta_\mathrm{t})\tau_r}{2\tau_r^2}}\left(1-\mathrm{Erf}\left[\frac{\sigma_\mathrm{t}^2+(-t+t_0+\Delta_\mathrm{t})\tau_r}{\sqrt{2}\sigma_\mathrm{t}\tau_r}\right]\right)\right). \end{aligned} \tag{8.3}$$

Using (8.1) and (8.3) and putting $t_0 = 0$ for functions $f(t, t_0)$ and $S(t, t_0)$, we obtain the distribution density of the time delay Δt for registering the same annihilation event in two identical detectors (in a coincidence scheme):

$$p_{CTR}(\Delta t) = \int_0^{T-|\Delta t|} p_s(t) p_s(t + |\Delta t|) dt, \tag{8.4}$$

where T is the time to reach the pulse amplitude or the duration of the leading edge of the scintillation pulse. In formula (8.4), $p_s(t)$ is defined as

$$p_s(t) = C_s Y S(t) P_h \left(1 - P_h \int_0^t S(\tau)\, d\tau\right)^{Y-1} \left(1 - \int_0^t S(\tau)\, d\tau\right), \tag{8.5}$$

where Y is the light yield corresponding to the absorbed energy, P_h is the probability of registering a single photon in the entire leading edge of the pulse, and C_s is a normalizing constant.

Expression (8.5) can also be applied to the whole scintillation pulse, since the expressions for functions $f(t, 0)$ and $S(t, 0)$ are valid on the whole time scale $t \in (0, +\infty)$, $T \to \infty$. Therefore, $P_h = 1$, and $\int_0^\infty S(\tau)\, d\tau = 1$, and the expression for $p_s(t)$ can be simplified to:

$$p_s(t) = C_s Y S(t) \left(1 - \int_0^t S(\tau)\, d\tau\right)^Y \tag{8.6}$$

Consequently, the expression for $p_{CTR}(\Delta t)$ will be as follows:

$$p_{CTR}(\Delta t) = \int_0^\infty p_s(t) p_s(t + |\Delta t|) dt \tag{8.7}$$

The variance of the random value Δt is

$$D[\Delta t] = \int_{-\infty}^\infty p_{CTR}(t)\ (t - M_{CTR}[\Delta t])^2 dt, \tag{8.8}$$

where

$$M[\Delta t] = \int_{-\infty}^\infty p_{CTR}(t)\ t\, dt. \tag{8.9}$$

The full width at half maximum (FWHM) of the distribution equals

$$2.355 \cdot D[\Delta t] \tag{8.10}$$

8.1.2 Accounting for the Energy Deposit Fluctuation Along the Scintillator

As a rule, in laboratory conditions, the event of annihilation of the positron emitted by a ^{22}Na source is used for CTR measurements. Due to this reason, we focus our CTR evaluation on the 511 keV γ-quanta energy deposit. A photo-absorption of γ-quanta in the scintillator is a random process. The probability to absorb a γ-quantum in a layer of the scintillator of the thickness x is described by the following well known equation [18]:

$$F(x) = 1 - \ exp\left(-\mu_{ph}x\right), \tag{8.11}$$

where the partial absorption coefficient $\mu_{ph} = n_0\sigma_{ph}$ depends on the concentration of absorbing atoms n_0 and the cross-section of the photo-absorption σ_{ph}. The probability density to absorb a γ-quantum in a slice $[x, x + dx]$

$$G(x) = \frac{dF}{dx} = \mu_{ph} \ exp\left(-\mu_{ph}x\right). \tag{8.12}$$

The expression for the probability density $G(t)$ of the time delay for the photo-absorption of the γ-quantum is obtained from the condition $G(x)dx = G(t)dt$, $x = ct$. Therefore,

$$G(t) = \mu_{ph}c \ exp\left(-\mu_{ph}ct\right). \tag{8.13}$$

Consider the case when the crystal has a finite dimension L along the trajectory of γ-quantum. Thus, the function G(t) has a non-zero value over the time interval [0, L/c]. In this interval, it should be normalized to one:

$$C_g{}^{-1} \int_0^{\frac{L}{c}} G(t) = 1, \tag{8.14}$$

$$C_g = 1 - \ exp\left(-\mu_{ph}L\right), \tag{8.15}$$

where Cg is a normalization constant. Thereby, $G(t)$ will take the following form:

$$G(t) = \frac{\mu_{ph} c}{1 - exp\left(-\mu_{ph} L\right)} \; exp\left(-\mu_{ph} ct\right). \tag{8.16}$$

The influence of the distribution of the energy deposition point of the γ-quantum is taken into account by integrating the probability density of creation the time stamp $p_s(t)$ over the time moment of the energy deposit of the γ-quantum t_0 with the probability density $G(t_0)$:

$$p_s'(t) = C_s' \int_0^{\frac{L}{c}} S(t, t_0) \left(1 - \int_{t_0}^{t} S(\tau, t_0)\, \mathrm{d}\tau\right)^{Y} G(t_0)\, \mathrm{d}(t_0). \tag{8.17}$$

The calculation of the distribution density $p'_{CTR}(\Delta t)$ of the time delay of the detection of one event in two identical detectors (in a coincidence scheme) taking into account the energy deposition distribution is accomplished using Eq. (8.7).

8.2 Coincidence Time Resolution Measurements

There are two extensively used methods to evaluate CTR: the measurement of annihilation products and the detection of energy deposit from a single charged particle. A typical scheme for the coincidence time measurements with a ^{22}Na source is presented in Fig. 8.1.

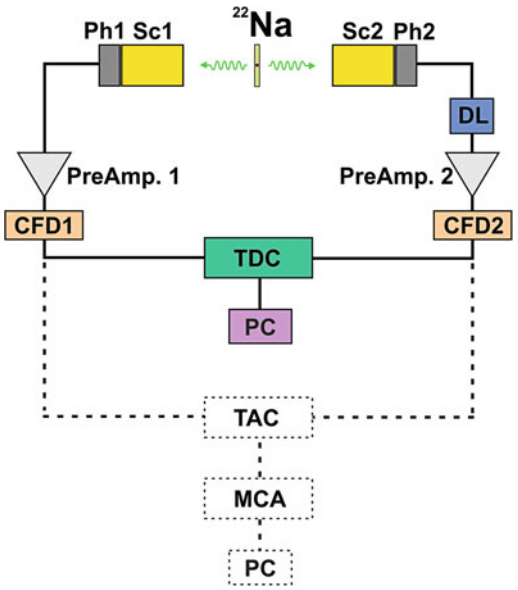

Fig. 8.1 Typical scheme for coincidence time resolution measurements

Preferably, all the samples used in comparable CTR experiments have to be cut in the same size and from the same crystal and measured at nominally the same conditions. In fact, the typical test bench design was developed on the demand by the PET community to evaluate detecting modules. They demonstrate the advantage of TOF capabilities for PETs and are in use by many groups for decades.

The ^{22}Na positron source, placed between two aluminium plates of at least 0.6 mm thick, is positioned on the main optical axis passing the scintillation crystals Sc1 and Sc2. Two annihilation γ-quanta, getting into the crystals, cause the formation of the signal recorded by photodetectors Ph1 and Ph2. One of the channels, for instance, channel Sc1 + Ph1, forms a start signal, whereas channel Sc2 + Ph2 is used to create a stop signal. The signals from both photodetectors pass through preamplifiers (Pre-Amp.1 and PreAmp.2, respectively). In addition, the stop signal passes through the coaxial delay line. This is necessary to shift the time scale for the distribution of the difference between the start and stop signals from zero. After that, the signals pass the Constant Fraction Discriminators (CFD1 and CFD2), which form the output signal along the leading edge of the scintillation pulse. When using the CFDs, the effect of changing the position of the time stamp for isochronous signals with different amplitudes is diminished. After CFDs, the signals pass on to a time-to-digital converter (TDC) or a bunch of time-amplitude converters (TACs) and a multichannel analyser (MCA). Then the generated data stream is sent to a PC, where a CTR histogram is built.

To avoid inconsistence due to different parameters of the CTR setups used by different research groups, the following discussion will be based on the CTR measurements of the group at Fondazione Bruno Kessler (FBK, Italy). The data reported by other research groups are regarded here in the context of the influence of different factors on the data obtained. To perform the measurements, nominally identical pixels with a cross-section of 3×5 mm^2 and a length from 3 to 20 mm were combined into detecting modules with SiPMs. In particular, two types of SiPMs have been used in the measurements: RGB-HD SiPMs and NUV-HD SiPMs, both with 4x4 mm^2 active area and 25 μm cell pitch and maximal photo-detection efficiency (PDE) in green and blue spectral ranges, respectively [6, 7]. The pixels were optically coupled to SiPMs by using Cargille Meltmount optical glue with refractive index $n = 1.539$. The pixels were wrapped in Teflon. Due to a strong sensitivity of SiPM noise parameters to temperature, the detection unit was thermally stabilized. As a rule, the data acquisition is performed at room temperature (RT) or a few tens of degrees below RT.

As discussed above, two nominally identical detecting modules in the CTR measurements are placed on the same axis with a radioactive source at the same distance from the source. The SiPM signal is red out by two double-stage amplifiers with two outputs each. The first output of the amplifiers is used to discriminate 511 keV events through charge integration of the scintillation signals. The second output of the amplifiers is for a Pole-Zero (PZ) compensation circuit, an analog filtering circuit allowing the pickup of low-noise signal at low threshold. The SiPMs are operated at an optimal overvoltage of 10–12 V. The CTR setup is placed in a climatic chamber with temperature and humidity control.

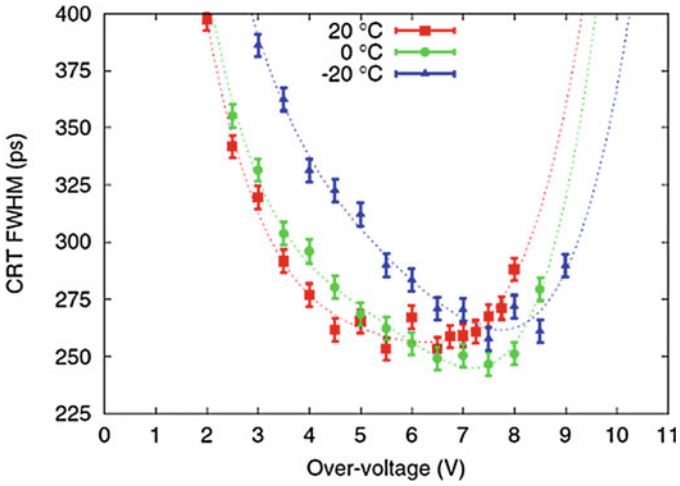

Fig. 8.2 Typical dependences of CTR FWHM on over-voltage measured with GAGG:Ce crystals of 3 × 3 × 5 mm in size at three temperatures (courtesy of Dr. A. Gola and Dr. A. Mazzi). Crystal was taken from the early stage of GAGG development by Fomos Crystals

The setup allows also the energy resolution (ER) measurements. In this case, just a single detector is operated. The energy spectra are obtained by charge integration of the scintillation signals with an integration window of 500 ns. The spectra are corrected for the SiPM nonlinearity by using the 1274 keV events of ^{22}Na. Comparison of the temperature dependence of CTR and energy resolution is quite useful to distinguish the role of temperature-dependent processes.

While working with SiPM, two parameters are optimised to get the optimal CTR. First, the silicon photomultipliers require the optimization of over-voltage applied to the device. Figure 8.2 shows typical over-voltage dependences of FWHM in CTR response. It is worth noting that the CTR value is sensitive to the temperature (see CTR curves measured at different temperatures in Fig. 8.2). Therefore, the temperature stabilization is mandatory in comparative measurements.

The next parameter of importance in CTR measurements is the measurement threshold. The threshold level is determined by the noise of the photo-receiver and electronics. Typical dependence of CTR FWHM on the threshold measured with GAGG:Ce crystal of last generation at an integration time of 850 ns at temperature of 20 ± 0.1 °C is shown in Fig. 8.3.

An optimal combination of over-voltage and threshold is always a compromise, which is also affected by the dark current noise.

In practice, a histogram following the distribution of delay between signals and called the coincidence time diagram is obtained. The shape of the diagram is close to a Gaussian distribution. The CTR is usually defined as FWHM of the distribution (Fig. 8.4).

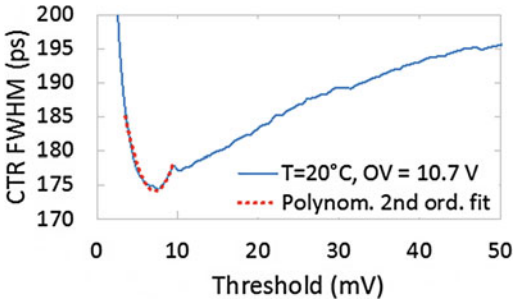

Fig. 8.3 Typical dependence of CTR FWHM as a function of the threshold measured with 3 × 3 × 5 mm GAGG multidoped crystals and RGB-HD SiPMs with 2 × 4 × 25 μm cell at a bias of 39 V and an over-voltage of 10.7 V. (Courtesy of Dr. A. Gola and Dr. A. Mazzi)

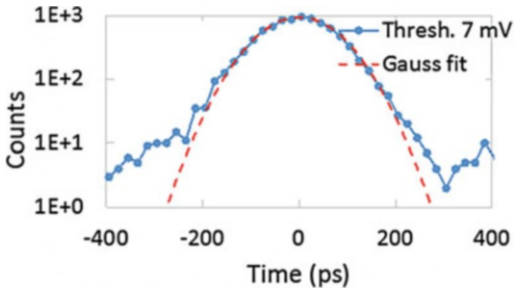

Fig. 8.4 Coincidence timing histogram measured with 3x3x5 mm GAGG multidoped crystals and RGB-HD SiPMs 2 × 4 × 25 μm cell at a threshold of 7 mV. CTR FWHM is defined to be 175 +/−2 ps. (Courtesy of Dr. A. Gola and Dr. A. Mazzi)

Another scheme utilizes the detection of the energy deposited by a charged particle via the light detection from opposite ends of a scintillation crystal, which is usually a bar with one dimension substantially longer than the other two.

One of the possible solutions for CTR measurements with *mip* is shown in Fig. 8.5. It might be based on the direct digitization of signals by digitizers. The charge particle beam passes through the micro-channel-plate detector (MCP), forming a reference signal, which is amplified in PreAmp. 3. After MCP, the beam enters the crystal bar, and scintillation is detected by SiPMs at the ends of the bar. All these three signals enter the digitizer board, for instance, CAEN V1742, in which the signals are directly digitized and time stamped. Future, an average signal of arrival time $(t_1 + t_2)/2$ is calculated and the histogram of the difference $(t_1 + t_2)/2 - t_{ref}$ is formed.

The minimum ionizing particles, particularly muons, are usually exploited in such type of measurements. However, due to a low rate of *mips* at the see level at the Earth (~200 p/m^{2}s) the routine measurements become enormously long, and high stability and long-term thermostabilization of the setup are required. Muon beam utilization reduces the duration of the data acquisition by orders of magnitude. Nevertheless, the particle beams are used quite rarely, just for strict assessment of the detector timing properties for high energy physics experiments. Otherwise, it is still not a tool for routine measurements. The spectrum of the energy deposited by a mip has a Landau shape due to stochastic fluctuations within a thin crystal, which makes the

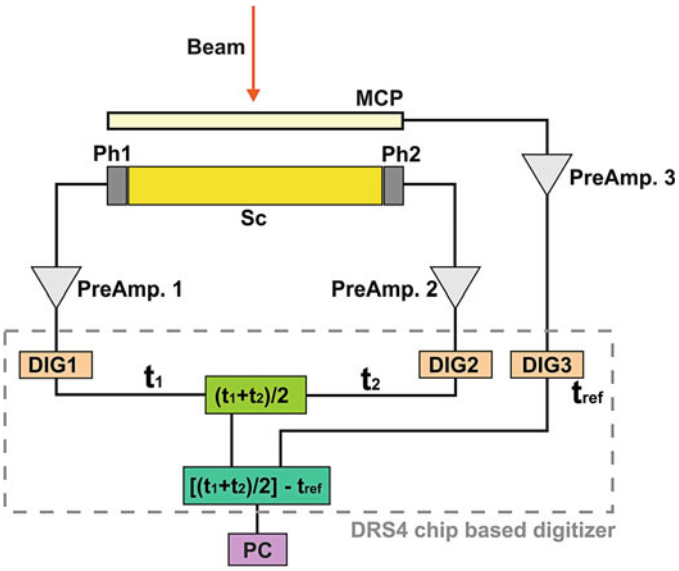

Fig. 8.5 Typical scheme for coincidence time resolution measurements with a minimum ionizing particle

analysis more complicated. Moreover, this method requires careful tracking of the *mip* entering the crystal to account for the difference in the time of the light walk to both SiPMs.

The dual end readout found a practical application: reading out the signal from 3x3x50 mm LYSO bars assembled in the Timing Layer Detector around the Tracker in the CMS Collaboration experiment at CERN with the detection by SiPMs from both narrow ends of the crystal, which allows for the improvement of the precision in the mip time stamp precision measurements at this facility down to a level of 30 ps [19].

The dual readout was also found to be quite useful to define the depth of interaction in pixels of detecting matrices in PET scanners [20]. By reading out both ends of a 20 mm-long LSO crystal pixel, the depth of interaction can be measured with the FWHM uncertainty bellow 5 mm corresponding to the timing uncertainty FWHM of ~10 ps.

8.3 The Influence of Non-ideality of the Detecting Chain

To show how the difference in properties of experimental detecting chains might cause the variation in the results obtained, let us consider a change of CTR as a result of the variation of parameters in the expressions described in previous paragraphs.

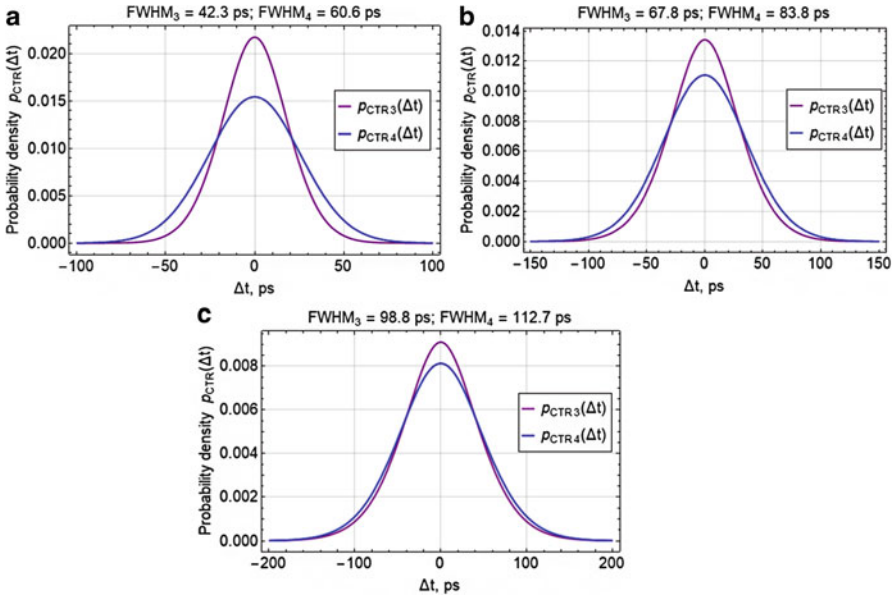

Fig. 8.6 The probability density distribution of the time delay Δt between the signals created by annihilation γ-quanta in two identical detectors equipped with 3 mm-long GAGG crystal at $\sigma_t = 0$ (red) and $\sigma_t = 17$ ps (blue) and different photodetection efficiencies of the photo-receiver: 1 (**a**), 0.4 (**b**), and 0.2 (**c**). The FWHMs of the distributions are indicated

As above, we use an example of GAGG crystal. To simplify the analysis, we approximate the experimentally obtained multicomponent decay curve by a single-exponential decay with the decay time constant $\tau_d = 80$ ns. In a thin, 3 mm-thick sample, CTR was evaluated using formulas (8.3, 8.4, 8.5, 8.6 and 8.7). The results are shown in Fig. 8.6. The curve $p_{CTR3}(\Delta t)$ corresponds to an ideal photo-receiver and detecting chain. The curve $p_{CTR4}(\Delta t)$ is calculated by taking into account the dispersion σ_t (see Chap. 1), from which σ_{sc} is excluded. For a numeric evaluation, as a starting point, we use σ_t achieved in the most advanced electronic part of the detecting system [19], which is designed for fast timing in CMS experiment at CERN. The CTR simulated for an ideal detecting chain with a photo-receiver having PDE = 1, is quite spectacular. As the PDE is reduced to 0.4 or 0.2, the deterioration of CTR becomes substantial and the FWHM exceeds 100 ps, as usually observed in practice.

Note that a low PDE is one of the key factors deteriorating the results of CTR experiments. The degraded PDE results in a smaller amount of the photons in the leading edge of the scintillation to be converted into photoelectrons.

In reality, σ_t has also a bench-to-bench scattering and influences the CTR value even in a stronger way than PDE. Fig. 8.7 shows the distribution of the time delay between the signals from two identical GAGG-based detectors with PDE reduced down to 0.4 and tripled σ_t. The simulated CTR is by a factor of two worse than that for ideal measurement conditions.

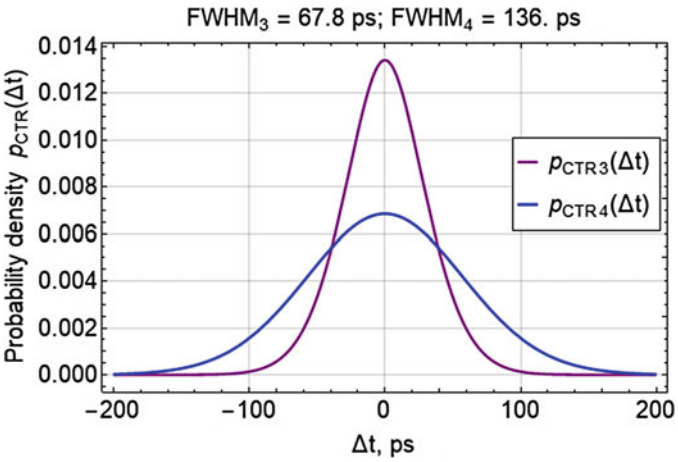

Fig. 8.7 The probability density distribution of the time delay Δt between the signals created by annihilation γ-quanta in two identical detectors equipped with 3 mm-long GAGG crystal at PDE = 0.4 and $\sigma_t = 0$ (red) and $\sigma_t = 51$ ps (blue). The FWHMs of the distributions are indicated

Evolution of the capabilities of the detector chains applied for time resolution measurements can be traced by following the development of the results for time resolution obtained with bismuth germanate (BGO) scintillator. First measurements [21] showed CTR FWHM at the level of 1.9 ns. The introduction of digital SiPMs [22] allowed for reaching a single device time resolution FWHM at the level of 220 ps for 3000 keV γ-quanta. Recently, combining Cherenkov and scintillation signals enabled obtaining CTR with a thin BGO crystal at the level of 165 ps [23].

8.4 The Influence of Fluctuations in Energy Deposition Time and Light Propagation Time

The fluctuation of the energy deposit time in a coincidence measurement scheme has also a contribution to the CTR deterioration. As in previous section, we use expressions (8.1, 8.2, 8.3, 8.4, 8.5, 8.6 and 8.7, 8.17) for evaluation of the fluctuations in time between energy deposit events of annihilation γ-quanta from a ^{22}Na source detected by two identical GAGG-based detectors. Figure 8.8 shows the distribution of the time delay between the signals from two identical detectors with GAGG crystals of different length. Figure 8.9 shows the normalized results of the FWHM simulation and experimental measurements [24, 25].

The experimental points are below the curves corresponding to the ideal photon detection conditions and are in between the curves simulated for $\sigma_e = 17$ and 51 ps and reduced PDE. This is an indication of a high technical level of the benches for the measurements reported in [24, 25]. Note that the CTR FWHM weakly depends on the crystal length when the detection system is not optimized, as evidenced by the

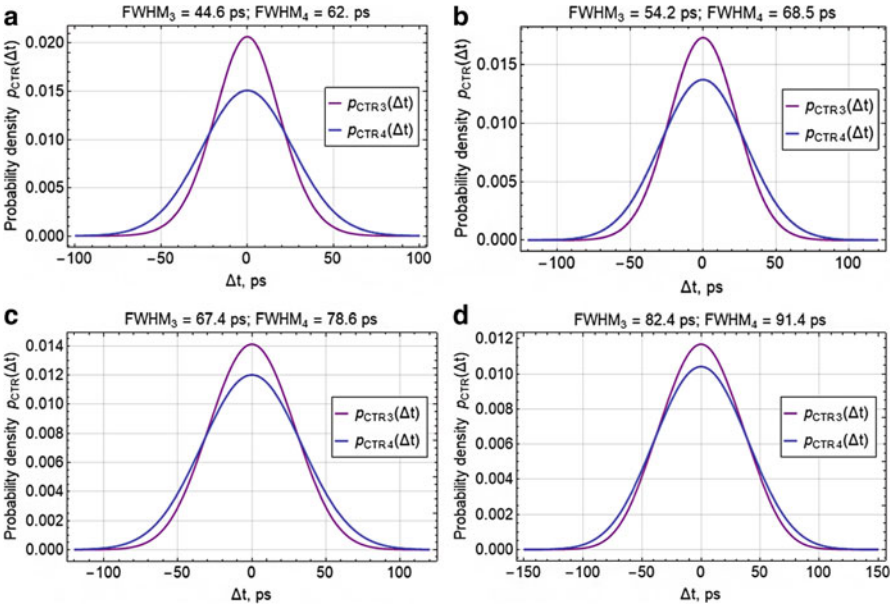

Fig. 8.8 The probability density distribution of the time delay between the signals from two nominally identical GAGG-based detectors at PDE = 1 and $\sigma_t = 0$ (red) and $\sigma_t = 17$ ps (blue) for different lengths of the GAGG crystal: 5 (**a**), 10 (**b**), 15 (**c**), and 20 mm (**d**)

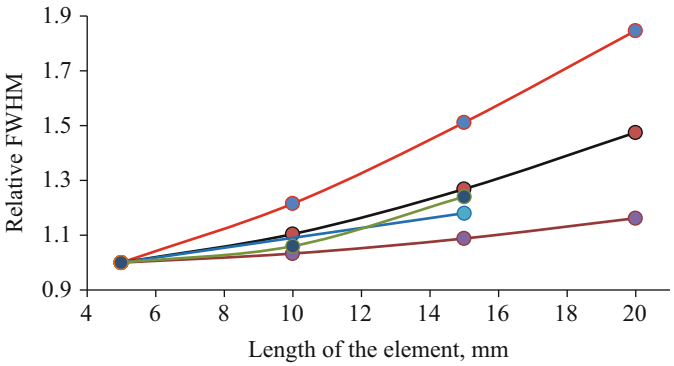

Fig. 8.9 Pixel length dependence of normalized FWHM simulated for CTR experiment using pixels of multidoped GAGG:Ce with a cross-section of 3x3 mm^2 for an ideal detecting system with $\sigma_t = 0$ and PDE = 1 (red), $\sigma_t = 17$ ps and PDE = 1 (black), and $\sigma_t = 51$ ps and PDE = 0.4 (brown), and the dependences obtained experimentally in [21] (marine) and [22] (green). The measurement error was +/−3%

curve simulated for $\sigma_t = 51$ ps and PDE = 0.4. Thus, the fluctuations of the energy deposit time begins to manifest itself when the CTR FWHM is less than 100 ps, whereas the test bench allows for the measurement of even narrower coincidence timing histogram with a shorter time per bin.

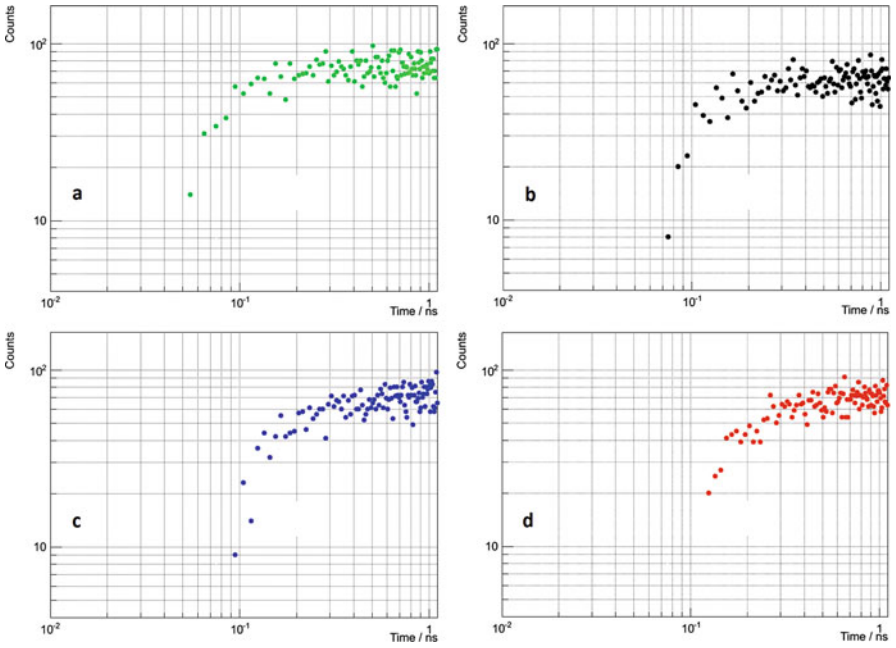

Fig. 8.10 GEANT4 simulated initial part of the scintillation pulse on the 3x3mm surface of GAGG scintillator of different length, 5 (**a**), 10 (**b**), 15 (**c**), and 20 mm (**d**), for 511 keV energy deposit at the middle of the scintillation element

The dependence of light collection on the dimensions of the scintillation element is another effect acting in the combination with the effect of the energy deposit time distribution discussed above. This effect was pointed out as a possible origin of the change of the light output in volumetric scintillation elements for the first time in [26, 27]. Moszynski et al. [28, 29] were the first who pointed out that the influence of light collection on the shape of the scintillation pulse in a large plastic scintillator has to be not overlooked.

In scintillation elements of a small volume, the light output does not depend on the crystal cross-section, however, it shows a reduction with increasing crystal length [15]. In crystals with a low Stokes shift, like in the luminescence centers Ce^{3+}, a decrease in the light collection coefficient in longer crystals is caused by self-absorption. The formation of a scintillation pulse in the case of energy deposit by high energy particles is discussed in Chap. 2. In a small detector element, which is used in CTR measurements, the formation of a light pulse depends both on the energy deposit position and the contribution of multiple photon scattering. Figure 8.10 shows the GEANT4 simulation results of the leading edge of the scintillation pulse on the crystal surface coupled to a photo-receiver for GAGG-based scintillator with a cross section of 3x3 mm wrapped in Teflon. The results are presented for different element length at the energy deposit at the middle of the scintillation element.

A combination of the direct and scattered photons makes the leading edge of the scintillation pulse less steep and, consequently, deteriorates the precision of the measurements in each channel, what results in increased CTR FHWM. In practical use, this effect is mitigated by several approaches as described in [30, 31].

8.5 The Time Precision Limit Set by Scintillation

In the last section of the chapter, we discuss the precision limits imposed to the measuring chain by a scintillator. We have shown that the accuracy of the time measurements essentially depends on the type of scintillator, whereas the shape of the leading edge of a scintillation pulse has a primary role in determining the accuracy of time measurements. The question with cross-luminescent and self-activated scintillators is quite clear: in both cases, the accuracy is improved by a better light yield and a short rise time. In activated scintillators, further progress is expected as a result of the search for the methods, physical and technological, to accelerate the energy transfer to luminescent centers and to facilitate the increase in the amount of the scintillation photons in the leading edge of the scintillation response. Meanwhile, the fundamental process determining the population of the radiating centers is intracentre relaxation. The intracentre relaxation time for Ce^{3+} ion was determined to be 500 fs (see Ch.5). Obviously, it weakly depends on the crystalline environment and is determined by energy gaps between the lower and higher excited states.

In an ideal activated scintillation medium, where the Onsager spheres cover the entire volume and exclude the free transfer of carriers, the intracentre relaxation is a fundamental constraint limiting the operation of scintillators in the measurements seeking a better time resolution. Of course, further progress and substantial improvement of photo-receivers and wideband electronics are necessary to ensure better operation of the detectors. However, the ambitious goal of achieving the accuracy of time measurements at the 10 ps level or even better using scintillators has no basic physical limits and is realistic. There is a physical ground to believe that the future development of scintillation material technologies will meet this challenge.

References

1. R. Post, L. Schiff, Statistical limitations on the resolving time of a scintillation counter. Phys. Rev. **80**, 1113 (1950)
2. E. Gatti, V. Svelto, Theory of time resolution in scintillation counters. Nucl. Instrum. Methods **4**, 189–201 (1959)
3. L.G. Hyman, R.M. Schwarz, R.A. Schluter, Study of high-speed photomultiplier systems. Rev. Sci. Instrum. **35**, 393–406 (1964)
4. L.G. Hyman, Time resolution of photomultiplier systems. Rev. Sci. Instrum. **36**, 193–196 (1965)

5. F. Lynch, in *Basic limitation of scintillation counters in time measurements. At Nuclear Science Symposium and 14th Scintillation and Semiconductor Counter Symposium*, Washington, DC, 11–13 December 1974
6. E. Gatti, V. Svelto, Revised theory of time resolution in scintillation counters. Nucl. Instrum. Methods **30**, 213–223 (1964)
7. E. Gatti, V. Svelto, Review of theories and experiments of resolving time with scintillation counters. Nucl. Instrum. Methods **43**, 248–268 (1966)
8. Y.K. Akimov, S.V. Medved, On the theory of the resolving time of scintillation counters. Nucl. Instrum. Methods **78**, 151–153 (1970)
9. S. Derenzo, M. Weber, W. Moses, C. Dujardin, Measurements of the intrinsic rise time of common inorganic scintillators. IEEE Trans. Nucl. Sci. **47**, 860–864 (2000)
10. M. Moszynski, Study of light collection process from cylindrical scintillators. Nucl. Instr. Methods **134**, 77–85 (1976)
11. S. Derenzo, W.-S. Choong, W. Moses, Fundamental limits of scintillation detector timing precision. Phys. Med. Biol. **59**, 3261–3286 (2014)
12. S. Siefert et al., A comprehensive model to predict the timing resolution of SiPM-based scintillation detectors: theory and experimental validation. IEEE Trans. Nucl. Sci. **59**, 190–204 (2012)
13. A. Schwarzschild, A survey of the latest developments in delayed coincidence measurements. Nucl. Instr. Methods **21**, 1–16 (1963)
14. M.V. Nemallapudi et al., Sub-100 ps coincidence tme resolution for positron emission tomography with LSO:Ce codoped with Ca. Phys. Med. Biol. **60**, 4635–4649 (2015)
15. S. Gundacker et al., State of the art timing in TOF-PET detectors with LuAG, GAGG and L(Y)SO scintillators of various sizes coupled to FBK-SiPMs. J. Instrum. **11**, 08008 (2016)
16. E. Pratiwi, K. Kamada, S. Yamamoto, M.N. Ullah, J.-Y. Yeom, A. Yoshikawa, J.H. Park, Studies on sub-millimeter LYSO:Ce, Ce:GAGG, and a new Ce:GFAG block detector for PET using digital silicon photomultiplier. Nucl. Instr. Methods **911**, 115–122 (2018)
17. S. Gundacker, Dissertation, Vienna University of Technology, 2014
18. A. Leroy, P.-G. Rancoita, *Principles of Radiation Interaction in Matter and Detection* (Word Scientific Publishing Co Pvt Ltd, New Jersey, 2016)
19. Technical Proposal for a MIP Timing Detector in the CMS experiment Phase 2 upgrade, Tech. Rep. CERN-LHCC-2017-027. LHCC-P-009, CERN, Geneva (Dec 2017)
20. Y.F. Yang, P. Dokhale, Depth of interaction resolution measurements for a high-resolution PET detector using position-sensitive avalanche photodiodes. Phys. Med. Biol. **51**, 2131–2142 (2006)
21. M. Moszunski, C. Gresset, J. Vacher, R. Odry, Timing properties of BGO scintillator. Nucl. Instr. Methods **188**, 403–409 (1981)
22. J. Petzoldt, K. Romer et al, in *Fast Timing with BGO (and Other Scintillators) on Digital Silicon Photomultipliers for Prompt Gamma-Imaging*, IEEE 978-1-4799-6097 (2014)
23. R. Martinez Turtos, S. Gundacker, E. Auffray, P. Lecoq, Towards a metamaterial approach for fast timing in PET: Experimental proof-of-concept. Phys. Med. Biol. **64**, 185018 (2019). https://doi.org/10.1088/1361-6560/ab18b3
24. A. Mazzi, Private communication, March 2018
25. N. Kratochwil, S. Gundacker, M. Lucchini, E. Auffray, *at VCI 2019 Vienna, Austria*, 18–-22 February 2019
26. P.B. Lyons, J. Stevens, Time response of plastic scintillators. Nucl. Instr. Methods **114**, 313–320 (1974)
27. B. Sipp, J. Miehe, Fluorescence self-absorption effect and time resolution in scintillator counters. Nucl. Instr. Methods **114**, 255–262 (1974)
28. M. Moszynski, Study of light collection process from cylindrical scintillators. Nucl. Instr. Methods **134**, 77–85 (1976)

29. M. Moszynski, B. Bengston, Light pulse shapes from plastic scintillators. Nucl. Instr. Methods **142**, 417–434 (1976)
30. Laser etched scintillation detector blocks with internally created reflectors, US Patent 9664800, 2016
31. Method of manufacturing garnet interfaces and articles containing the garnets obtained there from, US Patent 9650569, 2017

Glossary

Y	scintillation yield in photons
E_γ	energy of absorbed gamma quantum
$\beta \cdot E_g$	the mean energy necessary for the formation of one thermalized electron-hole pair
E_g	band gap
S	efficiency of the energy transfer to luminescence center
Q	quantum yield of luminescence
LY	light yield of scintillation in photons upon the absorption of one MeV energy of gamma-quanta
S(t)	scintillation intensity
λ	wavelength
ν	wave number
$\Delta\lambda_{sc}$	width of a scintillation band
E, E_{kin}	kinetic energy
E^i_{sh}	energy of an inner shell of an atom
K-, L-	inner electronic shells
M-	inner electronic shell
Z	charge of atomic nucleus
Ry	Rydberg energy
A	atomic number
c	speed of light
v_0	initial velocity
m, M	particle mass
GAGG	gadolinium aluminum gallium garnet ($Gd_3Al_2Ga_3O_{12}$)
SiPM	silicon photomultiplier
YAG	yttrium aluminum garnet ($Y_3Al_5O_{12}$)
PWO	lead tungstate ($PbWO_4$)
PWO-II	second-generation lead tungstate scintillator
LSO	lutetium silicate (Lu_2SiO_5)
LYSO	lutetium silicate with partial substitution of lutetium by yttrium

M. Korzhik et al., *Physics of Fast Processes in Scintillators*, Particle Acceleration and Detection, https://doi.org/10.1007/978-3-030-21966-6

YSO	yttrium silicate (Y_2SiO_5)
GdYAGG	gadolinium aluminum gallium garnet with partial substitution of gadolinium by yttrium
GdLuAGG	gadolinium aluminum gallium garnet with partial substitution of gadolinium by luthetium
YAP	yttrium aluminum perovskite ($YAlO_3$)
LuAP	lutetium aluminum perovskite ($LuAlO_3$)
$\mathbf{X_0}$	radiation length
$\mathbf{R_M}$	Moliere radius
BGO	bismuth trigermanate ($Bi_4Ge_3O_{12}$)
GEANT4	software package to make Monte-Carlo simulation of radiation with matter
LHC	large hadron collider
HL LHC	large hadron collider at high luminosity
ATLAS	a general-purpose experiment at LHC
CMS	a general-purpose experiment at LHC
PET	positron emission tomography
HEP	high energy physics
TOF	time of flight technique
FNRR	fast neutron radiography
FNRT	fast neutron resonance transmission
Am	amplitude
MCA	multi-channel analyzer
$\boldsymbol{\tau_d}$,$\boldsymbol{\tau_r}$	decay and rise constants of scintillation kinetics
σ	standard deviation
UV	ultraviolet
VUV	vacuum ultraviolet
IR	infra-red
e, $\mathbf{e^-}$	electron
h	hole
ex	exciton
CSDA	continuous-slowing-down approximation
ESTAR	program calculating stopping power, density effect parameters, range, and radiation yield tables for electrons in various materials
DOS	density of states
IBL	intraband luminescence
CL	cross-luminescence
STE	self-trapped exciton
$\mathbf{R_{Ons}}$	Onsager radius
$\mathbf{R_c}$	capture radius
$\mathbf{D_e}$, $\mathbf{D_h}$	diffusion coefficients of electrons and holes
$\mathbf{D_{ex}}$	diffusion coefficient of excitons
FTD	Frenkel-type defects
TSL	thermally stimulated luminescence

K	Bolzman constant
EPR	electron paramagnetic resonance
RE	rare earth ions
PMT	photomultiplier
CCD	charge coupled device
BBO	barium boron oxide
TCSPC	time-correlated single photon counting technique
LED	light emitting diode
DA	differential absorption
FWHM	full width at half maximum
XANES	X-ray Absorption Near Edge Spectroscopy
CT	charge transfer transitions
MPB	multiple parabolic bands model
CTR	coincidence time resolution
ER	energy resolution
PDE	photodetector efficiency
DAP	donor-acceptor pair
QD	quantum dot
NC	nanocrystal
CVD	chemical vapor deposition production method
HPHT	high pressure high temperature production method
GS20	Li-based scintillation glass

Index

M. Korzhik et al., *Physics of Fast Processes in Scintillators*, Particle Acceleration and Detection, https://doi.org/10.1007/978-3-030-21966-6